UNICA

UNIVERSITÀ
DEGLI STUDI
DI CAGLIARI

Ph.D. DEGREE IN
Electronic and Computer Engineering
Cycle XXXVI

TITLE OF THE Ph.D. THESIS

Development and Characterization of highly flexible and conformable electronic devices for wearable applications

Scientific Disciplinary Sector(s)

ING-INF/ 01

Ph.D. Student:	Antonello Mascia
Supervisor	Prof. Piero Cosseddu
Co-Supervisor	Prof.ssa Annalisa Bonfiglio

Final exam. Academic Year 2022/2023
Thesis defense: February 2024 Session

Abstract

As shown in the story, humanity has tried to develop objects, tools, and devices that could first help to survive in a difficult environment and then improve everyday life. The idea of creating objects that can be worn to restore or improve human abilities or to help during daily routine has fueled technological development and research since the beginning of technological advancement. Wearable technology goes back hundreds of years, and one of the first examples is the invention of glasses to restore the sight, or the wristwatch when big watches were reduced to something that people could take with them anywhere.

However, it could be considered that, only when the computer age was established, wearable electronic devices were developed and started to spread out and get into the market.

Wearable electronics are a category of technological devices that can be transferred into clothes or directly in touch with the body, typically as accessories or clothing, and these devices can be designed to provide different functionalities, such as notification sending, communication abilities, health and fitness monitoring, and even augmented or virtual reality experiences.

In recent years, organic electronics have been deeply investigated as a technology platform to develop devices using biocompatible materials that can be deposited and processed on flexible and even ultra-flexible substrates. The high mechanical flexibility of such materials leads to a new category of devices going beyond wearable devices to more-than-wearable applications.

In this context, epidermal electronics is a closely related field that focuses on developing electronic devices that can be directly attached to the skin with a minimally invasive, comfortable, and possibly enabling long-term application.

The main object of this PhD research activity is the development and optimization of a technology for the realization of wearable and more-than-wearable devices, able to meet all the new needs in this field, such as the low-cost production process and the mechanical flexibility of the devices and deposition over large areas on unconventional substrates, exploiting all the features and advantages of the organic electronic field, but also finding some solution to overcome the disadvantages of this technology. In this work, different application fields were studied, such as health monitoring through biopotential acquisitions, the development, and optimization of multimodal physical sensors able to detect simultaneously pressure and temperature for tactile and artificial skin applications, and the development of flexible high-performing transistors as a building block for the future of wearable and electronic-skin applications.

List of Publications

- Baldazzi, G., Spanu, A., Mascia, A., Viola, G., Bonfiglio, A., Cosseddu, P., & Pani, D. (2021, September). Validation of a Novel Tattoo Electrode for ECG Monitoring. In 2021 Computing in Cardiology (CinC) (Vol. 48, pp. 1-4). IEEE.

- Spanu A, Mascia A, Baldazzi G, Fenech-Salerno B, Torrisi F, Viola G, Bonfiglio A, Cosseddu P, Pani D, Parylene C-Based, Breathable Tattoo Electrodes for High-Quality Bio-Potential Measurements, Front Bioeng Biotechnol, 2022;

- Spanu, M. Taki, G. Baldazzi, A. Mascia, P. Cosseddu, D. Pani, A. Bonfiglio, Epidermal Electrodes with Ferrimagnetic/Conductive Properties for Biopotential Recordings, Bioengineering, 2022;

- R. Collu, A. Mascia, A. Spanu, M. Fraschini, P. Cosseddu and M. Barbaro, A wearable electronic system for EEG recording, 17th Conference on Ph.D Research in Microelectronics and Electronics (PRIME), Villassimius, Ca, Italy, 2022;

- Mascia, A. Spanu, A. Bonfiglio and P. Cosseddu, "Highly sensitive, flexible, force sensors based on short channel devices," 2022 IEEE International Flexible Electronics Technology Conference (IFETC), Qingdao, China, 2022;

- Spanu, A., Losi, T., Mascia, A., Bonfiglio, A., Caironi, M., & Cosseddu, P. (2023). Submicrometer-Channel Organic Transistors with MHz Operation Range on Flexible Substrates by a Low-Resolution Fabrication Technique. Advanced Materials Technologies, 8(1), 2200891.

- Sedda, G., Baldazzi, G., Spanu, S., Mascia, A., Spanu, A., Cosseddu, P., Bonfiglio, A. and Pani, D, A Modular BLE-Based Body Area Network Embedded into a Smart Garment for Rescuers Real-Time Monitoring in Emergency Scenarios, In Proceedings of the 16th International Joint Conference on Biomedical Engineering Systems and Technologies (BIOSTEC 2023) - Volume 1: BIODEVICES, pages 177-181;

- Mascia, A., Collu, R., Spanu, A., Fraschini, M., Barbaro, M., & Cosseddu, P. (2023). Wearable System Based on Ultra-Thin Parylene C Tattoo Electrodes for EEG Recording. Sensors, 23(2), 766.

- Mascia, A., Spanu, A., Bonfiglio, A. et al. Multimodal force and temperature tactile sensor based on a short-channel organic transistor with high sensitivity. Sci Rep 13, 16232 (2023).

Conference Presentations

- 21-24/08/ 2022 4th IEEE International Flexible Electronics Technology Conference (IFETC) 2022, Qingdao, China;
- November 28, 2022, MRS fall Meeting, Boston, Massachusetts;
- 06/09/2023-09/09/2023, 54° meeting annuale Società Italiana di elettronica, Noto (SR), Sicily, Italy;

Acknowledgment

This thesis work is the result of a journey that lasted three years, in which, among the various changes, I have grown academically, professionally, and personally. This work would not have been possible without the support and guidance of several individuals who contributed with their assistance, in one way or another, to the preparation and achievement of this result. I would like to express my deepest gratitude to my supervisor Professor Piero Cosseddu who guided me and enabled me to conclude my PhD with his indubitably expertise. Moreover, I am also extremely grateful for the relationship that was created with my supervisor, as I can say that it goes beyond the academic world. I also would like to mention all the co-authors of the different papers with whom I had the honor and possibility to work these years. The scientific support, knowledge, and expertise that they offered have been crucial for improving my personal experience and for achieving the conclusion of this work. Words cannot express my gratitude to professor Silvia Muceli, who extremely supported me during my abroad period at Chalmers University and gave me the possibility to work in the best conditions possible. Additionally, this endeavor would not have been possible without the financial support from the PON project “TEX-STYLE” ARS01_00996, PNR 2015-2020, and the project PRIN:Progetti di Ricerca di Rilevante Interessa Nazionale – Bando 2020 Prot. 2020 X7XX2P, that financed my research.

I would like to extend my sincere thanks to all my colleagues Andrea, Stefano, Giulia, Mattia, and Dave, for their help, feedback sessions, and support. Some of them saw my first academic steps and have been a fundamental example for me. Thanks should also go to my officemates for the moral support. I would like to especially thank my colleague and great friend Riccardo. We started our bachelor degree together and now we are completing our PhD. It was a long journey, but you managed to make it lighter.

Lastly, without the constant support of some special people and friends in my life, completing my PhD would have been much more difficult. Special thanks to my girlfriend Mary, who is the most important change of these three years in my life. Many thanks for the patience, support, and understanding you showed me, especially during the last months, when you helped me to keep my spirit strong. The most important acknowledgment is for my parents, whose love and support they have provided enabled me to achieve what I have.

Summary

1. Chapter I: Introduction to the wearable electronics

Nowadays, we live in an increasingly interconnected world, where electronic devices permeate every aspect of our lives. However, it is only in the last decades, with the advances of standard electronics that wearable devices are commonly worn and employed for several applications, such as communication, health and fitness monitoring, rehabilitation, and even for augmented or virtual reality experiences. The history of wearable devices goes back hundreds of years since humanity tried to improve everyday life by employing and wearing different objects and tools. The invention of eyeglasses to restore sight, for instance, can be considered as one of the first examples of wearable devices. Another interesting but obvious example is the wristwatch. In fact, this object was created in order to have a clock smaller enough that people could take it everywhere. Nevertheless, it is only with the establishment of the computer era that wearable electronic devices started to be de facto developed. From the first trials to develop portable computers, to the fabrication of several smart objects, the field of wearable devices increased their capabilities and possible applications rapidly in the last decades.

The first attempts to develop wearable electronic devices can be considered more portable devices, where electronic devices with some specific feature or applications were sufficiently small to be stored in a pocket, for instance. One of the most popular portable devices was the well-known Walkman, which was the portable audio player manufactured by Sony in 1979. Another interesting example is the wearable calculator watch, which became popular in the late 1970s and in all the ‘80s.

Over the decades, different devices started to be manufactured specifically for portable applications. However, the nowadays concept of wearable electronics is something significantly different. M. Billinghurst and T. Starner [1] in 1999 gave a definition of wearable electronics and an overview of the future (i.e. what we are currently living) about the new challenges and applications of this technology and how such devices moved from some specific application to a larger consumer base. Nowadays, wearable electronics are devices that can provide the possibility to have continuous access to communication, computation, and context sensitivity to enhance personal productivity and/or entertainment.

According to X. Tao [2], wearable electronics are electronic devices constantly worn by a person as unobtrusively as clothing to provide intelligent assistance that augments memory, intellect, creativity, communication, and physical senses. Moreover, the author stated that there are three main categories of wearable electronics: one based on standard devices that can be added to the clothes and that are detachable; a second category where devices are embedded into clothes by a micro-electronic packaging; a third category where the clothes are devices itself, i.e. the devices are in form of fabric. The development over the years of electronic devices and the advancement of technology has led to different kinds of wearable electronic devices, from an accessory that can be worn, to something completely embedded into clothing.

Different fields are pervaded by wearable electronics, but such devices are spreading out in the biomedical field [3], for sport and fitness [4], in clinical applications [5], and for human-machine interaction [6] since they can provide continuous monitoring and analysis of the body status. Thanks to those devices that enable continuous measurement of the physiological health state, early medical diagnostics are becoming extremely important. Thanks to the development of microelectronic devices that have led to a smaller footprint, and the improvement of wireless communication technologies, wearable monitoring systems have become more and more embedded in our lives. In Figure 1 an example of one of the most common portable and wearable electronic devices for monitoring and healthcare applications worn on body parts.

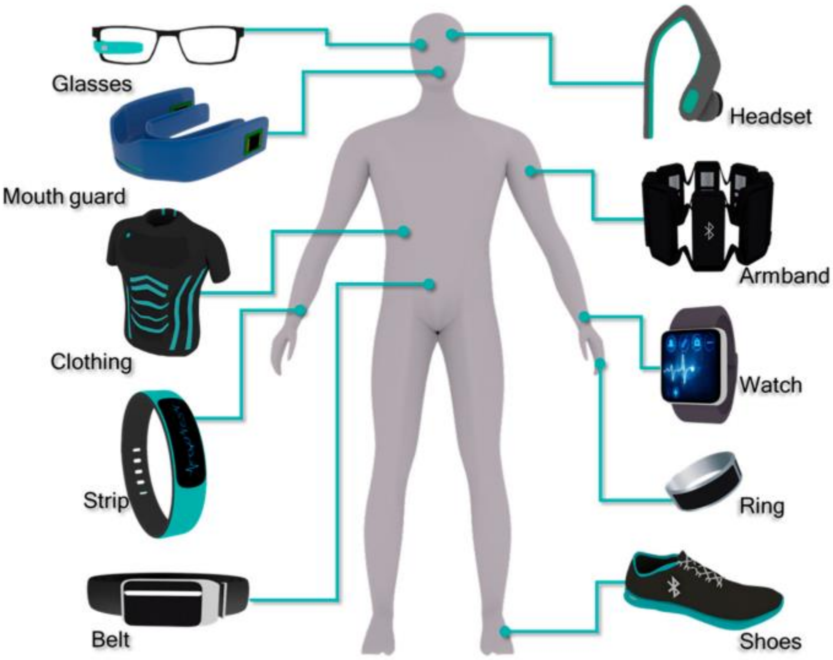

Figure 1 Wearable electronic devices worn on clothing or as accessories [3]

In this area, wrist-mounted devices are among the most commonly and commercially available devices that can be employed for different applications such as movement analysis[7], blood pressure measurement [8], [9], the non-invasive analysis of glucose levels through the sweat contents [10]. Recently, it has been demonstrated that such wrist-mounted devices with embedded gyroscope or accelerometers can be employed for the monitoring and analysis of the tremor and balance dysfunction in Parkinson’s disease (PD) patients, showing the possibility of employing commercial devices for medical applications [11].

Another wearable accessory that can be worn to have access to different functionalities is the smart glasses, also called head-mounted displays. Such devices are web-connected glasses that can show the user data onto the lenses and record images, videos, and audio files through a front-facing camera and microphone. Usually, those devices are employed in the augmented and virtual reality field for entertainment [12], but recently the possibility to employ those devices for different applications such as healthcare, clinical, and surgical application have been studied [13]. Moreover, there are different types of head-mounted wearable devices that can be devoted to the analysis of chemical species. Sempionatto et al. [14], for instance, presented an eyeglasses wireless multiplexed chemical sensing platform capable of real-time monitoring of sweat electrolytes and metabolites.

From a monetary perspective, the wearable device market is expected to continue to grow exponentially in the coming years. The forecast is that the growth rate will be over 20% per year, and the market is expected to reach more than 120 billion euros by 2026[15] and 161 billion dollars by 2033[16] Figure 2 shows the market analysis and the Wearable Technology Forecasts for 2023-2033, which is the research from the IDTechEx in wearable technology over the past decade.

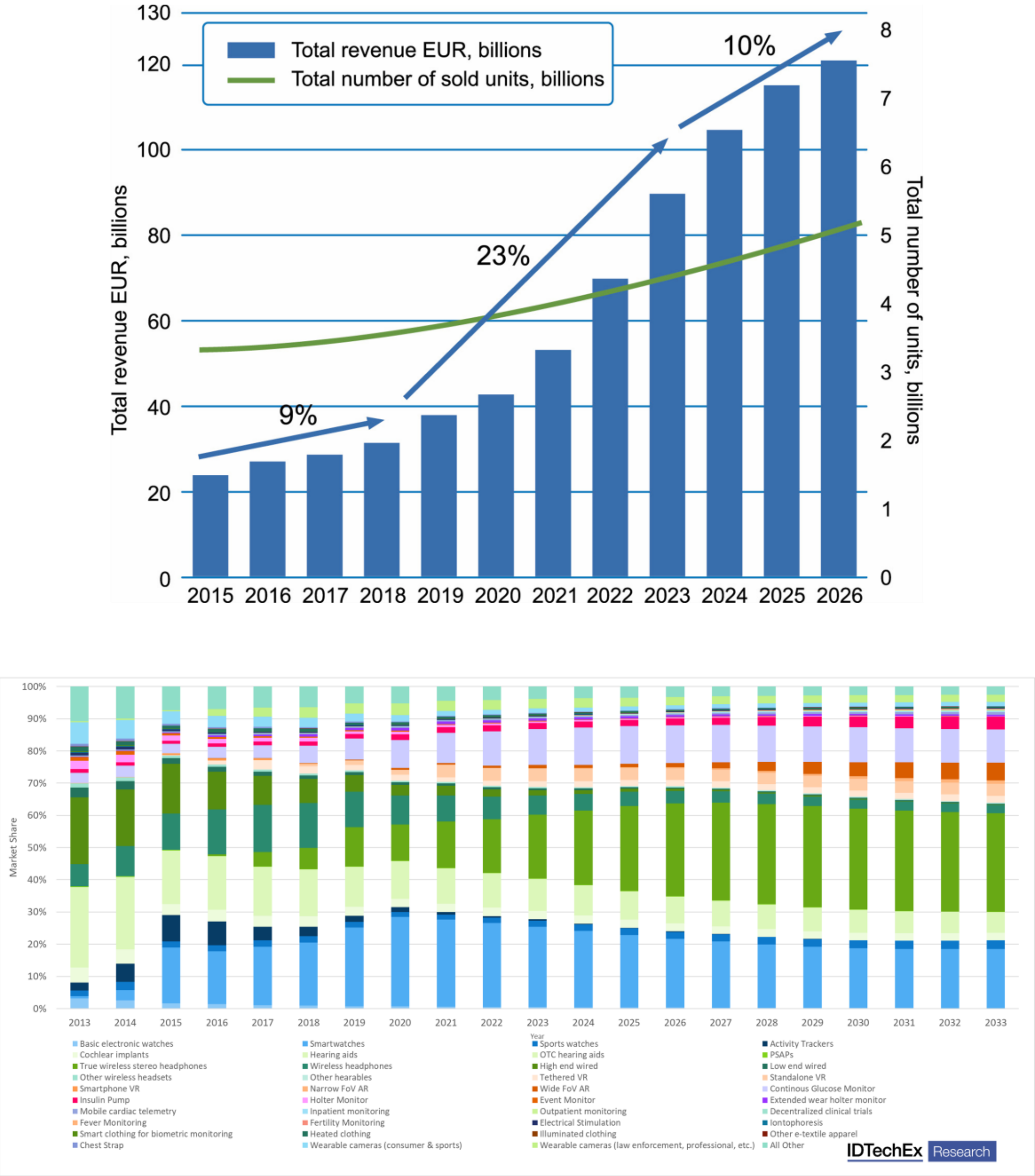

Figure 2 Wearable devices market report and analysis performed by IDTechEx [16].

Wearable electronic devices are nowadays more and more spread and daily they are changing human perspective since they provide the possibility to continuously communicate with the surrounding world, to receive notifications, to acquire body data for fitness and healthcare applications or even to create a virtual and augmented reality.

1.1. Thesis Objective

Among the different wearable devices and sensors presented so far, a new category of devices based on flexible, highly stretchable, lightweight, and soft materials is rapidly growing due to the development of organic materials technologies. The next generation of wearable electronic devices is characterized by a new device paradigm, where different features and characteristics are becoming crucial in the development of new electronic technologies. In particular, there are a plethora of new sensors where the final user comfort, the ultra-light way, and thickness, the unobtrusive employment are a central part of the device development and final design. In this context, flexible electronics and epidermal systems are growing fast and continuously optimized with the aim to develop a new generation of wearable devices. Therefore, several improvements have been already achieved and, thus, different devices have been developed to help monitor human physical health, to increase user comfort, and to make people's lives safer and more secure. Moreover, thanks to the improvement in the wearability of such devices, applications such as human-machine interfaces and long-term monitoring of vital parameters are becoming closer to the final user, making human interaction with electronic devices more accessible [17]–[20].

According to T. Someya and M. Amagai [21], the development of flexible and ultra-conformable devices that is ongoing in recent years, is allowing the possibility of manufacturing wearable systems that are intimately associated with the human body. However, there are still some limitations and issues to overcome, particularly if both device functionalities and mechanical proprieties to match skin characteristics have to be considered. For instance, in order to develop high-density and unobtrusive wearable systems and epidermal patches, it is necessary to reduce the device dimensions and to miniaturize its thickness. In the organic electronic field, decreasing the device dimension and designing and developing high-density matrices, is still a challenge if large area, cost-effective, and low-resolution production processes (which are one of the greatest advantages of this technology) have to be maintained. Moreover, for long term monitoring of individual health status, a sensor capable to detect the target parameter in a robust and reproducible way and have a long work-time in several environments is desirable. Therefore, the improvement of both precision on the measurement and robustness (in terms of device lifetime) is essential, particularly in a contest of daily applications. Highly sensitive devices with an optimize dynamic range are fundamental for the fabrication of wearable systems to monitor different human body parameters, in particular for early disease diagnosis. Moreover, since epidermal devices are directly attached to the skin and intimately associated to the human body, a key parameter is the biocompatibility of the materials employed for the fabrication of the wearable patches. In addition, there are several improvements to be achieved to limit and erase undesired effects due to disturbance of skin. To dramatically reduce skin irritations, the employment of thin, lightweight, stretchable non-cytotoxic and breathable materials to develop wearable devices is highly recommended. All these characteristics and improvements have to deal with low-cost and large area production processes, which are also hopefully up-scalable.

In order to achieve these goals there are different approaches that can be employed and all of them present difficulties, different problems to overcome and several limitations. In this PhD thesis, with the aim to achieve a step forward in the flexible and conformable electronic devices for the wearable electronic field, the development and optimization of a technology for the realization of wearable and *more-than-wearable* devices is presented. The need to meet all the new requirements in this field described above, such as the mechanical flexibility, the deposition of the devices over a large area on unconventional substrates exploiting a low-cost production process, has guided this PhD activity. In this work, different application fields were studied, such as health monitoring through biopotential acquisitions, the development, and optimization of multimodal physical sensors able to detect simultaneously pressure and temperature for tactile and artificial skin applications, and the development of flexible high-performing transistors as a building block for the future of wearable and electronic-skin applications. Therefore, the starting point of the research activity was to develop wearable and epidermal devices and sensor exploiting all the features and advantages of the organic electronic field. However, aware of the limitations, this work focused on finding some solutions to overcome the disadvantages of this technology.

Particularly, the next chapter will be focused on the description of the state-of-the-art in the wearable and epidermal electronic field. A fucus on the epidermal electronic concept will be provided, with a description of both the mechanical properties (which are fundamental in this context) and functionalities that characterized such devices. Moreover, several works will be presented with a particular attention on some specific devices, such as epidermal electrodes for biopotential recordings, devices and organic transistors for high-performing applications, and tactile sensors for artificial skin applications.

Afterward, chapter III will be focused on the description of an innovative approach for the development of dry epidermal electrodes capable to provide at the same time a low-cost and easy fabrication process over large areas and ultra-conformable substrates and at the same time capable of reducing skin irritations and issues. The chapter will deeply describe the tattoo electrodes fabrication process and its electrical characterization, specifically in terms of contact impedance. Moreover, an in-depth analysis of the results relating to the use of such electrodes for the acquisition of electrocardiography signals will be provided. Finally, the chapter will be focus on the breathability of the proposed electrodes and the advantages that this feature can provide in this filed.

Chapter IV will describe a wearable platform for the recording of the brain signals. In particular, there will be a description of the system, composed by a wearable custom electronic board that can detect the brain activity collected by the unobtrusive tattoo electrodes.

However, epidermal electronics still maintain open challenges and one of the most critical aspect is the connection between the ultra-thin patch and bulky recording systems. With the aim to provide a possible solution, in the chapter V a magnetic-conductive epidermal films for the acquisition of biopotential will be presented. A complete characterization of the film will be provided as well as a comparison between such tattooable electrodes and disposable Ag/AgCl electrodes.

Among the various building blocks that form an electronic system, the transistor represents the most important component in the design and development of such systems. However, nowadays the performance, especially in terms of frequency response, of OTFT-based systems is not up to the situation, limiting their real use in different fields of application and real-life scenarios. In the context of flexible wearable electronics or in IoT applications, where there must be intercommunication between objects, there is still a lack of high-performing organic transistors suitable for high-frequency communications (in the MHz and GHz range) that limit the possible use of such devices for real applications. For this reason, it is necessary to find solutions to reach the minimum frequencies required for these applications. However, up to now, a definitive solution to solve this issue has not already been found. To achieve this goal and fulfill all the requirements in this contest of high-frequency applications, scaling the transistor channel length is a possible solution, specifically in a technology contest in which the employed materials have low carrier mobility with respect to standard inorganic-based technology. However, reducing the channel length generally requires sophisticated fabrication techniques that are not up-scalable from a manufacturing point of view and that can negatively impact one of the main advantages of organic semiconductors-based technologies, i.e., the possibility of fabricating flexible circuits at low costs and high-throughputs. With the aim to provide an advancement in this field of research, a novel structure for the fabrication of high-performing organic transistor has been implemented. Specifically, Chapter VI will describe the sub-micrometer vertical channel organic transistor structure and its fabrication process. A focus on the optimization process of the device architecture will be give and both static characteristics and frequency response will be reported.

The last chapter of this thesis will be devoted on the description of a high-sensitive tactile sensor able to detect simultaneously temperature and force stimuli. Artificial skin is one of the most developed applications in the field of epidermal electronics and, in this contest, the idea is to provide a different approach for high-sensitive devices. The chapter will describe the sensor fabrication process and the complete analysis of both temperature and force characterization. In addition, a prototype of an integrated multimodal sensor will be reported.

2. Chapter II: State of the Art

In the last 15 years, the rise of highly flexible materials and electronic systems dramatically changed the wearable device landscape. The possibility to develop devices and systems based on organic materials paved the way for a new concept of wearable devices. Several approaches, device architecture, and novel materials have been employed with the idea to bring the electronics closer and closer to the human body. Such devices have the great advantage of being highly flexible and even conformable and intimately associated with human skin.

Since during this thesis work three main macro-arguments in the field of wearable electronics devices were studied, in this chapter there will be a detailed analysis and description of the state-of-the-art of the most employed approaches and methods for the fabrication of epidermal electrodes for biopotential recordings, high-performing transistor as a building block for the future circuits for wearable and electronics, and tactile sensors for artificial skin applications.

2.1.Epidermal Electronics

The new challenge in the wearable electronic field is to bring devices closer and closer to the human body. In the last decades, different electronic systems for monitoring and acquiring human parameters have been proposed with the aim to increase the interconnection with the human skin. However, to achieve a conformal and intimately adhesion with the body and to mimic the mechanical characteristics of the skin, it is necessary to develop a new category of soft, flexible, and stretchable materials for the next generation of wearable devices.

Nowadays, thanks to the rapidly growth of soft and flexible materials, a new variety of electronic devices and sensors can find their applications for the development of wearable sensors for human parameters monitoring.

2.1.1. *Mechanical properties of epidermal electronics*

The employment of flexible and soft materials, can allow achieving interesting device functionalities and mechanical proprieties thus enlarging the possible application scenario of electronic systems. According to the work proposed by Kim et al. [22] in 2010, epidermal devices are developed in order to match the epidermis properties, such as thicknesses, effective elastic moduli, bending stiffnesses, and areal mass densities. One of the greatest advantages of such technology is the possibility to transfer the devices directly onto the skin, unlike traditional wafer-based devices, resulting in a conformal contact that is solely based on electrostatic interactions (van der Waals forces). In this manner, the device is mechanically invisible to the user.

The human skin can be approximated as a bilayer composed by the epidermis with elastic modulus between 140 and 600 kPa and a thickness from 0.05 to 1.5 mm, and the dermis, which has a smaller elastic modulus (from 2 to 80 kPa) but a higher thickness (0.3 to 3 mm). The skin, moreover, is characterized by a linear elastic response to tensile strains smaller than 15%, which transitions to non-linear behavior at higher strains and with an adverse, irreversible effects beyond 30%. In addition, the skin surface is characterized by wrinkles, creases, and pits.

In this context and considering all these necessary features, the authors developed a system with effective moduli less than 150 kPa, that had bending stiffness smaller than <1 nN m, and areal mass densities of about 3.8 mg/cm^2. All these characteristics are orders of magnitude smaller than those possible with conventional rigid electronic and are well matched to the epidermis, with the ability to conform to the skin surface. Due to this intriguing properties, the authors referred to this class of technology as an “epidermal electronic system”(EES).

In Figure 3 a) the multifunctional electronics platform with physical properties that matches to the epidermis is shown. Interesting, in order to transfer the tattooable substrate to the skin, a sacrificial layer of the water soluble poly(vinyl alcohol) (PVA) film was used to place the structure against the skin. Subsequently, the dissolution with water of the PVA film leaved the device conformally attached to the skin exploiting only the van der Waals interaction between the two without any mechanical fixturing hardware or adhesive tapes. The schematic illustration in the inset of Figure 3 b) shows the cross-sectional layout, where it is possible to notice that the electronic circuit is placed on the neutral strain plane of the structure. Moreover, the epidermal system imposed a negligible mechanical or mass loading, as is highlighted in Figure 3 c); the tattooable device can be stretched and can be deformed in a reversibly way, without any damage or any constraints due to its attachment onto the skin. In addition, the authors showed that epidermal electronic can be integrated directly with already used commercial transfer tattoo, as an alternative to polyester/PVA substrates, thus reducing the fabrication process of the whole system and integrating interesting functionalities to the temporary tattoo (Figure 3 d)).

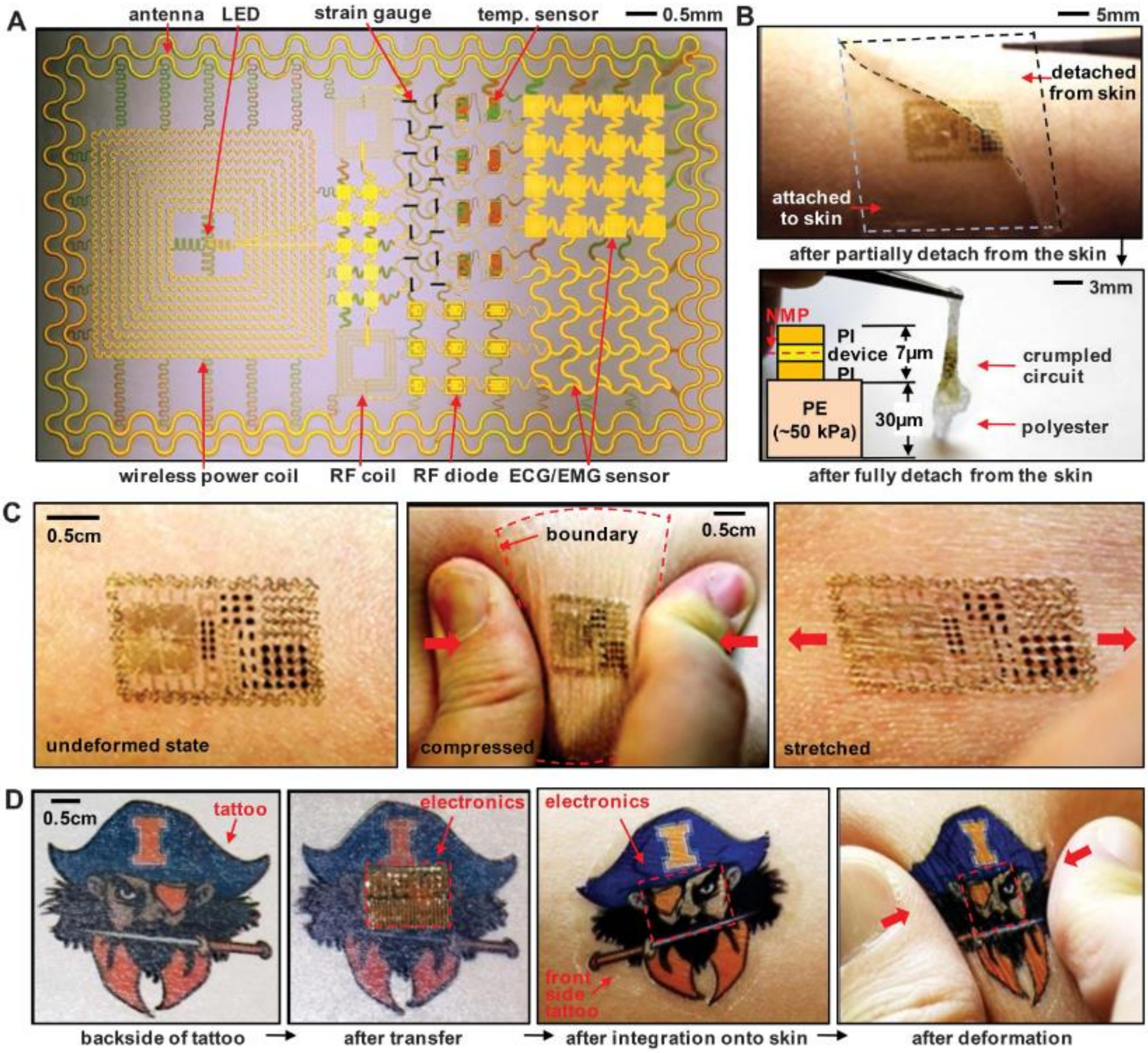

Figure 3 Epidermal electronic system proposed by Kim et al. [22]. A) image of the multifunctional platform; B) tattooable device and its cross-section, where it is possible to notice that the electronic circuit is placed on the neutral strain plane of the whole structure; C) demonstration of the device deformability; D) Alternative substrate to polyester/PVA substrate given by a temporary commercial tattoo, where an adhesive film was employed to improve bonding to the skin. Images are of the back-side of a tattoo (far left), electronics integrated onto this surface (middle left),and attached to skin with electronics facing down in undeformed (middle right) and compressed (far right) states.

Afterwards, Wang et al.[23] proposed a study of the mechanical characteristics of the Epidermal Electronics and in particular, the authors studied the contact between the electronic system and the skin as a key propriety for the development high-performance devices.

The authors studied both the macroscopic and microscopic properties of the device/skin interface and they noticed that the scaling law governs the conformal contact between epidermal electronic device and the skin. Devices with a thickness of 0.5 µm are characterized by a maximum contact pressure of about 12.5 kPa, which is below the human skin sensitivity (~20 kPa). This result, therefore, tell us that such devices are mechanically unnoticeable and would not induce discomfort. On the contrary, devices thicker than 1.2 µm give a contact pressure higher than 20 kPa, while devices thicker than 3.8 µm lose conformal contact to the skin. However, depending on the skin roughness those values can be different. For instance, rougher skin results in higher interfacial pressure, and the device thickness to lose conformal contact becomes much smaller (~1.5 µm). Therefore, as an obvious consequence, thinner and softer devices give smaller contact pressure and, thus, is more comfortable for the user. In other words, reducing the thickness allows obtaining a much more robust structure that can be conformably transferred onto complex surfaces. Such as the human skin. Figure 4 shows a sketch of the conformal adhesion between the epidermal electronic system and the human skin, modeling the skin roughness as a sinusoid. In addition, the conformal contact requirement for epidermal devices with different thicknesses and the contact pressure between a tattooable patch and the skin with different roughness are plotted

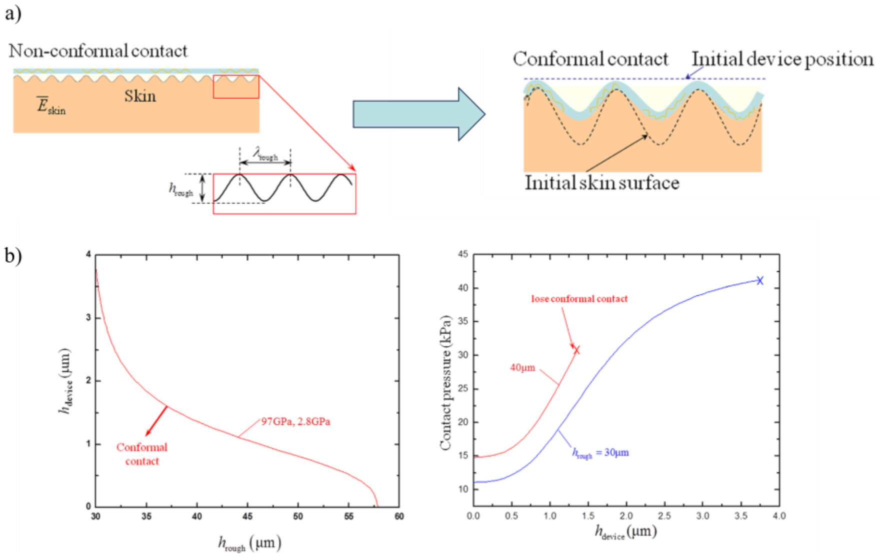

Figure 4 Wang et al. studied the mechanical proprieties and characteristic for the ideal epidermal electronic device [23] ;a) sketch of the conformal contact between the skin and the device; b) conformal contact requirement for epidermal devices with different thicknesses and the contact pressure between an the tattooable patch and the skin with different roughness

In the last 20 years, different approaches and materials for the fabrication of epidermal electronic systems have been employed, since the mechanical proprieties of the materials employed for such skin-like devices allow the development of several wearable applications in the biomedical field, such as the acquisition of biopotentials, the monitoring of the brain activities, but also to enhance the control of prosthetics [17]. Moreover, three main strategies can be followed to develop epidermal devices. In particular, the employment of soft materials with low young's moduli, the properly design of the device geometry and the active device on a neutral plane (Park et al. [24]).

An interesting example was developed by Jeong et al. [25], who proposed an epidermal electronic system for the acquisition of the sEMG for human-machine interactions. The authors developed the epidermal electrodes with the aim to improve and maximize the van der Waals forces that drive a sufficiently strong conformal contact between the human skin and the tattooable system. As reported in the work, the total energy associated with interfacial contact ($U_{interface}$) can be described as follow:

$$U_{interface} = U_{bending} + U_{Skin,elasticity} + U_{adhesion} \tag{1}$$

where $U_{EES\_bending}$, $U_{skin,elasticity}$, and $U_{adhesion}$ are the bending energy of the epidermal electronic system, the elastic energy of the skin, and the adhesion energy of the contact, respectively. Therefore, the conformal contact results when the adhesion energy is larger than the sum of the bending and the elastic energies, considering that the bending energy depends on the bending stiffness of the electrodes (thus the employed materials and the total thickness play a key role) while the elastic energy of the skin is mainly determined by the wavelength (140 μm) and modulus (≈130 kPa) of the skin.

Moreover, the electrical parameters are also affected by the quality of the skin/electrode contact, as well as by the skin hydration. The electrical impedance $Z_{interface}$ can be described as a function of the skin electrical resistivity (ρ), the inter-distance between electrodes (d), the contact area (A) with the skin, the signal source frequency (ω), and the skin dielectric constant (ε):

$$Z_{interface} = \frac{\rho d}{A\sqrt{1+(\omega\rho\varepsilon)^2}} \tag{2}$$

Therefore, the contact impedance decreases systematically and significantly as the electrode thickness decreases, since the contact area A is maximized; on the contrary for thicker patches, the impedance increases as the quality of the skin/electrode interface decreases. In addition to the contact area, the choice of the materials employed for the electrode fabrication can affects the impedance. Thus, the use of biocompatible, non-corrosive, electrochemically stable materials that resist surface oxidation is desirable, and gold offers such characteristics.

In Figure 5 the electrodes proposed by the authors are reported. The dimensions *S*, *h*, *W*, and *d* refer to the geometrical parameters used to design the electrode. Moreover, the analysis of both the electrode/skin interface and contact impedance are reported, showing that the thinner the patches the better the adhesion and thus the electrical characteristics of the acquired signal. In addition, an example of an EMG signal recorded form the index finger (*Vincula brevia*) and the forearm (*Flexor carpi radialis)* are reported.

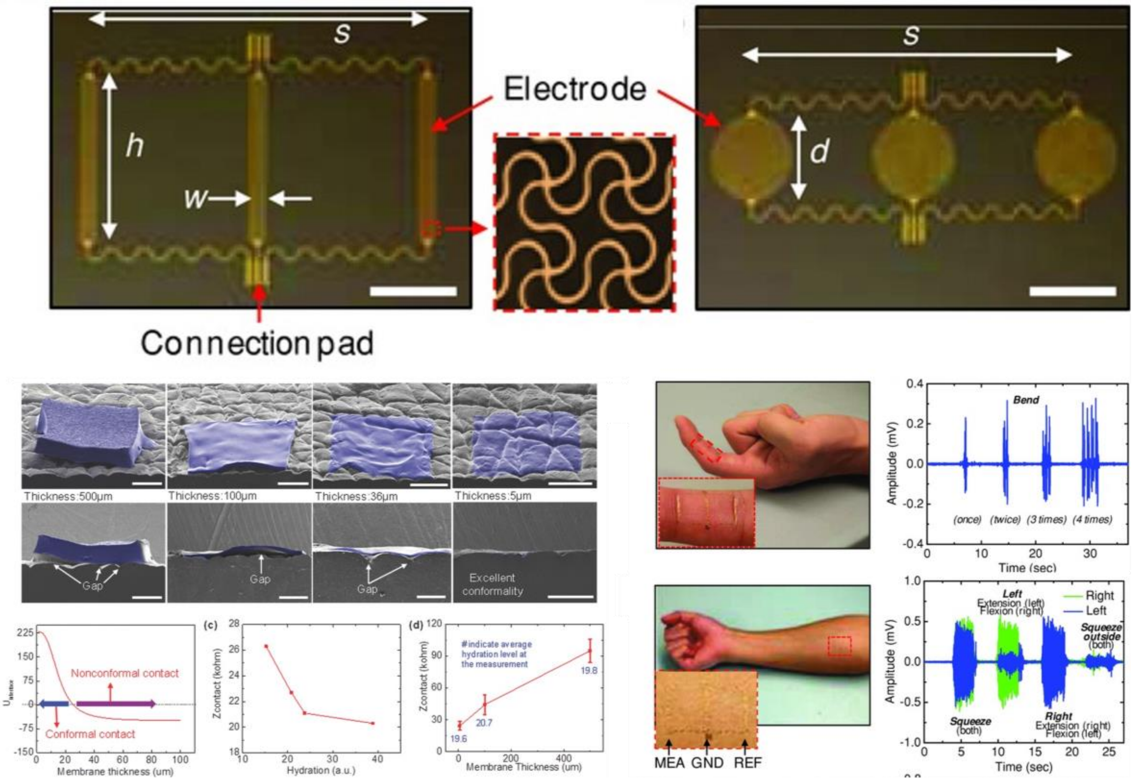

Figure 5 Epidermal electrodes for the recording of sEMG proposed by Jeong et al. [25]. The device was designed in order to optimize the acquisition of the signal and the conformal contact, and thus the contact impedance between skin and electrode. In addition, an example of recorded sEMG signal is reported.

Since the bending thickness and therefore the conformability (as well as the adhesiveness) varies with the thin film thickness cubed, decreasing the film thickness is a strategy to reduce the bending stiffness and thus making the device much more conformal and more adhesive.

With this approach, Nawrocki et al. [26] proposed a sub-300 nm thick device based on an organic field effect transistors (OFET) that incorporates a touch resistive-variable sensor and that can be laminated onto the skin, as it is shown in Figure 6 a), where an optical image of the tactile sensor laminated onto the skin is presented. In addition, the device substrate, as well as the encapsulation and the dielectric layer, was made by a thin film of the biocompatible polymer Parylene C, making the device suitable for wearable applications. In particular, the device can be considered as a pixel for a tactile active matrix of sensors, since the device was able to detect the force stimuli given by the contact. In Figure 6 b) the transconductance curves of the device with either no contact (green line), human finger contact (red line), or metallic object (blue line) contact is shown. As it is possible to notice, there is a difference on the device output current of about 4 orders of magnitude, thus the device can be employed as tactile sensor. In the inset, the corresponding electrical circuit is shown. Moreover, the authors tested the mechanical stress resistance of the device and in Figure 6 c) the device's transconductance curve pre and post stretch test is shown. The device mobility increased with physical stretching (0.34 and 0.39 cm^2 V s^{-1}, respectively).

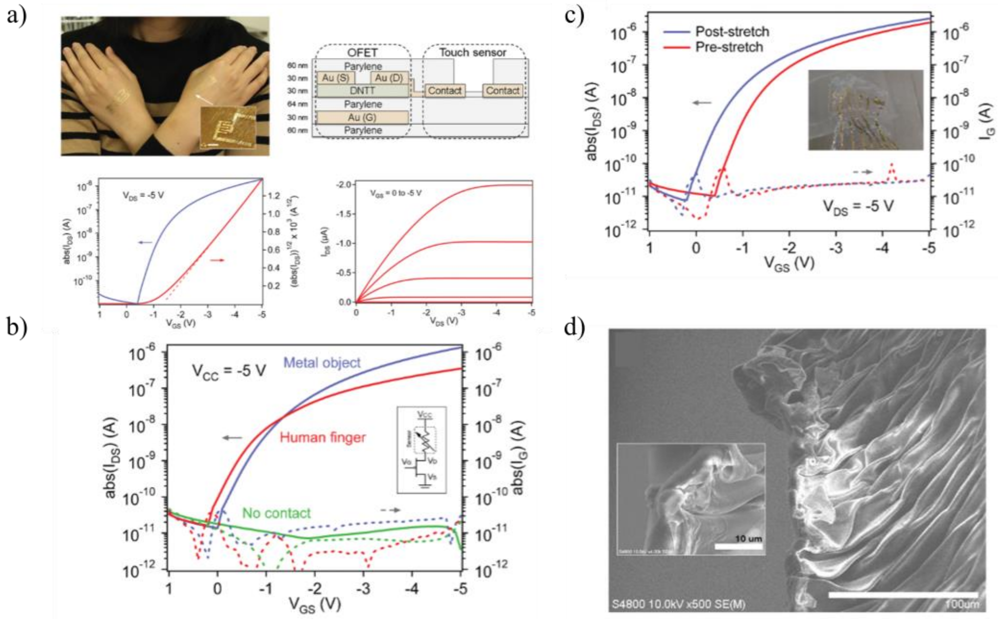

Figure 6 300 nm thick tactile sensor based on an organic field effect transistor coupled with a piezoresistive active part [26]. a) device structure with the employed materials highlighted; optical image of the device laminated onto the skin and static electrical characterization; b) the transconductance curves of the device with either no contact (green line), human finger contact (red line), or metallic object (blue line) contact. The difference in drain currents can be seen as being over four orders of magnitude, while the inset indicates electrical circuit diagram of the device; c) transconductance curve of the pre-stretched and post-stretched device. In the inset the device on a relaxed elastomer. In addition, the SEM image of OFET film on a pre-stretched elastomer, with the inset showing a zoomed image. The scale bars are 100 μm of the main image and 10 μm of the inset.

2.2.Epidermal electrodes for biopotential measurements

In the current epidermal sensors landscape, there are three main biological signals that are commonly involved in the measurement: Physical, chemical and electrical signals. Among the three commonly measured physical signals, there are strain, pressure, and temperature, while for chemical sensors, the development of wearable glucose monitors has been gained more importance. However, the measurement of electrical signals, such as electrocardiogram (ECG), electromyogram (EMG), and electroencephalogram (EEG) from the surface of the human skin remains the most developed application in this wearable electronic field.

Nawrocki et al. developed an interesting example of epidermal electrodes for biopotential acquisition [27]. The device was a self-adhesive, sub-300 nm thin, dry electrode for high-quality biopotential measurements. In particular, the surface electromyogram and surface electrocardiogram recordings were involved in the study, since those are one of the most commonly recorded bio-signals for wearable healthcare applications. The electrodes were fabricated using the biocompatible plastic material, namely Parylene C, and a gold film as an active recording site. Concerning the device structure, the gold film (100 nm thick) was sandwiched between two 100 nm thick Parylene C layers. In Figure 7 a) the electrode directly transferred onto the skin and the device cross-section are shown. Moreover, the mechanical characteristic of the tattooable patches were studied. Among the different approaches for the fabrication of flexible epidermal systems, the authors used the solution to transfer a thin-film electronic system on a pre-stretched elastomer. In this work, the authors reported the mechanical properties of the device, in particular, in terms of wrinkle periodicity (λ) and wrinkle height (A). In Figure 7 b), a comparison of films of various thicknesses laminated on a pre-stretched elastomer with and without an adhesive layer is shown. It is worth noting that the thinner and more conformable the film is, the less obtrusive and more comfortable it is for the user. Therefore, a sufficiently thick film does not adhere to the substrate and delaminates upon release, while a sufficiently thin film does adhere to the substrate due to van der Waals forces without any delamination. In addition, an electrical characterization, where both surface ECG and EMG signals were acquired, is reported in Figure 7 c). Since the Ag/AgCl wet adhesive electrodes are the most widely used for surface biopotential acquisition, the authors compered for both the two bio-signals, the signal acquired through the commercial electrode (blue curve in the plot) and the signal acquired with the 300 nm thick epidermal electrodes (red line in the plot). As a firstly, the ECG was acquired in order to assessing the performance of the epidermal sensors. Concerning the measurement set-up, two adhesive tape electrodes and two epidermal electrodes, both with an area of about 100 mm^2, were placed on a healthy subject's chest in position V2 and V6. The third reference electrode was placed on an elbow. The parameter to evaluate the sensor performances in terms of electrical characterization are the peak-to-peak value, the noise level, and signal-to-noise ratio (SNR, in dB). For the signal measured with the thin film electrodes those parameters were 1.775 mV, 156.6 µV, and 21.09, respectively, while for the wet adhesive electrodes 1.791 mV, 158.9 µV, and 21.04, respectively. Therefore, the dry electrodes showed comparable performances. Afterwards, the epidermal sensors were placed on the forearm to acquire the surface EMG signal. As it is possible to notice form Figure 7 c), the sEMG spikes for the dry epidermal electrodes and for the adhesive wet electrodes are indistinguishable. Moreover, the noise level reported were equal to 3.57 and 5.61 µV, respectively, and the SNRs (calculated on their RMS values) were 30.80 and 30.04, for the measurements obtained with the 300 nm and wet adhesive sensors, respectively, thus confirming the possibility to employ such electrodes for biopotential acquisitions.

Generally speaking, epidermal electrodes can be suitable for long term applications, since they are imperceptible for the user and thus, they can offer an high comfort. In order to prove the possibility to employ such sensors for a single-day-usage, sEMG measurements were conducted along 10 h. As it shown in the figure, shows individual measurements are virtually indistinguishable, thus the application of such electrodes for disposable single day usage were verified.

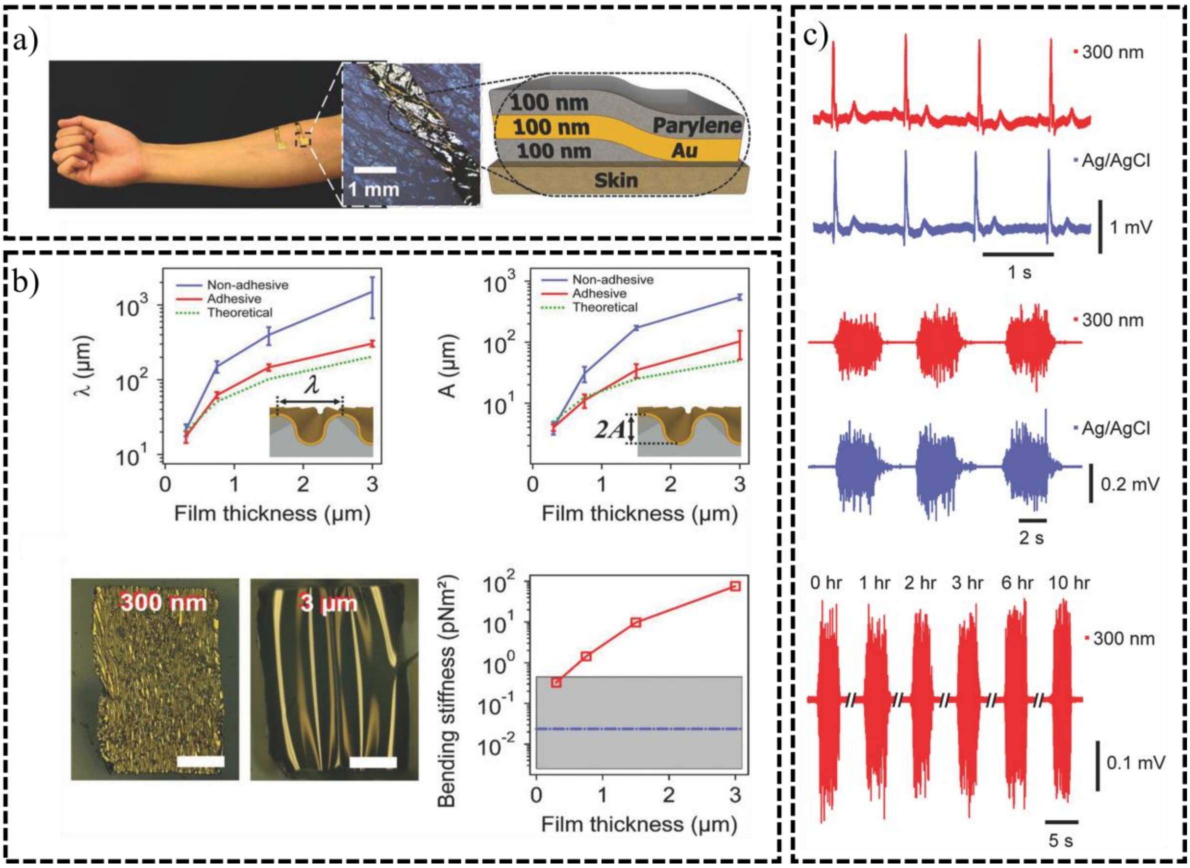

Figure 7 300 nm thick epidermal electrodes proposed by Nawrocki et al. [27]. A) epidermal electrodes laminated onto the skin and device cross-section; B) Mechanical properties of the epidermal films, where a comparison wrinkle periodicity λ and wrinkle height A of compressed films is shown for devices with and without adhesive layers. Moreover, an optical image (scale bar 400 µm) of a 300 nm thick and 3 µm is shown with a bending stiffnesses plot variation as a function of the film thickness; c) Comparison between ECG and EMG signals acquired with the proposed epidermal electrodes and with standard Ag/AgCl electrodes. In addition, a single-day measurement of the EMG signal of 300 nm thin film sensor, measured along time (after 1 h, 2 h, 3 h, 6 h, and 10 h).

Nevertheless, it is important to notice that lightweight, flexible, and conformal organic-based circuits are essential for the development of an all-integrated epidermal system for the recording of biopotentials from the skin surface. Recently, the Someya's group have made a step forward by the developed of a 270 nm thin organic electronics amplifying circuits that are self-adhesive, skin conformal, and long-term air-stable over 5 years (Mirshojaeian Hosseini et al. [28]). Based on the same approach describe above, the authors demonstrated the possibility to fabricate and characterize a 270 nm thick electronic skin (e-skin) that fits with both P and N type organic transistors. Thanks to the characteristics previously described (such as thickness and stiffness), the device can be attached to human skin and measure biological signals. In addition, in order to improve the design of such epidermal patches, the authors simulated both devices and circuits with the aim to reduce the cost of device preparation and validate the results of experimental characterization.

It is interesting to describe deeply the fabrication process of the epidermal electronic circuits. All the process starts form a glass substrate, in which a 85 nm-thick film of a fluorinated polymer played the role of releasing layer, and 5 µm of polyvinyl alcohol was used as layer to facilitates the handling of the film after delamination from glass. The epidermal circuits fabrication process started with the deposition of 60 nm of Parylene diX-SR and then a thermal evaporation of 30 nm of gold as gate electrode. On top of it, another 60 nm-thick film of Parylene diX-SR was deposited as dielectric layer. In this work the authors developed both p-type and n-type organic transistor, thus dinaphtho[2,3-b:2',3'-f]thieno[3,2-b]thiophene (DNTT) was deposited as p-type active layer, while the N,N'-bis(n-octyl),1,6-dicyanoperylene-3,4:9,10-bis(dicarboximide) (PDI-8CN2, sometimes also referred to as N1200) was employed for n-type OFETs. Both were deposited through a thermal evaporation process. The device architecture is a bottom gate, top contact, therefore following the organic active layer deposition, 30 nm of Au was deposited as the source, gate, and circuit interconnect, and encapsulated by a 60 nm thin layer of Parylene. The total structure thickness was ~270 nm. In order to electrically characterized the devices, the film was attached on a 125 µm-thick polyimide (PI) film. In Figure 8 a) the device structure is presented, both on a polyimide substrate and attached onto the skin, with the employed materials and the characteristic curves of the 270 nm p-type and n-type OFET highlighted. An all-integrated approach can have different interesting advantages. Firstly, it is necessary to consider that the biological signals have to be processed since they are usually weak (on the order of microvolts to millivolts). Therefore, components such as amplifiers or filters are fundamental. In addition, such signals have to be transferred because the front-end processing circuits are located away from the source of the signal. As a consequence, the signals are affected by noise artifacts. In this application, the role of ultra-thin epidermal organic amplifiers can be crucial because they can provide direct signal processing (such as amplification or filtering stages) close to the recording site and suppress the effects of transmission noise. The authors developed an organic p-CMOS (opCMOS) inverter with the aim to amplify the signal and simultaneously exploiting a simply and reliable fabrication process, with respect to the complimentary logic base don OFETs. However, since the complementary logic is commonly used for the design of circuits, the authors developed an inverter based on p-type and n-type organic transistors. In Figure 8 b), the schematic of both inverter circuits together with an optical image and a characteristic curve before and after buckling are shown. Moreover, as it is presented in Figure 8 c), the authors developed an organic ring oscillator based on five organic CMOS inverters, where the output of the actual stage inverter is connected to the input of the next stage. It is notable that the maximum gain of a five-stage organic CMOS exceeds 2358 in the backward direction while the bias (V_{DD}) is 8 V and the switching voltage is swinging around 5 V.

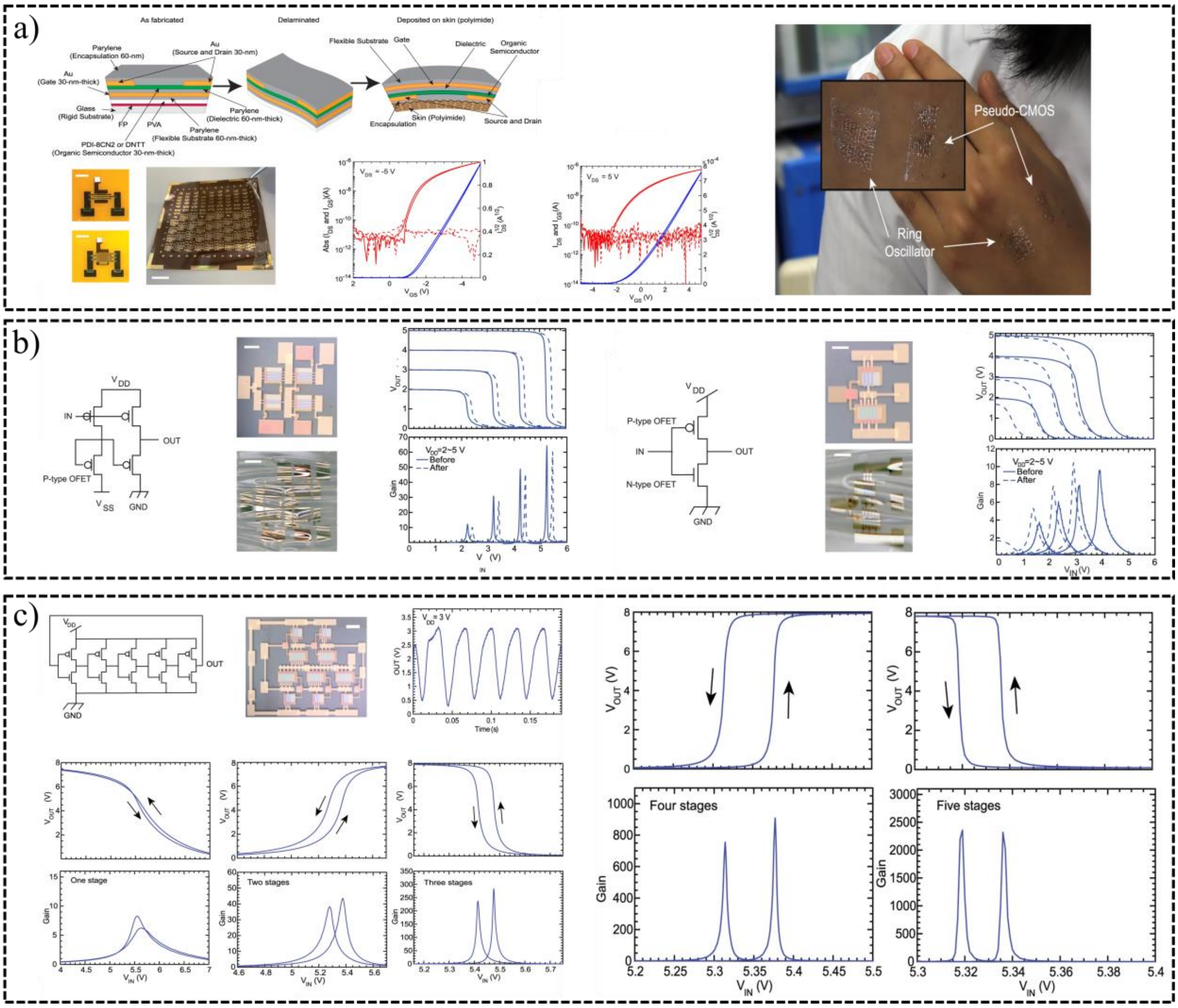

Figure 8 Epidermal electronic circuit proposed by Mirshojaeian Hosseini et al. [28]. a) device sketch with the cross-section and employed materials. The electrical characteristics of both p-type and n-type organic transistors are shown, together with an optical image of the 270 nm-thick device on a plastic carrier and laminated onto the skin; b) electric schematic of the pseudo CMOS inverter circuit based on p-type transistors and the CMOS inverter developed with both p-type and n-type organic semiconductor. Optical images and electric characteristic curves before and after buckling are shown; c) Organic ring oscillator (electronic schematic and optical image) composed of five-stage CMOS inverters. The characterization concern one stage up to five-stage amplifier.

In addition, the authors amplified previously recorded ECG and EMG signals in order to display the capability of the five-stage organic CMOS amplifier. In particular, a bio-signal generator as an artificial ECG and EMG input signal for the amplifier was used and, moreover, an input resistor (100 kΩ) in order to provide DC feedback to stabilize the circuit and a capacitor (2200 nF) in the input of the circuit were employed and added to the five-stage ring oscillator amplifier. In Figure 9 the artificial ECG signal (blue line) and the amplified signal (red line) are shown, as well as the artificial EMG signal and the amplified EMG and the RMS envelop of input and amplified EMG signal.

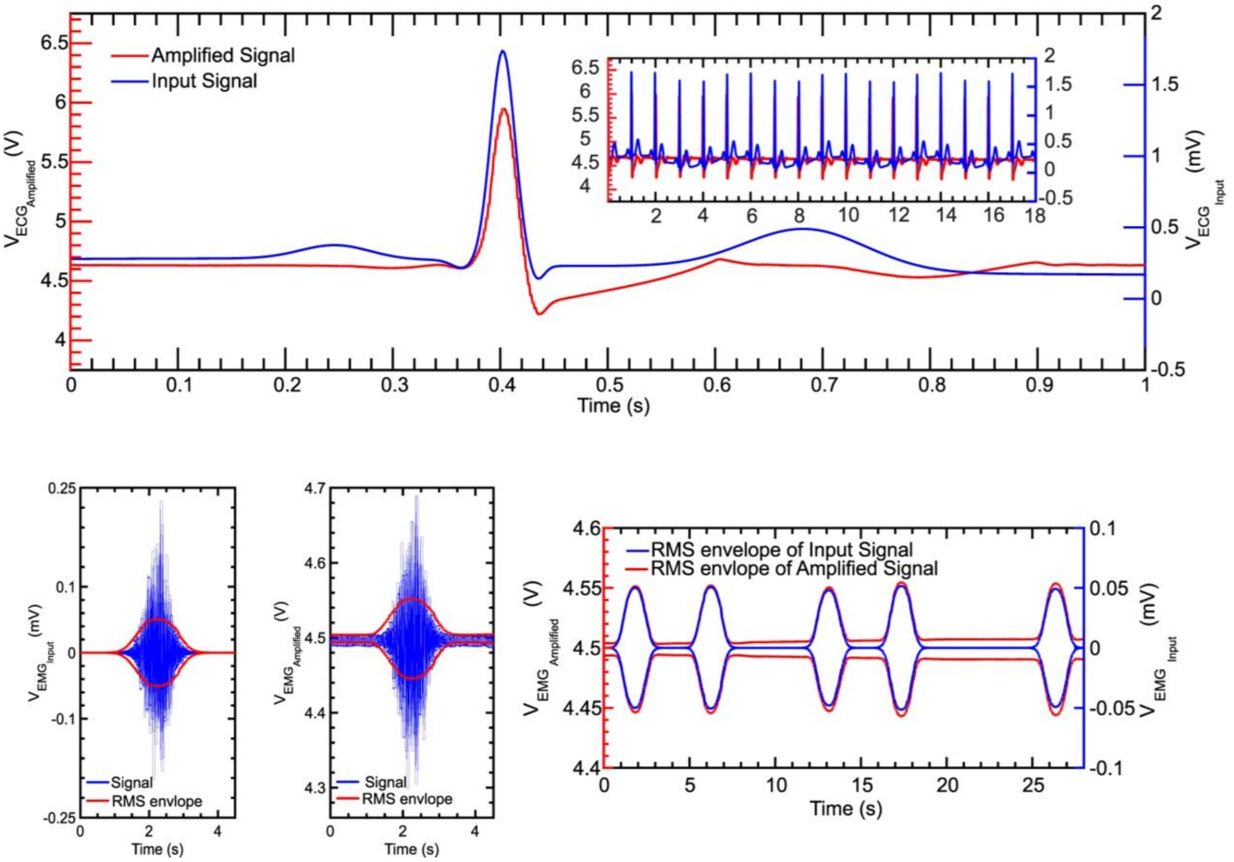

Figure 9 The five-stage amplifier based on the organic ring oscillator was employed to amplify an artificial ECG and EMG signal. Blue curves regard the input signal, while in red there are the amplified signals recorded at the output of the epidermal electronic circuit [28].

Kabiti Ameri et al. [29] developed an sub-micrometer electronic tattoo sensor made of graphene designed as serpentines and fabricated by a cost- and time-effective method. Thanks to the mechanical properties, as the thickness limited to a few hundred nanometers, the device can be simply transferred to the skin and can adhere through the sole van der Waals forces. Moreover, the open-mesh structure of the makes the tattoo electronic system breathable. The fabrication process, reported in Figure 10 a), started from copper substrate in which the graphene was growth at more than 1030°C. These temperature values are not compatible with flexible substrate and this is the reason why the copper layer was chosen as substrate. After that, in order to transfer the graphene onto tattooable substrate, a sub-micrometer-thick PMMA layer was spin-coated on the graphene, followed by the wet etching of the copper using copper etchant and rinsing with DI water. Afterwards, the PMMA/graphene layer was transfer onto a tattoo paper. Finally, to fabricate the serpentine, the graphene/PMMA bilayer was cut using a programmable mechanical cutter plotter and the excessive material was peeled off. It is worth to notice that the authors used a medical adhesive film (Tegaderm (3M)) to help the transfer of the tattoo electrodes onto the skin and thus perform the measurements. In Figure 10 b), the electrical characteristics of the graphene-based tattoo electrodes are reported. In particular, from the skin-electrode impedance analysis it is possible to notice that, even if the skin preparation was not performed, the graphene electrodes had a comparable impedance with respect commercial gel electrodes. Moreover, it such electrodes can be employed to acquire different bio-signals, as it is reported in the figure. In fact, the authors reported the EEG sensing, performed by pacing the electrodes (both commercial and tattoo electrodes), the acquisition of the ECG and the EMG form the subject’s forearm.

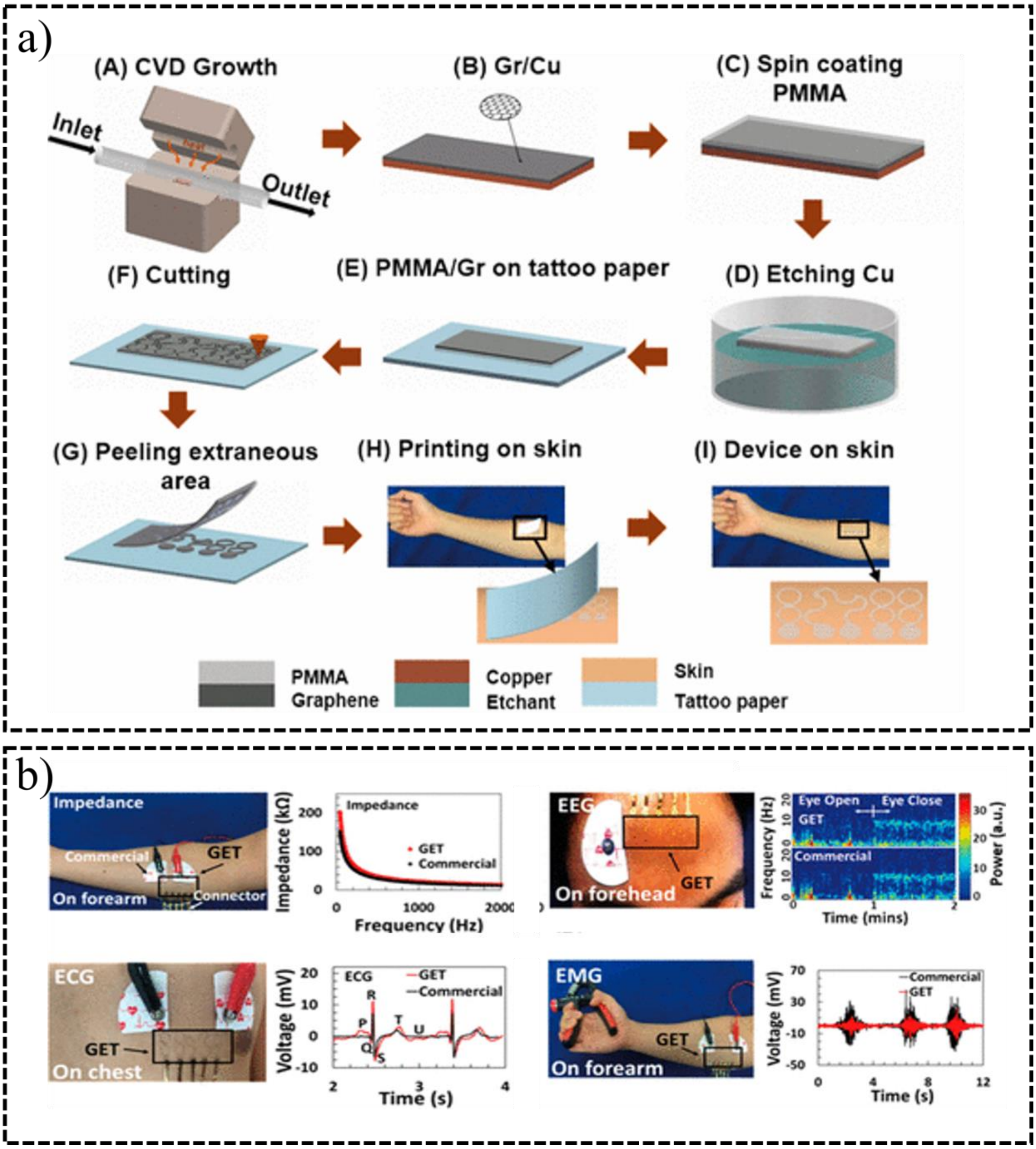

Figure 10 Kabiti Ameri et al. [29] graphene-based tattoo electrodes for biopotential acquisition. a) fabrication process of the proposed device. The graphene was growth onto a copper substrate by using atmospheric pressure chemical vapor deposition system at 1030°C.Afterwards, a sub-micrometer-thick PMMA layer was spin-coated on the graphene, followed by the wet etching of the copper using copper etchant and rinsing with DI water. Then, the PMMA/graphene layer was transfer onto a tattoo paper. Finally, to fabricate the serpentine, the graphene/PMMA bilayer was cut using a programmable mechanical cutter plotter and the excessive material was peeled off; b) electrical characterization of the graphene-based tattoo electrodes. The impedance is comparable with respect commercial gel electrodes. ECG, EMG and ECG acquisition.

Park et al. [30] developed a self-powered arterial pulse monitoring based on a epidermal piezoelectric sensor. In this work a PZT thin film was employed as real-time healthcare monitoring detector for measure the pulse form the radial and carotid arteries. The device showed a sensitivity of about 0.018 kPa^{-1} and a response time of 60 ms. In Figure 11 the device fabrication process and the bio-signals (artery pulse and saliva swallowing) acquisition are shown.

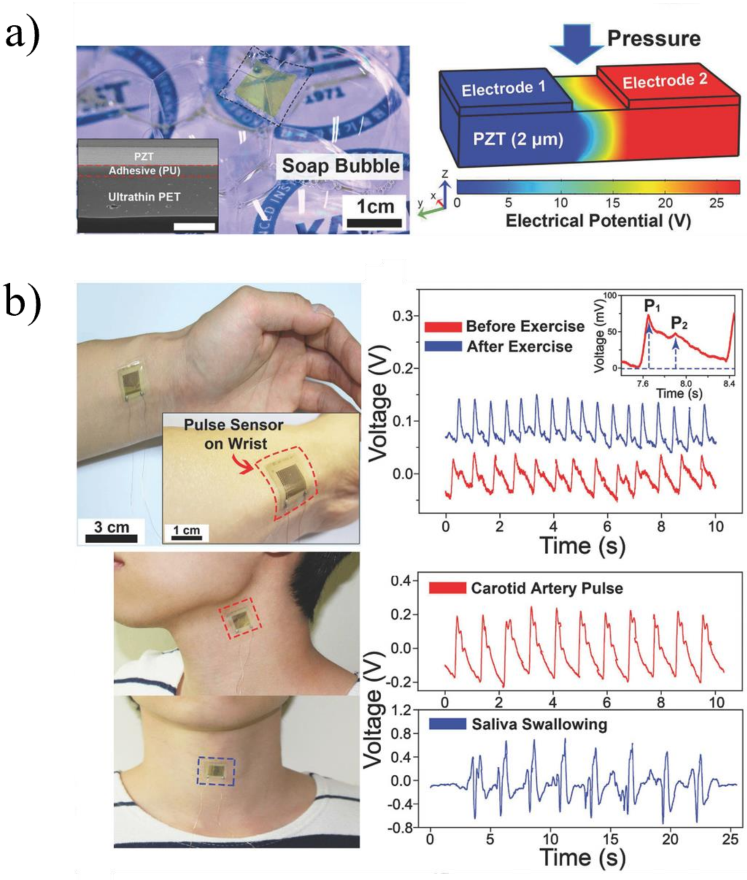

Figure 11 Self-powered epidermal sensor proposed by Park et al. [30] for real-time arteria pulse monitoring. A) device fabrication process; b) bio-signals measurements: measurement set-up and acquired signals.

One of the most studied healthcare applications for epidermal sensors is biopotentials acquisition. Transferable tattoo electrodes have shown in the last decades the most significant impact in the recording of biopotentials from the surface of the skin, and different approaches and methods have been proposed so far [31].

Barek et al. [32] developed a carbon ink-based electrodes deposited through a screen printing technique for the acquisition of sEMG. The main objective of the authors was to develope an electrode that could enable long-term acquisitions. In this contest, impedance reduction played a crucial role, in particular for the reduction of the noise levels and thus the improvement of the signal-to-noise ratio (SNR) to have high-resolution recordings. Therefore, the electrode-skin impedance was improved by a plasma polymerized 3,4-ethylenedioxythiophene (PEDOT) coating. The electrode fabrication process, as shown in Figure 12 a), was based on a standard screen-printing process, combined with laser cutting to make holes in a double-sided passivation layer, which also serves as a skin-adhesive material. The carbon ink was deposited onto a blank temporary tattoo paper. Afterwards, to reduce the skin/electrode impedance the authors implemented a PEDOT coating, and a ZIF socket with a custom-made printed circuit board was used for the connection with the recording instrument. In Figure 12 b) an optical image of the tattooable electrode array transfer onto the skin is shown.

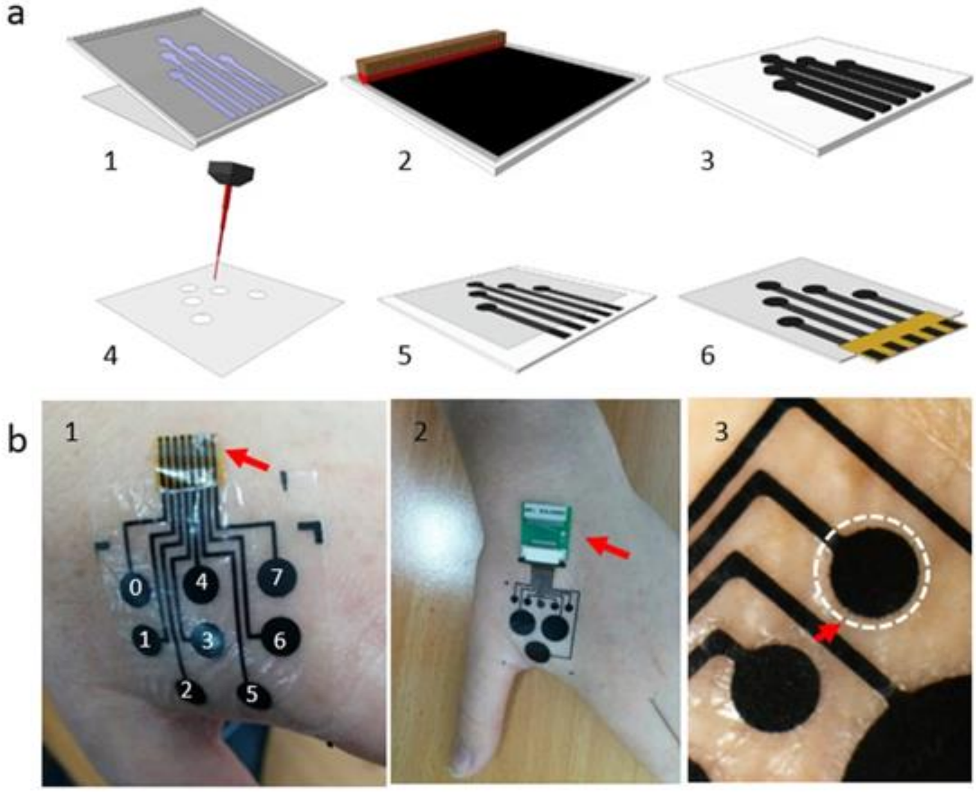

Figure 12 Screen-printed carbon-based electrodes array for surface EMG acquisition (Barek et al. [32]). a) Fabrication process workflow; b) electrode array laminated onto the skin.

In addition, for the authors to demonstrate the possibility of employing such electrodes for long-term acquisitions, two recording scenarios were investigated. As shown in Figure 13, the authors used the electrodes to acquire the signal from both the FDI and from the zygomaticus major (ZM) muscle of the face. Similar performances were obtained from both pre-gelled commercial electrodes and the carbon-based tattooable array and the authors were able to discriminate from the surface electromyographic signal different facial expressions (neutral, smiling, sad, and angry). It is worth to mention that even if the carbon ink-based electrodes showed good electrical performances, the tattooable patches need an adhesion layer to be placed onto the skin.

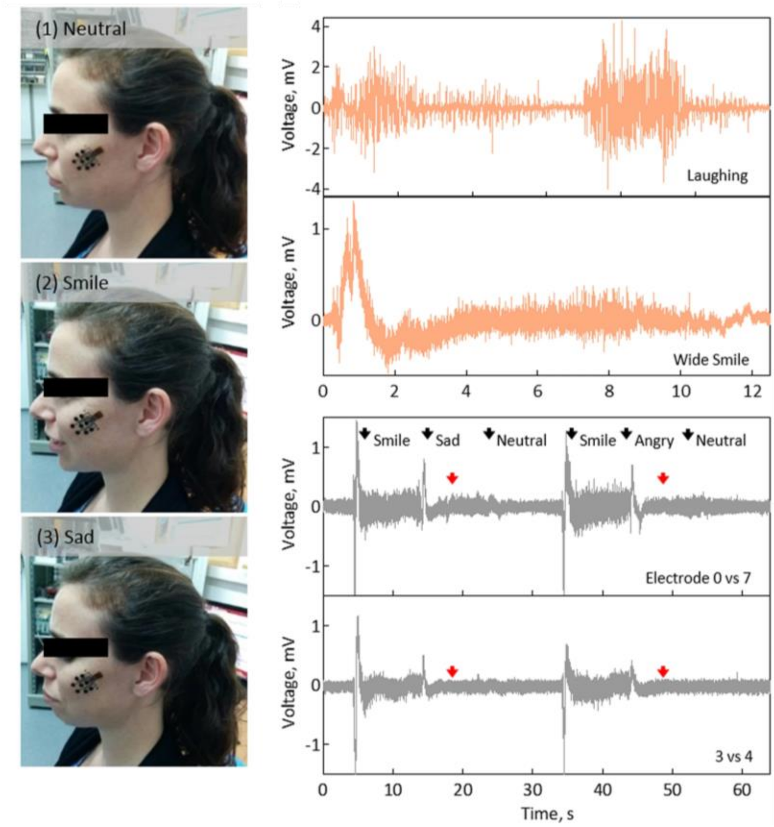

Figure 13 Barek et al. [32] sEMG signals acquired from the FDI and from the zygomaticus major (ZM) muscle of the face. The bio-signal related to different facial expression were studied and recorded

Afterward, the research group developed a wearable high-resolution facial electromyography system to record facial expressions[33]. In particular, the authors proposed a sEMG system able to capture three muscles involved in different smiles from the surface of the human face. In Figure 14 the facial activations and the corresponding differential sEMG (filtered) from 5 electrode pairs are shown.

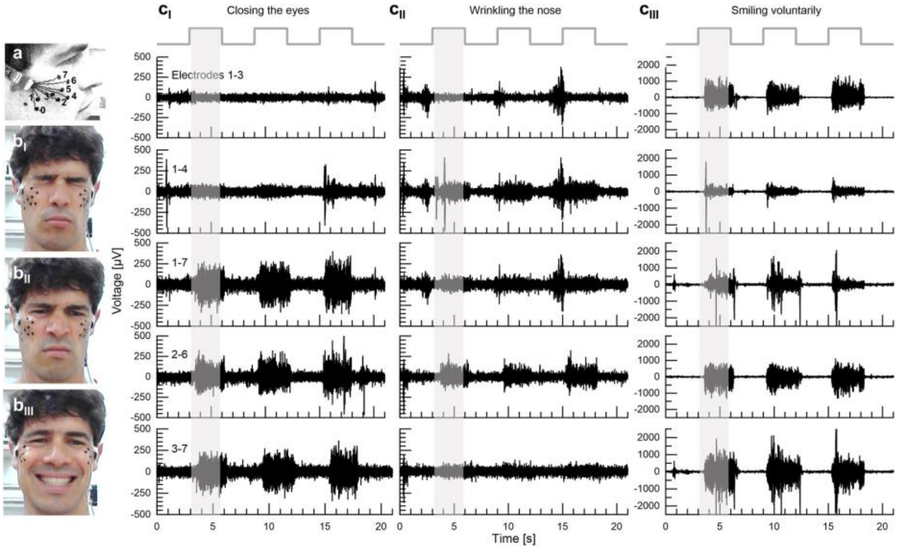

Figure 14 Wearable tattoo patches for facial electromyography system to record facial expressions [33]

Usually, wet Silver/Silver-Chloride (Ag/AgCl) is employed as the active site of disposable commercial electrodes. The adhesive layer which is used to guarantee a good interface with the skin allows also to have a resistive low contact impedance. However, especially for long-term applications, they show several limitations in particular related to the gel drying out which gives a limited connection time. Moreover, the strong adhesive layer could lead to several issues and be painful to remove, and repeated electrode removals lead to skin irritation.

Casson et al. [34] developed ECG electrodes fabricated by the inkjet printing of Silver nanoparticles onto a tattoo substrate that guarantees high quality connection to the body for many days. The printed electrodes were designed as a 25 mm circle (for active area) with a 7 mm tab (for connecting recording wires). As connectors, ECG standard 1.5 mm touch-proof wires were attached to the tab using silver-loaded paint, and a layer of surgical tape placed over the connection point to strengthen the contact was employed. Figure 15 a) shows the printed electrodes for ECG acquisition and a comparison between the commercial wet Ag/AgCl electrodes and the tattoo electrodes, where R peaks are seen in both the time and CWT domains. Moreover, R peaks and the P and T waves are annotated on the conformal, showing the possibility of discriminating the ECG features. Moreover, the authors investigate the possibility of employing such printed tattoo electrodes for long-term acquisition. Figure 15 b) illustrates five segments of ECG recordings performed on subsequent days. As it is possible to notice, a clear QRS complex can be discriminated over days, allowing one to perform heart rate and heart rate variability analyses. However, a high SNR was maintained, as it was still above 30 dB on average, although there was a systematic decrease in days 4 and 5. Also in this work, as in the previous, the tattoo electrodes were deposited on a 10 µm thick substrate and thus the adhesion to the skin was mainly performed by an adhesive film layer placed over the electrode surface.

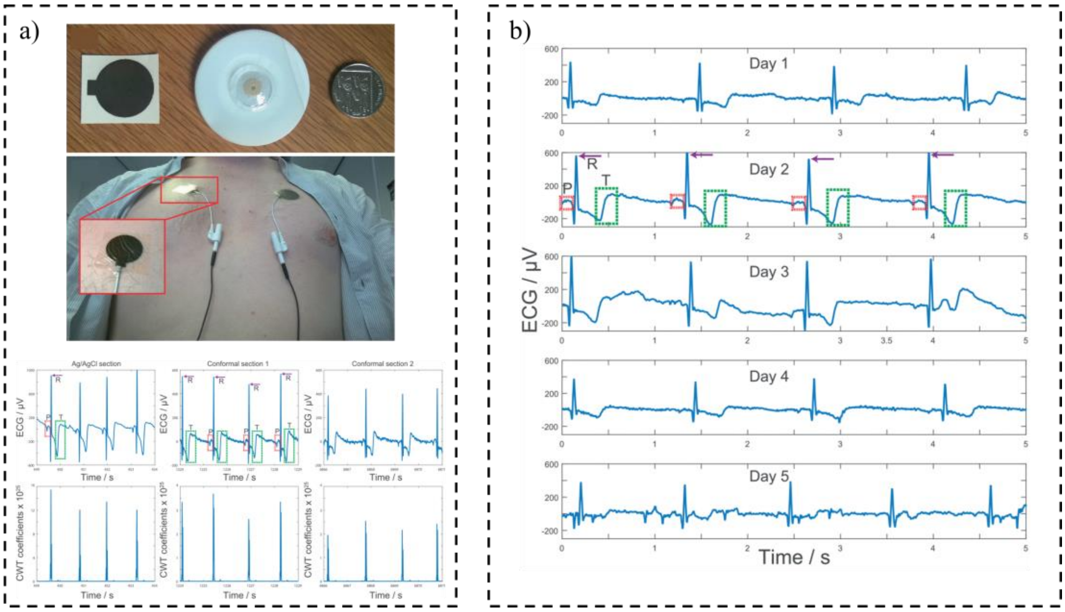

Figure 15 Casson et al. [34] printed Silver electrodes for long-term acquisitions. a) the electrodes presented a 25 mm circle for the active area and a 7 mm tab for connecting the recording wire; b) five segments of ECG recordings were performed on a subsequent day.

A different approach for the fabrication of tattoo electrodes was proposed by Guo et al. [35] which consists of a self-wetting electrode composed of a layer of ethyl-cellulose fiber paper coated with PEDOT/PSS (PCwPEDOT) and a thin layer of Parylene. The whole idea behind is the employment of the moisture naturally created by the skin under the tattooable patch to self-wet the electrode. Thanks to this method, the authors were able to develop a cost-effective tattoo electrode for the acquisition of biopotential with low skin/electrode impedance. The design of the electrode, in particular the back layer of the paper coated with a 3 µm thick Parylene layer, was aimed to increase the humidity of skin thus acting as electrolyte-containing ions. Thanks to this, the authors were able to increase the effective contact area between the electrode and skin, and decrease the impedance of the electrode, even if the total thickness of the tattooable patches was equal to 33 µm.

Concerning the fabrication process, the electrode was composed of two main layers: the barrier layer and the reservoir layer. The first, which was a thin layer of Parylene was used to collect sweat evaporating from the skin, while the latter, which was a layer of ethyl-cellulose fiber Paper coated with PEDOT/PSS (PCwPEDOT), had the aim to preserve the sweat. Therefore, when the electrode was soaked with sweat, the efficient contact area between the skin and the fibers-tissue patch was enlarged. Figure 16 a) shows the fabrication process and an optical image of the device. The authors studied the Skin-Electrode contact impedance and Figure 16 b) shows the resulting plot. Two electrodes were placed 2 cm apart on a forearm and a sinusoidal signal with 5 mV of amplitude was applied to measure the contact impedance. The input AC signal varied from 0.1 to 1000 Hz. The same approach was employed to study the contact impedance of a pair of commercial Ag/AgCl pre-gelled electrodes. In addition, the long-term stability was studied by applying the electrodes on a subject's forearm for two days and the impedance was tested every two hours for 2 days. In Figure 16 c) an example of an ECG signal recorded from the self-wetting wearable electrodes before and after the 24 hours of wearing is shown.

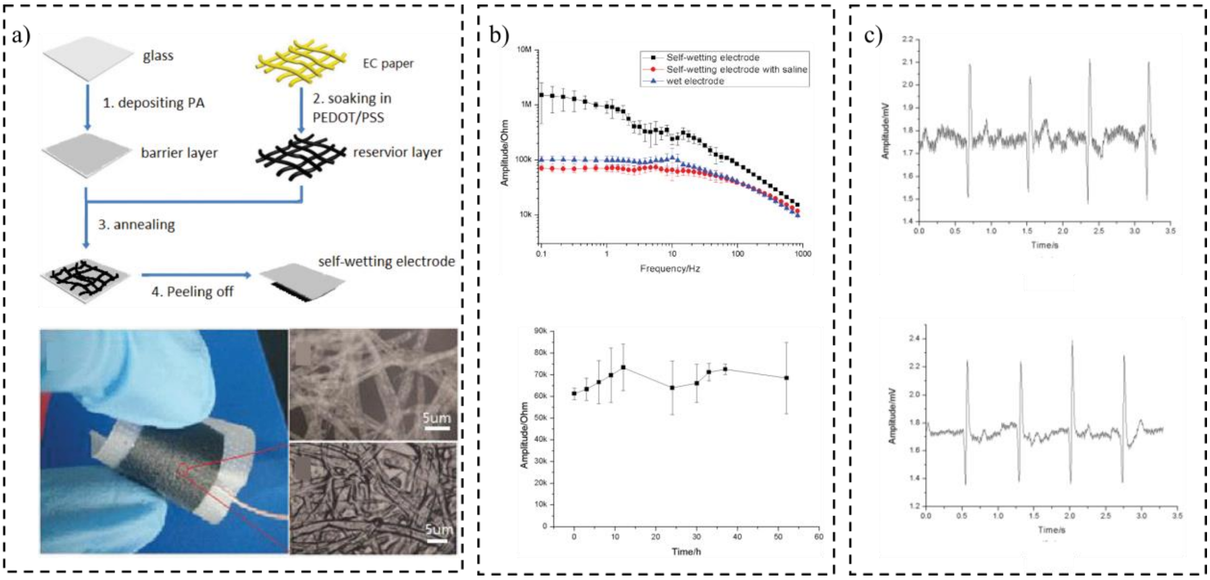

Figure 16 self-wetting wearable electrodes proposed by Guo et al. [35]. a) tattoo electrode fabrication process and images of the wearable patches; b) contact impedance analysis; c) ECG signal acquired before and after 24 hours of wearing.

Shustak and co-workers [36] developed a wearable system to record simultaneously EMG, EEG, and EOG signals for home monitoring sleep applications. The gold standard for sleep monitoring is an overnight sleep in a polysomnography (PSG) laboratory. However, this measurement suffers from some difficulties for the patient, and it is far from the usual sleep environment. Thus, it could affect somehow the measurement. In this context, the authors developed a wearable system to demonstrate the use of printed electrode technology as a novel platform for sleep monitoring. The electrode array was specifically designed to record EEG, EOG, and EMG and the fabrication process started on thin polyurethane films where a silver layer was applied to establish the connecting lines. Afterward, as an active electrode site, a second carbon layer was deposited. Finally, the authors used a double-sided adhesive to establish a stable attachment to the skin and a soft headband was used to secure the amplifier unit, which was connected through a Zero-Insertion-Force (ZIF) connector to the electrodes array. Figure 17 a) shows the proposed system with the 8 electrodes, the 8 channels amplifier, and the wireless system to communicate that consists of an Intan chip integrated on a customized printed circuit board (PCB), a Bluetooth low-energy (BLE) chip, and a battery. Moreover, Figure 17 b) reports the data from the validation tasks; blinking, eye movements, smiling, and swallowing of four representing channels are reported for EMG, EOG, and EEG from top to down.

While EMG and EOG signals have a relatively high amplitude, EEG signals are usually weak. Therefore, to validate the EEG acquisition performances, the authors demonstrated the capability to capture Alpha waves, one of the most common features in brain signals analysis. After eye closure and relaxation which also erase the typical noise from the eye blinking, from the spectral power analysis an onset of Alpha waves at ~10 Hz is clearly distinguishable.

In addition, the authors showed an example of a full night recording at home from one subject. All those acquired signals are reported in Figure 17 c).

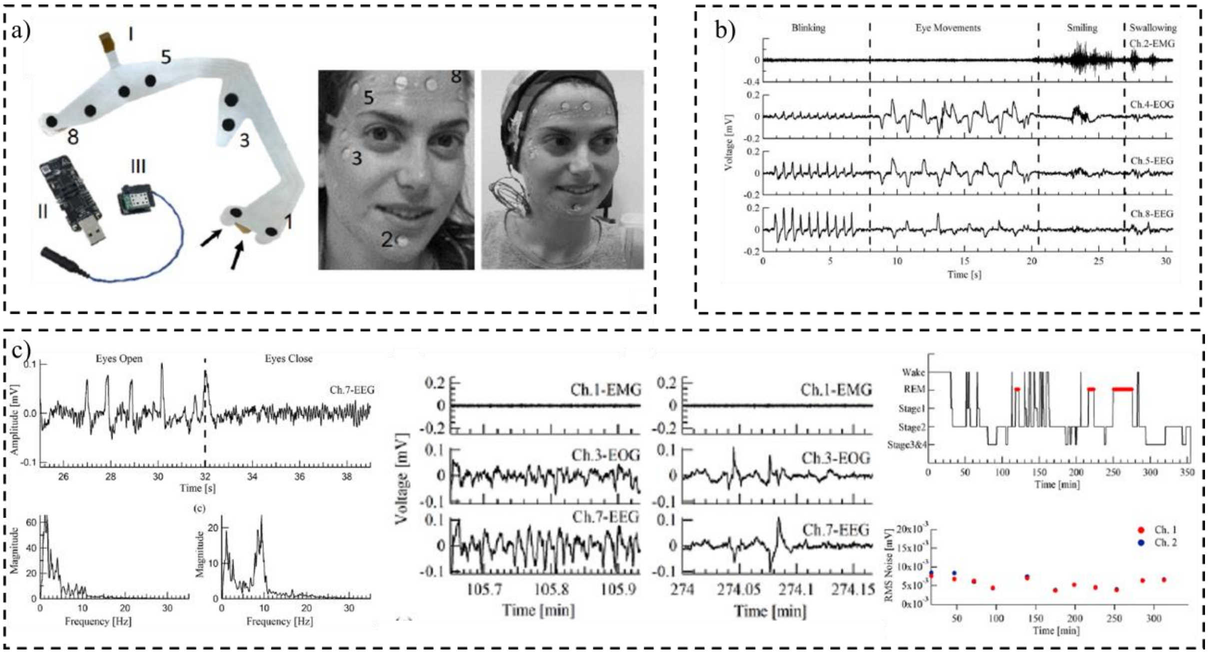

Figure 17 Shustak and co-workers [55] developed a wearable system to acquire EEG, EOG, and EMG for home monitoring sleep applications. A) the electrodes array and the custom PCB to record the signal and wireless communicate the data; b) an example of bio-signals recorded during a validation task; c) EEG validation and spectral power analysis and an example of full-night recording.

It is worth noticing that for biopotential recording the conformal contact with the skin (without the use of any conductive gel) and the feature of being unobtrusive are particularly convenient and appealing. For a tattoo system, the main requirements are biocompatibility and chemical inertness, features that can minimize adverse skin responses. In addition, a tattoo system has to be skin-conformable to enhance effective electrode/skin interface adhesion thus greatly improving signal acquisition and minimizing motion artifacts.

In this contest, Wang et al. [37] developed a low-cost, open-mesh epidermal tattoo with a total thickness of just 1.5 µm, which can be directly attached to the human skin and can conform to natural skin texture. In addition, the tattoo was tape-free and designed into an open-mesh filamentary structure, which makes it breathable and exhibits negligible stiffness. In fact, breathability is a recent important key characteristic for epidermal electronic systems, especially for long-term monitoring, such as in an intensive care unit or dynamic ECG (Holter) applications, and critical applications such as neonatal care and monitoring of heavily wounded or burnt patients. For this purpose, the authors developed the following cut-and-paste production process (Figure 18 a)): (i) liner removal from a commercial tattoo paper; (ii) lamination of the 1.4-µm-thick transparent PET sheet on the tattoo paper; (iii) Cr/Au deposition (110 nm total thickness) with thermal evaporator; (iv) patterning of the Au/Cr/PET sheet with a commercial cutter plotter; (v) peeling off the extraneous parts from the tattoo paper; (vi) for the application on human body, the skin was firstly wetted (vii) and then the epidermal tattoo was pasted (viii) on the skin from tattoo paper. Moreover, the figure shows an optical image of the patch and how it responds to mechanical stress and stimuli when placed on the skin. The electrical characterization showed the relation between thicker and thinner electrodes and thus how the thickness affected the contact impedance. However, even the thinner epidermal electrodes presented a higher impedance with respect to gelled ones. Considering the biopotential acquisition, the authors simultaneously recorded the ECG signal by a 13-µm-thick e-tattoo, 1.5-µm-thick e-tattoo, and gel electrodes. As it is possible to notice from Figure 18 b), the tattoo electrode performances are comparable with respect to disposable gel electrodes.

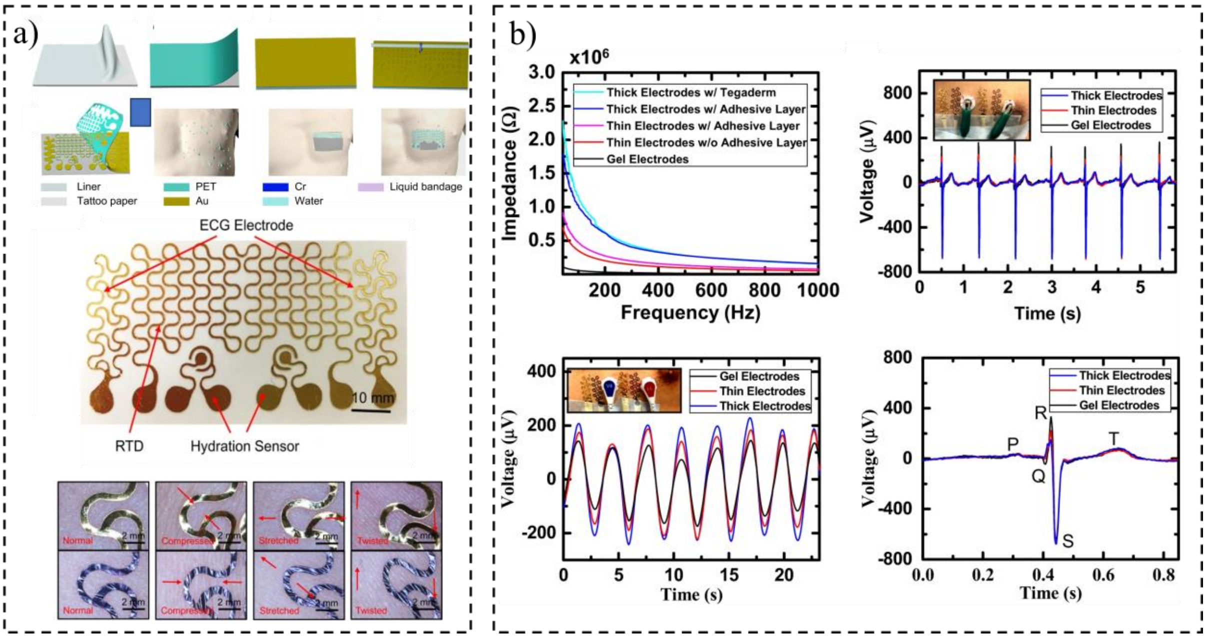

Figure 18 Breathable tattoo electrodes for biopotential recording (Wang et al. [37]. a) Fabrication process of the electrodes and optical images; b) Tattoo electrical performances in terms of contact impedance and ECG signal recording.

Later, with the same cut-and-paste approach Wang et al. fabricated large-area, soft, breathable, substrate- and encapsulation-free electrodes [38]. In particular, the electrodes developed by the authors were substrate-free and designed as filamentary serpentine ribbons, with a thickness of about 1.2 µm. As a consequence, the tattooable electrodes were sweat and heat-permeable, skin-conformable due to the reduced thickness, and extremely stretchable and lightweight. Thanks to this improvement, the authors were able to capture various biopotentials in high fidelity at scale, including 16-channel sEMG on the forearm for the interpretation of sign language and prosthesis control, 16-channel sEMG on the neck for activity classification, and 16-channel ECG on the chest for cardiac health monitoring. In addition, the authors studied a technique based on the Cartan curve to successfully transfer the tattoo electrodes over large areas with the aim of reducing the mechanical stress that could yield fractures or wrinkles.

A different approach for the fabrication of tattoo electrodes was proposed by Zhang et al. [39]. The authors developed a fully-organic dry electrode that presented self-adhesiveness and stretchability properties, by mixing PEDOT:PSS, WPU, and D-sorbitol (Figure 19 a)). This process allows to obtain a PWS film that can be placed on several surfaces. The authors studied the conformability and adhesiveness of the film as shown in Figure 19 b). In particular, it is interesting to note that the adhesion force of the PWS film to the skin was equal to 0.43 N/cm. However, these values slightly increased when the film was stretched due to a reduction of the thickness (from 20 μm of the pristine state to 15 μm at a strain of 30%). Therefore, the better force adhesion of the stretched film can be attributed to the better compliance of the thinner film to the skin. Moreover, the PWS films presented low electrode-skin electrical impedances in the frequency range of 1–10^4 Hz, comparable with respect to commercial gel electrodes.

The authors demonstrated the possibility of employing the PWS electrodes to detect different biopotentials. In this study, ECG, EMG, and EEG signals were recorded and together with the acquisition set-up they are reported in Figure 19 c).

Figure 19 Zhang et al. [39]: fully organic dry, conformal, and self-adhesive electrodes for biopotential recording. a) fabrication process; b) conformability, adhesiveness, and contact impedance study; c) biopotential acquisitions: ECG, EMG, and EEG signals recording.

Another interesting approach was proposed by Aguzin et al. [40] who developed a dry electrode based on the combination of the conductive polymer PEDOT:PSS, an ionic electronic conductor material, and deep eutectic solvents (DESs). Thanks to this easy and cost-effective method, the authors obtained a film with high conductivity values (450 S cm^{-1} for the electrical conductivity and 0.16 S cm^{-1} for the ionic conductivity). The eutectic solvents (DES) are biocompatible mixtures of pure compounds that are characterized by an easy and green synthesis, which avoids solvent and purification steps and possesses low toxicity and cost because their components are often renewable resources. The employment of Deep Eutectic Solvents (DES) additives induces the gellification of the compound thus leading to the formation of conducting eutectogels with high conductivity that can be directly written in different shapes and patterns. In addition, flexible and skin-conformal dry conductors could be obtained thanks to thermal annealing, showing the possibility of employing it as an electrode for biopotential acquisition.

As shown in Figure 20, the authors employed an adhesive paper to better place the conductive film onto the skin to acquire the biopotential (in this study EMG from the forearm and the thumb were recorded).

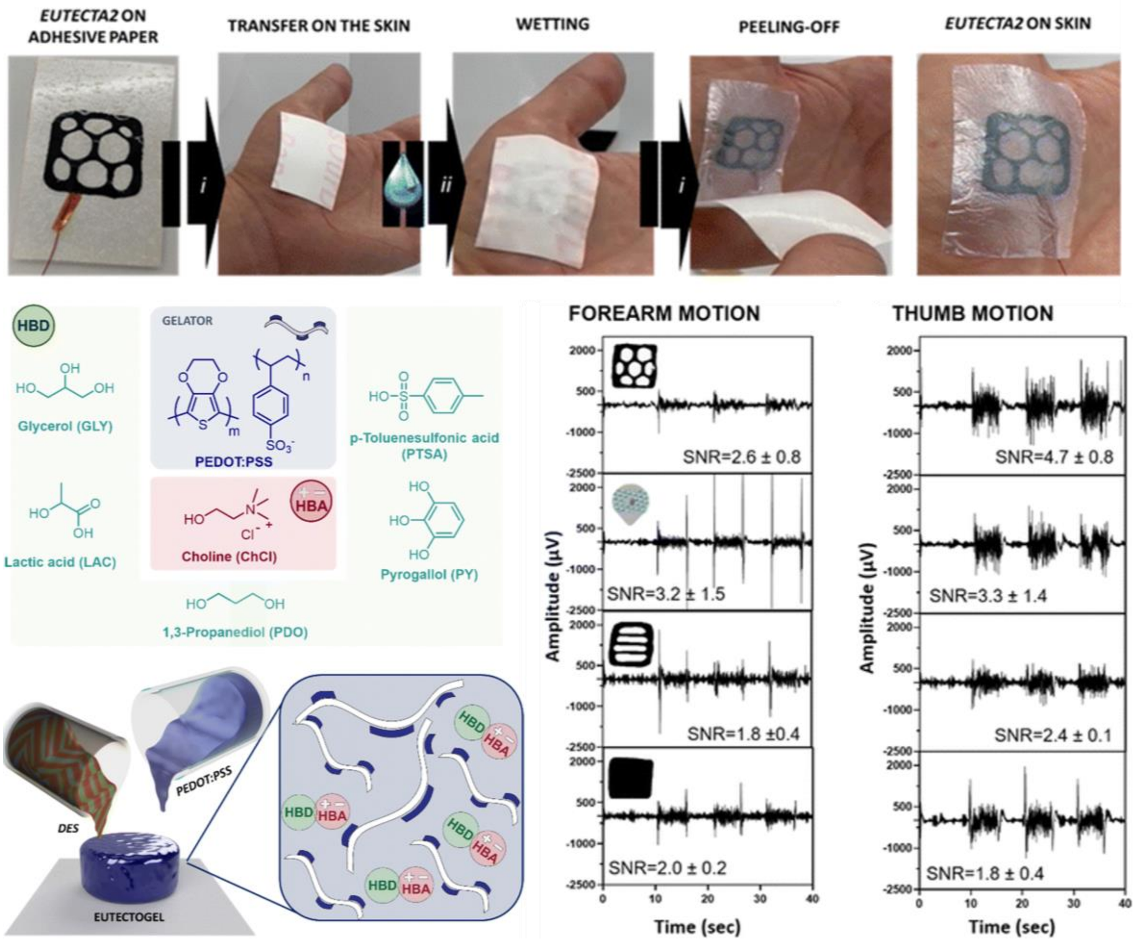

Figure 20 Aguzin et al. [40]dry-electrodes based on the mixture of the conductive polymer PEDOT:PSS, an ionic electronic conductor material, and deep eutectic solvents (DESs).

Another interesting approach characterized by low-cost materials and simple fabrication techniques was developed by Zucca et al. [41], who reported on the fabrication of ultra-conformable conductive electrodes made of PEDOT:PSS with submicrometric thickness deposited onto a temporary tattoo paper. The transfer paper sheet employed consisted of three layers, i.e. the paper, the starch–dextrin coating (water-soluble layer), and the ethylcellulose (EC) layer, which is the layer that after wetting the paper is released due to starch–dextrin dissolution. Thanks to the tattoo paper thickness, the electrode can adapt conformally to the skin microfeatures, as shown in Figure 21 a), where the SEM image of the device placed on a PDMS replica of the human skin is reported. The tattoo electrodes were employed to acquire the sEMG signal from the flexor carpi ulnaris muscles of one healthy subject and compared it with the signal recorded by pre-gelled Ag/AgCl electrodes (Figure 21 b)).

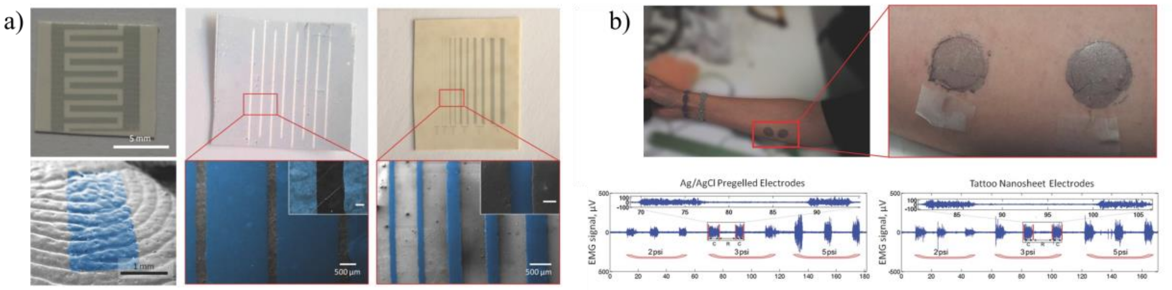

Figure 21 tattoo nanosheet based on PEDOT:PSS electrodes and temporary transferable paper [41]. a) SEM image of the tattoo electrodes on a PDMS replica of the human skin; b) sEMG signal acquired from a subject's forearm.

Greco's group, later, developed an inkjet-printed ultra-comfortable electrode for electrophysiology [42]. The authors fabricated dry, temporary tattoo electrodes by inkjet printing onto commercial transfer paper with the conductive polymer PEDOT:PSS. The conformal adhesion to the skin was guaranteed by an electrode's thickness smaller than 1 µm, thus the user comfort and mobility were increased. The manufacturing process aimed to employ low-cost and large-area methods and thus compatible materials. Therefore, transferable tattoo paper based on ethylcellulose was used as the substrate, since it is skin-safe and compatible with large-area processes, while inkjet printing, cutting, and lamination were the fabrication processes employed since they allowed low-cost and large-area device production. Moreover, the employment of materials with submicrometer thickness and Young's modulus closer to the modulus of the human skin (1 GPa) allowed to obtain a conformal adhesion with the human body. In Figure 22 a) a sketch of the proposed electrodes with the interconnections, the colorized SEM image, and an optical image of the tattoo electrode attached to a skin are shown. Moreover, the authors studied the contact impedance short-term and long-term of the ultra-thin electrodes and they compared them with a standard wet Ag/AgCl electrode and a dry metal electrode. Considering the short-term impedance study, as it is possible to notice from Figure 22 b), the tattoo electrode showed a higher impedance with respect to wet Ag/AgCl and dry metal electrodes, with a value around 300 kΩ at 60 Hz. For the long-term study, indeed, the authors evaluated the impedance variation over 48 h, and a slight increase in the modulus of the impedance was reported. Nevertheless, the printed tattoo electrodes were successfully employed to acquire several biopotentials from the surface of the human skin as shown in Figure 22 c). Particularly, the ECG signal was simultaneously recorded with tattoo and standard electrodes with the same active area to compare the quality of the two signals. Moreover, the electrodes were employed to capture the EMG signal from the mandibular muscle on the efface. It is interesting to observe that even if the user's hair grew through the electrodes since they were placed on the skin for more than 24 hours, the tattoo electrodes were able to acquire a good EMG signal. In addition, the authors developed a multielectrode array, whose final design can be easily modified depending on the final application thanks to the fabrication process employed. In particular, the recording active area made of PEDOT:PSS was inkjet-printed on the substrate (i.e. the tattoo paper) and a gold layer was employed for internal interconnection and deposited through a sputtering deposition method. Finally, the tattoo was assembled with a shaped glue layer and wires for external contact.

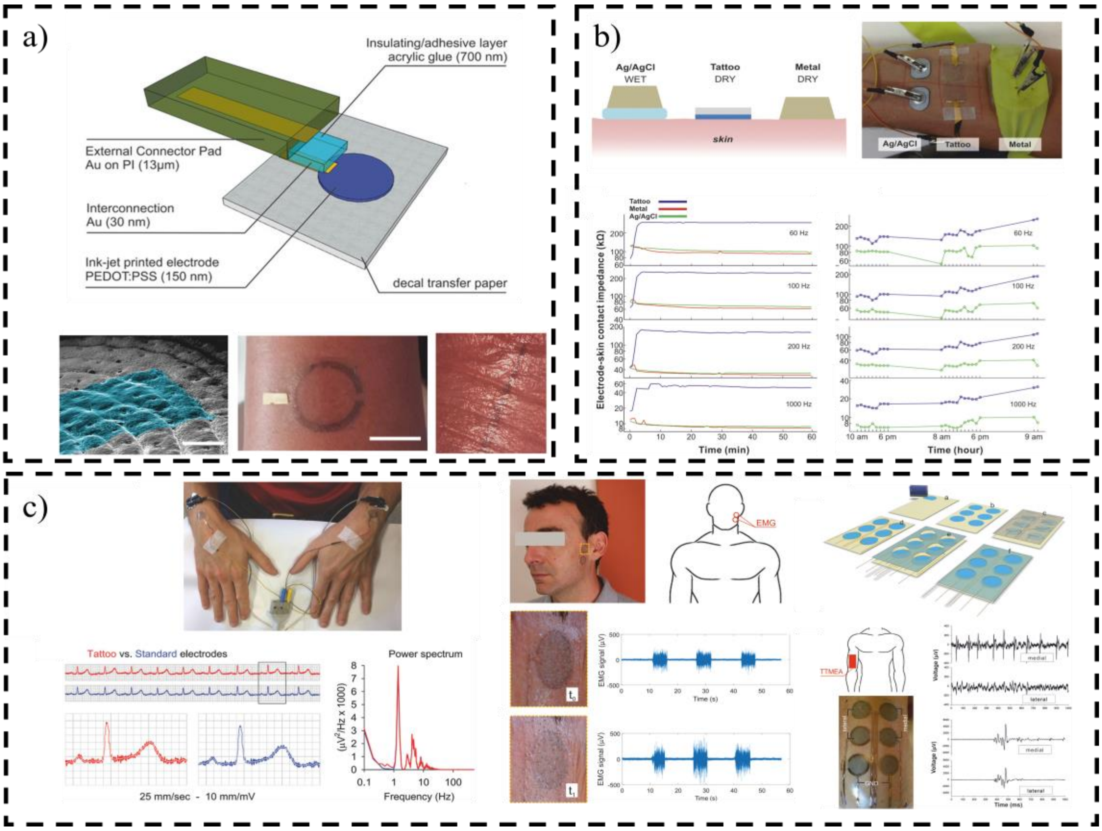

Figure 22 Ultra-conformable tattoo electrode fabricated through an inkjet printing technique for electrophysiological applications [42]. a) sketch of the device where the interconnection for the acquisition of the signal is highlighted; b) Contact impedance of the tattoo electrodes compared with respect to wet Ag/AgCl and dry metal electrodes. The impedance was studied within 60 minutes and 48 hours; c) biopotential acquisitions. The authors reported the acquisition of the ECG, the EMG signal, which was acquired also through a multielectrodes array.

The group, afterwards, presented another possible application for the PEDOT:PSS-based temporary tattoo electrodes. Ferrari et al. [43] investigated the performances of the electrode for EEG signal acquisitions and their potential integration in a standard clinical evaluation protocol for brain health assessment, which can be usually performed together with magnetoencephalography recordings. The device fabrication process is reported in Figure 23 a) as well as an optical image of the tattoo electrode placed onto the skin. As it is possible to notice, the device presented a layered structure, however only the ethylcellulose film with the PEDOT:PSS electrode was laminated onto the skin, thus resulting in an imperceptible film for the user. With respect to previously presented works, the authors optimized the tattoo electrodes for the acquisition of EEG signals. Both the electrodes and external connector were designed to achieve high quality and low noise recordings since EEG signals are weak compared with other biopotentials (i.e. ECG and EMG). The authors chose a 1.5 µm thick tattooable substrate with the aim of improving the mechanical stability of the electrodes on the skin. Moreover, it is worth mentioning that the connection between soft and ultrathin devices with hard external electronic circuits is one of the most critical issues in the epidermal electronic field. The authors developed an external connection made of a 1.3 µm thick polyethylene naphthalate (PEN) sheet and a dedicated plastic clip to improve the robustness of the connection and simultaneously record reliable brain signals. This aspect will be also discussed later in this thesis.

In Figure 23 b) the brain activity measured by placing the tattoo electrodes according to the 10–20 international system is reported. From the spectrogram reported in the figure, it is possible to clearly notice the Alpha waves (10 Hz) which are the brain waves related to the relaxation of the subject. Moreover, the figure shows the time-frequency plot of alpha wave recorded with both tattoo and Ag/AgCl electrodes.

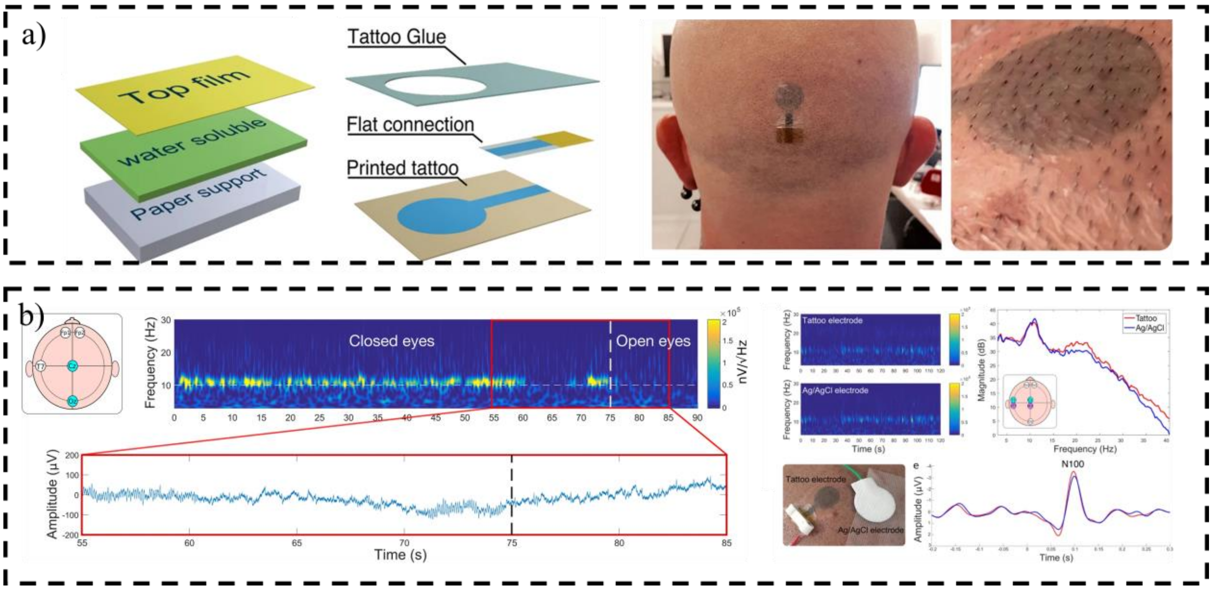

Figure 23 Ferrari et al. [43] tattoo electrodes for EEG recordings compatible with magnetoencephalography acquisitions. a) device fabrication process and tattoo electrode laminated onto the skin; b) Brain activity recordings, where alpha waves are clearly notable from the time-frequency plots.

Another interesting approach based on ultra-thin and highly conformable electrodes was proposed by Ameri et al. [44], who developed a graphene-based electrode for electrooculography (EOG). Thanks to this method, the authors developed a system able to detect eye movement with an angular resolution of 4°, moreover, the eye movement can be accurately interpreted, thus enabling the possibility to employ the ultra-thin graphene electrodes for human–robot interface (Figure 24 a)).

Ha et al. [45] developed an ultra-thin electronic tattoo to perform seismocardiography (SCG), which is a measure related to the chest vibration associated with heartbeats. In this field, wearable SCG sensors are still based on either rigid accelerometers or non-stretchable piezoelectric membranes. The authors developed a filamentary serpentine mesh of 28-µm-thick piezoelectric polymer, namely polyvinylidene fluoride (PVDF) which can be directly attached to the chest to improve the comfort and the wearability for the user during SCG recordings. In addition, by integrating a pair of gold electrodes and one PVDF vibration sensor on the same Tegaderm substrate, the authors developed a sensing tattoo capable to record ECG and SCG signals for continuous measurements and extracting various cardiac time intervals including systolic time intervals (Figure 24 b)).

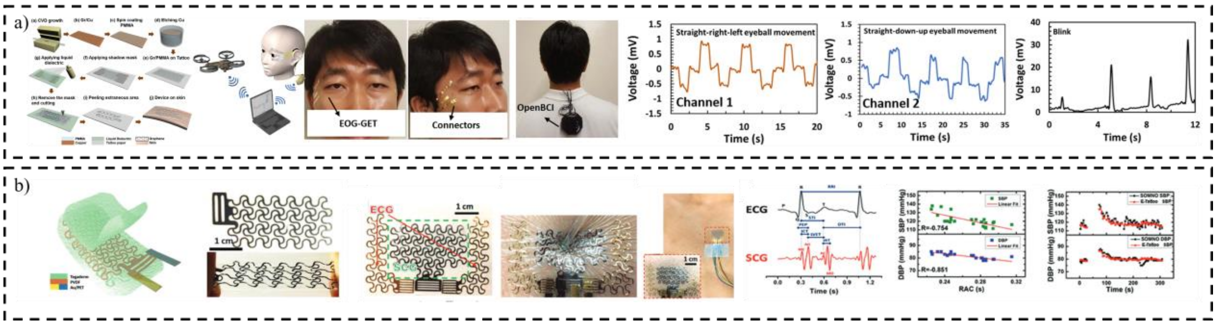

Figure 24 Ultra-thin tattoo electrodes and systems developed to a) acquire the EOG for Human-Machin interactions [44], and b) to perform SCG and ECG acquisitions [45].

Ultra-thin and highly conformable electrodes can be obtained and fabricated through several methods. Liu et al. [46], for example, developed a sub-micrometer thick epidermal electrode by simultaneously performing an electrospinning of polyamide nanofibers and electrospraying of silver nanowires to form a homogeneously convoluted network. Thanks to the reduced thickness, the film could conform to human skin via van der Waals force and the contact impedance was 50% lower than the one obtained for commercial gel electrodes. The robustness showed by the nanomesh makes the electrodes particularly interesting to perform ambulatory measurements of physiological signals for healthcare applications. In Figure 25 a) the fabrication process and the mechanical characteristics of the sub-micrometer film are reported. The fabrication process was performed by simultaneously electrospraying the polyamide-6 as a structural component of the electrode, since it ensures biocompatibility and good mechanical properties, and by electrospraying silver nanowires onto the same metal collector. This fabrication method allowed to obtain a homogeneous film, where the silver nanowires were not only at the top of the structure but also across the nanofiber-based scaffold. Moreover, the film had a total thickness of about 500 nm, thus ensuring a conformable attachment to the skin.

Moreover, the ultrathin electrodes showed a lower contact impedance with respect to Ag/AgCl wet electrodes as shown in Figure 25 b). The authors asserted that these electrical performances were obtained thanks to the high conductivity of the film and the high conformability. In addition, figure b) reports several ECG signal measurements performed with both the epidermal electrode and commercial Ag/AgCl electrodes. It is interesting to notice that the ECG signal remained stable during the user's physical activity, thus demonstrating the robustness of the device and the possibility to perform biopotential measurement for healthcare applications.

A similar approach was employed by Jiang et al. [47] who designed an epidermal electrode consisting of Ag NWs and polyurethane (PU). The structure of the device can be described as a layering of nanofibers and nanowires and the adhesion between the two was achieved via interfacial hydrogen bonds. Such structure allowed a high conductivity of the film (9190 S cm^{-1}) and a total thickness of less than 3 µm, which ensured a relatively good adhesion with the skin without the use of any glue or gel. In Figure 25 c) a SEM image and a sketch that illustrates the adhesion between layers inside the film are reported. The authors demonstrated that such nanostructured film can be employed as breathable electrode for continuous electrophysiological signal recording (as the contact impedance is comparable with respect to standard Ag/AgCl electrodes) or as a epidermal strain sensor for joint motion detection. In Figure 25 d) highlights the device laminated onto the skin and the electromechanical characterizations as strain sensor and epidermal electrode for biopotential measurement.

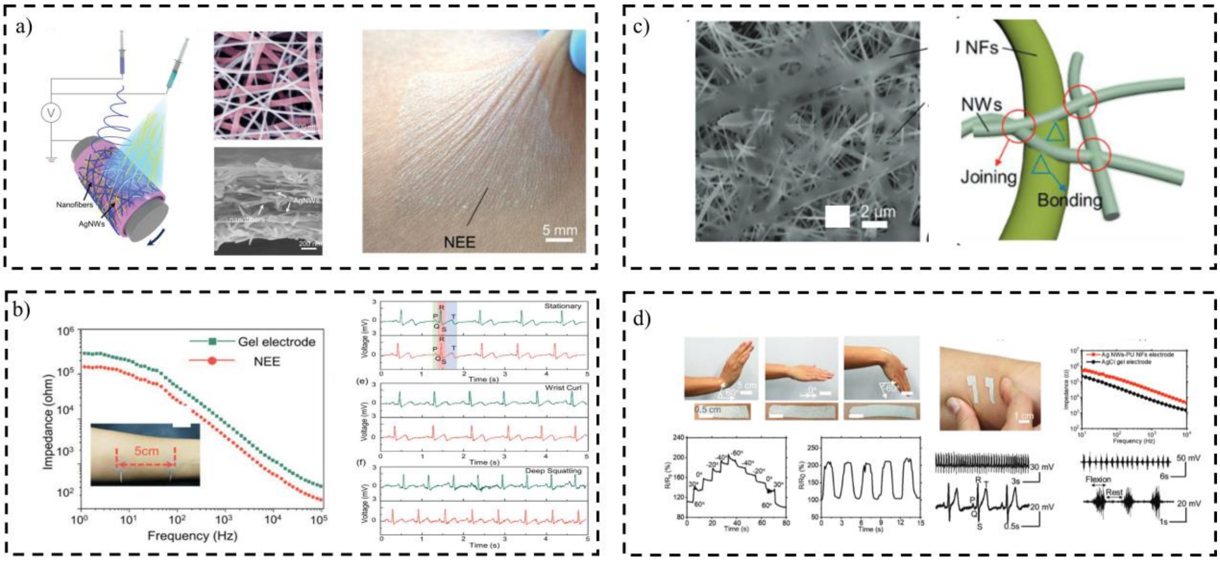

Figure 25 Ultra-thin epidermal electrodes based on a nanofiber/nanomesh film. a) Fabrication process and different images of the AgNW electrodes (SEM and optical figure); b) Contact impedance measurement of the tattoo electrodes (red line) and Ag/AgCl standard electrodes (green line). ECG signals were acquired simultaneously with wet standard Ag/AgCl electrodes and the epidermal electrodes. Work by Liu et al. [46]; c) SEM image and sketch of the adhesion of the nanofibers and nanomesh in the conductor; d) epidermal film employed as strain sensor for joint motion detection and electrode for ECG and EMG measurements. Work from Jiang et al. [47].

Stretchability is one of the most interesting characteristics that can be related to epidermal electronic systems. By the integration of metal electrodes in elastomers, Shahandashti et al. [48] developed a stretchable dry electrode for the long-term monitoring of the ECG and EMG signals. In particular, the authors embedded a thin film of metal into a polydimethylsiloxane (PDMS) film, used as primary material for the fabrication of the electrodes. Metal films are usually rigid and cannot be stretched due to their high stiffness. However, by reducing the film thickness and using a meander shape, it was possible to obtain a stretchable electrode. The authors studied the contact impedance in the short-term (10 minutes after the application of the dry stretchable electrode) and in the long-term (20 hours after the application of the electrodes) and they compared it with wet commercial Ag/AgCl electrodes. As a result, the authors noticed that the contact impedance of the dry electrode was comparable to the wet electrode in a short time. Moreover, the contact impedance decreased in time showing that the stretchable electrodes can be successfully employed in long-term applications. Finally, the authors measured the EMG and ECG signals with relatively good performance by employing the stretchable dry electrodes.

Using a different approach, Cao et al. [49] developed a stretchable, organic, and solution-processable electrode by drop casting an aqueous solution consisting of poly(3,4-ethylenedioxythiophene):polystyrenesulfonate (PEDOT:PSS), poly(vinyl alcohol) (PVA), tannic acid (TA), and ethylene glycol (EG). The electrodes showed a stretchability of 54 % thus they were capable of reproducing skin movements. Moreover, the self-adhesive given by the properties of the film induced by both PVA and TA made the electrodes suitable for stable acquisitions even during user activities. In fact, the electrodes showed lower contact impedance values when compared to Ag/AgCl electrodes and also were less affected by external noise due to the deformation of the skin. The authors successfully acquired both ECG and EMG signals either during user physical movement or rest.

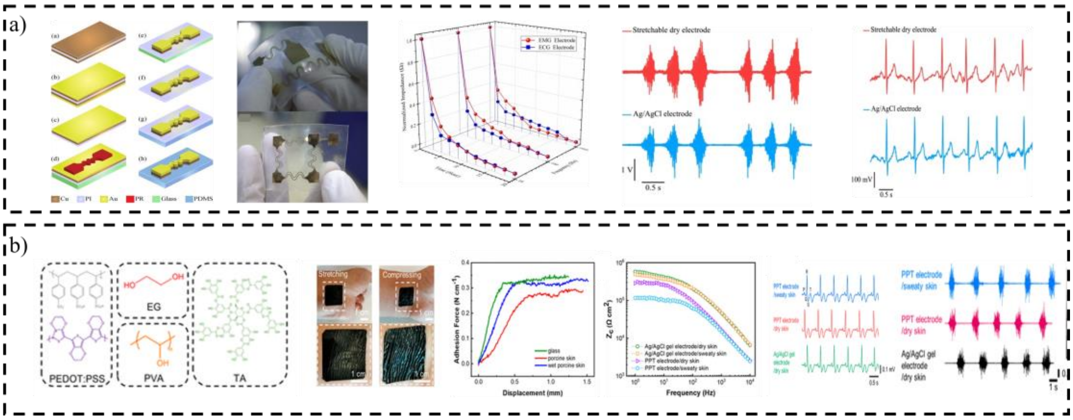

Figure 26 Stretchable electrodes for the acquisition of biopotential developed by a) Shahandashti et al. [48] and b) Cao et al. [49].

Among the different wearable applications for the acquisition and monitoring of different physiological parameters and biopotentials, particularly intriguing are all those novel applications involving the non-clinical monitoring of EEG (electroencephalography) signals. Several devices and applications have been recently reported, ranging from human-machine interfaces to innovative approaches for biometry and emotion recognition [50]–[55].

Unfortunately, the recording of brain activity usually requires bulky measurement setups with up to 256 electrodes in high-density systems [56], and it can be carried out only in controlled, often restricted, and uncomfortable clinical environments (Figure 27).

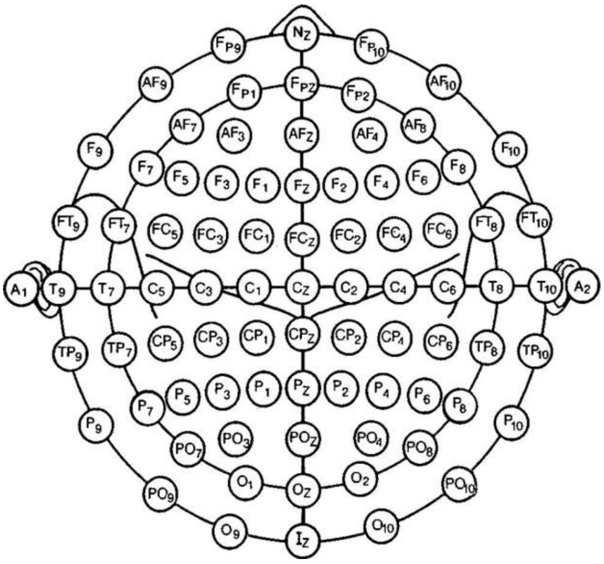

Figure 27 10–10-system, extended with anterior and posterior electrodes in the inferior chain [56].

Recently, alternative approaches have been proposed, such as the in-ear EEG [57]–[60]. This interesting solution allows to reduce the device size and the encumbrance of the set-up. In fact, ear EEG method is based on the employment of electronics systems in which the electrodes devoted to acquire the brain signals are placed outer the ear or inside the ear. However, such an approach is limited mainly to the detection of event-related potentials (ERPs). In Figure 28 some ear-EEG method at the state-of-the-art are reported.

Although at the moment some wearable devices for the acquisition of EEG signals are already present on the market [61], [62], they suffer from some drawbacks that are still limiting their widespread employment. In particular, such wearable systems for the acquisition of the brain activities present some issues and limitations that are mainly related to the size of the acquisition electronics, the data storage capability, the battery life, and the quality of the employed electrodes. In fact, since the EEG signal is usually weak, especially if compared to other biopotentials, such as ECG and EMG signals, an ideal electrode for wearable EEG systems should ensure a good signal quality while still being comfortable and, possibly, imperceptible to the user.

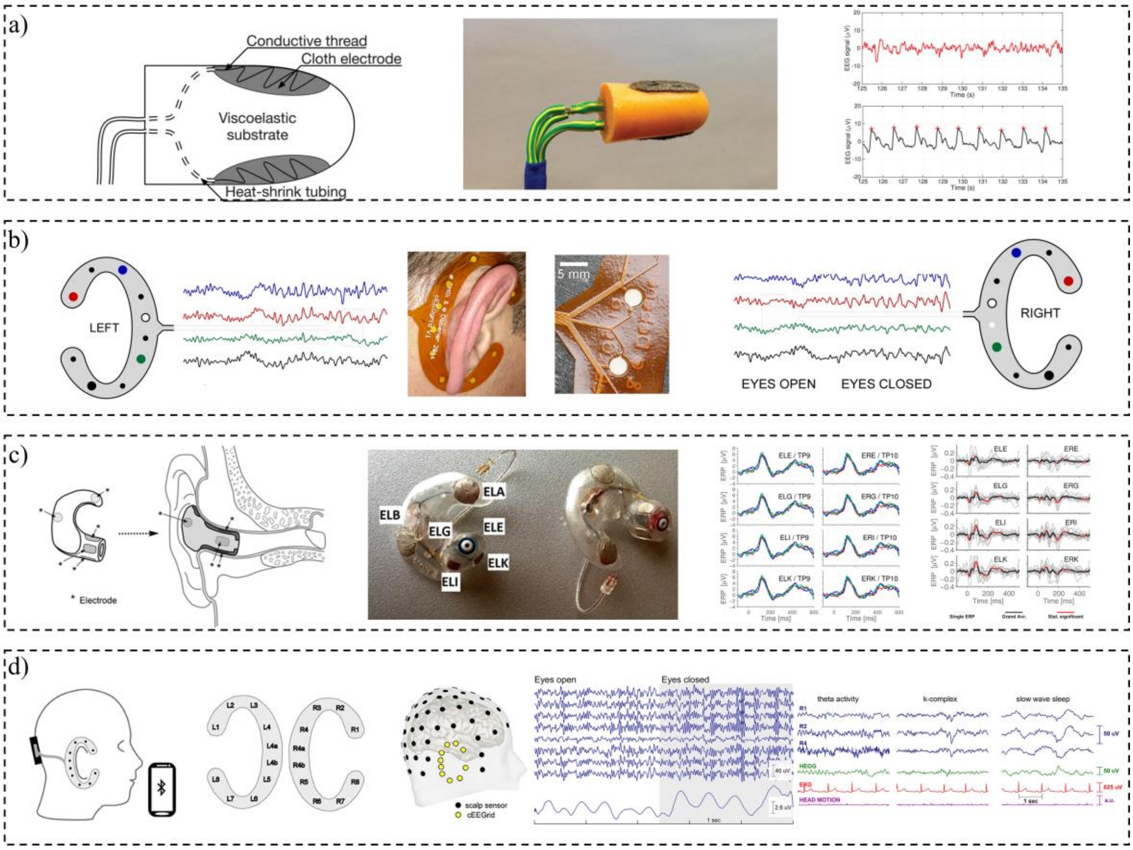

Figure 28 Wearable ear-EEG methods for the monitoring of the brain activities. a) Goverdovsky et al. [57] approach based on viscoelastic generic earpieces; b) Debener et al. [58] developed an unobtrusive ambulatory EEG acquisition system using a smartphone and a flexible printed electrodes to place around the ear; c) Mikkelsen et al. [59] reported an EEG recording system from the ear and its characterization; d) Bleichner and Debener [60] proposed an unobtrusive and transparent acquisition system to acquire the EEG signal from the outside of the ear.

Recently, some epidermal electronic systems were reported for the acquisition of the EEG signal. For instance, Norton et al. [63] developed a soft electronic designed to intimately conform to the complex surface topology of the auricle and the mastoid, to provide a high-fidelity EEG recording for brain computer interfaces (Figure 29 a)).

Peng et al. [64] proposed a different approach for the fabrication of an electrode for the acquisition of the biopotential. In particular, the electrode was based on porous titanium (Ti) and the proposed system presented a reservoir with 200 μl of an electrolyte that, when pressed, permeated from micro-holes of the porous Ti onto the skin. Therefore, the liquid provided continuous wet interface between electrode and skin to maintain low and stable contact impedance. Hower, this system lacks of conformability and it needed a continuous pressure to guarantee a sufficiently good contact with the skin. Figure 29 b) shows the porous electrodes and the EEG signal acquisition.

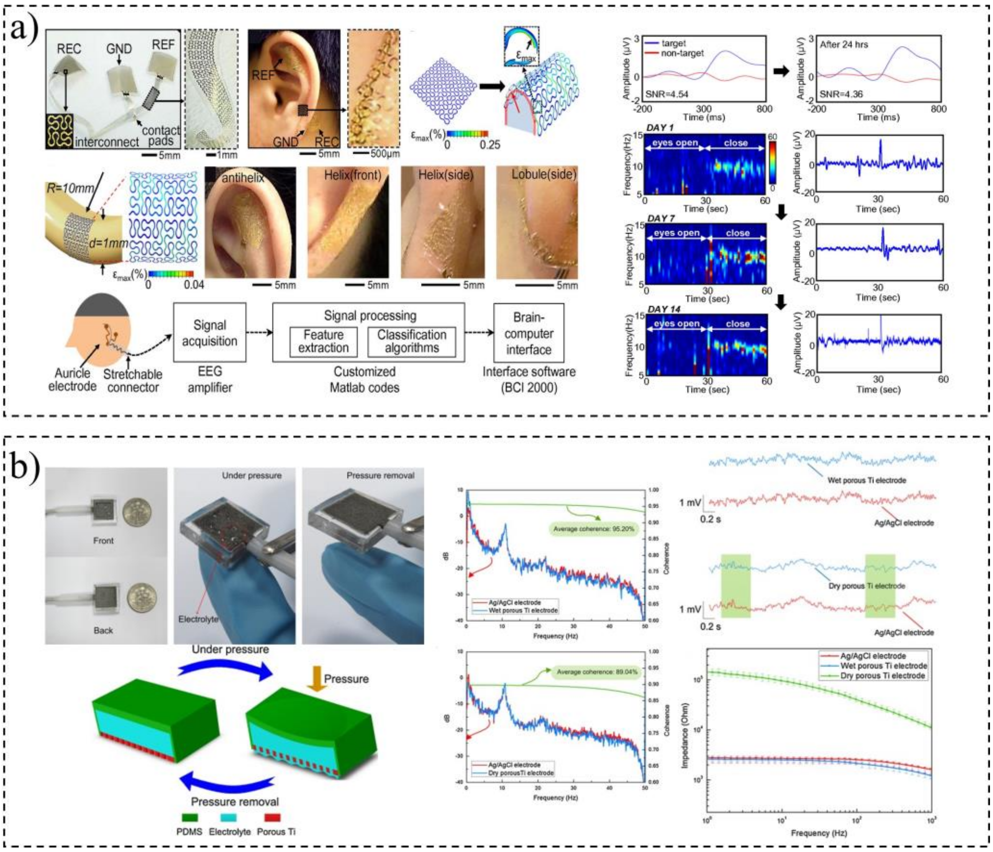

Figure 29 EEG recording system. a) Norton et al. [63] developed a ultra-conformable system for the monitoring of the brain activity by placing the electrodes into the ear; b) Peng et al. [64] reported a porous titanium electrode with a reservoir that, when pressed, release an electrolyte that pass through the electrode holes to the skin.

2.3.High-performing transistors for wearable applications

Among the organic electronic devices that nowadays drive the interest of the research community, organic field-effect transistors (OFETs) undoubtedly occupy a prominent role, thanks to their versatility and the several advantages that they can offer in terms of low fabrication costs, mechanical flexibility, and compatibility with large area deposition techniques [65]. However, despite their interesting features and apart from few examples, the full potential of OFETs has not been deployed yet in mass real-life applications. There are several fields that could greatly benefit from flexible and low-cost organic transistors, especially in real application scenarios [66]. In this context, the use of cost-effective electronic tags that can enable the link to smart objects at viable costs are an fundamental for wearable electronics applications. Yet, highly performing devices are required to intercommunicate and exchange continuous information in real time at high frequencies, i.e., in the high frequency to the ultrahigh frequency bands, from MHz to GHz. Such frequency range is still largely prohibitive for organic OFETs, especially when scalable, large-area processes must be adopted. In fact, up to now, the development of OFETs is mostly limited to those fields where a fast response is not strictly necessary. Moreover, when high currents levels are required, due to OFETs relatively low charge mobility, a large-width (*W*) organic transistors are usually employed, and this contributes to the increase of the area required to host simple electronic functions.

Among the different approaches to enlarge the transistor form factor, the reducing of the channel length (*L*) is one of the most commonly employed, since it is a process that has been efficiently employed by standard MOSFET technologies along the years, leading to a continuous miniaturization of the silicon-based MOSFET area and, as a consequence, to the increase of the density of devices per unit area, as well as the maximum operating frequencies.

Many strategies have been proposed so far for the fabrication of short-channel organic transistors, but in general it is possible to dived into two main categories: short-channel planar organic transistors and short-channel vertical organic transistor.

2.3.1. *Coplanar organic transistors*

Among the different approaches for the realization of short-channel transistors, the employment of photolithography methods, such as stencil lithography, nanoimprint lithography, and electron beam lithography, is one of the most commonly used and exploited. In particular, nanoimprint lithography allows to obtain channel lengths down to few tens of nm. Austin and Chou [67] in 2002 developed a thin film organic transistor with channel lengths from 1 μm down to 70 nm with high yields. The authors found that by decreasing the channel length, the drive current density increased (as expected) while the on/off current ratio remained the same (10^4). However, at short-channel lengths, OTFTs no longer saturated due to space charge limiting current effects. Figure 30 a) reports a SEM image of the device and the characteristic curves of the organic thin film transistor for three different channel lengths.

Li et al. [68] optimized the nanoimprint lithography fabrication technique thus obtaining a sub-20 nm alignment. In particular, the authors by exploiting the “beat” grating image (Moiré fringe) generated by overlaying two sets of gratings with slightly different periods, were able to obtain resolution better than 10 nm in nanoimprint lithography. Thanks to this, the author achieved an accuracy of 20 nm for single point alignment, sub-150 nm alignment for a 1 in area die, and sub-250 nm for a full 4 in wafer (Figure 30 b)).

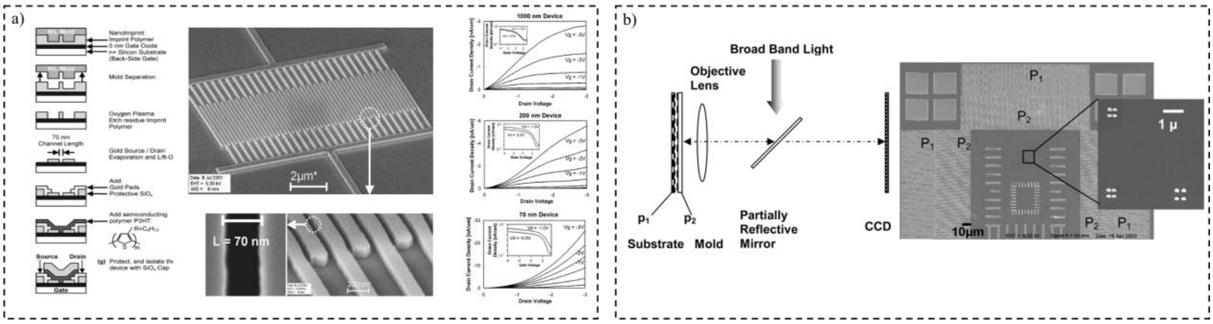

Figure 30 nanoimprint lithography method. a) Austin and Chou [67] organic thin film transistor with a 70 nm-channel. Fabrication method and SEM images are reported, as well as characteristic curves for three different channel lengths (1000 nm, 200 nm and 70 nm, respectively); b) Li et al. [68] nanoimprint lithography with "beat" grating image (Moiré fringe) generated by overlaying two sets of gratings with slightly different periods.

This fabrication technique was then successfully employed for the fabrication of organic thin film transistors. Haas et al. [69] fabricated a pentacene-based OFET onto a flexible substrate. Specifically, the nanoimprint lithography was employed for the patterning of the source and drain electrodes and processed directly on the gate dielectric, the structured gate electrode, and the flexible substrate. Moreover, thanks to the sub-100-nm thin organic gate dielectrics, a full drain current saturation for devices with channel lengths down to 500nm was observed. IN addition, the submicrometer organic transistors exhibited negative threshold voltages with an absolute value well below 5V and had subthreshold swings around 0.5V/decade.

The nanoimprint lithography was even adopted for roll-to-roll manufacturing. Leitgeb et al. [70] demonstrating that R2R-UV-NIL is a versatile tool for high-speed (>10 m/min) continuous fabrication of micro- and nanopatterns with high aspect ratios, high resolution, and 3D-like form factor on flexible substrates. The authors were able to obtain metallic patterns with only 200 nm line width, thus showing a high-throughput system for high resolution patterning techniques.

Another interesting method for the fabrication of high-resolution organic transistor was developed by Zschieschang et al. [71], [72], who proposed an effective stencil lithography approach for the development of both n-type and p-type submicrometer-channel OFETs on flexible substrates. The authors obtained an organic transistors with a channel length of 300 nm and a large channel-width-normalized transconductances of 1.5 S/m for the p-channel and 0.2 S/m for the n-channel transistors. Moreover, the transistors exhibited a steep subthreshold slopes of 80 and 200 mV/decade and an on/off current ratios of about 10^6. Figure 31 shows the organic transistor sketch with the employed materials. Specifically, the authors used as the semiconductor the DNTT for the p-channel TFTs and the N1100 for the n-channel TFTs. Moreover, for the dielectric layer two different Sam were employed: a n-tetradecylphosphonic acid for the SAM of the DNTT TFTs and a pentadecafluoro-octadecylphosphonic acid for the SAM of the N1100 TFTs.

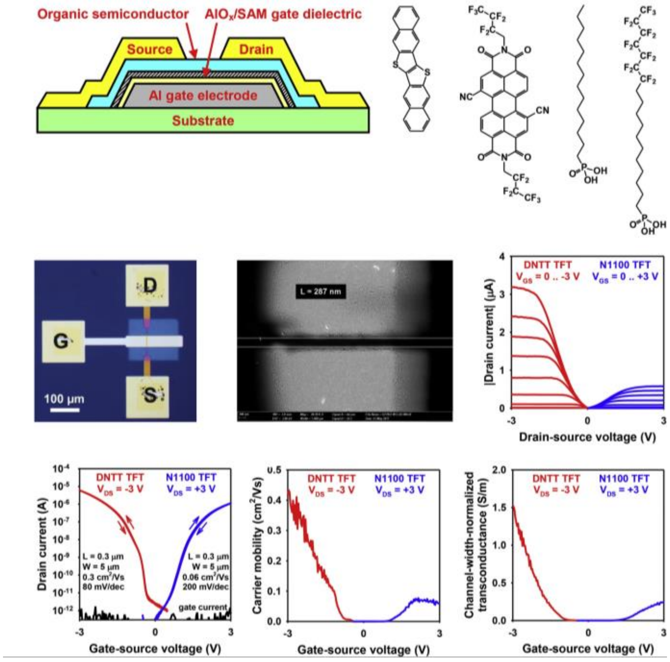

Figure 31 Organic transistor developed by a nano-imprint lithography proposed by Zschieschang et al. [71], [72].

Another interesting lithography approach is represented by the e-beam lithography, which is well known for enabling the realization of short-channel devices with channel lengths in the 100 nm range. Tsukagoshi et al. [73] developed an interface modification of a pentacene field-effect transistor with a submicron channel, fabricated through e-beam lithography. The authors modified the substrate interface with a thin polyparaxylylene film, obtaining a higher field-effect mobility of the short-channel transistor (300 nm). Figure 32 a) shows the schematic of the fabrication process and the electrical characteristic of the organic transistor.

With the aim to suppress undesirable short-channel effects in organic transistors with nanoscale lateral dimensions, Ante et al. [74] proposed an aggressive gate-dielectric scaling by the use of an ultra-thin monolayer-based gate dielectric and an area-selective contact doping, exploiting a strong organic dopant. The e-beam lithography processes were used for the fabrication of the metallization of the device, thus obtaining a submicrometer channel length. In Figure 32 b) the device structure, the SAM images of both the cross-section and the top view as well as the characteristic curves are shown.

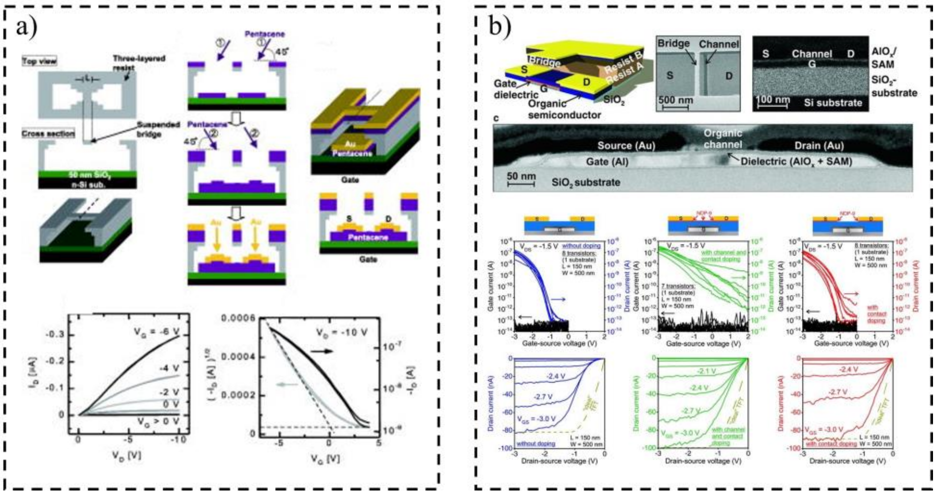

Figure 32 Sub-micrometer channel organic transistor fabricated through e-beam lithography proposed by a) . Tsukagoshi et al. [73] and b) Ante et al. [74]

Besides high-resolution lithographic techniques, non-lithographic, maskless, fabrication methods have been recently successfully employed to fabricate sub-micrometer channel-length organic transistors.

In particular, the recent work from Passarella et al. [75] demonstrated the potential of direct-writing approaches, such as fs-laser sintering of printed metallic inks, for develop short-channel devices. The authors reported a downscaled p-type polymer field effect transistors (FETs), fabricated on both rigid and flexible polymer substrates, by a combination of coating and direct-writing techniques. This fabrication technique enabled to achieve radio-frequency operation. In fact, transistors with the shortest channel of 1.2 μm can operate up to 22 MHz at a relatively low bias voltage of −12 V, as measured by scattering parameters (Figure 33 a)).

In terms of transition frequency (f_T) normalized by the applied gate-to-source voltage (f_T/V_{GS}), the transistor was able to achieve the value of 1.83 MHz V^{-1}, that is one of the highest for solution-processed organic transistors on plastic substrates.

Similarly, Perinot et al. [76] with a solution-processed and direct-written technique, designed and fabricated an organic field-effect transistors able to achieve a maximum transition frequency of 160 MHz. In particular, the organic transistor exhibit a f_T/V_{GS} of 4 MHz V^{-1}, that was obtained by implementing a combination of scalable laser-based direct-writing techniques and solution-based deposition of organic polymers. Figure 33 b) shows the device structures and the electrical characteristics of the transistor.

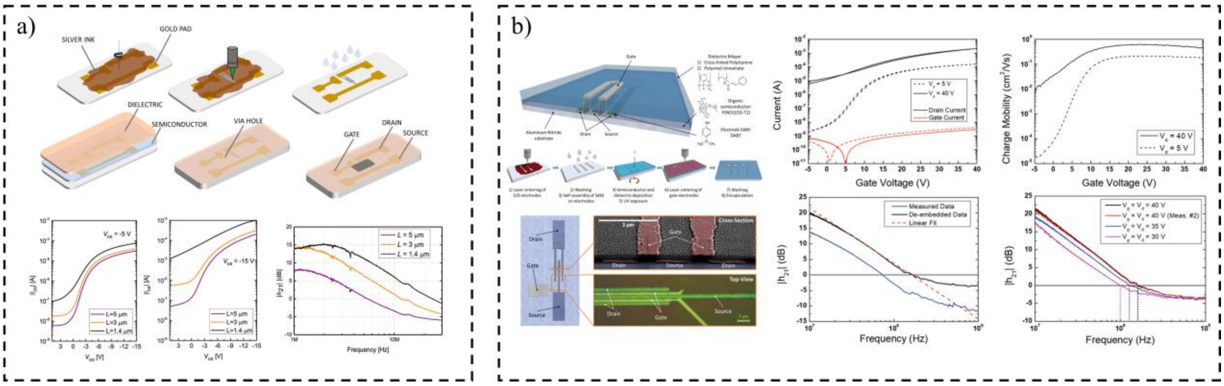

Figure 33 Non-lithographic, maskless, fabrication approach for the development of sub-micrometer channel-length organic transistors. a) Passarella et al. [75], who was able to achieve a transition frequency of about 22 MHz and b) Perinot et al. [76] who achieve the impressive transition frequency of 160 MHz, with a combination of scalable laser-based direct-writing techniques and solution-based deposition of organic polymers.

Other maskless approaches for the fabrication of short-channel OFETs is the reverse-offset printing. With this printing fabrication method, Fukuda et al. [77] developed an organic thin-film transistor with submicrometer channel length (Figure 34 a)). The authors were able to fabricate organic transistors with remarkable performances, and, in particular, the field-effect mobilities was equal to 0.27 $cm^2\ V^{-1}\ s^{-1}$ for channel lengths of 2.4 μm and $9.0 \times 10^{-3}\ cm^2\ V^{-1}\ s^{-1}$ for the channel length of about 0.6 μm. The reported on/off current ratios were greater than 10^5.

Similarly, Takeda et al. [78] developed with a reverse offset-printing method a complementary ring oscillator with a stacked-structure and an operational amplifier (OPA) onto a large-area substrate, as shown in Figure 34 b). The devices presented wires with a 30 μm width and a channel length of 10 μm. Moreover, the circuits were fabricated using a solution process with a printing method, except for the insulating layer. Interestingly, p-type organic thin-film transistor (OTFT) and n-type OTFT were stacked with a common gate electrode layer.

The authors were able to fabricate a complementary ring oscillator circuit with a frequency oscillation of 2 kHz (12.5 V, five stages) and operated at 1.25 V (96 Hz, nine stages). In the other part, the fabricated OPA circuit had an output/input voltage ratio of 20.

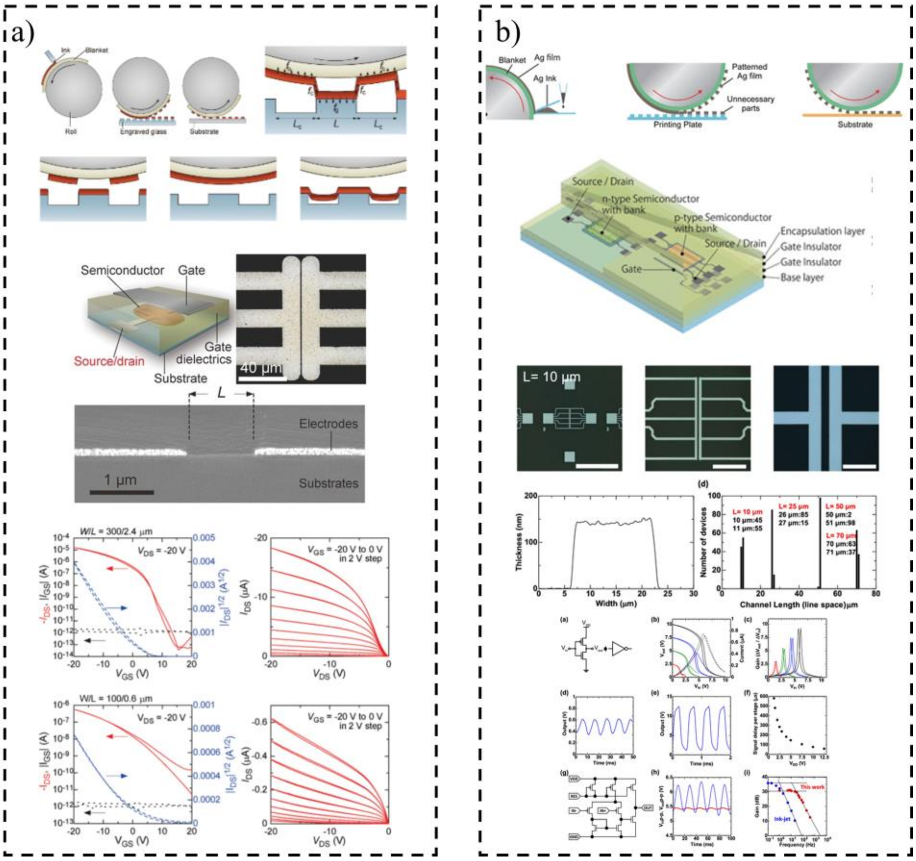

Figure 34 Short-channel transistors fabricated through a reverse-offset printing technique, developed by a) Fukuda et al. [77] and b) Takeda et al. [78].

A sophisticated inkjet solutions with sub-femtoliter accuracy was proposed by Sekitani et al. [79] for the fabrication of high-performance p-channel and n-channel transistors and low-power complementary circuits, characterized by single-micrometer resolution metal contacts, printed on the surface of high-mobility organic semiconductors. Figure 35 a) shows the device structure. The authors developed p-type transistor using pentacene as organic semiconductor and for n-type transistor employed $F_{16}CuPc$. In addition, with these transistors, an organic complementary inverter was fabricated (Figure 35 b)).

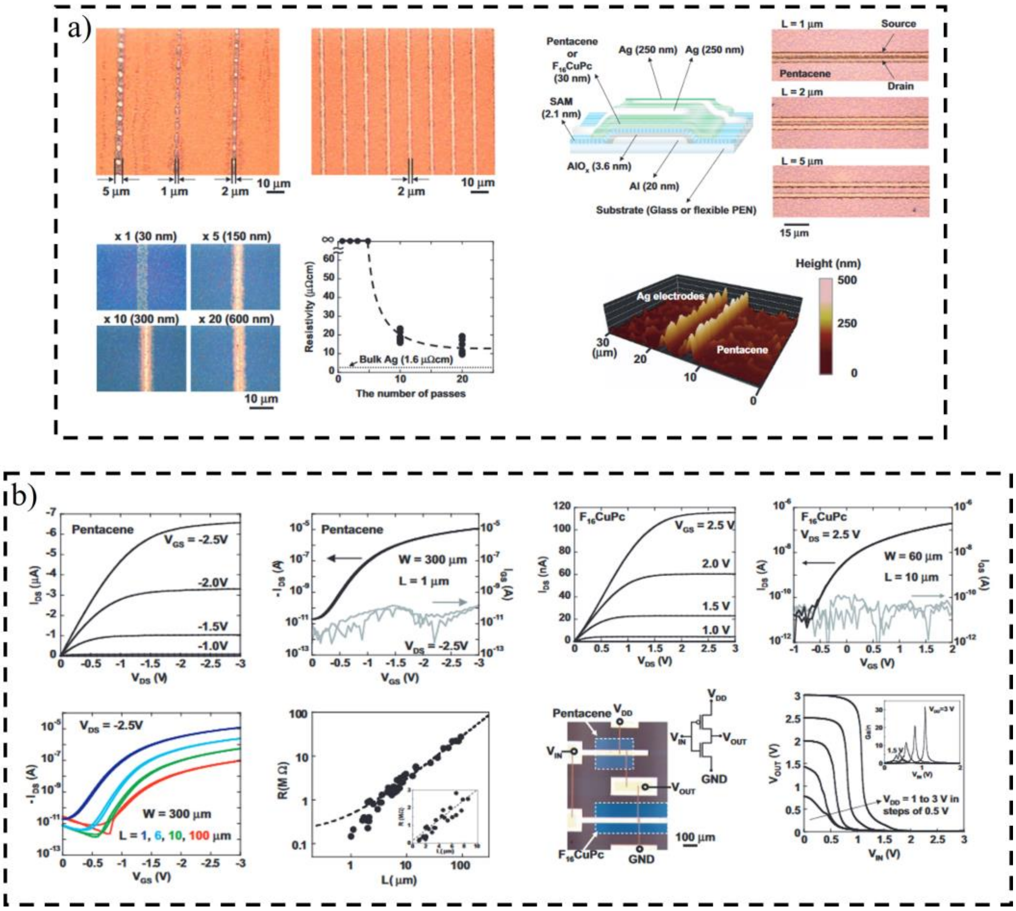

Figure 35 A sophisticated inkjet solutions with sub-femtoliter accuracy proposed by Sekitani et al. [79] for the realization of p-type and n-type organic transistors. a) device architecture and b) electrical characterization and complementary inverter.

These high-resolution printing techniques represent promising solutions to reach channel lengths in the micrometer range.

2.3.2. *Vertical-OFET*

Another different approach, in addition to the aforementioned solutions, to obtain short channels transistors is the employment of vertical channel transistors (vOFETs), which are peculiar structures where the channel, differently from standard coplanar structures, develops perpendicularly with respect to the substrate [80]. To date, the most widespread target application of vOFETs is optoelectronics, where different kinds of vertical organic light-emitting transistor (vOLETs) and combinations of vOFETs and OLEDs have been proposed [81]–[85].

Among the several structures and materials that have been explored to fulfil the goal of obtaining high-performing vOFETs, Schottky Barrier vertical organic field-effect transistors (SB-vOFET) represent an interesting solution. This structure was reported the first time by Ma and Yang [86]. These devices are characterized by a peculiar structure, in which source electrode, active semiconductor, and drain electrode are vertically stacked, while the gate electrode is below the source electrode, separated through a thin insulating layer (Figure 36 a)). Therefore, the effective device channel length is determined by the thickness of the deposited organic semiconductor. Moreover, the interface between source electrode and semiconductor is a Schottky-like contact, which is a rectifying contact. Therefore, the operation of the SB-VOFET relies on the modulation of the height of this Schottky barrier by the gate potential, rather than a direct manipulation of the charge carrier densities as in conventional field-effect transistors.

Ben-Sasson et al. [87] reported a SB-vOFET, whose architecture was based on the nanopatterned source electrode, developed by a soft-lithography and a lift-off processes, which facilitates the fabrication of 50–100 nm openings in a 10 nm thin metal electrode (Figure 36 b)). Similarly, Sheleg et al. [88] fabricated onto p++ doped silicon wafer a vertical transisotr with a gold patterned source electrode, onto which a thin film of organic semiconductor (N,N'-dioctyl-3,4,9,10 perylenedicarboximide) PTCDI-C8 was deposited. In Figure 36 c) a sketch of device structure is reported.

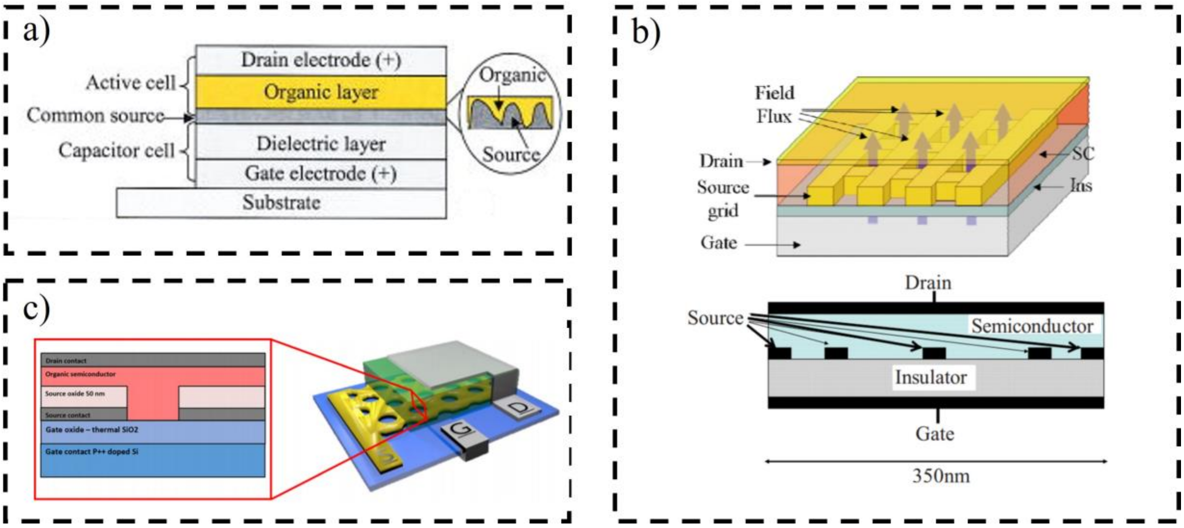

Figure 36 Schottky Barrier vertical organic field-effect transistors (SB-vOFET). a) Ma and Yang [86] developed the first SB-vOFET; b) Ben-Sasson et al. [87] modified the structure by introducing a nano-patterned source electrode and c) Sheleg et al. [88] reported a similar structure.

Graphene vOFETs represent an interesting solution for the fabrication of high-performing devices. Liu et al. [89] reported a method for the fabrication of vertical transistors based on the heterostructure of graphene compatible with different organic semiconductor thin films. Specifically, the authors employed the tunable work function of graphene in order to modulate the vertical carrier transport across the graphene–organic semiconductor junction. The design of the transistor allows to obtain a sub-micrometer channel transistor (<200 nm), since the organic thin film thickness determines the channel length rather than by lithographic resolution. As reported in Figure 37 a), the peculiar structure had the organic channel sandwiched and naturally protected between the source and drain electrodes, which function as the self-passivation layer to ensure device stable operation. The authors reported an operation frequency up to 0.4 MHz, and complementary circuits with voltage gain and stable both p-type and n-type transistors.

Similarly, Kim et al. [90] developed a high-performance vertical transistor based on graphene electrodes doped using the underside doping method. This method enabled effective tuning of the graphene work function while maintaining the surface properties of the pristine graphene, which enhance the crystalline microstructures of the overlying organic semiconductors grown on the graphene surface. Figure 37 b) reports the fabrication method, the electrical characteristics of both p-type and n-type transistors and the voltage transfer characteristics of the complementary inverter.

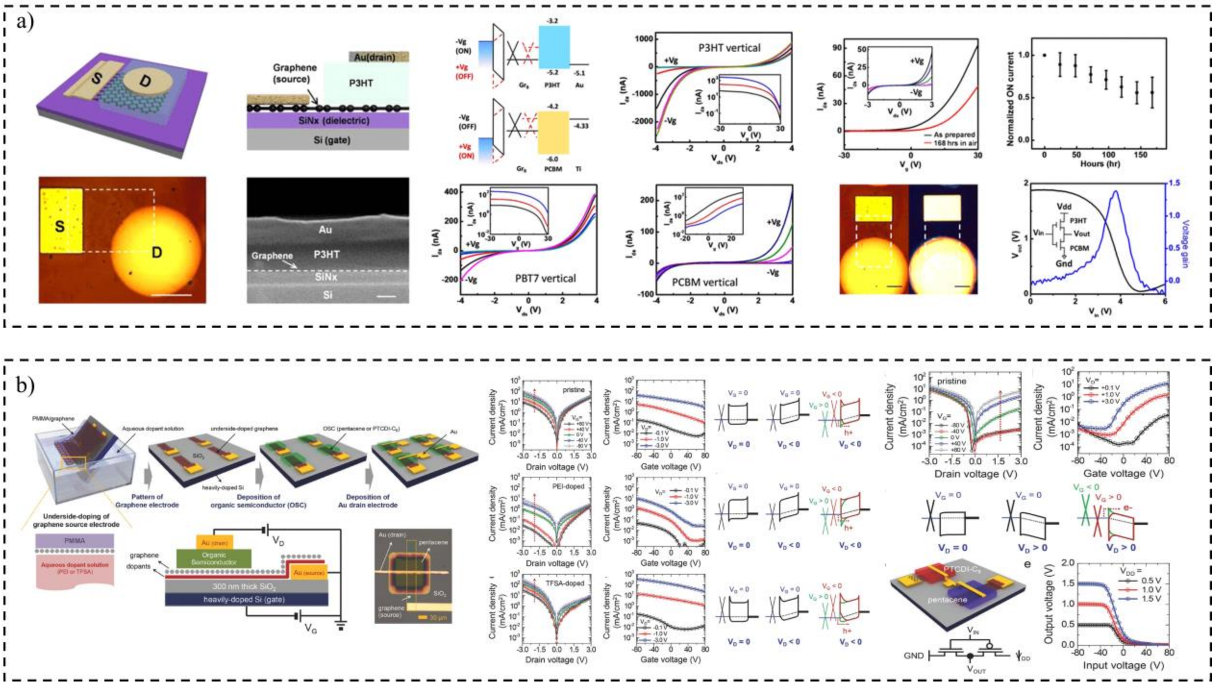

Figure 37 Graphene-based Vertical transistor developed by a) Liu et al. [89] and Kim et al. [90].

Recently, Dogan et al. [91] reported a vertical organic field-effect transistor structure in which highly doped silicon nanopillars are utilized as a gate electrode. The structure was based on a gate electrode consisting of massively parallel highly doped silicon nanopillars, which defines a vertical edge along the direction the charge carrier transport occurs Source and drain electrodes were positioned adjacent to the pillar edge and vertically stacked and separated by the semiconductor layer and an additional insulator, which suppress the underside bulk current. In this way, the device stack resembles a pseudo-VOFET with the gate attached at the side of source and drain electrode. The current density and switching speed of the devices were in the order of 0.1 A cm^{-2} and 0.1 MHz, respectively, at biases of only a few volts, while the On/Off ratio was equal to 10^6. In Figure 38 the device structure and the electrical characterization (both static and dynamic) are reported.

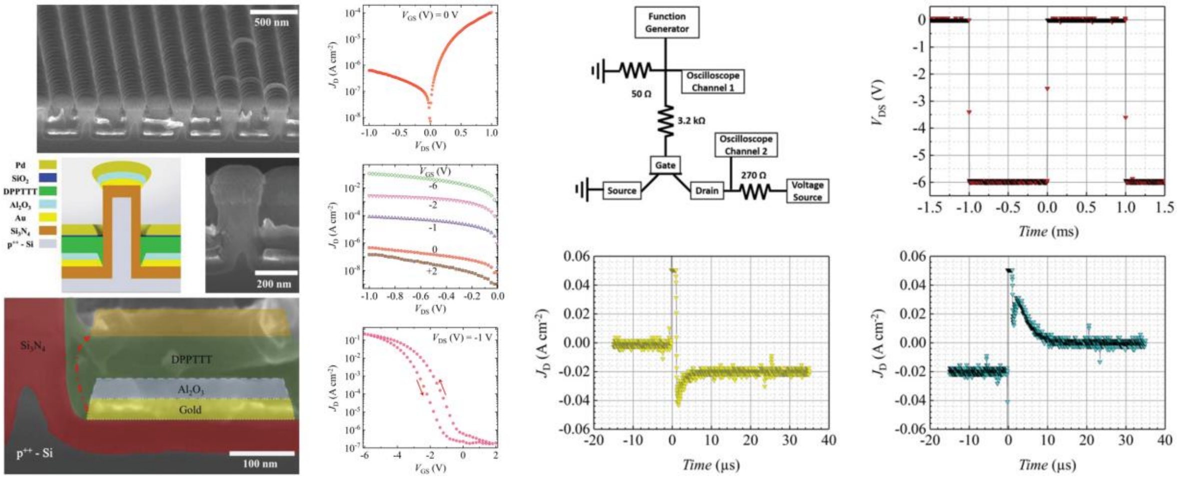

Figure 38 vOFET fabricated with strongly parallel nanopillars as the gate, developed by Dogan et al. [91]. From the SEM images of the nanopillars and the schematic of a single pillar gate, it is possible to notice the peculiar structure. Electrical characterization is then reported.

Furthermore, vertical organic static induction transistors (OSIT), also known as space-charge-limited transistor or solid-state vacuum triode, have attracted particular attention over the years. In this transistor, the insulating layers are applied above and below the porous base electrode in order to separate it from the other electrodes. Due to this, vOSITs usually show superior off-state performance compared to other vertical organic transistors. Moreover, the base electrode is usually fabricated by a top-down methods, which allows to have a high degree of process and device control.

Kudo et al. [92] in a pioneering work proposed in 1998 a static induction transistor sing copper phthalocyanine films and aluminum Schottky gate electrode. In Figure 39 a) the device structure and the electrical static and dynamic characteristics are reported.

Chao et al. [93] proposed a OSIT able to achieve a high on/off ratio of $3 \cdot 10^5$ at a low operation voltage of 1.5 V and a maximum output current density of 1.7 mA/cm^2 with current gain greater than 1000. From In Figure 39 b) it is possible to notice that the pin-holes dimension are in the order of 200 nm, while the output current does not achieve the ideal saturation. This issue was caused by the larger diameter of the openings and nonideal insulation layers.

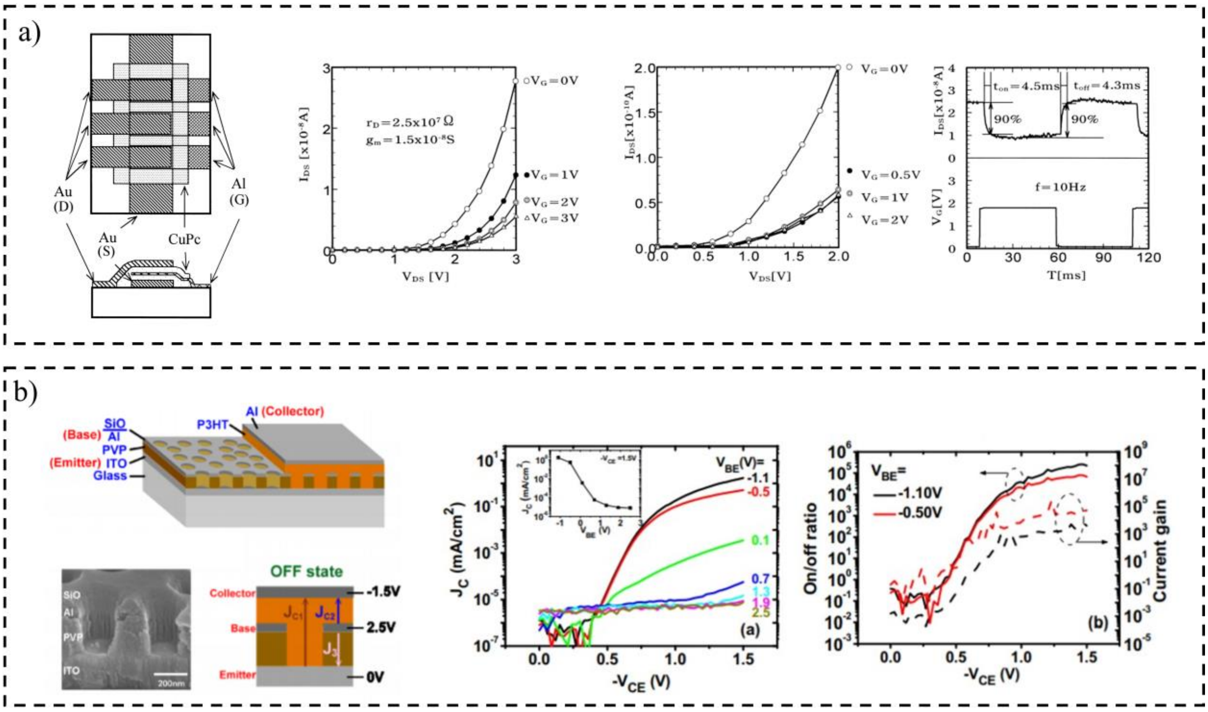

Figure 39 Vertical Organic Static Induction Transistors (OSIT) proposed by a) Kudo et al. [92] and b) Chao et al. [93].

In these structures, one of the main objectives of the fabrication process is the structuring of the base electrode. This layer presents a perforated shape with pinholes in the manometer range. In particular, the fabrication of such holes has great importance for the device behavior. Large pinholes cause the OSIT can still be turned off, however, small holes might limit the on-current. In addition, insulating layers have to be applied above and below the base electrode without closing the holes, which makes the base fabrication difficult. Therefore, complex and high-resolution fabrication processes are needed.

Recently, organic permeable base transistors (OPBTs) have attracted considerable attention thanks to their very interesting performances. Such devices represent a substantially different vertical transistor concept, since the structure resembles a vacuum triode where a thin metal electrode (denoted as the base) is sandwiched between the charge carrier injecting electrode (called the emitter) and the electrode for charge carrier extraction (also known as the collector). In particular, the base electrode is employed to modulate the current flow from the emitter to the collector electrodes, as a result the device function is controlled. The main characteristic of this peculiar structure is that the base must be permeable (hence the name of this familiar of vertical organic transistors) to the charge carriers moving from the emitter to the collector [94]. Moreover such permeability have to be controlled by the base electrode potential itself.

Fujimoto et al. [95] reported an organic permeable base transistor, where C_{60} and perylene derivatives were used for the channel layer and the collector current of the transistor was able exceed 300mA/cm^2, while Fischer et al. [96], employing the same semiconductor combined with annealing at elevated temperatures (150°C for 2 h) , were able to developed a transistor with a current density of 1 A/cm^2 at a driving voltage of 3 V, together with an extremely high transconductance of 30 mS and a voltage gain above 1 up to 1.5 MHz in a simple inverter circuit.

More recently, Klinger et al. [97] reported an OPBT able to achieve a current densities above 1 kA cm^{-2} with a limited off current, achieved thanks to the native passivation aluminum oxide obtained by exposing the base electrode to ambient air during fabrication. However, one of the physical limit in this structure was the effective mobility, that was reported equal to 0.06 cm^2 V^{-1} s^{-1}. Therefore, the device architecture may have much more potential if different materials optimized for the vertical geometry would be employed. In Figure 40 a) the device schematic with the employed, materials and the electrical characterization are reported. It is interesting to notice that these devices show an important contact resistance, given not only by the injection resistance at the metal electrode but rather by the vertical transport resistance of the connecting semiconductor layer, even if the doped semiconductor reduced this effect with respect previously reported OPBT.

Afterward, the author optimized the transistor structure thus obtaining a fully thermally-evaporated vertical permeable-base transistors with physical channel length (L) of about 200 nm, fabricated using C_{60} fullerene as organic semiconductor. In addition, the authors reported an advanced circuit for the frequency characterization of the device. Specifically, the system is able to simultaneously applies an accurate large-signal pulse bias and a small-signal sinusoidal excitation to the transistor [98]. Moreover, the proposed circuits was able to reduce the self-heating of the transistor, that was one of the reported issue of such structure. Therefore, a small-signal characterization over 10 times in a wider bias I–V range was enabled, with 10^5 times less bias-stress effects.

Figure 40 b) shows the characteristic of the reported device and the proposed circuits for the frequency measurement of the transistor. An intrinsic gain up to 35 dB, and a transition frequency (f_T) of about 40 MHz at 8.6 V were achieved. Interestingly, no saturation in $f_T - I$ and transconductance ($g_m - I$) was observed at high currents.

With this approach, Guo et al. [99] developed an organic vertical n-channel permeable single- and dual-base transistors, and vertical p-channel permeable base transistors to fabricate integrated complementary inverters and ring oscillators.

However, many issues related to the fabrication process have been successfully solved, and the realization of a high-performing permeable base transistor is still challenging. For instance, to further advance with the OPBT technology it is necessary to better control the mechanisms behind the pinhole formation within the base layer in order to develop robust and scalable fabrication techniques, with a high yield [100].

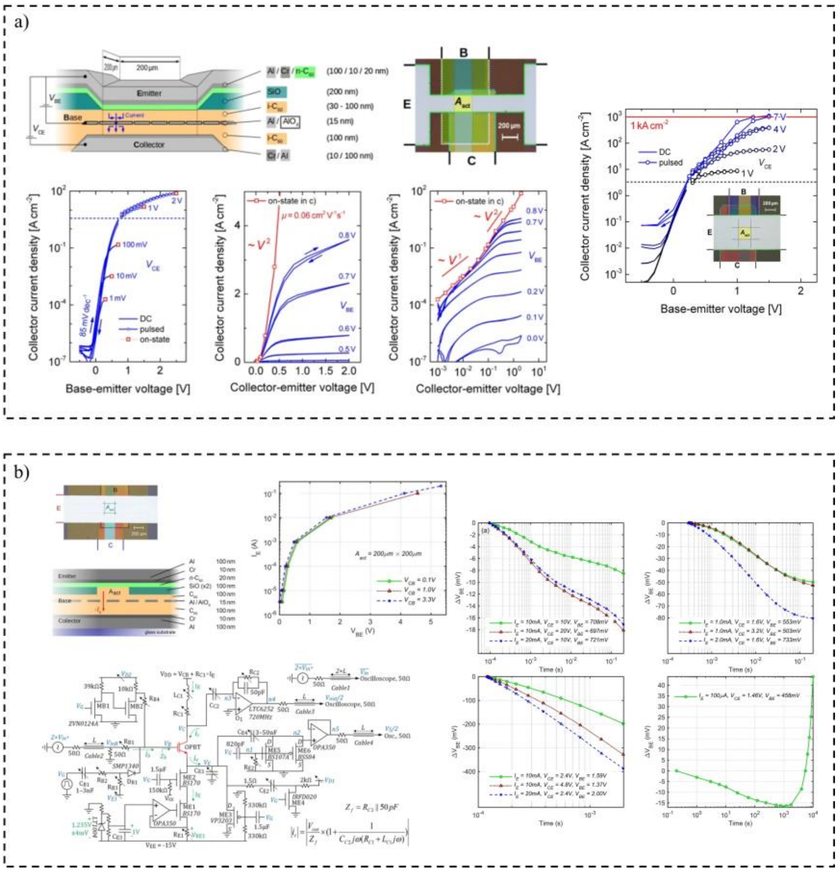

Figure 40 Organic Permeable Base Transistor (OPBT) proposed by a) Klinger et al. [97] able to achieve a current densities above 1 kA cm^{-2} and b) by Kheradmand-Boroujeni et al. [98] with a transition frequency (f_T) of about 40 MHz in a pulsed mode.

Among the different kinds of vertical channel FET structures, the so-called step-edge vertical OFET offers a very interesting solution. In this architecture, the vertical channel is obtained by employing a thin dielectric spacer (whose thickness defines the channel length) that separates the source and the drain contacts in a vertical stack. Depending on the chosen approach, it is possible to obtain both standard BG (Bottom Gate)-vOFETs and TG (Top Gate)-vOFETs

[101]–[103], however for the fabrication process of the different step-edge structure usually it is not necessary to employ a high-resolution technique.

Chen et al. [104] developed a top contact vertical channel transistor using P3HT (poly~3-hexylthiophene) as organic semiconductors. The authors were able to fabricate a transistor with channel lengths of 5 μm with a simple procedure that needed only two photolithography steps (two photo masks) with no need for high-resolution and precision alignment for channel definition. Figure 41 a) shows the device architecture and the electrical characterizations.

Stutzmann et al. [105] proposed vertical-channel organic field-effect transistors on flexible poly(ethylene terephthalate) substrates with a submicrometer channel (between 700 and 900 nm) defined by the thickness of a spin-coated PVP insulator layer and a top gate electrode fabricated by a self-aligned printed technique with the aim to minimize the overlap capacitance and thus increase the device's performance. Figure 41 b) reports the fabrication method and the characteristic curves.

Later, Uno et al. [106] proposed a bottom gate architecture, characterized by a multi-columnar structure fabricated on a plastic substrate. This particular multi-columnar structure, fabricated through a standard photolithographic process, had the organic semiconductor channels on its sidewalls so that accumulated charges in the organic materials flow perpendicularly to the substrate surface from a source contact up to a drain contact. Thanks to this approach, the vertical channel is less likely to be deformed, even when a substrate is bent, as illustrated in Figure 41 c). This would help with the construction of flexible devices. In addition, the transistors showed fast dynamic switching within 250 ns, which corresponds to 4 MHz operation, even with the modest carrier mobility reported (of 0.2 $cm^2 V^{-1} s^{-1}$).

However, the main drawback of the fabrication process was the semiconductor deposition, since the organic semiconductor was deposited by vacuum evaporation from a diagonal direction with an incident angle of about 30° to the plastic substrate, obtaining a film with a thickness of 50 nm. Therefore, such deposition technique does not allow a high process reliability.

Similarly, Kleeman et al. [107] proposed a vertical organic transistors comprising pentacene for p-type operation and C_{60} for n-type operation. The transistors were manufactured by photolithography and specifically fluorinated photoresist and solvent compounds allowed for photolithographically patterning directly and strongly onto the organic materials, thus simplifying the procedure.

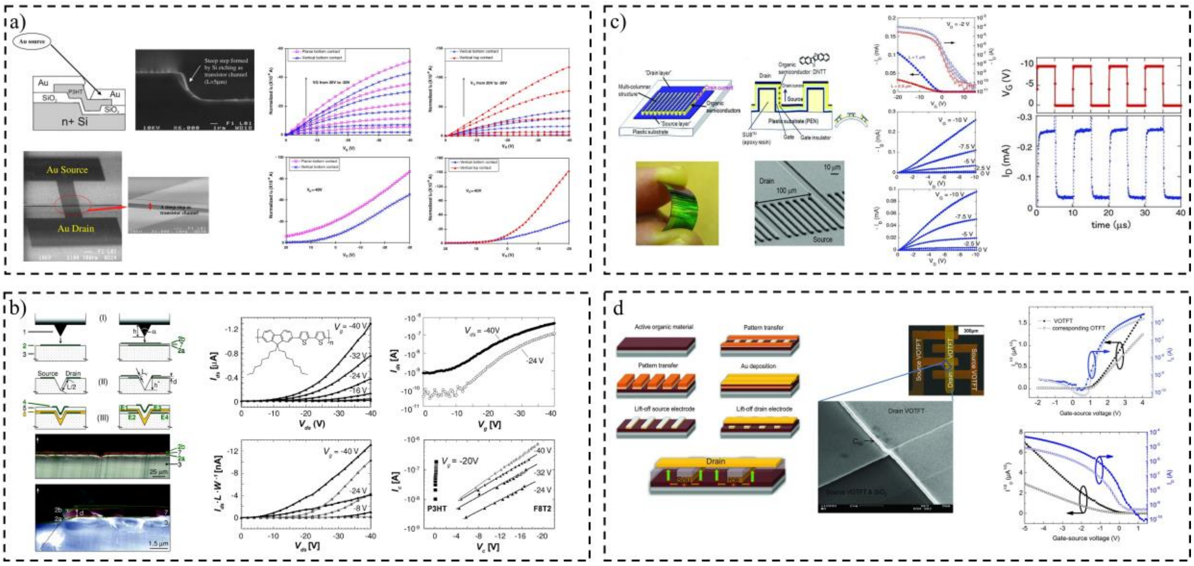

Figure 41 Step-edge vertical Organic field Effect Transistors (OFET) developed by a) Chen et al. [104], b) Stutzmann et al. [105], c) Uno et al. [106] and d) Kleeman et al. [104].

The vertical step-edge architecture was employed even for the fabrication of vertical organic electrolyte-gated OFETs (vEGOFETs).

Lenz et al. [108] proposed a sub-100 nm channel EGOFET with a footprint of 2 × 80 × 80 nm^2 able to achieve a high on-state current densities of above 3 MA cm^{-2}, an on/off current modulation ratios of up to 10^8, and a large transconductances of up to 5,000 S m^{-1}. Such characteristics were realized using electrolyte gating. Later, the authors [109] were able to further miniaturize the device and obtain a sub-5 nm channel transistor, thanks to the use of a hexagonal boron nitride with atomically precise thickness and flatness as a spacer to separate the vertically aligned source and drain electrodes (Figure 42 a)). The authors reported that the transistors had an output current densities of about 2.95 MA cm^{-2} at −0.4 V bias, on–off ratios of up to 10^6, and a steep subthreshold swing of down to 65 mV dec^{-1}. The transconductance calculated was equal to 714 S m^{-1}.

Donahue et al. [110] proposed a Vertical Organic Electrochemical Transistor (vOECT) where the channel length was defined by the thickness of the Parylene C dielectric layer separating the vertically stacked source and drain contacts, while a PEDOT:PSS layer was employed as an active layer. This approach allowed to obtain a sub-micrometer channel down to 450 nm length. The resulting vertical transistors exhibited a reduced footprint, increased intrinsic transconductance of up to 57 mS, and a geometry-normalized transconductance of 814 S m^{-1}. Figure 42 b) shows the device schematic and the electrical characterization.

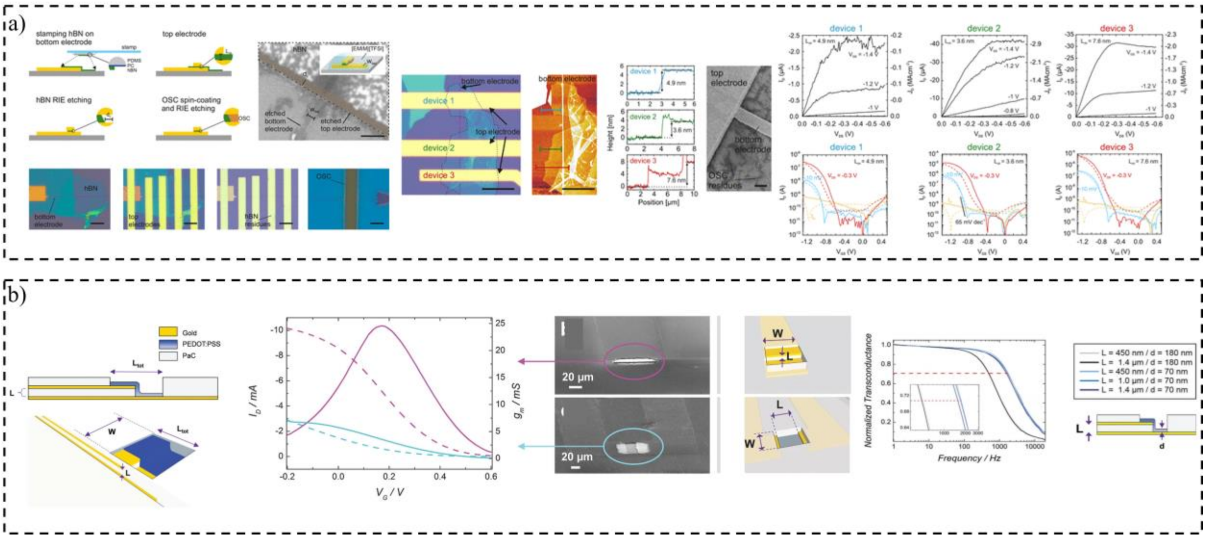

Figure 42 a) vertical organic electrolyte-gated OFET (vEGOFET) [108], [109] and b) vertical organic electrochemical transistor (vOECT)[110] both developed with the step-edge architecture.

However, the reported approaches generally relies on high-resolution techniques, as those based on excimer laser, high-resolution masks alignments, and deposition of metal electrodes with nonconventional techniques (as oblique-incidence vacuum deposition technique), which make the proposed processes not easily up-scalable at low costs.

2.4. Artificial skin

Artificial skin is one of the most widespread research topics that in the last decades has been studied since the reproduction of human skin sensitivity and mechanical properties has found different applications in soft-robotics, healthcare, prosthetics, and rehabilitation fields. Several approaches have been proposed and with the outburst of the organic electronics and its novel materials, different devices and systems able to mimic both sensory and mechanical human skin functionalities have been developed.

2.4.1. *Flexible devices based on the organic electronic technology*

Flexible devices are an intriguing category of wearable devices, where, differently from the standard Silicon-based devices, an important feature is the human-body adaptability due to the flexibility of the employed materials. Such devices can provide an accurate and reliable sensing without compromising a user’s natural movement and comfort. Usually, those devices are fabricated directly on plastic substrates, such as PC, polyethylene terephthalate (PET), and polyurethane, exploiting all the advantages given by the organic electronic technology. Moreover, several soft and stretchable materials have been adopted in this field, such as polydimethylsiloxane (PDMS). The organic electronic technology allows the fabrication of devices with a low-cost process, exploiting deposition techniques over large areas at low temperatures over flexible and ultra-flexible substrates. Moreover, the next-generation wearable electronics and personal and portable health care devices have to be biocompatible, since they are directly in contact with the human body.

Among all these characteristics, there are still some disadvantages that affect this technology. Organic materials present a lower carrier mobility and thus there are still some limitations in terms of frequency response with respect to standard electronics. Moreover, it is worth to consider the limitations in terms of resolution. For this reason, new technology, materials, and device architectures are studied and developed for the fabrication of flexible wearable electronic devices. In Table 1 the main general characteristics of the flexible wearable devices are summarized.

Table 1 General characteristic of the organic-based flexible wearable devices

Advantages	Disadvantages
Low-cost fabrication processes	Low carrier mobility
Large Area deposition technique	Limitation in frequency
Flexibility	Low-resolution fabrications
Conformability	Reliability
Biocompatibility	

In this contest, as opposed to conventional, rigid, silicon-based electronics, several examples and approaches have been employed for the fabrication of systems based on flexible or soft materials for wearable electronics and artificial skin applications [111], [112]. One of the parameters of interest in the wearable field (particularly for artificial skin systems) is the detection of physical quantities such as pressure/force and temperature. Different approaches have been proposed along the years, with the aim to reproduce the human skin properties, however improving the density of devices (i.e. number of sensors per area), reproduce the sensitivity, the time response of the skin receptors and the mechanical characteristics of the epidermis is a challenge still open.

For complex wearable and artificial skin systems, with multimodal sensors and different transducers, there are several constrains and limits, such as the specificity of the sensor to avoid cross-talking (i.e. electrical couplings related to the presence of low resistance paths between the sensors), functional stability, low power consumption and low fabrication costs. In this contest, the organic electronics play a fundamental role.

2.4.2. *Pressure sensors*

In 2004 Someya et al. in a pioneering work applied an organic transistor as the readout element for conductive rubber pressure sensors [113]. The basic unit of the matrix array was the organic transistor with the rubber pressure sensor. The authors developed a peculiar architecture, where a via hole was drilled through laser-based techniques and filled with gold, to electrically connect the rubber to the transistor. As in it is shown in Figure 43, on one side of the flexible substrate the sensing element was fabricated, while on the other side, authors developed the organic transistor, with the source connected to the electrode of the piezoresistive rubber through a via hole.

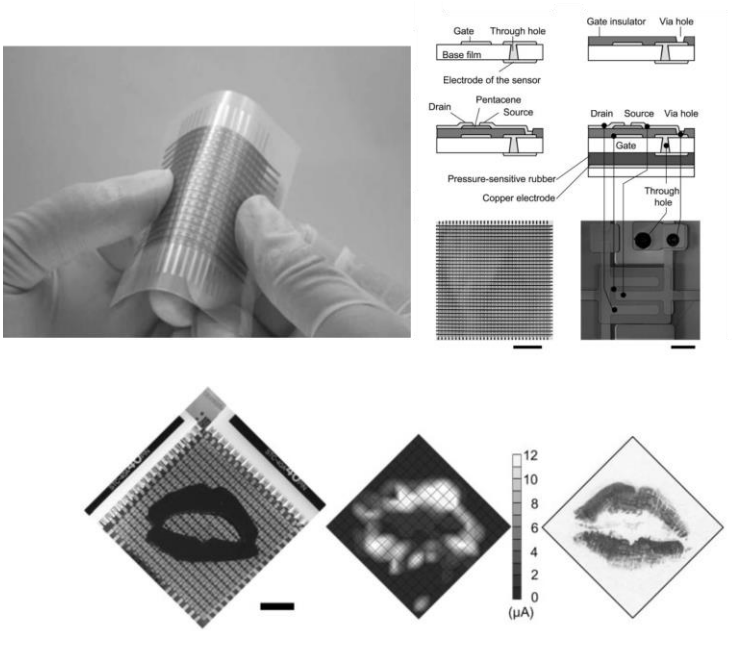

Figure 43 T. Someya et al. pressure matrix. The 32x32 matrix is shown as well as the fabrication process workflow. Manufacturing process flow (Scale bar 2 cm.). A pressure image of a kiss mark was taken by using the pressure matrix consisting of 16x16 units. The matrix was pressed with a lip-shaped rubber replica and the pressure image can be compared with the print on paper [113].

Another interesting approach for the fabrication of pressure sensors was developed by Z. Bao's group [114], [115]. The sensor pressure detection is based on the variation of the gate dielectric in a transistor structure due to the applied stimuli, which cause the transistor current output modulation. Since the current is directly proportional to the dielectric capacitance of the gate, the use of compressible and microstructured insulating layers in OFET devices offers the possibility to design high-sensitivity structures. The sensor consists of two separate layers, which were laminated to form the final device. One layer contains the source-drain electrodes and the semiconductor Poly-isoindigobithiophene-siloxane (PiI2T-Si), which is coated by a 700 nm thick PDMS layer with the aims of preventing damages during lamination process and ensuring a good semiconductor/dielectric interface; while the second contains the gate electrode and the microstructured PDMS dielectric layer.

As it is reported in the work, the flexible pressure-sensitive organic thin film transistors shows a maximum sensitivity of 8.2 kPa^{-1}, a fast response time of <10 ms, high stability over >15,000 cycles and the device shows a linear response range up to 60 Kpa. It is worth to consider the possible applications of such devices. Authors showed the radial artery blood pressure measurement, thus demonstrating the possible application of the flexible pressure sensor in a wearable contest (Figure 44).

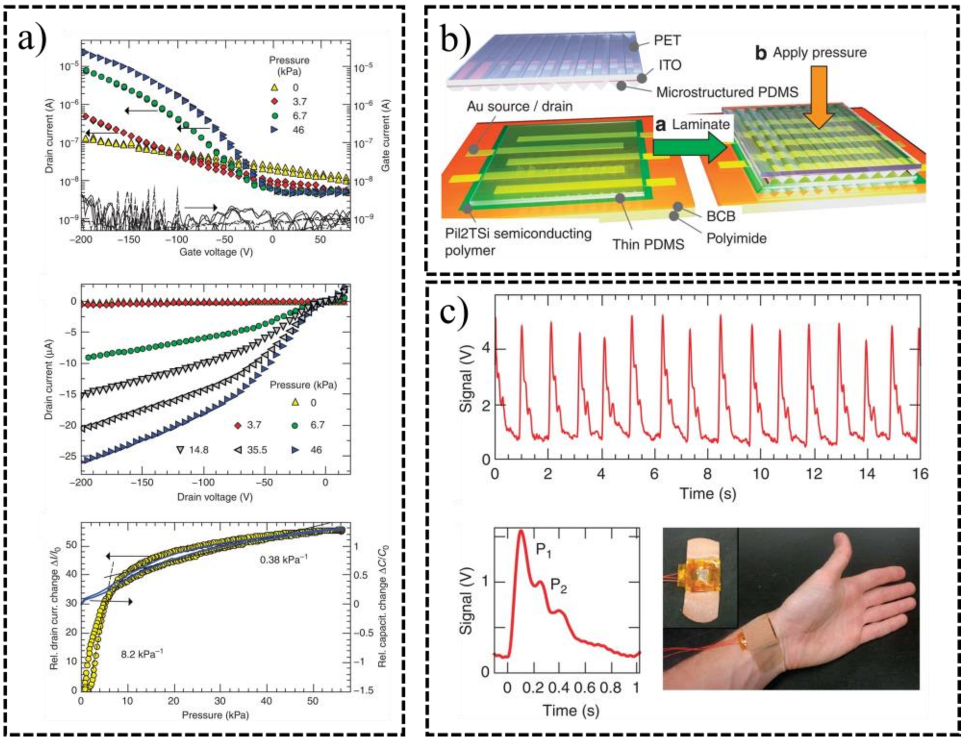

Figure 44 flexible polymer transistor with high sensitivity proposed by Schwatz et al. [115]. a) device static electric characterization and pressure calibration curve; b) fabrication process workflow and sketch of the final resulting device; c) radial artery pulse measurement;

More recently, S. Baek et al. developed a flexible pressure sensor based on an organic transistor operating in the subthreshold regime [116] (Figure 45). The device consisted of a deformable source and drain electrodes integrated on a staggered TFT. The pressure sensor operating principle is based on the variation of the contact resistance of the source and drain electrodes. When a pressure was applied to the device, the deformation of the electrodes on the organic semiconductor layer leads to a modulation of the drain current caused by the variation in both the channel geometry and contact resistance. Authors fabricated the deformable electrodes by embedding conducting single-walled carbon nanotubes on the surface of microstructured polydimethylsiloxane (PDMS) and pattering the source and drain geometry through a laser technique (λ= 532 nm). After that, the fabricated deformable electrodes were integrated on the DPP-DTT based organic transistor array to complete the active matrix. In Figure 45a) the fabrication process workflow is shown.

In order to strategically reduce the power consumption and simultaneously increase the dominance of the contact resistance because of the gated Schottky contact, authors performed the electromechanical characterization of the transistor in the subthreshold regime. Thanks to that, the sensor had an ultralow power consumption in the order of 101 nW and showed a high sensitivity of about 18.96 kPa^{-1} (Figure 45b)). Moreover, the authors demonstrated the possibility to attach to the skin the active pressure matrix with a 5×5 proof-of-concept array. Figure 45c) shows microscopic image of each pixel of the PCT array and the optical photograph of the matrix peeled off from a glass carrier and placed onto the skin. To illustrate the pressure matrix response, in Figure 45c) a photograph of letter “E”(≈4 kPa) positioned over sensor and the corresponding press-map in above-T and sub-T regimes are shown.

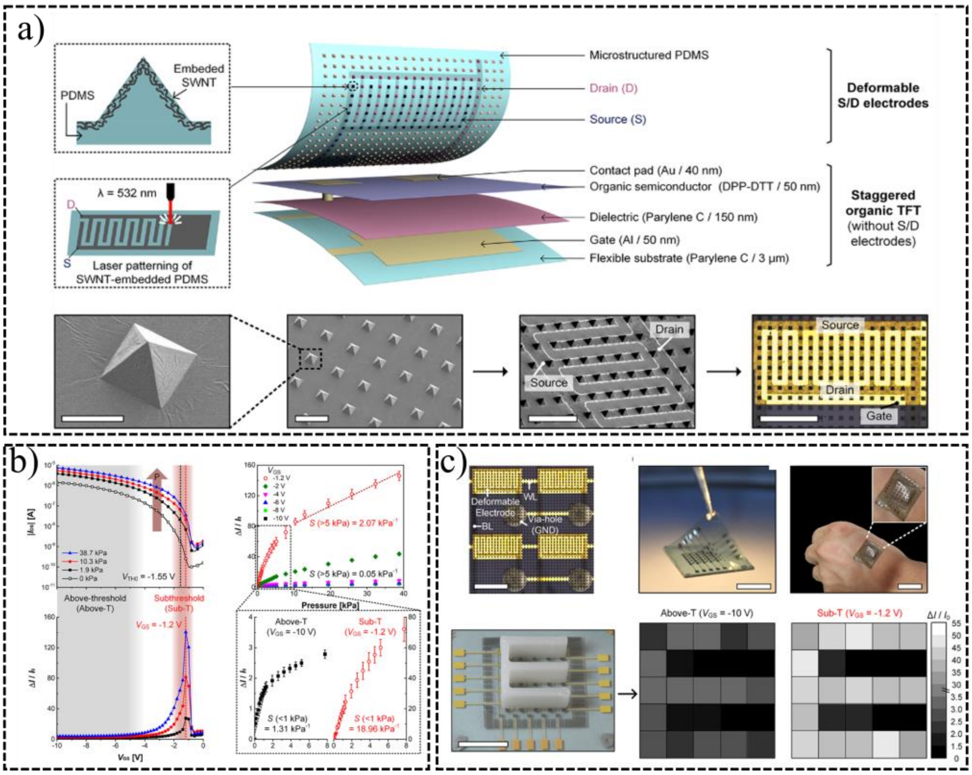

Figure 45 Flexible pressure sensor based on an organic transistor[116]; a) fabrication process workflow; b) pressure characterization in above-threshold and sub-threshold regime. The device shows a higher response in the sub-threshold regime, with a sensitivity equal to 18.96 kPa^{-1}; c) proof-of-concept of the device directly attached to the human skin and press-map of a letter "E" in the two functioning regimes.

With a similar approach, Kim et al. [117] reported a microstructured, multi-functional OFET array, in which the gate dielectric layer was composed by a highly crystalline, organic ferroelectric material, the poly(vinylidenefluoride-trifluoroethylene) (P(VDF-TrFE)).

A bottom-contact top-gate OFET structure was employed and the reported transistor presented an organic/inorganic hybrid passivation layer, composed by tetratetracontane (TTC) deposited by thermal evaporation at relatively low temperature as organic material and an inorganic material of Al_2O_3 formed by atomic vapour deposition at 200 °C as the inorganic part. PVDF-TrFE microstructured layer was transferred onto the passivation layer by using a thermal tape, prior to depositing the gate electrode.

As it is shown Figure 46, the larger piezoelectric effects in pyramidal shaped microstructures allowed to increase the device sensitivity and a limit of detection equal to 20 Pa was estimated. Moreover, both static and dynamic device responses were studied, reaching a maximum sensitivity of about 1.02 kPa^{-1} (low pressure regime: 20 – 80 Pa) and 0.028 kPa^{-1} (from 0.3 to 5 kPa at a frequency of 5 Hz), respectively. Considering the array structure, is it important to notice that the device power consumption was around 10 µW, due to the low output current (in the order of and the nA), but the response time reported was about 20 ms.

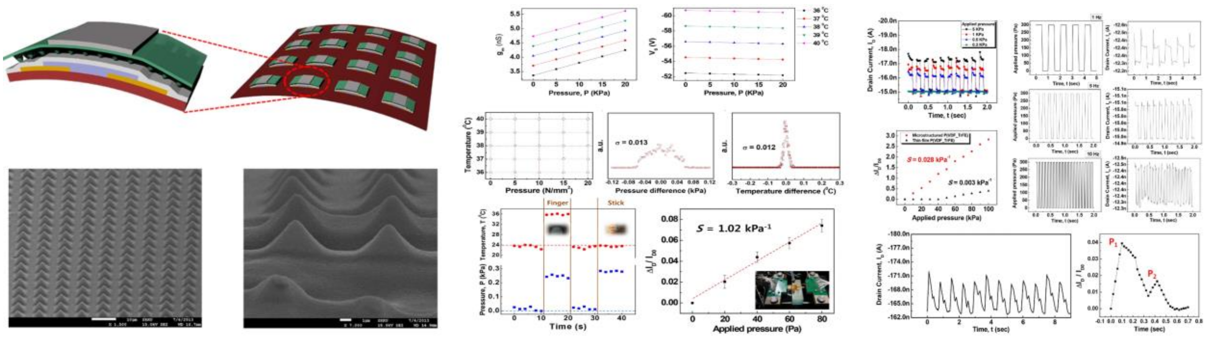

Figure 46 Pressure array based on microstructured, multi-functional OFET array, in which the gate dielectric layer was composed by a highly crystalline, organic ferroelectric material, the poly(vinylidenefluoride-trifluoroethylene) (P(VDF-TrFE)) reported by Kim et al. [117]

Suspended gates devices represent a large category of sensors with a wide range of applications, that also find extensive use as tactile sensors. Generally, the device architecture is characterized by an air gap space between the top gate and the insulator layer, which also encapsulate the semiconductor and the bottom source-drain electrodes. When an external force is applied, the gate is deformed, which results in a change of the dielectric layer capacitance as a function of the applied pressure, consequently the output current changes depending on the stimulus.

Zang et al. [118] developed a suspended gate organic thin film transistor (SGOTFTs) that paved the way for ultra-sensitive pressure detection, with a maximum sensor sensitivity of 192 kPa^{-1}, a low limit-of-detection pressure of <0.5 Pa and a short response time of 10 ms. Concerning the power consumption, authors reports a value lower than 100 nW. Moreover, thanks to the peculiar device architecture, the device sensitivity can be fined tuned by the suspended gate, so as to expand the application ranges of the device, as shown in Figure 47 a) in which it is shown the possible application of the device as bloody pressure from the artery of the wrist.

Afterwards, Shin et al. [119] reported a new concept of fabricating a pressure-sensitive active-matrix, based on graphene FET array with air-dielectric layers, formed by folding an origami substrate, which is composed of two plastic panels and a foldable elastic joint (Figure 47 b)). The elastic joint which connects these two plastic parts allows the substrate to be completely folded without any damage. Thanks to this, the integrated arrays of top-gated transistors with local air gaps as dielectrics can be formed by folding this substrate to stack these two panels, one with source/drain and the other with gate. This approach showed a wide detection range from 250 Pa to ~3 MPa and the sensitivity reported was about ~2.05×10^{-4} kPa^{-1} below 500 kPa (lower pressure regime) and ~9.43×10^{-6} kPa^{-1} up to 3 MPa (higher pressure regime).

Liu et al. [120] with the aims to simultaneously increase the sensitivity and decrease the transistor operation voltages reported a suspended gate OTFT based on polyelectrolyte gate dielectric of PAA:PEG and an air gape obtained thanks to a thin tape support, laminated onto the flexible substrate. The sensing device can be divided into two part, as shown in Figure 47 c). In the bottom part, thin polyethylene naphthalate (PEN) was used as a flexible substrate, on which gold electrodes were patterned to form source and drain terminals. Then, a support of thin tape was laminated on the PEN to control the small gap space to form the suspended gate structure. On the other part, the PAA:PEG blend (30 wt% PEG) as dielectric layer together with the stable organic semiconductor layer of PIDT-BT:TCNQ, were deposited on the flexible gate electrode of indium tin oxide (ITO)-coated PET. The polyelectrolyte dielectric is the key point to reduce the transistor operation voltages. Finally, the whole top part was fixed upside down onto the supporting tape to form the suspended gate OTFT sensor. The device response to pressure can be divided in two parts; in the low-pressure region (below 7 kPa), the pressure sensors exhibit a high sensitivity of 452.7 kPa^{-1}, while the sensitivity in the medium-pressure region drops to 29.8 kPa^{-1}, when the applied stimulus was increased to 32.8 kPa, at an operating voltage of −0.7 V.

More recently, the device was further improve by changing slightly the polyelectrolyte dielectric, thus achieving a sensitivity up to 691.9 kPa^{-1} in the low-pressure region of 0–7.5 kPa, while in the high-pressure region (7.5–33.43 kPa) it also attains a relatively high sensitivity of 42.5 kPa^{-1} [121] .

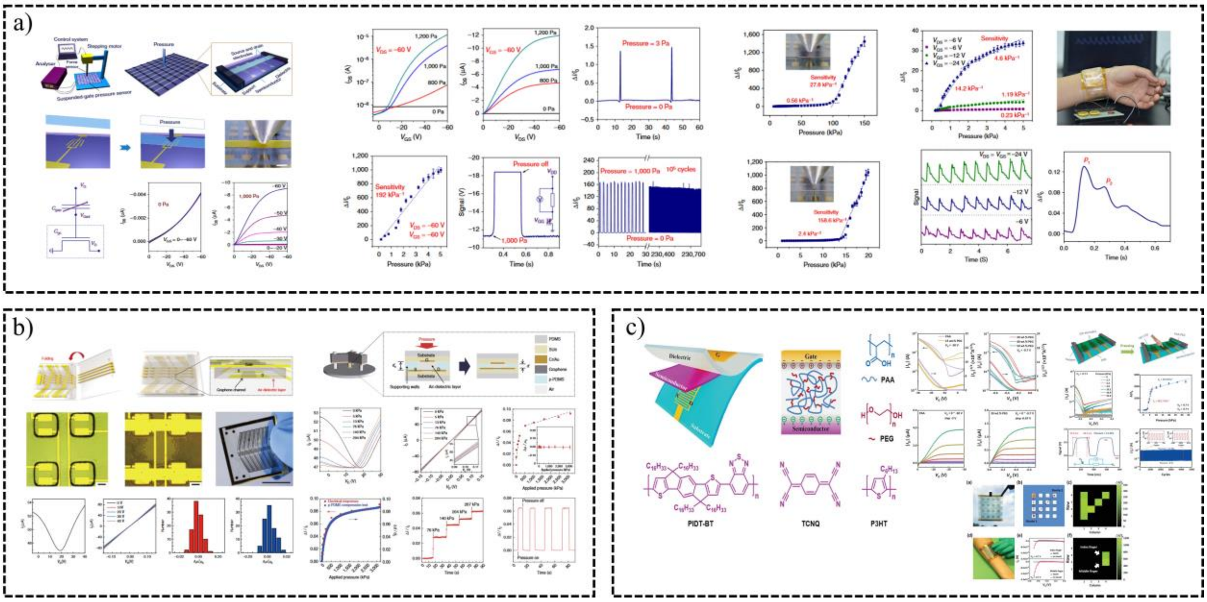

Figure 47 Suspended gate transistors are largely employed for the development of pressure sensors. Here some examples of devices proposed by a) Zang et a. [118], b) Shin et al. [119], and c) Liu et al. [120].

2.4.3. *Temperature measurement*

A crucial parameter for evaluating the human activity is the body temperature, thus several portable devices for the continuous measurement of the temperature have been developed.

In order to obtain a precise and effective measurement of human body temperature, direct contact is usually preferred and since traditional rigid detectors cannot achieve conformal contact, they cannot achieve high performances. In this context, flexible temperature sensors play a crucial role in the development of the next generation wearable devices.

Several categories of temperature sensors, such as Resistance Temperature Sensors (RTD), thermocouples and thermistors are largely employed in different fields. At the state-of the-art, those devices are developed with standard rigid electronic, however in the last decades the employment of flexible materials has been considerably studied [122].

Dankoco et al. [123] realized a printed and flexible sensor to measure the surface human body temperature. The device was a thermistor whose meanders were ink-jet printed with a silver ink on a Polyimide substrate. The authors reported a sensitivity equal to 2.23 10^{-3} C^{-1} in the temperature range of 20–60 °C.

Vuorinen et al. [124] similarly developed a flexible temperature sensor based on a graphene/PEDOT:PSS ink printed on top of a skin-conformable polyurethane plaster (adhesive bandage). In Figure 48a) the sketch of the temperature sensor is shown, while Figure 48b) represent an optical image of the device attached to the skin thanks to the adhesive bandage properties, which allows a conformal contact with the skin.

The ink-jet printed thermistor showed a sensitivity of about 0.06% per degree Celsius with a negative temperature dependence. The characterization was performed in argon atmosphere, as it is shown in Figure 48c),d). Hower, the thermistor characterization in ambient atmosphere showed a high hysteresis (Figure 48d)).

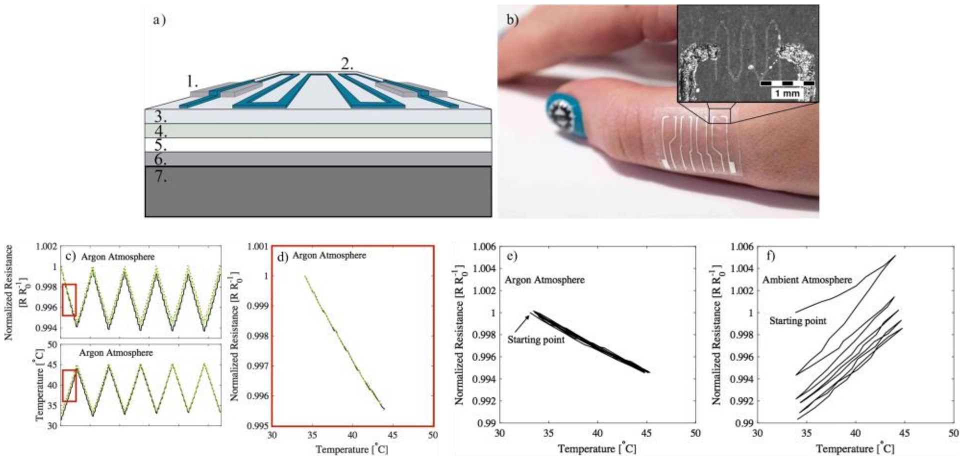

Figure 48 Ink-jet printed graphene/PEDOT:PSS thermistor developed by Vuorinen et al. [124]; a) sketch of the temperature sensor; b) photograph of the device attached to the skin; c) Device response to temperature variation on argon atmosphere; d) Calibration curve that shows the negative temperature dependence; sample characterization in Argon atmosphere e) and in Ambient atmosphere.

Among the different temperature sensor categories, Zhu et al. developed an active device based on a intrinsically stretchable organic transistor [125], with an inaccuracy within 1 °C with uniaxial strains from 0-30 %. Stretchability and conformability are key points for the wearable devices, particularly for the detection of the temperature. Therefore, the possibility to develop a strain-insensitive temperature sensor based on an active device paves the way for a high-accuracy surface temperature measurement. In fact, unlike passive two-terminal devices, active sensors based on organic transistors have several advantages. For instance, it is relevant that the third electrode allows to change of the charge conduction state in the device, thus it is possible to exploit the device functionalities and to ensure the device works in the best condition possible. In addition, the transistor can implement without any further element the addressing functionality in complex systems such as arrays and matrices of sensors, for which a transistor would in any case be required. Simultaneously, the active device allows a reduction of the cross-talk phenomena. Therefore, in a complex system, the number of devices can be reduced, since both the sensing and the addressing element can be carried out by the transistor. In Figure 49, the device cross-section with the employed materials is shown, as well as the temperature characterization and the device placed on a human hand.

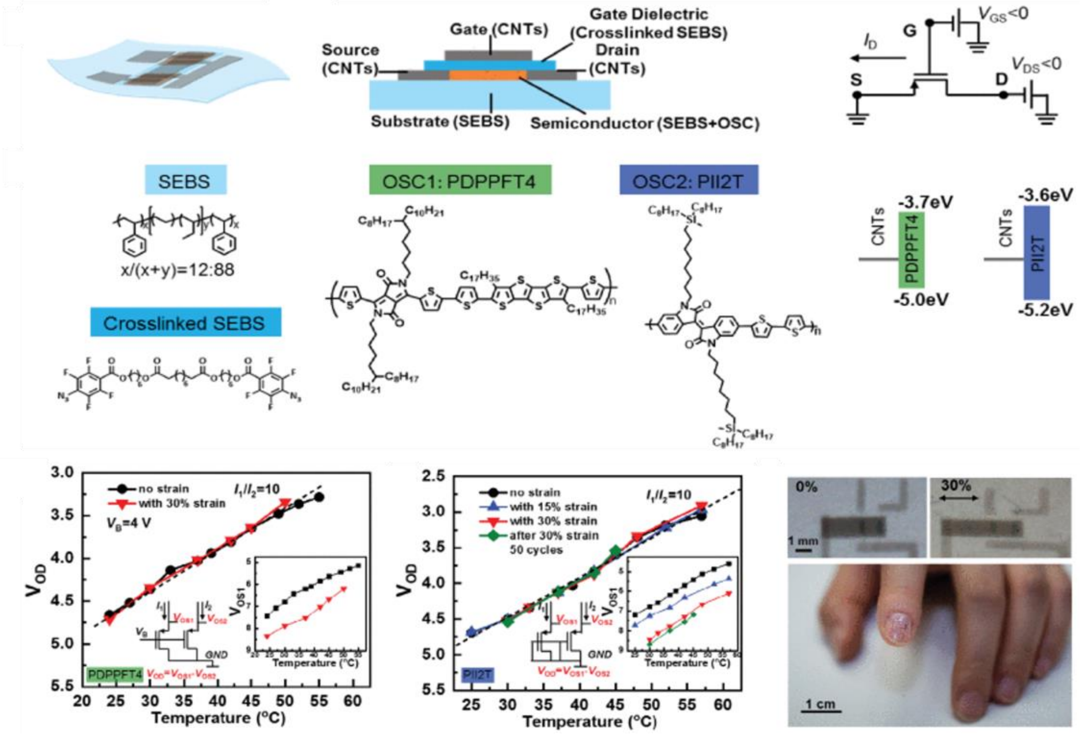

Figure 49 Stretchable strain-insensitive temperature sensors proposed by Zhu et al. [125].

Wu et al. [126] proposed a thermally stable biomaterial-based OFET to detect temperature variations. In particular, the charge- trapping effect induced by polar groups of the dielectric was successfully employed to enhance the temperature sensitivity of the transistor. The authors developed a skin-like sensor array which combined the advantages of transparency, flexibility, thermal stability, and biocompatibility. Interesting, from the transfer characteristics of the tascPLA–OFET composed of the DNTT semiconductor, it is possible to notice that at temperatures ranging from 25 °C to 150 °C, the transistor output current improved from 2.13 to 37.8 μA.

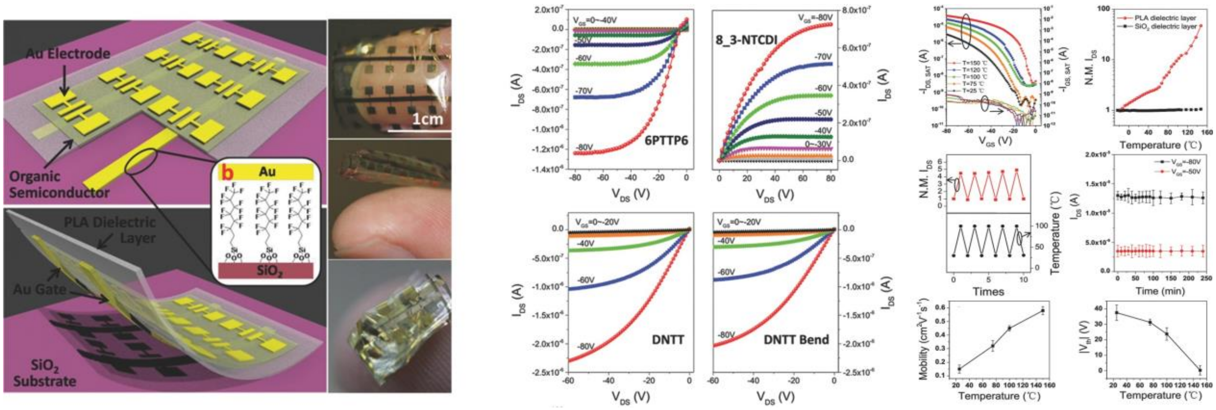

Figure 50 Thermally stable biomaterial-based OFET capable to detect temperature variations in a broad range [126].

Ren et al. [127] proposed a 16×16 temperature sensor array able to provide information of the objects placed in contact, even if the object has an irregular shape, with a overall sensitivity temperature coefficient of resistance (TCR) of 0.044. The authors developed each pixel of the array by thermally evaporating an Aluminum layer (as gate electrode) and using anodized Al_2O_3 as dielectric film. Before the deposition of the semiconductor, the authors employed an octadecylphosphonic acid (ODPA) SAM deposited onto the. It is interesting to notice that DNTT was used as the active layer of the OFETs (because of the thermal stability), while to developed the thermistor (i.e. the temperature-sensitive part), silver nanoparticles were embedded into the pentacene thin film. A 6 µm thick Parylene C was used as the encapsulation layer because it can reduce the bending stress at the active layer by positioning it close to the neutral bending position across the film. For the external connection, laser-drilled holes and screen-printed silver contacts were utilized to connect the thermistor to the word lines on the reverse side of the substrate. Figure 51 shows the schematic of the sensor array and the device composition of each pixel. Moreover, the device characterization and the application of the patch onto several surfaces are shown.

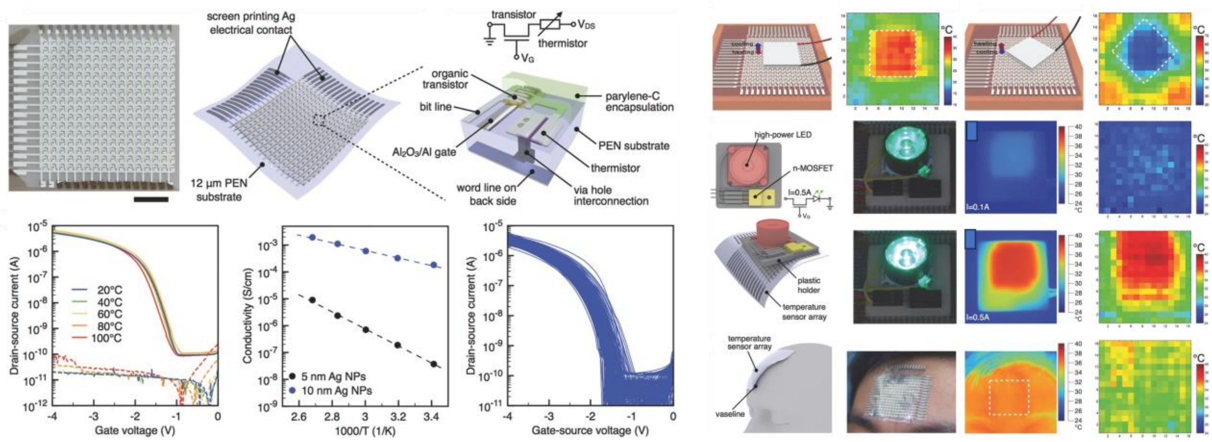

Figure 51 Temperature sensor array based on an organic semiconductor developed by Ren et al. [127].

2.4.4. *Multimodal tactile sensors*

Among the different approaches to developed both force/pressure and temperature sensors, very few examples of integrated multimodal sensors, capable to detect at the same time different stimuli have been reported so far.

An interesting solution to this important requirement is represented by the work of Zhang et al. [128], who reported about the development of flexible dual-parameter temperature–pressure sensors based on microstructure-frame-supported organic thermoelectric (MFSOTE) materials. The device is able to transduce both temperature and pressure stimuli into two independent electrical signals, thus permitting the instantaneous sensing of temperature and pressure with a temperature resolution of 0.1 K and a pressure sensitivity up to 28.9 kPa^{-1}. In Figure 52 a) both the temperature and pressure characterization are reported. As it possible to notice, the device was able to detect simultaneously temperature, with a resolution of about 0.1 K, and pressure variations over 10^4 cycles.

More recently, Shin et al.[129] reported about the employment of an interlocked microstructure of polarity-modulated ferro-electric thin films, capable to detect at the same time temperature and pressure (Figure 52 b). The device exploited both the triboelectric and pyroelectric effects of the ferroelectric microstructures that enable the simultaneous detection of mechanical and thermal stimuli in a single device. The multimodal tactile sensor provides ultrasensitive pressure and temperature detection capability. In particular, the sensitivities reported for the pressure and temperature stimulations were 2.2 V kPa^{-1} and 0.27 nA $°C^{-1}$, respectively, over a broad range of 0.1–98 kPa for the pressure and − 20 to 30 °C for the temperature.

A similar structure, still based on chemically modified piezoelectric thin films, was reported by Fastier-Wooller et al.[130], [131] for the fabrication of tactile sensors for robotic applications capable of discriminating between dynamic and static pressure events.

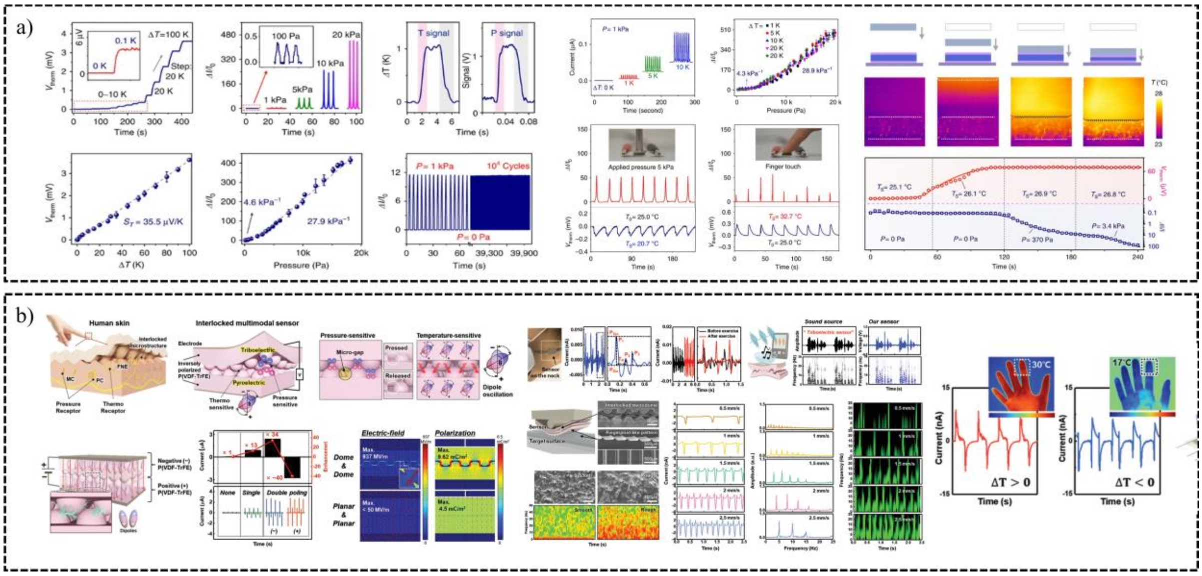

Figure 52 Multimodal tactile sensor for the detection of pressure and temperature stimuli reported by a) Zhang et al. [128] and b) Shin et al.[129].

Park and co-authors [132] developed a fingertip skin–inspired microstructured ferroelectric skins for the detection of static/dynamic pressure stimuli and temperature variations. The author reported that the tactile sensor can detect tiny static pressure down to 0.6 Pa, and the patches enabled the sensitive monitoring of air flow pressure variations ranging from 0.6 to 2.2 Pa, with no noticeable degradations for repetitive cycles (5000 times at 0.3 Hz) of normal force (20 kPa). In addition, the piezoelectric current of the interlocked films depended on the applied normal forces with a sensitivity of 35 µA/Pa below 2.45 kPa and 5 µA/Pa in the range of 2.45 to 17.15 kPa. Concerning the temperature detection, the sensor exhibited a TCR of 3.15%/°C under zero pressure, that significantly decreased to 1.2%/°C at a normal pressure of 1.2 kPa.

The multimodal sensor was employed to measure the pulse waveform of the radial artery, as shown in Figure 53, where the device structure and the sensor characterization are also reported.

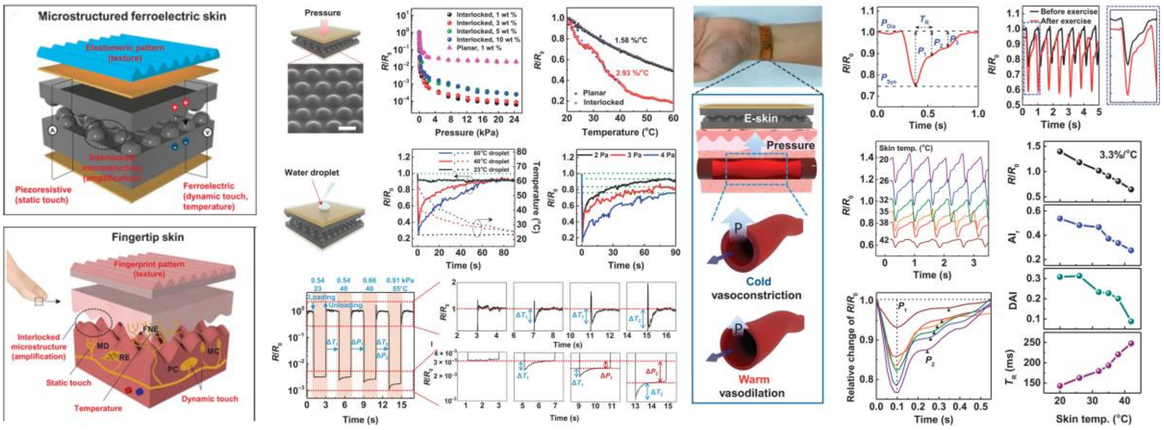

Figure 53 Park and co-authors [132] developed a fingertip skin–inspired microstructured ferroelectric skins for the detection of static/dynamic pressure stimuli and temperature variations for wearable applications.

A different approach for the fabrication of a multimodal tactile sensor was employed by You et al., who developed a deformable ionic-based receptor that can distinguish simultaneously spatial profiles of temperature and strain without signal interference [133]. From the analysis of the ion relaxation dynamics, the authors can derived simultaneously strain and temperature vales. Particularly, the normalized capacitance (C/C_0) is the temperature-insensitive extrinsic variable related to the strain, while the charge relaxation time (τ)) is the strain-insensitive variable to measure the absolute temperature. The authors demonstrated that the strain measurement (C/C_0) has a linear response in the range between 0 and 50%, while the temperature related signal ln(τ) is used to detect the temperature without geometrical information of the sensor. The temperature sensitivity was 10.4% per °C. Figure 54 a) shows the device structure and conceptualization, and the multimodal characterization. Interesting, the authors employed the device to measure the body temperature from the neck of the user.

Recently, Wang et al. [134] proposed a self-powered multimodal pressure/temperature tactile sensor based on flexible Bi–Te thermoelectric film and porous micro-coned elastomer (Figure 54 b)). The authors showed that the integration of the two films allows a multimodal measurement. Particularly, the Bi–Te based thermoelectric film enables the sensor to transduce the temperature with high resolution (< 0.1 K) and with an excellent sensitivity of 3.77 mV K^{-1}. Meanwhile, the porous microconed elastomer responds to the pressure variations, with low-pressure detection (16 Pa) and a high sensitivity of 37 kPa^{-1}. The authors were able to employ the multimodal sensor for the analysis of the body temperature and the heart beat rate, by applying the patch on a user wrist.

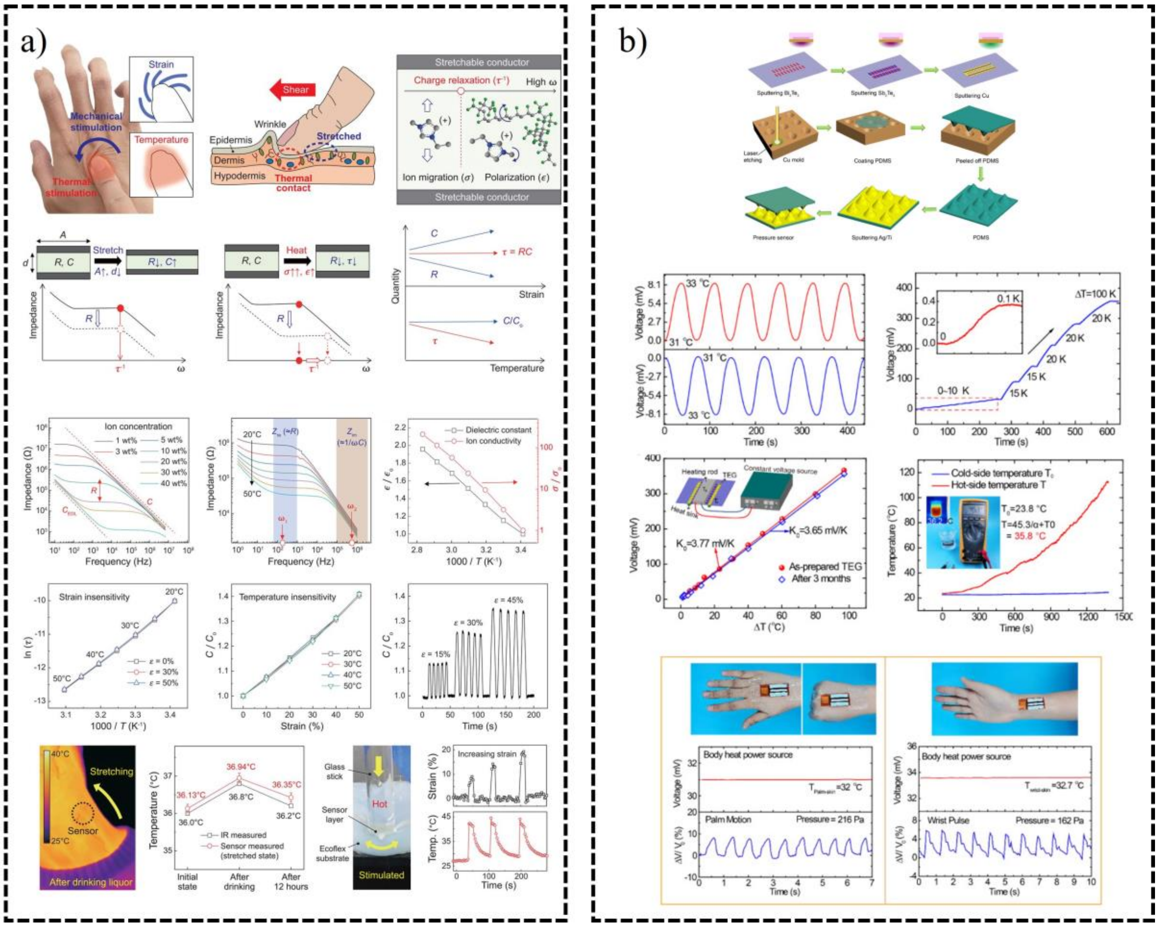

Figure 54 Multimodal tactile sensor for artificial skin and wearable electronic sensors applications. a) You et al., developed a deformable ionic-based receptor that can distinguish simultaneously spatial profiles of temperature and strain without signal interference [133]; b) Wang et al. [134] proposed a self-powered multimodal pressure/temperature tactile sensor based on flexible Bi–Te thermoelectric film and porous microconed elastomer.

While there exist many publications of two terminal devices for multimodal sensing, very few works have been reported on the employment of flexible transistor architectures to tackle the same goal. In fact, the employment of a transistor structure for the realization of a sensing system has several advantages. First of all, the transduction mechanism can be modulated and locally amplified by the vertical gate field. Moreover, when arrays or matrices of transducers are required, which is actually the case when developing artificial skin systems, the switching capabilities of the transistor can allow to dramatically reduce the overall system design complexity.

Very interesting implementations of this approach have been proposed by Someya’s group, who developed one of the earliest example of a multimodal pressure/temperature sensor base on an organic thin film transistor [135]. Figure 55 a) reports the device structure and the images of the proposed multisensory array.

Other examples are those developed by Trung and co-workers, who studied different organic multimodal transistor-based sensors including infrared light, strain, temperature and pressure transducers [136], [137], where the key component was the highly crystalline co-polymer P(VDF-TrFE), integrated directly into the OFETs as a multi-functional gate dielectric layer with piezoelectric and pyroelectric characteristics. As it possible to notice from Figure 55 b), the device was able to detect simultaneously force and temperature variations.

More recently Meng et al. [138] developed a pentacene-based organic thin film transistor integrated with a piezoelectric ceramic for the realization of a dual mode pressure–temperature sensor (Figure 55 c)). In their work, the authors showed the relationship between the mobility and temperature with a linear response of the device to the temperature change in the range from 20 to 60 °C. Furthermore, once pressure stimulation was applied to the device, the output current varied accordingly.

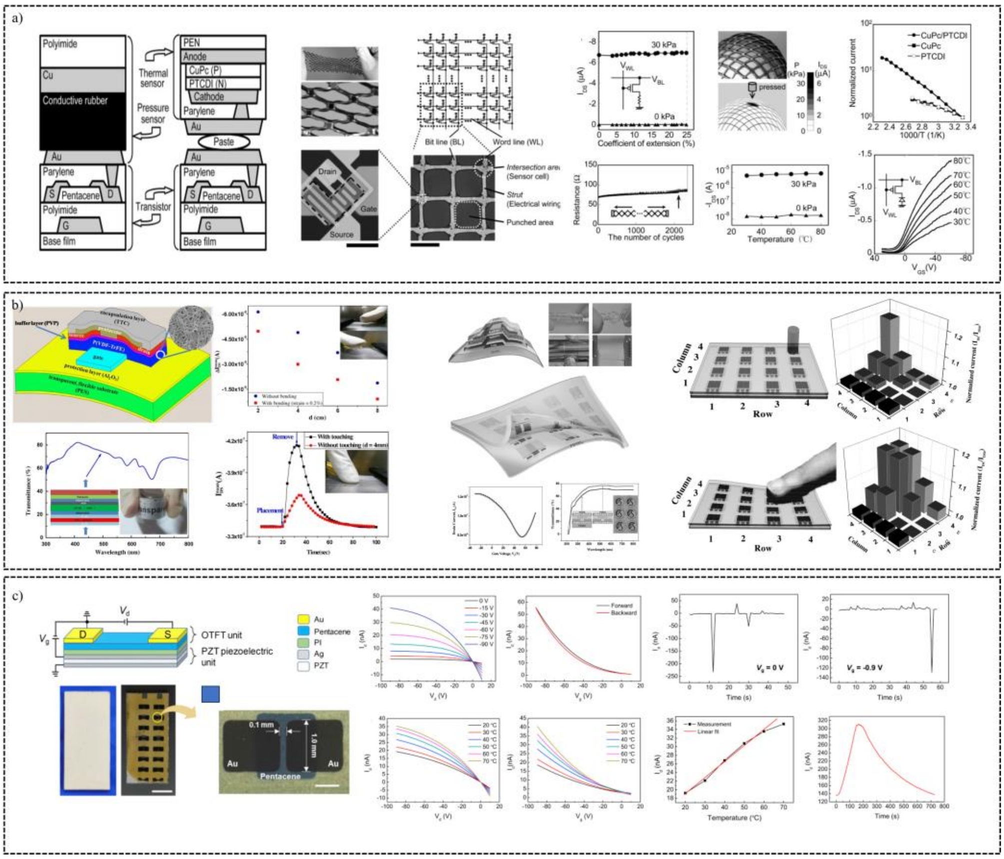

Figure 55 Multimodal tactile sensors based on the employment of organic thin film transistors. a) Sensor array proposed by Someya's group [135]; b) Trung and co-workers, who studied different organic multimodal transistor-based sensors including infrared light, strain, temperature and pressure transducers[136], [137]; c) pentacene-based sensor proposed by Meng et al. [138].

Another interesting approach was employed by Viola et al. [139], who proposed a multimodal tactile sensor based on an organic transistor coupled with a spin-coated PVDF-trifluoroethylene (PVDF-TrFE) polymer able to detect force and temperature stimuli. The device, among the different characteristics, was developed on an ultra-thin Parylene C-based substrate that enabled the possibility to attach the tactile sensor onto the human skin surface. As shown in Figure 56, the device, had good conformability and, after its placement onto the skin, maintained the electrical characteristics. Moreover, the authors showed a preliminary temperature detection of cold and hot stimuli when the sensor was placed onto the skin.

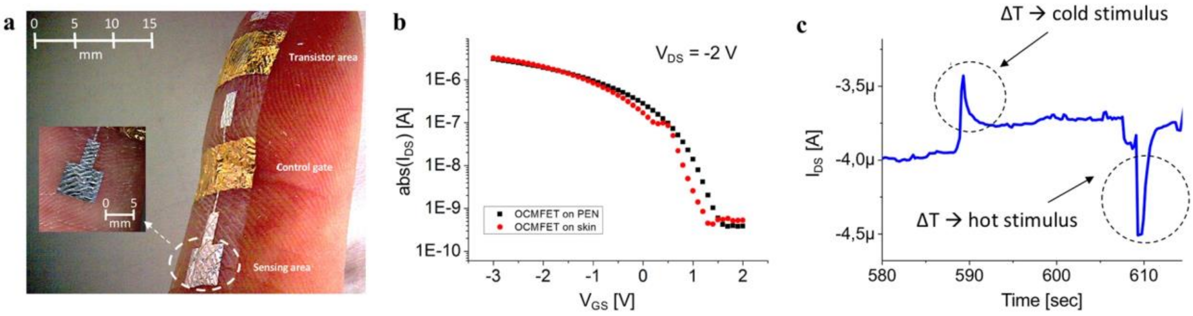

Figure 56 tactile sensor proposed by Viola et al [139]. a) the device had good conformability when placed onto the skin and b) showed stable electric characteristics after the peel-off from the plastic carrier; c) hot and cold temperature stimuli were detected by the epidermal sensor attached onto the skin..

3. Chapter III: Parylene C-based tattooable electrodes for ECG measurement

In the previous chapter, several examples and approaches for the fabrication of epidermal electrodes have been presented. Among the different methods, a definitive solution to provide at the same time a low-cost and easy fabrication process over large areas and ultra-conformable substrates and at the same time capable of reducing skin irritations and issues to produce dry electrodes for the detection of biopotentials from the surface of the skin has not been proposed yet.

The goal of the approach employed during this thesis work, which led to the publication of an article [140], is to identify a possible solution to these several issues using one of the most promising materials in the biomedical field, i.e. Parylene C. In fact, Parylene C has been successfully employed for several biomedical applications, and for the realization of both conformable electronic devices and electrodes in direct contact with the skin because of its biocompatibility, chemical inertness, and the possibility of obtaining ultra-thin sub-micrometer layers through a reliable and high-throughput chemical vapor deposition technique [26], [27], [139], [141]. Specifically, my contribution to this work was mainly on the design, fabrication, and electrical characterization of the dry ultra-thin electrodes, in terms of skin/electrode impedance analysis and data acquisitions.

3.1. Parylene C-based tattoo electrode fabrication process

The electrodes fabrication process started from a 250 µm thick plastic carrier (polyethylene terephthalate (PET) or polyethylene naphthalate (PEN)) in which a sacrificial layer of poly (vinyl alcohol) (PVA; a 6 wt% in a PVA solution in deionized water) was spin-coated at 700 rpm for 45 seconds on the substrate and then baked for 5 min at 90°C on a hot-plate. This PVA layer is needed to perform all of the fabrication steps without premature detachment of the nanofilm and moreover, it ensures an easy tattoo film peel-off from the plastic carrier. A first layer of Parylene C of approximately 500 nm was subsequently deposited onto the carrier. This layer is the core of the device structure. On top of it is possible to develop several devices. In this specific case, in order to fabricate the tattoo electrode for biopotential recordings, the negative pattern of the electrode array was obtained using a standard and low-resolution photolithographic process. Afterward, this patterned photoresist film was covered with 70 nm of evaporated metal layer. During this thesis work both silver and gold electrodes were fabricated. It is worth mentioning that a slight plasma oxygen activation of the surface was performed at 60 s at 100 W before the metal evaporation. The electrode pattern was obtained by stripping the device in a sonicated acetone bath. Depending on the application and on the target biopotential to be acquired, it is possible to develop several electrode geometries. For instance, a circular active area with a diameter of 1 cm was employed to record the ECG signal.

After this lift-off process, a second Parylene C layer of approximately 200 nm, which acts as a passivation layer, was deposited on the substrate, with the only exception of the connector of the array and the electrode recording area, which were covered with a polydimethylsiloxane patch during the deposition process and then removed.

During this thesis work, an additional feature to the ultra-thin Parylene C-based electrodes was added. Despite very good chemical and mechanical properties, Parylene C lacks breathability. This material is characterized by outstanding chemical robustness, which makes it an ideal barrier against water and oxygen interdiffusion. For this reason, it is routinely used as a protection layer in many electronic applications. However, this aspect represents a limitation for epidermal electronics applications. To overcome this issue, while retaining the features of the Parylene C nanofilms, an optimization process to easily obtain a highly reproducible large-area perforation technique was performed. Particularly, a photolithographic process was executed by spin-coating a layer of photoresist and patterning with the desired hole density. After the removal of the metal within the holes with a quick wet etching, the substrate was exposed to oxygen plasma (7 min at 200 W) to perform the dry etching of the Parylene C layer.

Figure 57 a) reports the complete fabrication process workflow.

The final electrode has an overall thickness of approximately 700–800 nm. The thicknesses of the different layers were evaluated on sacrificial substrates using a contact profilometer (Bruker DektakXT), as shown in Figure 57 b). After this low-cost and easy fabrication process, the tattooable patch was peeled-off and eventually transferred to a piece of paper which acted as a carrier to help handle the ultra-thin device (Figure 57 b). A small amount of deionized water was used to dissolve the PVA sacrificial layer. After the sample was dried out, the tattoo electrode was ready to be transferred to the skin.

This process was relatively easy to perform, since by simply placing the patch on the desired location of the body and wetting the back of the carrier, the paper can then be removed by sliding it away, leaving the tattoo electrode tightly adhered to the skin. Thanks to the sub-micrometer thickness of the whole device structure, the tattoo electrode can guarantee a robust adhesion to the skin without the use of any glue or gel, but only via van der Walls interactions.

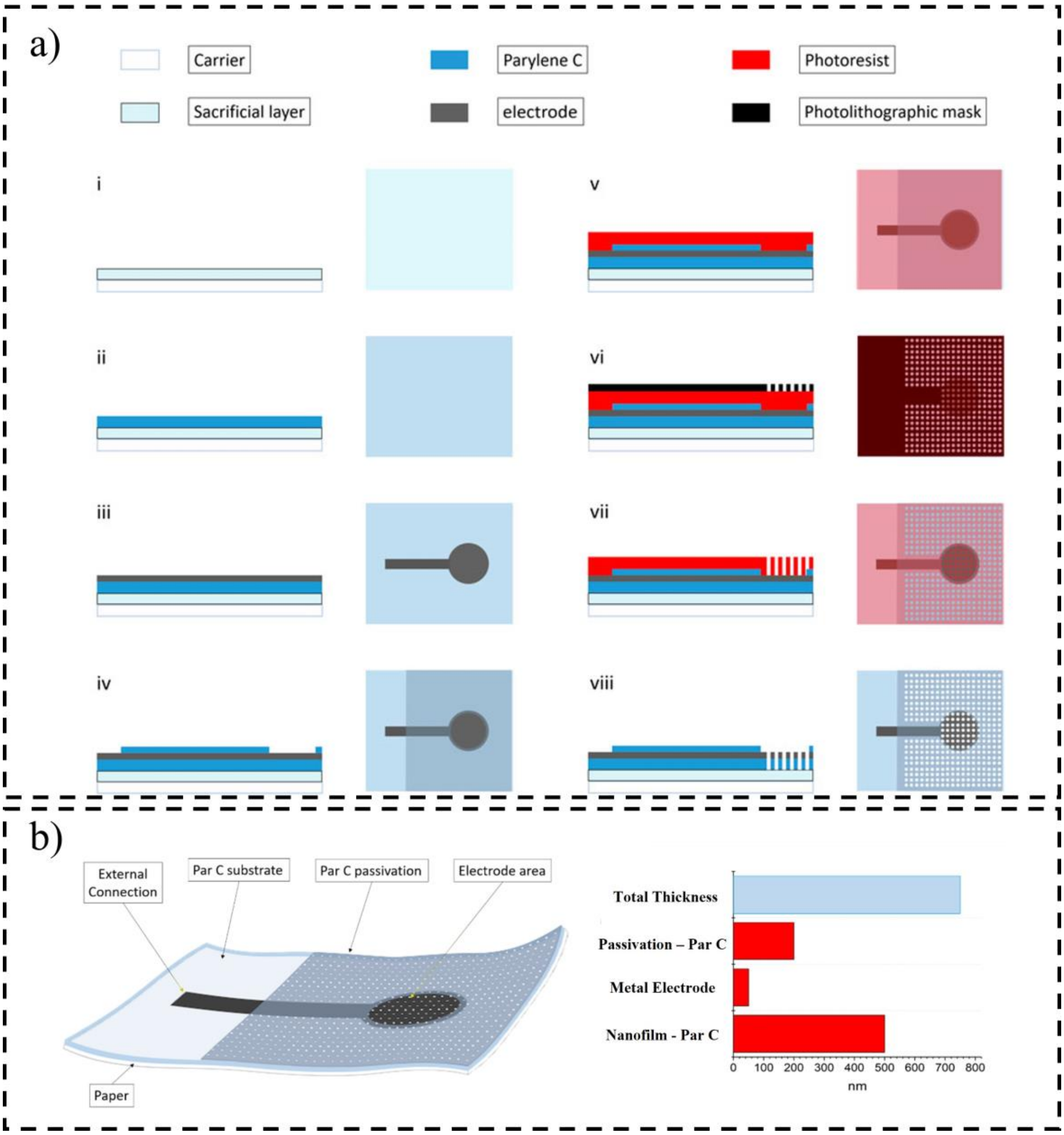

Figure 57 Parylene C-based tattoo electrodes for biopotential acquisition. a) fabrication process of the breathable electrodes (with materials). The fabrication starts with the deposition of a PVA sacrificial layer onto the plastic carrier (i); the Parylene C that acts as the substrate is deposited on the sacrificial layer through chemical vapor deposition (ii); deposition and patterning of the metal electrode (iii); another layer of Parylene C, which acts as a passivation layer, is then deposited on the electrode with the exception of the connector and the recording regions (iv); the perforation is performed using a photolithographically patterned photoresist layer as a mask (v, vi,vii) to selectively remove the metal layer and Parylene C using a combination of wet etching (for the metallic film) and plasma oxygen etching (for the Parylene C); after the perforation is complete, the photoresist is removed (viii)

and the electrode is ready to be peeled-off and transferred to the paper. (b) Sketch of the Parylene C electrode on the paper carrier. The external connection area and electrode area are exposed, while the remaining parts are passivated. The Parylene C substrate, passivation layer, and electrode area have holes to guarantee the breathability of the structure; thickness of the three layers constituting the electrodes, namely the first Parylene C layer that acts as the substrate (i), the metal layer (ii), and the Parylene C passivation layer (iii).

To connect the epidermal electrodes to the recording device it is necessary to employ a sufficiently robust method that ensures a good interconnection between ultra-thin electrodes and rigid recording system. A possible solution can be placing the exposed back contact of the electrode on a small silver-coated neodymium magnet (×3 5 mm with a thickness of 1 mm) connected to a clip contact through a passivated copper wire. Another magnet can be eventually placed on the film to keep it firmly in place. Figure 58 a) shows the interconnection system employed to connect the breathable nanofilm after its positioning on the skin. As it possible to notice, the electrode is positioned face down in order to have the exposed recording area in contact with the skin. By using a water droplet the paper carrier can be removed by sliding it away thus the electrode is positioned onto the skin without any gel or adhesive tape, exploiting the van der Walls interaction between the human body and the tattooable patch. Figure 58 b) reports an optical image of the electrode positioned on the skin while the inset highlights the holes on the recording area.

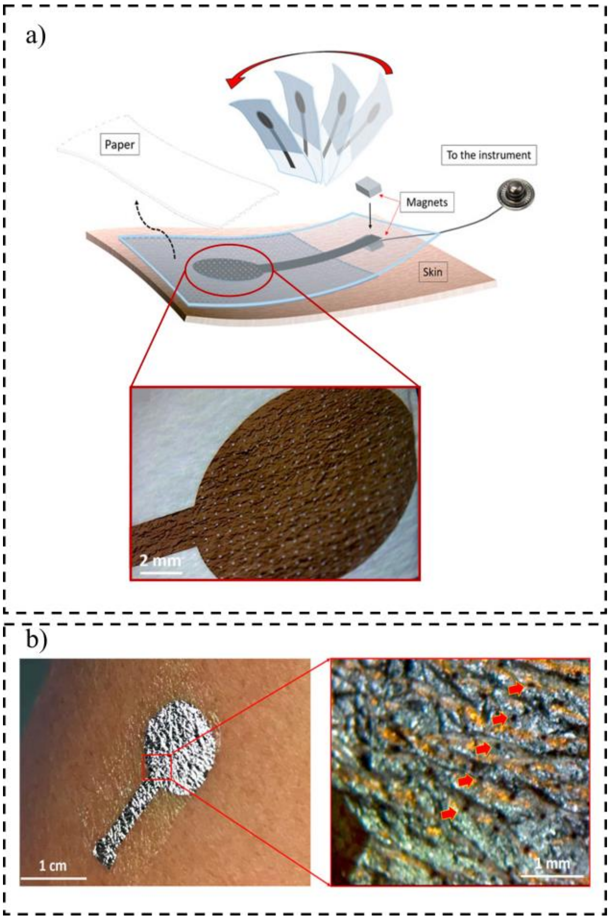

Figure 58 Breathable nanofilm positioning on the skin. a) The electrode was placed face down on the skin and the paper was removed using a few droplets of deionized water and sliding it away. The electrode contact was placed on a metalized magnet connected to a clip contact. A second magnet was placed on top of the first to improve the contact between the film and the first magnet; d) A breathable nano-electrode after its lamination on the skin. The inset shows a micrograph of the electrode on the skin. Thanks to the sub-micrometer thickness, a conformal interface can be obtained; it is also possible to spot the pores (red arrows).

The ultra-thin Parylene C-based electrodes showed an incredible conformability to the skin. The low stiffness and the characteristics of the Parylene C nanofilm enabled outstanding mechanical properties.

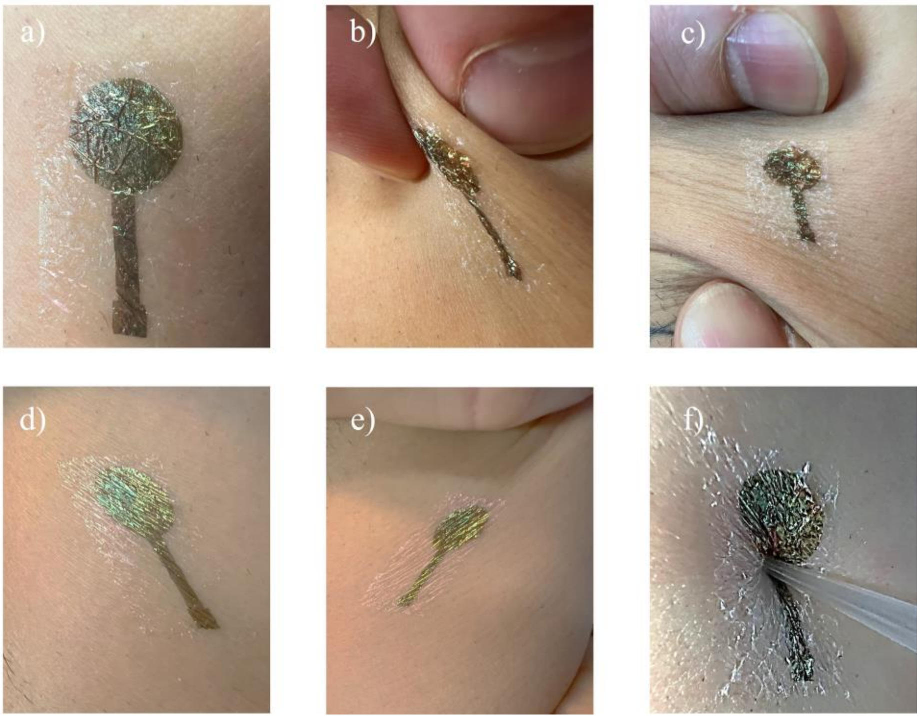

Figure 59 Parylene C-based electrode attached to the skin. The tattoo patch after the a) lamination is able to adhere to the skin without any adhesion layer/glue and it can also undergo various mechanical deformations, such as b) pinches, c) compressions, d) extensions, e) twists, and f) pressures, without any mechanical damage to the structure of the device

3.2. Contact Impedance Measurements setup

Contact impedance is one of the most important parameter to described the electrode performances. It is dramatically affected by the skin/electrode interface, therefore a conformal contact between the tattoo patch and the human body decreases the impedance and, as a consequence, increase the quality of the biopotential measurement.

Moreover, it is worth to mention that the physical and electrical behaviors of a dry electrode and wet Ag/AgCl electrode are different. In particular, the dry electrode lacks of an ionic wet conductor that increases both surface adhesion and electrical contact with the skin as it happens with the standard Ag/AgCl electrodes.

During this thesis work, Parylene C-based electrodes were characterized in terms of skin-electrode contact impedance by using an Agilent 4284A precision LCR meter (Agilent Technologies Inc., Santa Clara, CA, United States). A low sinusoidal current was injected on the body, performing a 4-probe measurement in the frequency range between 20 and 500 Hz.

The measurement set-up is shown in Figure 60, where the position of the electrodes and the equivalent electrical scheme are highlighted. A local gentle skin abrasion by a preparation cream (NuPrep, Weaver and Co., CO, United States) was performed before the contact impedance evaluation and the measurement was performed between the experimental electrode (Z_{tattoo}) and the parallel of five commercial pre-gelled electrodes (Z_{comm}) (BlueSensor N, Ambu A/S, Denmark). This electrical scheme allows to make the commercial electrodes impedance almost negligible and thus having a more accurate measurement of the impedance resulting by the skin/tattoo interface.

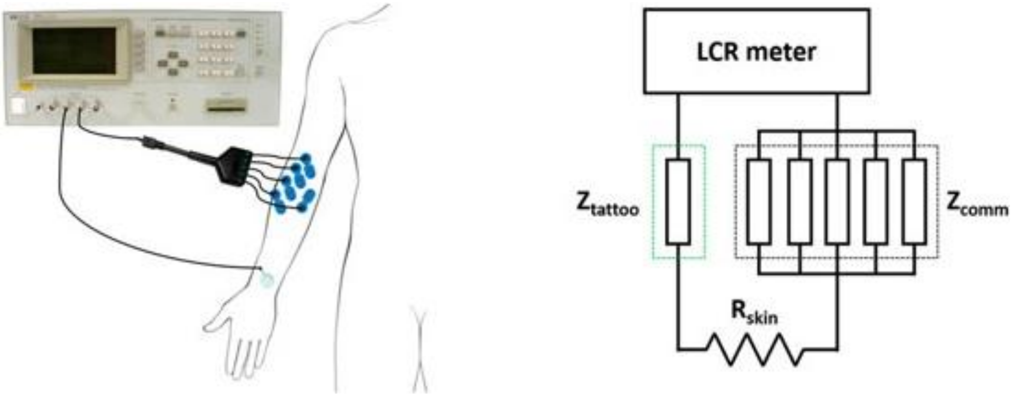

Figure 60 Contact impedance measurement, where the positioning of the electrodes and electrical scheme are highlighted. The Z_{tattoo} *has been evaluated against the parallel of five commercial electrodes (*Z_{comm}*) in order to make the latter negligible and thus having a more accurate measurement.*

3.3.Permeability Measurement Setup and results

Air permeability measurements were performed on a TexTest 3,340 MinAir device at 20°C. Prior to the sample measurements, the device gaskets were wiped down with propan-2-ol and calibrated on a 20 cm^2 standard calibration plate (358 mm/s, ± 3 mm/s), at 200 Pa. Sample measurements were taken using a pressure drop of 100 Pa with a 5 cm^2 adapter and relative humidity of 37% or 63%.

The evaluation of the electrodes breathability were performed on two different holes, with a diameter of about 100 and 50 µm respectively, both with a hole density of four holes/mm^2.

Air permeability measurements taken at 100 Pa and 37% relative humidity showed mean air permeability (δ) of 99 mm/s and 364 mm/s for 50 and 100 µm pores, respectively. The δ increased respectively to 109 mm/s and 377 mm/s at 63% relative humidity, as shown in Figure 61. Previous work on textiles suggests that some materials may swell with an increase in relative humidity, which in turn affects the porosity of the material (Gibson et al.[142]). This may be responsible for the increase in air permeability at higher relative humidity in our samples.

It is interesting to compare the breathable nanofilms with others wearable devices reported at the state-of-the-art. The electrode’s air permeability exceeds that of a range of novel wearable structures. Peng et al. [143] reported a breathable electronic skin with an air permeability of 120 mm/s at ≥125 Pa, while Yang and Lu [144] reported a paper electrodes with a permeability of 330 mm/s at 300 Pa. A novel wound dressings proposed by Liu et al.[145] was characterized by a permeability of 324 mm/s at 200 Pa, while several electronic textiles reported in the state-of-the-art had smaller values in the range between 88 and 160 mm/s at 100 Pa (Cao et al.[146] ; Qiang et al.[147] ; Wang et al.[148]). Moreover, these values are greater than some common textiles, such as jeans (∼50 mm/s at 300 Pa) (Yang and Lu [144]), and approaches the values obtained for knitted clothing (>500 mm/s at 100 Pa) (Selli and Turhan [149]). Table 2 summarize the air permeability of several breathable devices reported above.

Table 2 Air permeability comparison between the proposed Parylene C electrodes and several devices at the state-of-the-art

Device	Air permeability
Peng et al. [143]	120 mm/s at ≥125 Pa
Yang and Lu [144]	330 mm/s at 300 Pa
Liu et al.[145]	324 mm/s at 200 Pa
Cao et al.[146]; Qiang et al.[147]; Wang et al.[148]	88–160 mm/s at 100 Pa
Jeans permeability (Yang and Lu, [144])	50 mm/s at 300 Pa
Knitted clothing (Selli and Turhan [149])	>500 mm/s at 100 Pa
Parylene C based breathable tattoo electrodes	377 mm/s

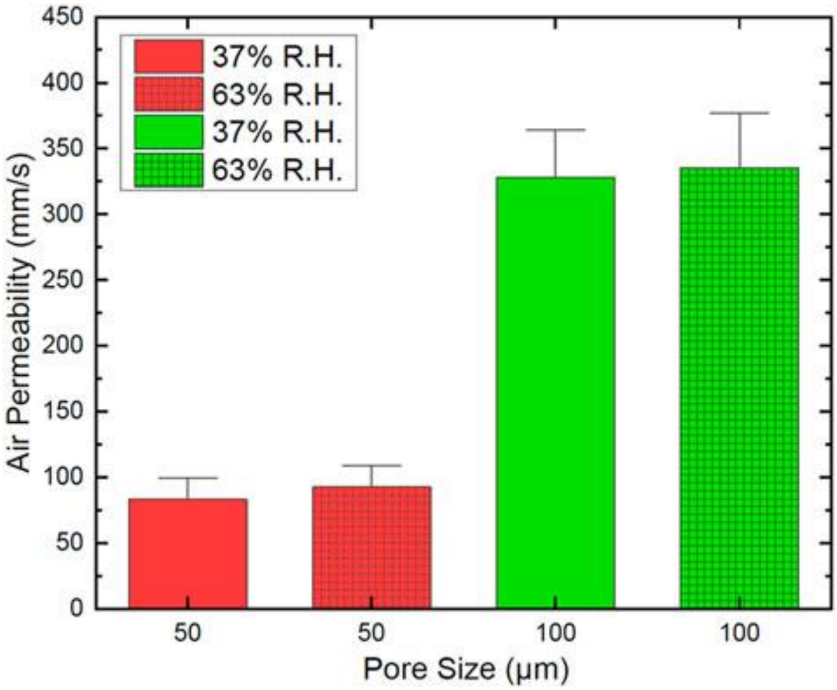

Figure 61 Air permeability of two sets of breathable Parylene C nanofilms with different pore sizes (50 and 100 µm, respectively) evaluated for two values of relative humidity.

This Parylene C-based ultra-thin tattoo electrodes can be employed for the measurement of several biopotentials. In this thesis work the focus will be on the recording of the ECG signal [140] and the EEG signal [150].

3.4. ECG signal recording

The ECG signals were recorded using both non-breathable and breathable tattoo electrodes with Silver as active material to detect the biopotential. To evaluate the performance of the two electrodes based on Parylene C, a comparison was made in terms of signal recording quality using Ag/AgCl wet electrodes as a gold standard.

3.5. Contact impedance measurements

The contact impedance was evaluated following the measurement set-up described in 3.2. Both non-breathable tattoo electrodes and breathable (with holes diameter equal to 100 µm) tattoo electrodes were studied. Figure 62 shows the contact impedance evaluated in two different days on the forearm of the same subject to minimize the differences due to the inter-person variability of the skin characteristics. For each day, 20 tattoo electrodes were alternately tested by positioning them on the skin using a few droplets of deionized water, after a skin preparation.

The largest part of the measured impedance can be ascribed to the skin-tattoo contact and the skin-electrode contact impedance showed good reproducibility within the same recording session, with marked differences between the two sessions, which was highly predictable considering the strong dependence of the skin impedance from several factors, both physiological and environmental, regardless of the electrode technology. Values in the range of 40–60 kΩ at 20 Hz were recorded. Overall, the contact impedance of the electrodes is comparable (or even lower) with that of other epidermal electrodes that can be found in literature[32], [42]. Moreover, no relevant differences between the breathable (in black) and standard tattoo electrodes (in red) in terms of impedance were observed.

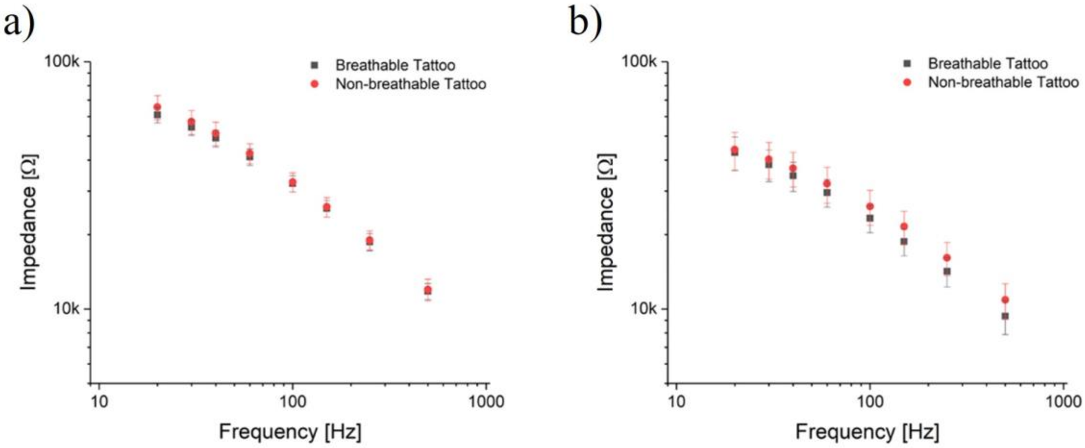

Figure 62 Contact impedance evaluated in the range 20-500 Hz. The frequency dependency of the skin-electrode contact impedance was measured on the same subject (and on the same spot in the forearm) on two different days a) and b), using 20 electrodes each session. Non-breathable and breathable tattoo electrodes showed similar contact impedance in the range of 40–60 kΩ at 20 Hz.

3.6.ECG signal recording experiment setup and results

The analysis was performed on 18 ECG signals, recorded from four healthy volunteers (age: 32 ± 10, BMI: 22.8 ± 1.9, heart rate: 63 ± 7 bpm). Concerning the experimental protocol, the principles outlined in the Helsinki Declaration of 1975, revised in 2000, were followed.

Tattoo electrodes were placed onto a conductive magnet, which was also connected to a snap connector in order to fit with the recording system cables. In particular, a 32-channel Porti7 electrophysiological recording system (TMSI, The Netherlands) at a sampling rate of 2048 Hz, with an effective bandwidth of 553 H was employed. To accurately assess the cardiac rhythm, lead II was chosen for all ECG signal acquisitions as it is commonly used to record the rhythm strip and it provides good P wave representation [151]. Specifically, Figure 63 shows the positioning of the electrodes employed for this recording session. In particular, lead II was recorded by adopting a pair of electrodes on the torso according to the Holter electrode placement configuration, while LL electrode was placed on the left anterior axillary line, and the RA electrode was placed slightly under the right manubrium. The ground electrode was placed near the right hip.

In order to demonstrate the tattoo electrodes performance in terms of biopotential recording, the ECG was simultaneously recorded using standard Ag/AgCl wet electrodes, non-breathable tattoo electrodes, and breathable tattoo electrodes. It is worth noting that the different pairs have been spaced preserving the same inter-electrode distance to simultaneously record cardiac electrical activity from the three different electrode pairs and limit the impact on the morphology and amplitude of the signal.

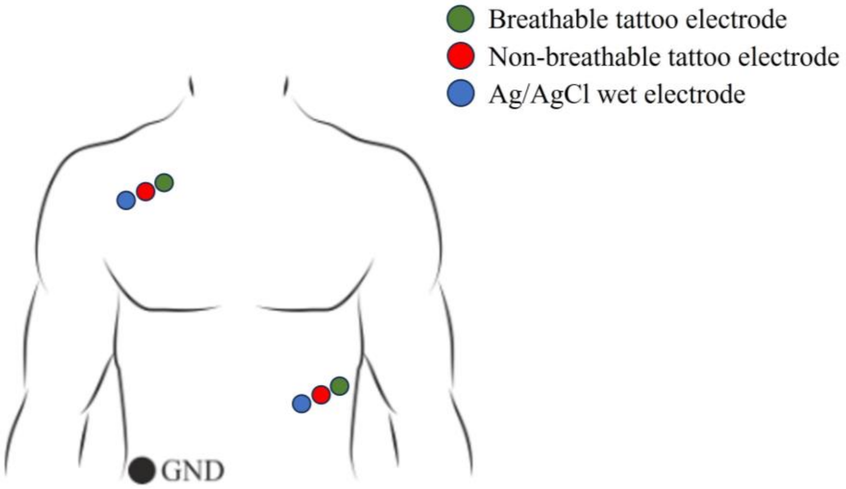

Figure 63 Electrode positioning adopted for the single-lead ECG recordings. Recording electrodes were placed as indicated by circles, by using Ag/AgCl (in blue), non-breathable tattoo electrodes (in red) and breathable tattoo electrode (in green) simultaneously, preserving the same distance between bipolar sensing electrodes

The statistical analyses revealed that no significant differences were possible to observed among the ECG measurements computed on the signals recorded by the different electrodes ($p > 0.05$ for all the ECG measurements).

Some filtering steps were applied to erase the baseline wander artifact. It is worth noting that no other filtering step, such as notch filters to suppress powerline interference, was introduced. Since the goal of this analysis was to compare the performance of the different electrodes, it is necessary to consider that the amount of powerline noise is related to the skin-contact electrode impedance and the stability of such an interface. Therefore, from the ECG measurements a median beat in terms of median values and 25th and 75th percentiles over the whole dataset were extracted. Table 3 shows the measurements for each electrode type in terms of median values and 25th and 75th percentiles.

Moreover, from a clinical perspective, all ECG intervals were compliant with those expected for healthy subjects and similar, especially for the R–R intervals, suggesting that the adoption of these new electrodes may be applicable to heart rate variability analyses. However, the quality of the recorded ECG signals was assessed by exploiting the quantitative figures of merit and from a clinical perspective.

Table 3 Statistical analysis from the ECG measurement

	Non-breathable tattoo	Breathable tattoo	Gelled Ag/AgCl
QRS amplitude (mV)	3.23 [2.96;3.28]	3.16 [2.85;3.25]	2.96 [2.85;3.21]
P duration (ms)	117.19 [113.28;125.00]	119.14 [113.28;125.00]	117.19 [113.28;125.00]
QRS duration (ms)	83.98 [66.41;101.56]	97.66 [66.41;101.56]	85.94 [66.41;101.56]
T duration (ms)	181.64 [171.88;195.31]	175.78 [167.97;187.50]	189.45 [179.69;199.22]
PQ interval (ms)	158.20 [152.34;164.06]	156.25 [144.53;164.06]	156.25 [152.34;160.16]
RR interval (ms)	914.06 [885.25;1050.78]	913.82 [885.25;1050.78]	912.60 [885.25;1050.78]
QTc interval (ms)	388.52 [366.55;393.76]	388.38 [377.15;396.61]	386.08 [365.83;396.42]

Figure 64 shows an example of 15s-long ECG recordings with the highest qualitative score for the different electrode types, namely Ag/AgCl electrodes (top row), non-breathable tattoo electrodes (middle row) and breathable tattoo electrodes (bottom row). Such figure confirm a remarkable similarity among the different signals.

Figure 64 Examples of 15s-long ECG recordings with the highest qualitative score for the different electrode types (as such, they are taken from different subjects and not simultaneously).

The signal-to-noise ratio (SNR) is another key parameter to quantify the quality of the acquired signal. In particular, both low-frequency (lower than 0.5 Hz) and high-frequency noise (higher than 0.5 Hz) that affect the ECG recordings were considered. Furthermore, being the SNR typically adopted for the assessment of ECG signal quality [152], it was also included and computed following its standard definition:

$$SNR[dB] = 20 \log_{10} \left(\frac{A_{pp}}{4\sigma} \right) \tag{3}$$

where A_{pp} identifies the peak-to-peak amplitude of the median beat template of each ECG signal contribution and σ is related to the high-frequency noise content, and as such it was evaluated as the median RMS derived from the isoelectric intervals. The results of this analysis are reported in Figure 65, where the low-frequency (a) and high-frequency noise (b) RMS as well with the SNR estimations (c) on the three different electrode types are reported. Particularly, the boxplots include the median values (central thick line), 25th and the 75th percentiles (lower and upper box edges, respectively) and extreme values for each distribution (whiskers) and outliers (red crosses). It is worth to notice that the statistical study reports a significant difference among the three acquisitions regarding the baseline wander artefact. Specifically, breathable and non-breathable tattoo electrodes showed significantly greater RMS values than gelled electrodes ($p < 0.0005$), assuming similar values to each other ($p > 0.05$). Moreover, in the low-frequency noise root-mean-square representation, two outliers for non-breathable tattoo electrodes (close to 1.4 and 1.8 mV, respectively) and one for breathable tattoo electrodes (near 1.2 mV) were not represented for the sake of clarity. However, the high-frequency noise contributions and SNRs showed no statistical evidence ($p > 0.05$), suggesting that tattoo electrodes, both breathable and non-breathable, have noisy contributions similar to Ag/AgCl electrodes. Remarkably, this outcome is achieved without removing the powerline interference.

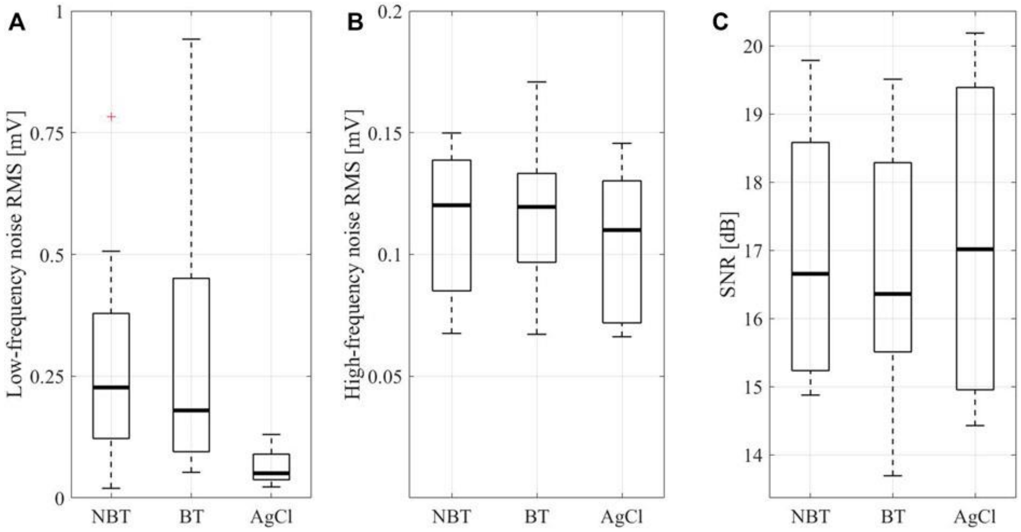

*Figure 65 Root-mean-square values for low-frequency (less than 0.5 Hz, a) and high-frequency (greater than 0.5 Hz, b) noises and the SNR values **c)** characterizing the ECG recordings acquired by non-breathable tattoo (NBT), breathable tattoo (BT), and commercial gelled Ag/AgCl electrodes (AgCl).*

In addition, a qualitative scores was provided by the clinician for the different high-pass filtered ECG traces and their corresponding median beat template. The cardiologist's analysis was performed to demonstrate the suitability of the Parylene C-based electrodes for ECG detection. Figure 66 reports the qualitative scores (in the range 0–10) expressed for the whole 15s-long ECG signals acquired by the three electrodes (NBT: non-breathable tattoo, BT: breathable tattoo, AgCl: gelled Ag/AgCl), their corresponding median beat templates and the Person's correlation coefficient computed between median beat templates acquired by the different electrode types. The provided scores were generally greater than 8/10 for the 15 s-long signals and 9/10 for the median beats. Furthermore, the Pearson's correlation coefficient computed between each pair of median beats was typically greater than 0.99, as shown in, thus suggesting remarkable similarity among the different templates.

Moreover, Figure 66 b) shows an example of median beats with the highest (top row) and lowest (bottom row) qualitative scores for the different electrode types (taken from different subjects and not simultaneously).

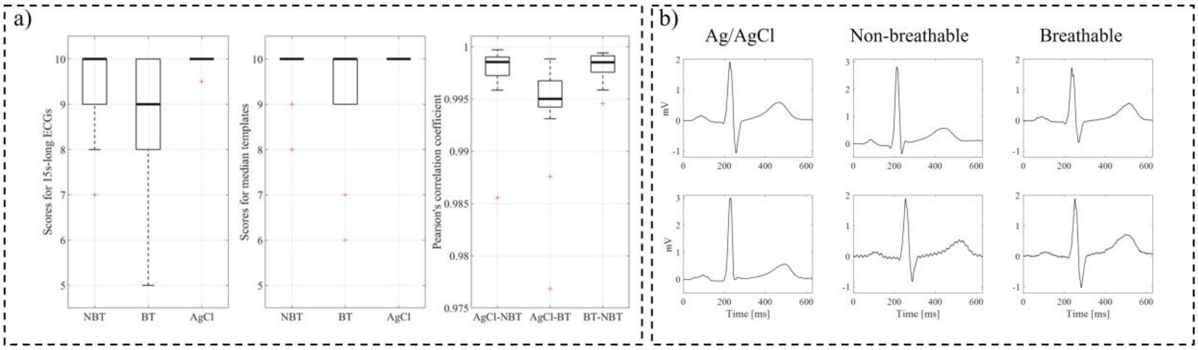

Figure 66 a) Qualitative scores expressed in the range 0–10 for the whole 15s-long ECG signals acquired by the three electrodes (NBT: non-breathable tattoo, BT: breathable tattoo, AgCl: gelled Ag/AgCl), their corresponding median beat templates and the Person’s correlation coefficient computed between median beat templates acquired by the different electrode types: Ag/AgCl vs. non-breathable tattoo (AgCl-NBP), Ag/AgCl vs. breathable tattoo (AgCl-BT) and breathable vs. non-breathable tattoo (BT vs. NBT); b) median beats with the highest (top row) and lowest (bottom row) qualitative scores for the different electrode types (taken from different subjects and not simultaneously). In the left column the best commercial gelled Ag/AgCl electrode (score of 10/10 for both) is reported, while the central column is devoted to non-breathable tattoo electrodes (highest score 10/10 and lowest score 8/10), and the right column for breathable tattoo electrode (highest score 10/10 and lowest score 6/10).

The use of epidermal electronic devices for long-term applications is one of the important goals of such technology. To achieve this possibility, the use of breathable devices is a key point to reduce skin irritation and increase user comfort.

The electrical performances of the electrodes were studied during a 9-h span to demonstrate the advantages offered by the ultra-thin breathable tattoo electrodes. The Parylene C-based electrodes behaved quite homogeneously over time, with a slightly worse performance compared to the adhesive electrodes with liquid electrolytic gel, as expected.

Low-frequency and high-frequency noise estimations were reported in Figure 67 a) and b) respectively, while Figure 67 c) shows non-breathable tattoo (left column) and breathable tattoo (right column) signals recorded at different hours, i.e. at 0 h (top), 4 h (middle) and 9 h (bottom).

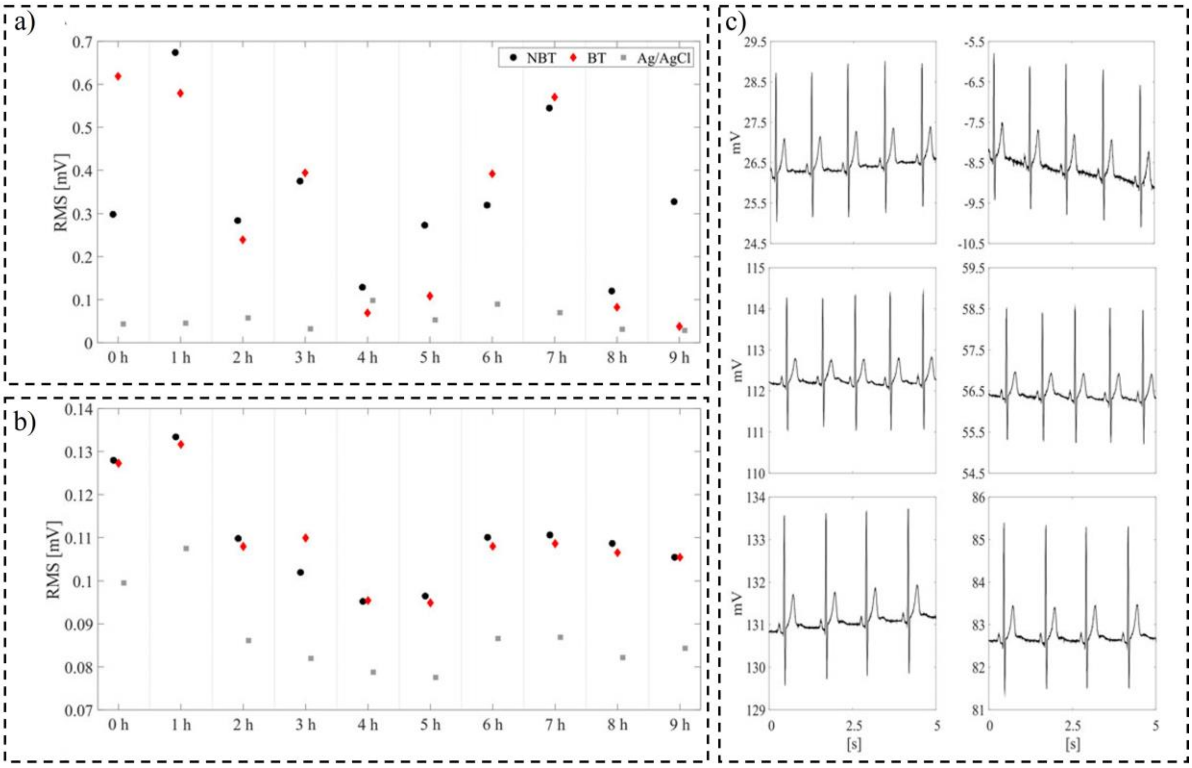

Figure 67 Long-term ECG signal recording. a) Root-mean-square level for the low-frequency noise for the three types of electrodes; b) Root-mean-square level for the High-frequency noise for the three types of electrodes; c) non-breathable (left column) and breathable (right column) signals recorded over 9 hours, specifically at 0 h (top), 4 h (middle) and 9 h (bottom).

During the whole experiment, the skin contact impedance has been also evaluated. The same measurement approach described in 3.2 was used for the assessment of the variation of the impedance over time. However, in this case due to the different placement of the electrodes, a medical grade impedance-meter with a fixed frequency of 10 Hz (EIM-105 Prep-Check, General Devices) was employed. Figure 68 shows the contact impedance variation over time measured at 10 Hz for the three types of electrodes. As it is possible to notice, the breathable electrodes showed a faster increase of the contact impedance with respect to both the non-breathable and the commercial one, due to the faster rate of sweat evaporation. However, despite the faster degradation of the impedance, the breathable electrodes maintained excellent recording performances. The impedance was measured at 1-h intervals between the electrode under test and the parallel of five commercial pre-gelled electrodes as depicted in Figure 68, where the measurement setup employed is shown.

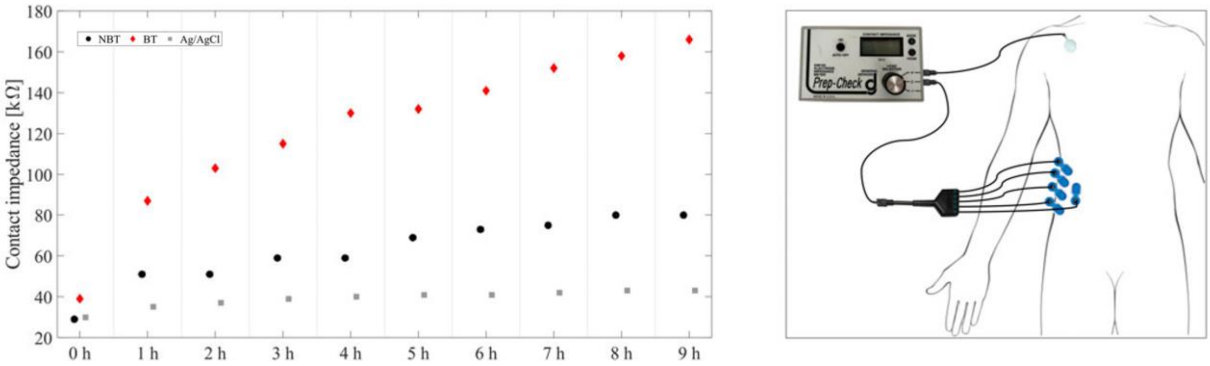

Figure 68 Contact impedance variation over time for breathable, non-breathable and wet Ag/AgCl electrodes. A faster increase of the contact impedance is notable for breathable electrodes with respect to both the non-breathable and the commercial one, due to the faster rate of sweat evaporation. The impedance value was measured at 1 hour intervals using the highlighted measurement setup, where the value of the impedance were acquired between the device under test and the parallel of five commercial wet electrodes.

The tattoo electrodes showed clearly better skin compatibility if compared with the commercial electrodes, which have an adhesive layer to guarantee contact with the skin. As is interesting to note in Figure 69, where the effect of the three electrode types on light skin is presented, breathable tattoo electrodes showed almost no effect, even if compared with the non-breathable electrodes, thus confirming their potential for preserving the patient’s comfort during longer monitoring sessions.

All of these characteristics corroborate the idea that the breathable Parylene C electrodes could represent a valid alternative to commercial electrodes in critical applications, such as bio-monitoring of elderly and new-born patients or intensive care of severely burnt people, where imperceptibility and breathability are of great importance.

However, a critical aspect of this technology is the external connection with the recording devices because of the extremely low thickness (< 1 µm) of the electrodes. The proposed connection approach proved to be effective, allowing recording up to 9 h. However, further efforts are needed for the realization of better performing connections.

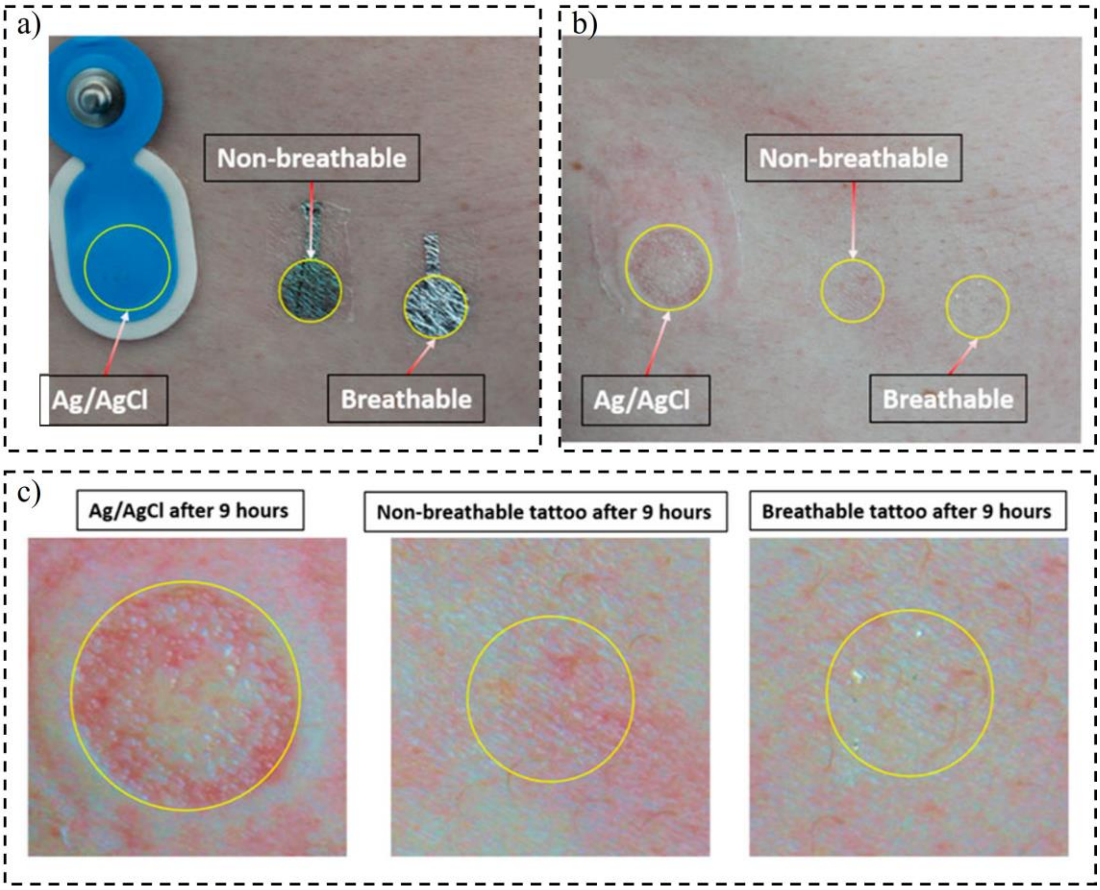

Figure 69 Effect of the electrodes on the skin. a) The three types of electrodes placed on the right hip of the subject and b) the same spot after the removal of the electrodes (9 h); c) the magnification of the same area, where it is possible to notice the worse skin irritation induced by the commercial electrode with respect to the Parylene C electrodes.

4. Chapter IV: A wearable platform for EEG Measurements

This chapter describes a new solution for the acquisition of the EEG signal capable to combine the advantages of the wearable approach to those of epidermal imperceptible electrodes. The system consists of a custom Printed Circuit Board (PCB) fabricated using off-the-shelf components and a modified headband that has been specifically designed to conveniently interface unconventional ultrathin tattoo electrodes.

The idea was to drastically reduce the amount of adhesive required for commercial pre-gelled electrodes, and at the same time develop a new wearable system capable of conveniently and unobtrusively monitoring brain signals [150], [153]. The contribution I provided to this work was mainly on the design and fabrication of the tattoo electrodes and on the design of the headband to conventionally interface the ultrathin electrodes. Moreover, I contributed to the contact impedance analysis and data acquisition set-up.

4.1.Materials and method

The tattoo-electrodes fabrication process follow the workflow described in the chapter 3.

However, for the acquisition of the EEG signals, the electrodes were fabricated in a slightly different way. Firstly, onto a 175 µm-thick poly(ethylene terephthalate) (PET) substrate, a poly(vinyl alcohol) (PVA) sacrificial layer was deposited through a standard spin coating technique. After the PVA deposition, a 500 nm Parylene C layer was deposited through a chemical vapor deposition (CVD). Afterwards, gold electrodes (50 nm-thick) were thermal evaporated onto the Parylene C film and patterned using a standard photolithographic lift-off process. Finally, the electrodes were passivated (with the exception of the recording and the connection areas) with a 200 nm-thick second Parylene C layer. Figure 70 a) shows the fabrication process workflow with the employed materials highlighted.

The final electrodes had a thickness of about 800 nm (measured using a stylus profilometer—DektakXT, BRUKER, Madison, WI, USA), which ensured a conformal contact with the skin. In Figure 70 b) the average thickness of each part of the electrode is reported, while Figure 70 c) shows the ultra-conformable Parylene C tattoo-electrode applied on the forehead and positioned on a 1 cm metal plate for the signal acquisition.

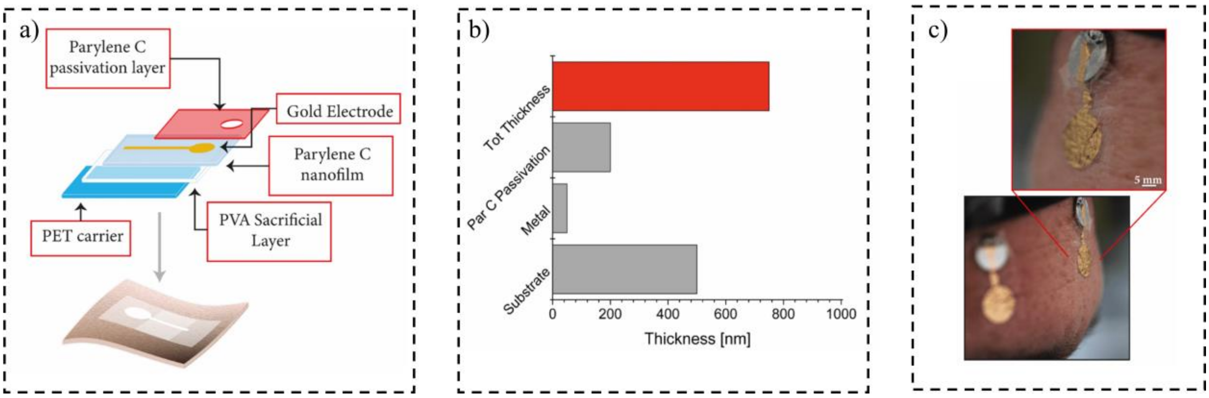

Figure 70 Ultra-thin Parylene C electrodes. a) fabrication process flow where all the different layers are highlighted; b) Average thickness of the proposed tattoo-electrodes; c) tattoo electrode applied on the forehead and positioned on a 1 cm metal plate for the signal acquisition

4.2. Contact impedance measurements

As it was already mentioned in this manuscript, the contact impedance is an important parameter for recording a high-fidelity biopotential signal and thus to assess the electrode performances. In addition, the EEG signal is relatively low with respect other physiological signals. Therefore, in order to select the most suitable electrode dimension, and at the same time ensure that the skin-electrode impedance was sufficiently low, as required for electroencephalography [154], three different sets of electrodes with different areas were produced and tested for the electrode-skin impedance, 7.84 cm^2, 0.78 cm^2, and 0.15 cm^2 respectively. For this purpose, 10 electrodes for each dimension were measured with respect the parallel of 5 pre-gelled Ag/AgCl electrodes, in the range 20-500 Hz on the forearm of the same subject and in the same day (following what previously reported in 3.2).

Figure 71 reports the contact impedance characterization as a function of the frequency of the set of Parylene C-based electrodes with different areas. As it possible to notice, the maximum value of impedance was obtained for the smaller electrode, as expected. Moreover, there is no evident different between the electrodes with area equal to 0.78 cm^2, and 0.15 cm^2 respectively. The biggest electrode (7.84 cm^2), instead, reported a contact impedance largely smaller than the other two.

Interestingly, the obtained impedances are in line with the contact impedance of other types of semi-dry electrodes, as reported by Li et al.[155]. However, to ensure the best comfort while at the same time guaranteeing an optimal skin/electrode impedance, all the electrodes were fabricated with an overall contact area of 0.78 cm^2.

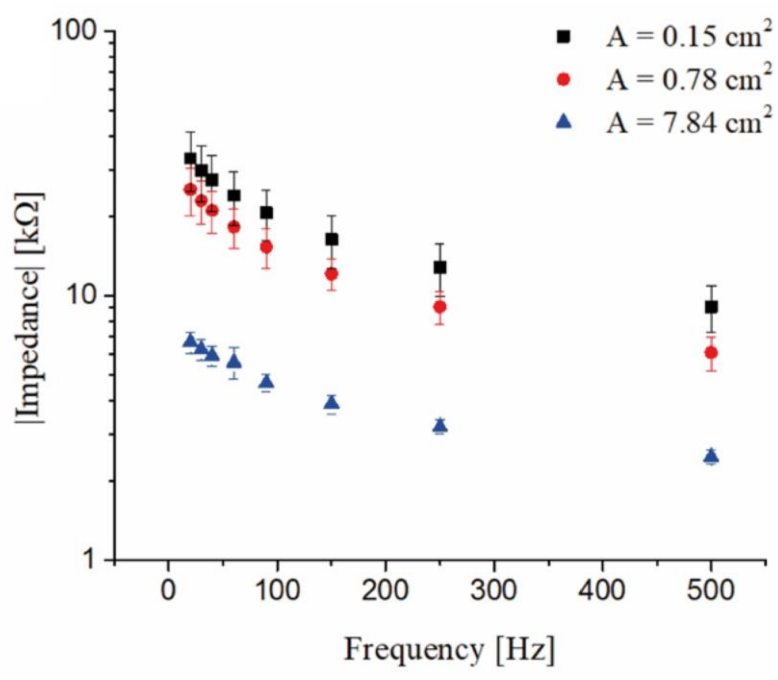

Figure 71 Average electrode-skin impedance evaluated for three different contact areas 7.84 cm^2, 0.78 cm^2, and 0.15 cm^2

4.3. Wearable custom electronic board

To developed a wearable acquisition system, a custom microcontroller-based PCB was fabricated with off-the-shelf components (COTS). The aim was to develop an efficient signal acquisition and simultaneously to obtain a low-size and low-power consumption electronic board. Specifically, the brain signals collected by the tattoo electrodes are acquired by means of a Texas Instrument 24-bit ΣΔ analog-digital converter ADS1299. Through the ADC, it is possible to turn off the undesired channels (each of which is composed of an instrumentation amplifier with programmable gain between 1 and 24), a feature that gives the system the flexibility to properly choose the number of recording channels according to the specific experiment. Moreover, the communication with a remote PC can be handled through Bluetooth and/or USB systems. The employed microcontroller is the MSP430F5529, that is a low-power microcontroller that manage the whole system. To feed the board, a 3.7 V–200 mAh battery able to give an estimated run-time of about 28 h was employed. Figure 72 reports the acquisition system.

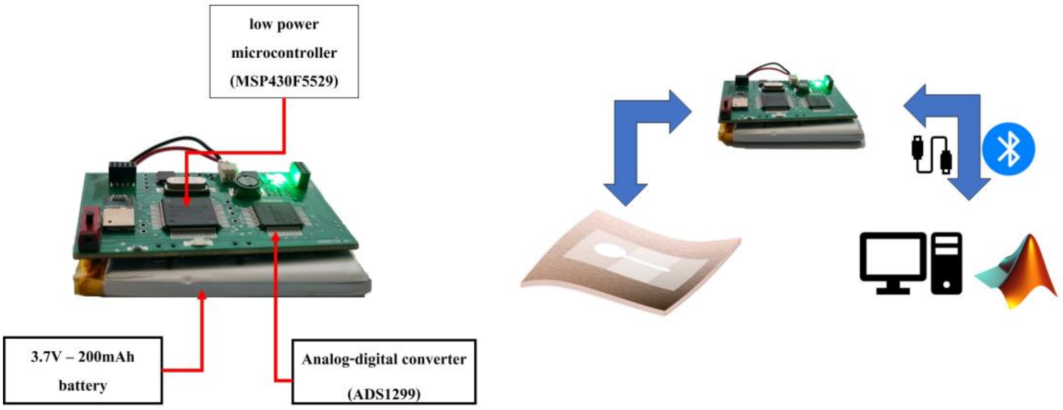

Figure 72 EEG signals acquisition system. The custom PCB acquired the signal detected by the Parylene C-based tattoo electrodes and transmit it to a computer using Bluetooth or USB connection. All the elaboration was done offline using MATLAB

4.4.EEG signal recording experiment setup and results

Portability and wearability were the main characteristics that fed the development of the EEG acquisition system. Therefore, the dry tattoo electrodes were placed according to the 10-10 standard.

To validate the system, a standard resting-state experiment was performed, and eyes-closed and eyes-open conditions were contrasted. The resulting performances were compared to that of the commercial wearable system MUSE headset (InteraXon Inc., Toronto, ON, Canada) [156]–[158]. Moreover, it was decided to mimic the configuration of this commercial system, thus five electrodes were positioned on the forehead and on the mastoid, respectively, on *AF7*, *Fpz*, *AF8*, *TP9* and *TP10*, as shown in Figure 73. The electrode on Fpz was used as a reference electrode and the other active electrodes were measured with respect to it, in a unipolar configuration. It is worth noting that this electrodes configuration allows to maximize the detection of the alpha waves, especially in the occipital region, and the beta waves, on the frontal lobe, according to physiology [159]. In order to reduce the power line noise, an interconnection with 0.3 mm diameter micro coaxial cables (Alpha Wire) were employed. This approach enabled the reduction of the power line artifacts, due to the shielding, while still having flexible wires that could be easily integrated into a low-cost commercial headband. Each wire ended with a thin metal contact (1 cm in diameter in this preliminary version of the system), which was positioned on the skin using a small piece of non-conductive and skin-friendly adhesive tape. The electrodes were simply placed face down with the recording area on the skin and the non-passivated final part on the metal contact. The obtained flexible and lightweight structure allowed an easy adaptation to the subject's head, thus guaranteeing comfort and portability. The headset was physically connected to the PCB using a standard multipin connector placed at the end of a custom cable, while the communication between the device and the PC was handled using a custom MATLAB® interface.

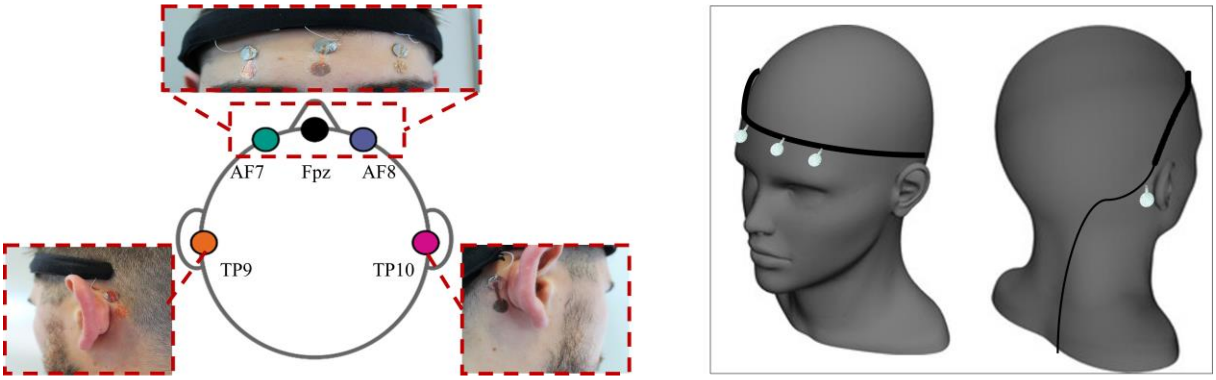

Figure 73 EEG signal acquisition setup. The electrodes are positioned following the 10-10 system where the electrodes placed in position AF7,AF8, TP9 and TP10 are measured with respect to the electrode in position Fpz, which was used as reference. The interconnection system was composed by a commercial headband in which 0.3 mm diameter five micro coaxial cables (Alpha Wire) were integrated with the aim to reduce the power line noise, thanks to the shielding, while still having flexible wires.

For both systems, i.e. the custom-made based on the Parylene C electrodes and the MUSE headset, the EEG traces were recorded from a single subject during two minutes of eyes-closed and eyes-open resting-state conditions.

Data were sampled at 250 sps, since it was the frequency rate for the MUSE headset, and elaborated offline using EEGLAB toolbox (version v2022.0) [160]. Some filtering steps were performed after the experimental sessions, both for the data measured using the wearable system based on the Parylene C tattoo electrodes and the data acquired with the Muse. In particular, A band-pass filter in the frequency range of 1-40 Hz to eliminate low-frequency drift and at the same time limit as much as possible the contamination of the signal due to muscle activity was applied, according to [161]. All the traces were successively inspected to remove residual artefactual segments. Figure 74 reports the signal acquired from the 4 electrodes where the typical EEG artifacts, namely eyes blinking and teeth grinding, are clearly notable. These signals ensured the correct positioning of the electrodes.

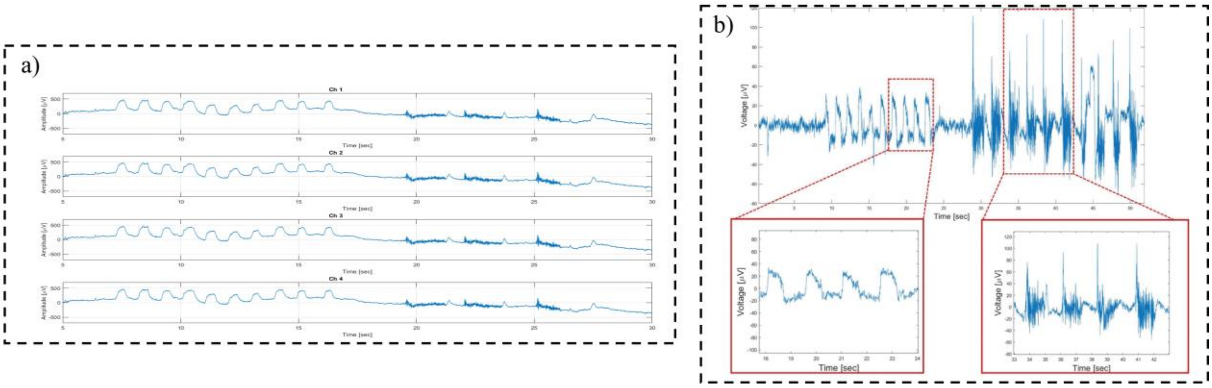

Figure 74 Signal recorded form the wearable system. a) 4 channels signals with eyes blinking (sec 7-17) artifacts and teeth-grinding (sec 19-26); b) magnification of an acquired signal with the typical noise is highlighted.

Since the Muse system has the reference channel located in correspondence to the Fpz position, which is not far from the frontal channels, asymmetric estimates compared with those evaluated using conventional montages had to be performed. Therefore, the frontal channel AF7 and AF8 were re-referenced to the TP9/TP10 mastoid electrodes [156].

The evaluation of the recorded neural activity and the derived spectral measures obtained with the tattoo electrodes were performed by comparing them with those derived from the MUSE headset. In particular, the reliability of the system and the capability to capture the differences between the two experimental conditions (namely, eyes-closed and eyes-open resting-state) were tested by performing the same analysis for signals detected by the tattoo electrodes and the signals acquired with the MUSE system.

Specifically, the power spectral density (PSD) was computed using the pwelch function in MATLAB R2021b (The MathWorks Inc., Natick, MA, USA) for each of the frontal EEG channels separately and, successively, the average between the two channels was computed and used for the statistical analysis. The analysis was performed using, for each system and each condition, eighteen EEG segments (epochs) free of artifacts of 5 s extracted from the filtered traces, as reported by Fraschini et al. [162]. Figure 75 reports an exemplifying time-course of the EEG traces for one subject. The channel spectra and maps for the two different acquisition systems (i.e. Tattoo and MUSE in the figure) in the two different experimental conditions, namely eye-closed (EC) and eyes-open (EO).

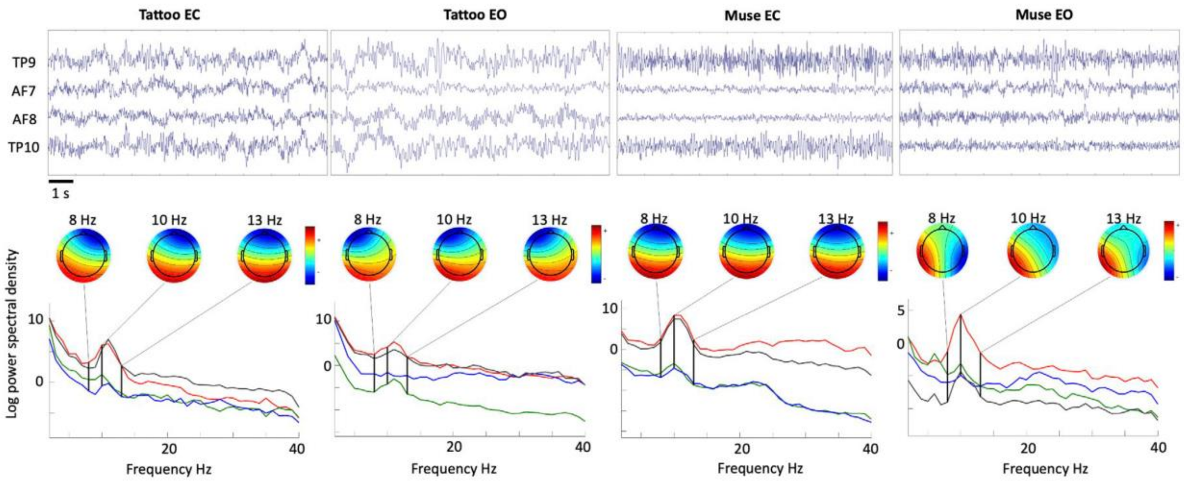

Figure 75 Exemplifying time-course of the EEG traces, channel spectra and maps for the two different acquisition systems and two different experimental conditions. EC and EO, respectively, refer to resting-state eyes-closed and eyes-open conditions. Each line represents a different channel, namely TP9 (red), TP10 (black), AF7 (green), AF8 (blue).

The acquisition system was then tested on other two healthy subject and Figure 76 reports the exemplifying time-course of the EEG signals and their channel spectral and maps. Also in this case, both tattoo-based acquisition system and MUSE systems are represented.

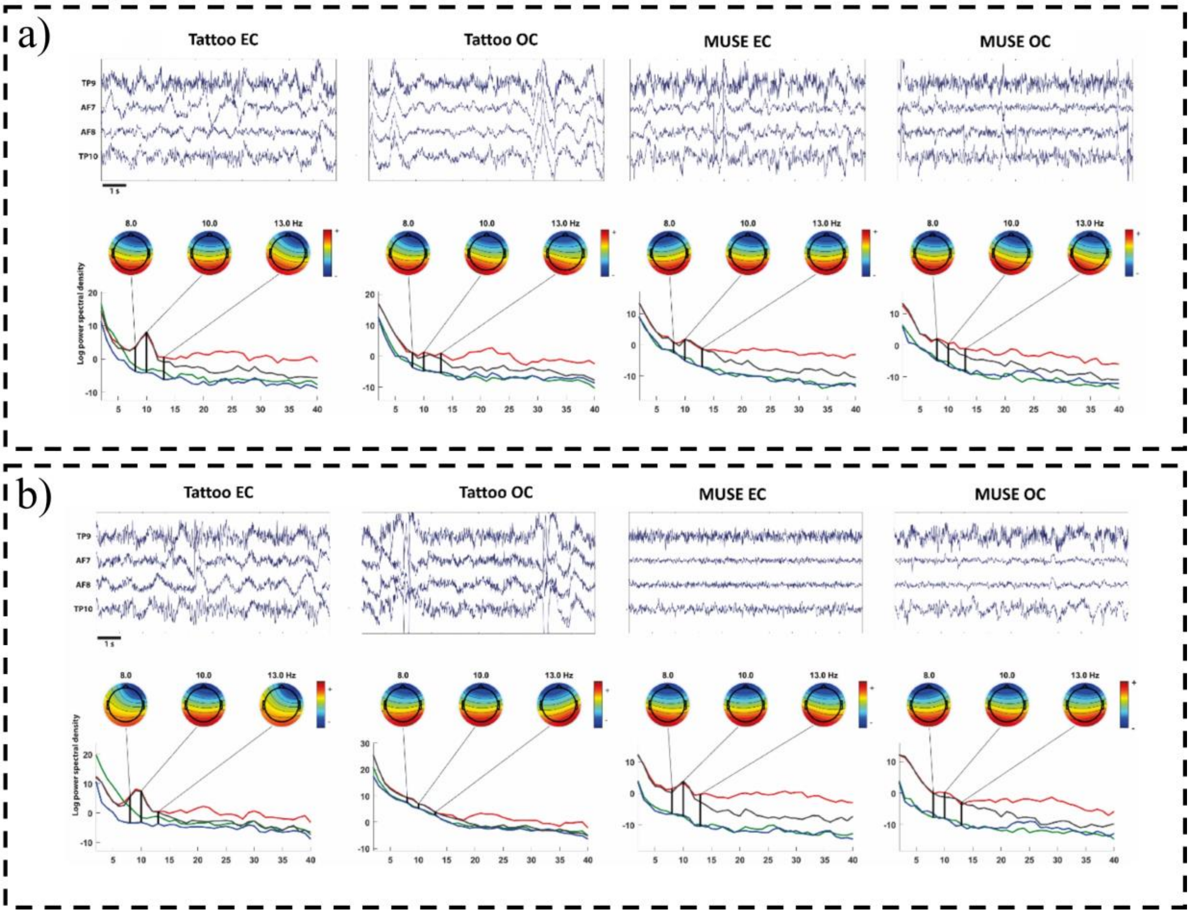

Figure 76 Exemplifying time-course of the EEG traces and channel spectra and maps for the two different acquisition systems and two different experimental conditions (resting-state eyes-closed – EC – and resting state eyes-open - EO), recorded from subject 2 (a)and 3 (b). Each line represents a different channel, namely TP9 (red), TP10 (black), AF7 (green), AF8 (blue).

JASP software (version 0.16.2—Apple Silicon) with a paired nonparametric Wilcoxon signed rank test was used to perform the statistical analysis and performed. The summary of the inference statistics, together with significance (p value threshold was set to 0.05) and effect size (rank-biserial correlation), are reported in Table 4 the two systems separately.

As reported in the table, the results showed an increase in the relative power spectral density during the eyes-open resting state conditions when compared to the eyes-closed conditions for both the proposed system ($z = -2.286$, $p = 0.021$) and the Muse headset ($z = -3.385$, $p < 0.001$). A slightly higher effect size for the Muse headset (−0.935) compared to the tattoo electrode-based system (−0.614) was observed. However, the two effects have the same direction, as expected.

Table 4 Summary and inference statistics for the two systems when comparing the two experimental conditions.

Wilcoxon signed rank test

Measure 1		Measure 2	W	z	p	Rank-Biserial Correlation
Tattoo - EC	-	Tattoo - EO	33.000	-2.286	0.021	-0.614
Muse - EC	-	Muse - EO	5.000	-3.385	< .001	-0.935

From the raincloud plots, showed in Figure 77, the underlying distributions of the relative power spectral density values for the two systems when contrasting the two conditions (namely, eyes-closed and eyes-open resting state) are reported. These results clearly show that the tattoo electrodes are able to detect the differences between the two tested experimental condition in a reliable way. Moreover, the wearable system does not really differ from the Muse headset, which were previously validated [156].

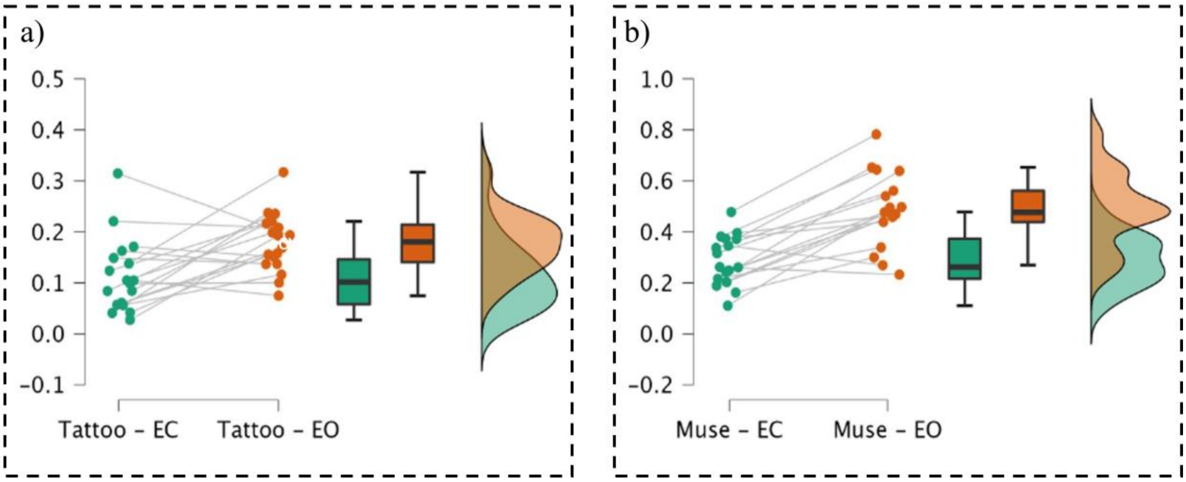

Figure 77 Raincloud plots for tattoo-based EEG system a) and the Muse headset b), with the underlying distributions of the relative power spectral density computed for the alpha frequency band.

Table 5 summarizes the characteristics of different wearable EEG systems and compares them with the proposed system. The Parylene C ultra-thin electrodes showed the possibility to be integrated into a portable custom PCB to developed a comfortable system for the acquisition of the EEG signal. The reduced thickness, the detection of brain waves, and the easy positioning of the electrodes allow the development of a discrete system capable of discriminating between two different states, which is the first step to producing human-interaction systems. Therefore, such system based on tattoo electrodes can pave the way to the production of a new generation of patient-centered EEG portable devices for applications such as non-invasive brain-computer-interfaces, for prosthetics control, and clinical neurophysiological studies.

Table 5 Comparison between several wearable EEG systems based on bioelectronic interfaces.

EEG recording systems	N° of recording channels	Electrodes Placement	Brain wave detected/ ERPs	Portability/Wearable acquisition system	Electrodes	Electrodes Thickness [µm]
This epidermal system	4	AF7, Fpz, AF8, TP9, TP10	Alpha and Beta	Custom portable PCB	Tattoo dry electrodes	0.7-0.8
J. J. S. Norton et al. [63]	1	Ear	P300 ERP	Bench amplifier	Tattoo dry electrodes	3
L. M. Ferrari et al. [43]	1	CZ - OZ T7 - CZ	Alpha N100	Bench amplifier	Tattoo dry electrodes	1.5
H. L. Peng et al. [64]	1	FP1	N100	Bench amplifier	Semi-Dry electrodes	1200
S.Shustak et al. [36]	4	F7, F8	Alpha, k-complexes and spindles	portable PCB	Dry electrodes	//
V. Goverdovsky et al. [57]	1	Ear	SSVEP ASSR	Bench amplifier	Cloth electrode	//
S. Debener et al. [58]	16	Ear	Alpha, Beta and ERPSs	SMARTING (mBraintrain) mobile EEG amplifier	Flexible printed electrodes	//

5. Chapter V: Ferrimagnetic/Conductive epidermal electrodes for Biopotential Recordings

This chapter proposed a solution for one of the open issue in the epidermal electronic filed. In fact, the interface between ultrathin functional films for epidermal applications and the external recording instruments or readout electronics still represents one of the biggest challenges in the field of tattoo electronics. First, the problem of interconnecting ultra-thin electrodes with bulk electronics will be presented. Some proposed solution at the state-of-the-art will be discussed, with a focus on the advantages and disadvantages. Afterward, the production process of a free-standing electrode made of a composite thin film based on the combination of the conductive polymer PEDOT:PSS and ferrimagnetic powder will be detailed described. The chapter will reports the film characterization and the ECG signal recordings through such epidermal electrodes [163].

5.1. Interconnection problem: possible solutions

One of the biggest challenges still present in the field of epidermal electronics is the interfacing of ultra-thin functional films with external rigid recording instruments or readout electronics circuits. Among the different applications, such as tactile sensors for artificial skin systems, epidermal sensors for biochemical analysis, and tattoo electrodes for biopotential recording, the interconnection with external readout systems for data acquisition and processing is a well-known problem. Generally, rigid and bulky connectors are used to collect the signal from the epidermal sensors thus strongly limiting the benefits from the use of imperceptible ultrathin devices. To overcome these limits, several techniques and approaches have been proposed over the years [164], [165], however, the use of magnetic interactions to build up the connection systems is one of the most interesting approaches.

In a recent work, Jang et al. [166] proposed a micro-structured conductive and elastic metallic mesh, which is folded around a magnetic rubber patch that can be connected using magnetic connectors. The fabrication process involved the use of soft composite materials and a layout with embedded magnetic materials in a folded configuration. As a result, the dry interface with the skin could be applied several times with a reversible magnetic coupling to perform different measurements. Moreover, the device was employed for the acquisition of several physiological signals, such as ECG, EMG, EOG, and EEG signals. Figure 78 a) shows the micro-structured conductive and elastic metallic mesh folded around a magnetic rubber and the biopotential signals acquisition set-up and recordings. Despite the interesting solution, this approach presents some limitations. In fact, the folded conductive and stretchable mesh gave rise to a thick ferrimagnetic electrode, that cannot be defined as conformal film. The use of the ferrimagnetic rubber core leads to a total thickness on the order of 500 μm. As a consequence, an adhesive layer must be used in order to ensure the adhesion between the electrodes and the skin.

Another interesting approach was developed by Taccola et al. [167] (Figure 78 b)). The authors proposed a free-standing PEDOT:PSS-based conductive films that can be connected with a magnet through a stretchable connection made of a silver ink–based glue. For the connection of the conductive film, the use of the soft and stretchable Ag ink enabled a robust interface between materials of different thickness and Young’s moduli, in particular, the PEDOT:PSS-based tattoo electrode, which was conformally attached to the skin and the polyimide film. In addition, the external magnetic connection allowed the communication with the external device.

This solution, although ultra-conformable and free-standing, cannot be directly connected using magnetic connectors. As a matter of fact, the film had to be connected to an external electronic device using a silver ink–based acrylic glue, that was needed to create a robust interface between the different materials involved. In addition, the magnets presented in the external device, glued on the opposite side of it, served the sole purpose of ensuring contact with the magnetic connector, which was placed on the top to allow electrical contact

Another different approach involving a magnetic connection was reported by Dai et al. [168], who proposed a very interesting functionalization and printing process to obtain flexible magneto–electrical interfaces, films but also flexible circuits. Concerning the films, the authors developed electrically conductive structures that exhibited good magnetic properties, that, however, cannot be defined as conformable. Moreover, such devices needed to be integrated with actual epidermal patches for their use as biomedical devices for the recording of biopotentials, thus acting more like an interface between the sensor itself and the communication circuit. In addition, in order to achieve the desired magnetic properties, a high-voltage step must be included in the fabrication process, thus making it not easily up-scalable.

Figure 78 c) shows the proposed approach developed by the authors and the application of the magneto–electrical films for the acquisition of biopotentials.

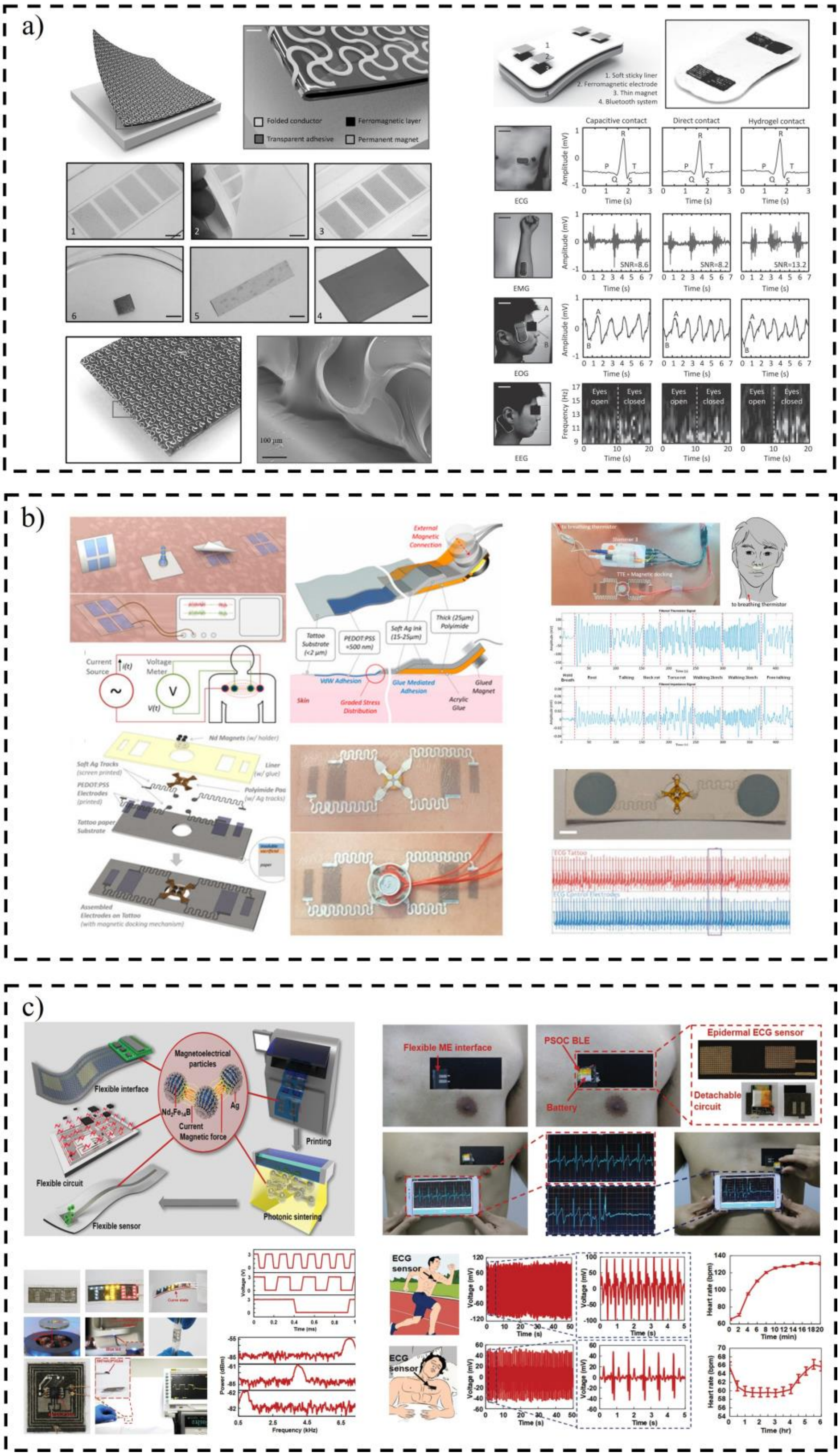

Figure 78 Magnetic-based approaches for the connection of the epidermal films with the external rigid electronic devices. a) Micro-structured mesh folded on a magnetic rubber proposed by Jang et al. [166]; b) free-standing PEDOT:PSS-based conductive films connected with a magnet through a stretchable connection made of a silver ink–based glue; c) Dai et al. [168] magneto–electrical films for the acquisition of biopotentials.

With the intent of overcoming the interconnection issues and thus providing an innovative approach for an epidermal electrode interface, during this thesis work it was developed a simple fabrication process to obtain ultrathin functional films that can be easily contacted using magnetic connectors. The core of this structure is the free-standing conductive and ferrimagnetic films based on a blend of the conductive polymer PEDOT:PSS and PVA, fabricated through an easy and low-cost technique.

5.2.Fabrication process

The composite films are made of a conductive PEDOT:PSS ink mixed with a PVA solution and ferrite powder, fabricated using a layer-by-layer process which alternates the PVA/PEDOT:PSS ink blend and the ferrite powder. The polymeric conductive ink was prepared by mixing 70% in volume of PEDOT:PSS (Clevios PH1000, by Heraeus, Hanau, Germany) with 30% in volume of ethylene glycol (by Merck KGaA, Darmstadt, Germany). Afterward, a Glycidyloxypropyl trimethoxy-silane—GOPS (by Merck KGaA, Darmstadt, Germany) was added to the conductive ink as cross-linker 1% (in volume of the previous blend). Separately, the PVA solution was prepared by diluting the PVA (molecular weight: 205 kg/mol) in de-ionized water (10% by weight). One of the main drawbacks of using PVA in this context is its well-known detrimental effect on the electrical properties of PEDOT:PSS. In order to maintain the advantages offered by the PVA without significantly compromising the electrical properties of the deposited layers, two different blends with different PVA solution percentages, namely 7% and 2% in volume, were employed in different steps of the fabrication procedure.

In particular, the fabrication process started with the spin coating of the PEDOT:PSS/PVA blend with 7% PVA (spin speed = 700 rpm, spin time = 60 s) on a PET substrate, which acted as a carrier (Figure 79 a)). The aim of this first step, in which the higher PVA concentration was used, consisted of helping the removal of the final film from the PET carrier. After the deposition of the first layer, the samples were baked at 75 °C for 20 min. Later, the ferrite powder was deposited over one half of the film in order to obtain a two-part electrode: a thin conductive part for an optimal skin interface, and a thicker portion both conductive and ferrimagnetic, which can be used for the magnetic connection. One of the most important aspect to be considered is that a good distribution of the ferrite powder must be achieve, in order to minimize the formation of big particle clusters. To achieve this, the ferromagnetic powder was deposited using a filter constituted by a thin perforated Parylene C film (thickness: 500 nm; hole diameter: 50 µm). Figure 79 b) reports this fabrication stage.

After the ferrite deposition, the PEDOT:PSS/PVA mix with the lowest PVA concentration (2% in volume) was spin-coated at spin speed equal to 700 rpm and spin time of about 60 s to form a second layer and then baked at 75 °C for 5 min. A lower PVA concentration allows retaining the PVA film-forming properties without significantly affecting the conductivity of the blend. The second and third steps of the process, i.e., ferrite deposition and subsequent PEDOT:PSS/PVA ink spin coating, can be repeated several times in order to achieve the desired mechanical and conductive properties (Figure 79 c)). After the last PEDOT:PSS/PVA deposition, the sample was baked at 75 °C for 20 min to ensure the complete evaporation of the solvent.

To obtain an optimal mechanical strength due to the ferromagnetic part and a sufficiently high conductivity to form a good interface with the skin, each electrode consisted of nine layers with same planar size of 15 mm × 40 mm.

Finally, with the aim to further minimize the contact resistance between the ferrimagnetic-conductive part of the film and the external magnetic connection, a thin Ag layer of about 50 nm was thermally evaporated over the portion of the film containing the ferrite particles (Figure 79 d)).

It was noticed that this step allowed a great improvement of the electrical connection of the film with the flat, rigid magnetic connector. In fact, as the film is placed onto an uneven substrate (the human skin), it exposes a limited number of contact points, thus demanding a decrease in the specific contact resistance of the film with the magnet. Figure 79 e) summarized the materials employed and the perforated Parylene C based-nano film.

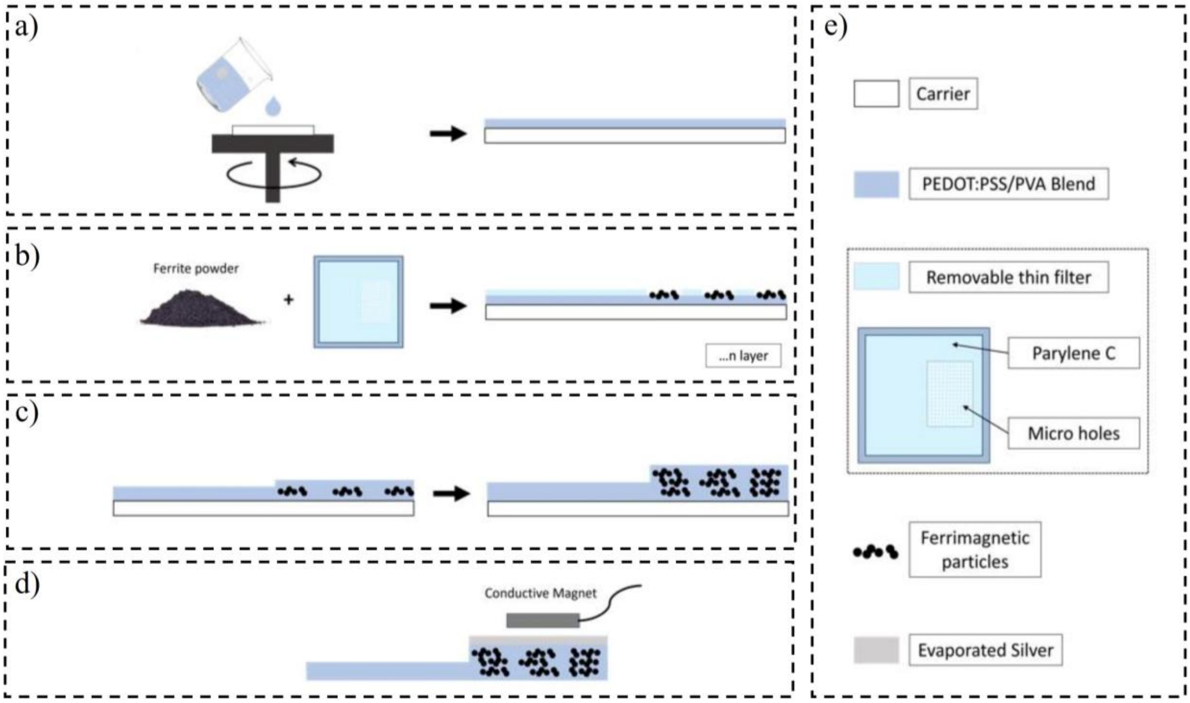

Figure 79 Conductive-magnetic composite film fabrication process. a) PEDOT:PSS/PVA blend with 7% PVA deposition through by spin coating on the PET carrier; b) the ferrite powder was deposited over one half of the film using a filter constituted by a 500 nm thick perforated Parylene C film having holes diameter of about 50 µm; c) spin coating of a second conductive layer and ferrite powder deposition thus obtaining a thicker ferrimagnetic-conductive portion; d) thin Ag layer evaporation onto the ferrimagnetic-conductive portion of the film in order to improve the magnet–film interface; e) materials employed and the perforated 500 nm thick Parylene C filter with holes diameter of 50 µm.

After the fabrication process, the film can be eventually peeled-off from the PET carrier and placed on a piece of paper using a few droplets of deionized water, to easily handle the positioning on the body, in fact from here it can be conveniently transferred onto the skin.

It is worth noticing that the final electrodes were thus characterized by a thin part (the one without the ferrite powder), which offers an optimal interface with the skin, and a thicker one, i.e. the conductive and ferrimagnetic part for the magnetic interconnection.

From the morphological investigation on the two portions of the film, performed by means of atomic force microscopy (AFM), an estimated RMS roughness of 3.8 nm for the ultrathin-conductive part and 120 nm for the ferrimagnetic-conductive part were obtained. Both images were performed in semi-contact mode. Figure 80 shows the ferrimagnetic-conductive electrode after the deposition on a piece of standard paper, with the thin, conductive part for an optimal skin/electrode interface and the thicker part, both conductive and ferrimagnetic for the magnetic connection. In the inset, the AFM micrographs of both film areas are reported. The ferrimagnetic-conductive electrode can be easily hung with a magnet after the peel-off from the PET carrier.

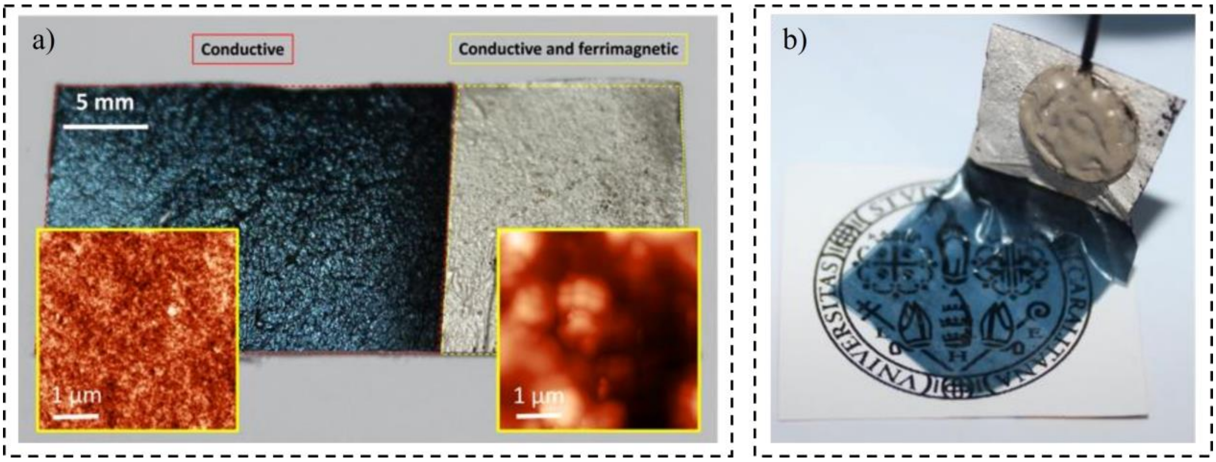

Figure 80 a) optical image of the ferrimagnetic-conductive electrode after the deposition on a piece of standard paper. Both thee thin, conductive part (developed for an optimal skin/electrode interface) and the thicker part, (developed with the aim to obtain a conductive and ferrimagnetic film for the magnetic connection) are highlighted. In the inset: AFM micrographs of both film areas; b) A ferrimagnetic-conductive electrode hanging from a magnet after the peel-off from the PET carrier.

5.3.Film characterization

The composite film were characterized in terms of thickness, magnetic force of interaction, and conductivity.

5.3.1. *Thickness characterization*

The thickness of both the conductive and the ferrimagnetic-conductive portions of the films was evaluated after each layer deposition using a profilometer (Dektak XT by Bruker, Billerica, MA, USA).

For a nine-layer electrode, the thickness of the ferrimagnetic-conductive part was around 30 µm, while the thin conductive part was around 3 µm thick. The first ensured a sufficiently magnetic strength, while the latter enabled a good skin/electrode interface without the use of any adhesive layer (Figure 81).

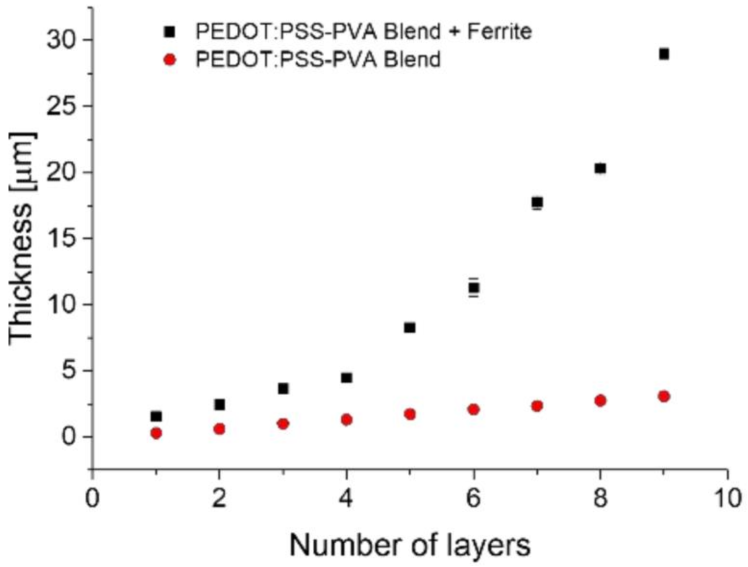

Figure 81 Thickness characterization of the epidermal electrode. For a nine layer electrode, the thin conductive film resulted in a thickness of about 3 µm (in red), while thickness of the ferrimagnetic-conductive part was around 30 µm (in black).

5.3.2. *Magnetic Force of Interaction*

The attractive force of interaction between the film and the magnet was evaluated by means of a commercial dynamometer (FCA-DS2-50N by IMADA, Northbrook, IL, USA) mounted on a vertical motorized stand (MX2 by IMADA, Northbrook, IL, USA).Figure 82 a) shows the setup employed to measure the attractive force of interaction. Specifically, a magnet was glued to the end of a flat indenter and placed in contact with the film (as it is shown in the inset). The indenter was then slowly moved away from the surface of the film and the subsequent attraction force was recorded right before the magnets detaches from the film. In Figure 82 b), the quantification of the interaction of the conductive-ferrimagnetic part versus number of layers is presented. For a nine-layer electrode, the maximum measured pressure (a parameter that gives an indication on the magnetic force of interaction) was 12 g/cm^2, with an average of 9 g/cm^2.

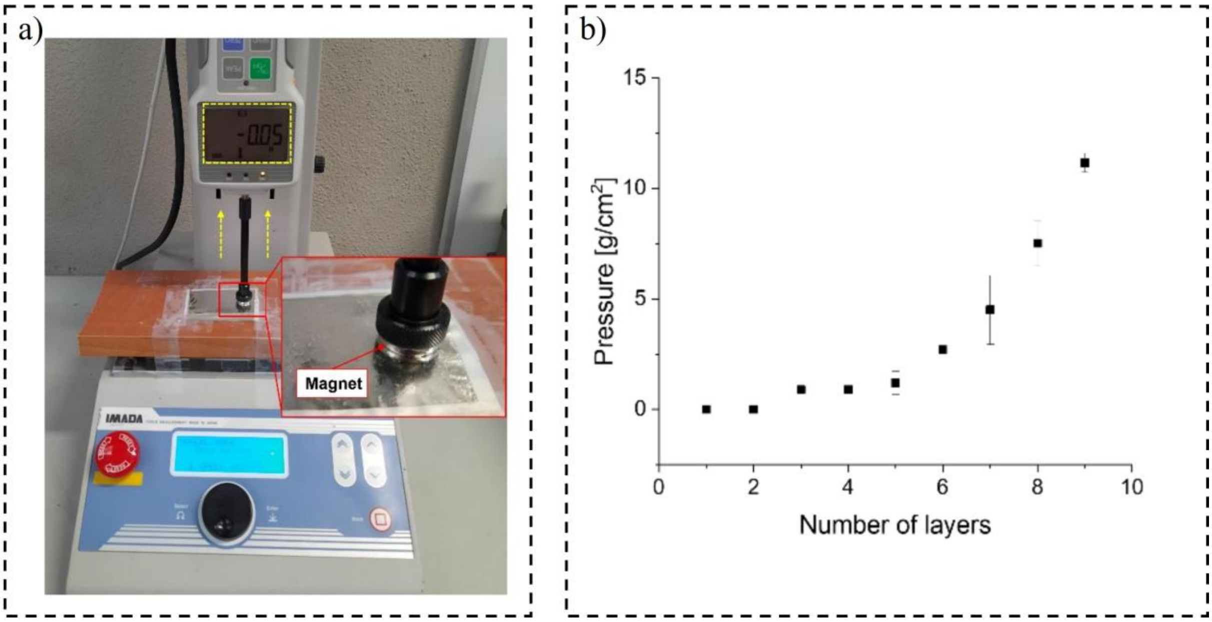

Figure 82 Magnetic force of interaction measurement. a) acquisition setup, where in the inset it is possible to notice the magnet glued on the flat indenter and placed in contact with the film; b) quantification of the interaction of the conductive-ferrimagnetic part, expressed as pressure over area [g/cm^2] versus number of deposited layers.

5.3.3. *Conductivity characterization*

The conductivity of both the conductive and the ferrimagnetic-conductive part of the structure was evaluated before the silver deposition using a 4284A LCR-meter (by Agilent, Santa Clara, CA, USA). The probes were placed at a lateral distance of 10 mm, one on the top face and one on the bottom face of the film in order to consider the contribution of both the vertical and the planar conductivity. This aspect is very important since, in the proposed approach, the external connector is placed on the opposite side with respect to the skin/electrode interface, thus the vertical conductivity must also be adequate for this application. The average conductivity of the thin conductive part was 8.7 ± 0.2 S/cm, while that of the ferrimagnetic-conductive part was 3.2 ± 0.1 S/cm. As expected, the presence of the non-conductive ferrimagnetic particles slightly reduced the conductivity of the ferrimagnetic part. However, the conductivity of the thin conductive part is in line with that already reported for other PEDOT:PSS-based epidermal films [169].

5.4.ECG signal measurement

In order to evaluate the suitability of the composite conductive-ferromagnetic films for biopotential recording applications, the performances achieved by the ferrimagnetic-conductive epidermal electrodes were compared to that of disposable gelled Ag/AgCl electrodes

(BlueSensor N by Ambu, Ballerup, Denmark). Specifically, an ECG signal was acquired on a healthy volunteer using a 32-channel Porti7 electrophysiological recording system (TMSi, EJ Oldenzaal, The Netherlands) at a sampling frequency of 2048 Hz, with an effective bandwidth of 553 Hz. The experimental protocol was conducted following the principles outlined in the Helsinki Declaration of 1975, as revised in 2000. The two electrode types were exploited for the recording of an ECG signal, simultaneously and repetitively, thus providing a total of seven 30 s long ECG traces in about one hour. The ferrimagnetic-conductive electrodes were contacted using custom-made magnetic connectors with a snap contact for the connection to the instrument shielded cables, as shown in Figure 83. To better appreciate the QRS complex in the recordings, lead II was chosen for all ECG signal acquisitions following a Holter configuration. As such, the LL electrode was placed on the left anterior axillary line, the RA electrode was placed slightly under the right manubrium, and the ground electrode was placed near the right hip. The electrode pairs were arranged on the torso in order to preserve the inter-electrode distance, thus avoiding any mismatch in signal amplitude and morphology.

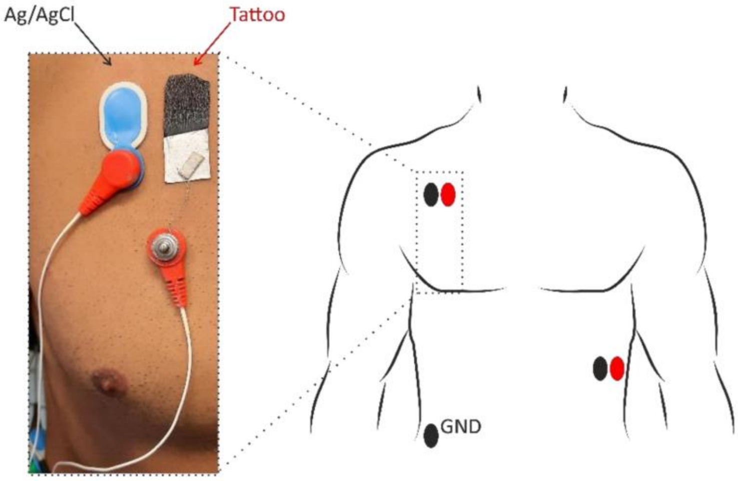

Figure 83 ECG signal acquisition setup. Tattoo electrodes are in red, while disposable Ag/AgCl electrodes are in black in the schematic.

ECG detection performance was evaluated in terms of signal-to-noise ratio (SNR), entity of baseline wandering (BW) artifact, and cross-spectral coherence (SpCoh) between the new ferrimagnetic-conductive electrode and the commercial Ag/AgCl one. Specifically, the SNR estimation was carried out after removing all low-frequency interferences by digitally filtering each signal by a zero-phase 2nd-order IIR Butterworth high-pass filter with cut-off frequency of 0.67 Hz. SNR was evaluated from the ration between the peak-to-peak amplitude of the median beat template and four times the noise standard deviation estimated on the central isoelectric segment of each T-P interval (reported in dB), as shown in equation$SNR[dB] = 20\log_{10}\left(\frac{A_{pp}}{4\sigma}\right)$ (3) of the Chapter III. BW was quantified as the root mean square (RMS) value of the residual of each ECG signal below 0.67 Hz. Figure 84 reports the scheme of the overall signal analysis.

In the frequency domain, the similarity of the ECG recordings acquired with the two electrode types was assessed by the magnitude-squared SpCoh. This figure of merit was estimated for each pair of simultaneous ECG recordings acquired by Ag/AgCl and ferrimagnetic-conductive epidermal electrodes as:

$$SpCoh = \left|P_{xy}^2\right|/(P_x P_y) \tag{4}$$

where which P_x and P_y represent the power spectral estimates for the signal x and y respectively, whereas P_{xy}^2 is the cross power spectral estimate of x and y. As such, the more the SpCoh approaches 1, the higher the similarity between the signals x and y.

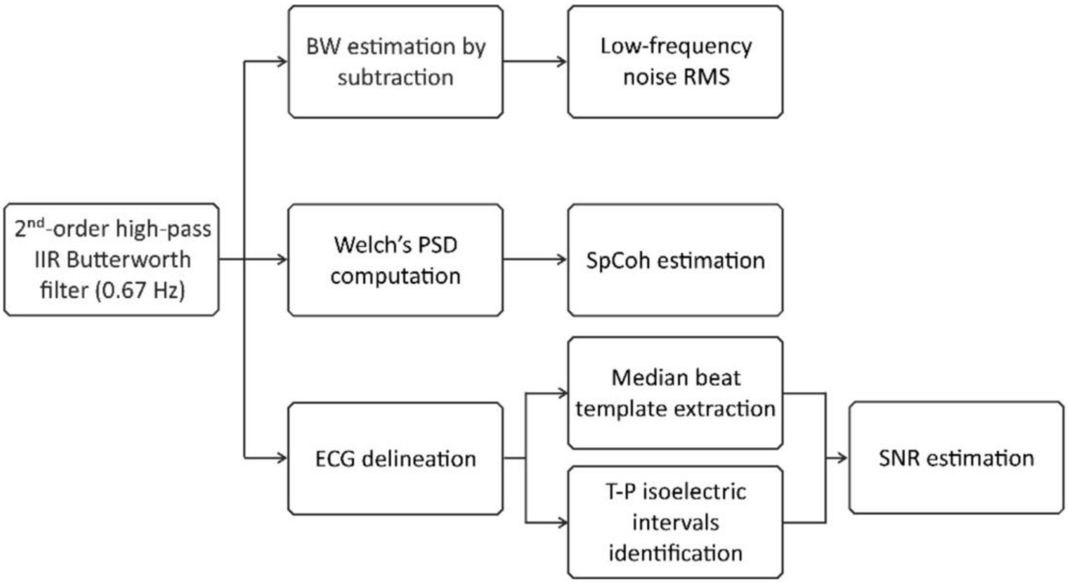

Figure 84 Processing chain of the ECG signals. After the acquisition, the signals are firstly high-pass filtered by a digital zero-phase 2nd-order IIR Butterworth filter with cut-off frequency at 0.67 Hz. After that, on the one hand, the SNR is computed by performing ECG delineation to identify a median beat template and the central portion of T-P isoelectric intervals, while on the other hand, the cross spectral coherence is analyzed by considering Welch's overlapped averaged power spectral densities (PSDs). Finally, BW is quantified by subtracting the high-pass signal from the corresponding raw signal and evaluating the RMS.

The skin–electrode impedance of the films was evaluated every 10 min for one hour during the ECG recording session with an electrode impedance meter (EIM105-Prep-Check by General Devices, Ridgefield, NJ, USA, operating frequency: 10 Hz). In particular, the epidermal electrode impedance was acquired with respect the parallel of five Ag/AgCl commercial pre-gelled electrodes, following the same acquisition set-up previously reported.

Figure 85 reports the results of skin–electrode contact impedance (a), SNR (b), and BW (c) during the recording session fir both the electrodes involved. As can be seen, no trend revealing increasing or decreasing values of SNR and BW could be appreciated over time, even though the skin–electrode contact impedance slightly increases over time.

Interestingly, the proposed ferrimagnetic-conductive epidermal electrodes showed a skin–electrode contact impedance comparable to that of other ultra-conformable tattoo electrodes describe in the Chapter 3, paragraph 3.2.

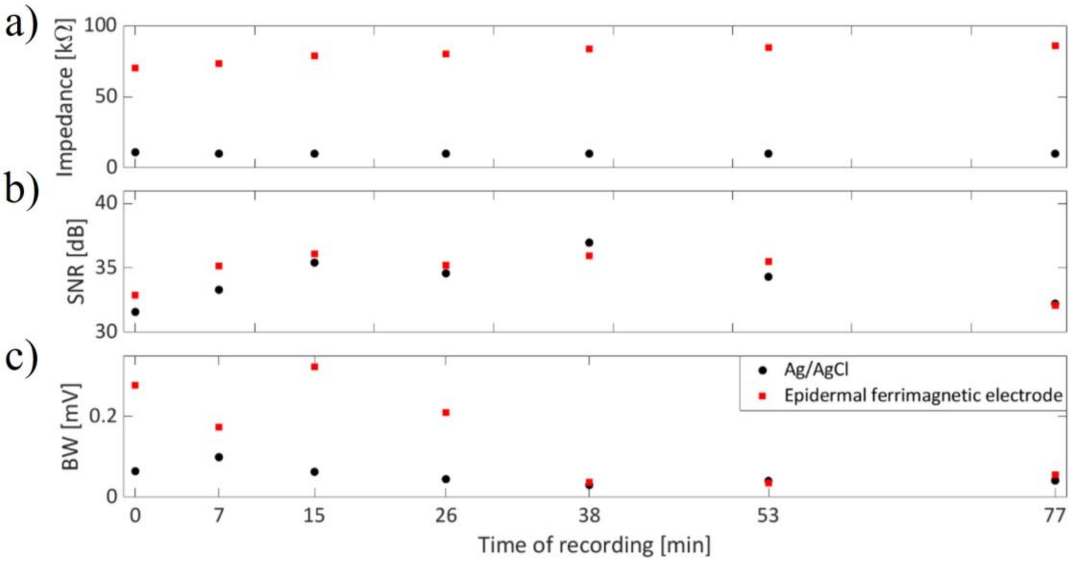

Figure 85 Analysis of the performances of the epidermal ferromagnetic electrode (in red) for a) the skin–electrode contact impedance, b) SNR, and c) BW, compared with respect the Ag/AgCl electrodes (in black) and valuated at the different recording times. The 0 min time of recording refers to the first ECG acquisition, while the last time of recording (77 min) refers to the last recording session, which was performed on the same subject, after 77 min.

The time-domain characterization of the electrodes is reported in Figure 86. It worth noticing that the ferrimagnetic-conductive epidermal electrodes suffer from higher BW artifacts and have higher contact impedance, if compared to the Ag/AgCl electrodes. Nevertheless, the SNR values obtained by the ferrimagnetic-conductive epidermal electrodes are comparable or even higher than those achieved by the gelled Ag/AgCl ones (Figure 86 b)). In this regard, some slight amplitude differences can be appreciated in the ECG recordings acquired with the different types of electrodes, which can be ascribed to the different sensing area sizes and the close (but not identical) electrode placements. Remarkably, ferrimagnetic-conductive epidermal electrodes allowed recording very high-quality ECG signals even after being applied to the skin for more than one hour (Figure 86 d)).

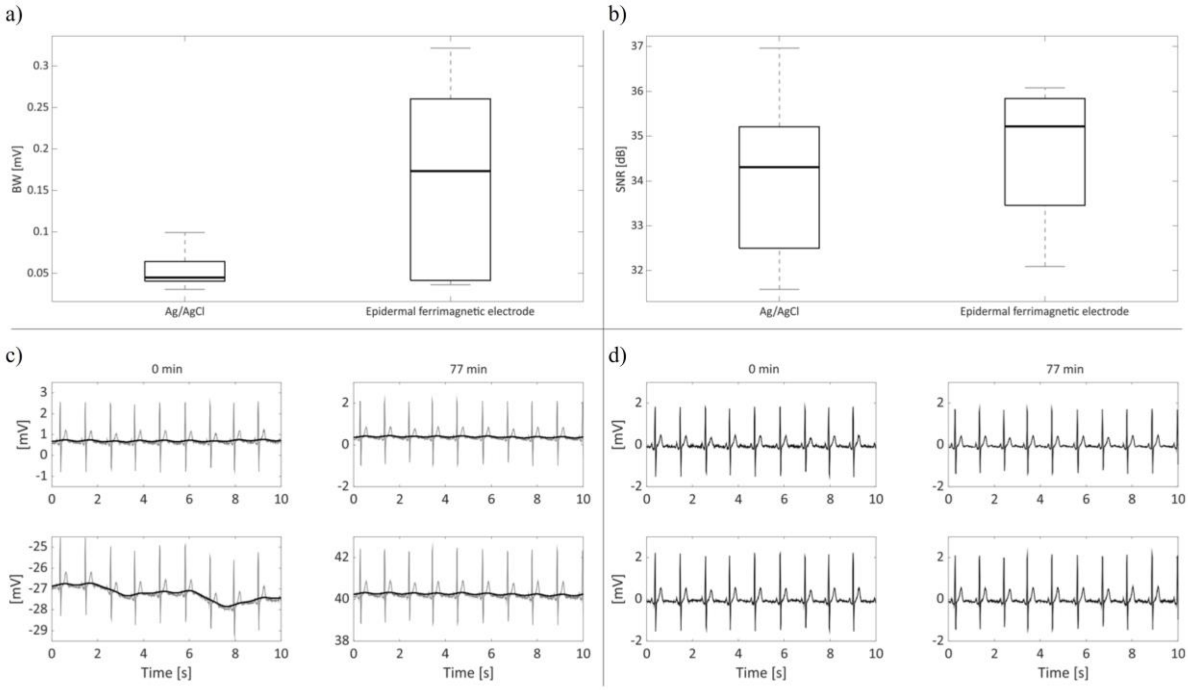

Figure 86 Time-domain performances characterization of the epidermal ferromagnetic electrodes. a) BW and b) SNR computed values for the epidermal and the Ag/AgCl electrode; c) raw ECG signals (in grey) recorded at the first (i.e., 0 min, left column) and last recording sessions (i.e., after 77 min, right column) with the corresponding BW artifact (in black) for the Ag/AgCl and the ferrimagnetic-conductive epidermal electrodes; d) filtered ECG signals recorded when the recording session started (0 min, left column) and at its end (i.e., after 77 min, right column) for both Ag/AgCl electrodes and epidermal electrodes

The results of the frequency–domain analysis are reported in Figure 87. Specifically, ECG signals recorded with the ferrimagnetic-conductive epidermal electrodes and gelled Ag/AgCl electrodes showed high coherence, well represented by the SpCoh (Figure 87 a)) below 30 Hz, while in the range between 30 and 40 Hz, low SpCoh values were obtained. Nevertheless, the power contributions in that specific band were found to be negligible (i.e., about 10^{-5}), as can be seen in Figure 87 b). Remarkably, the main PSD peaks reflecting the physiological contributions of heart rate, T wave, P wave and QRS complex are also well represented in all the different recordings.

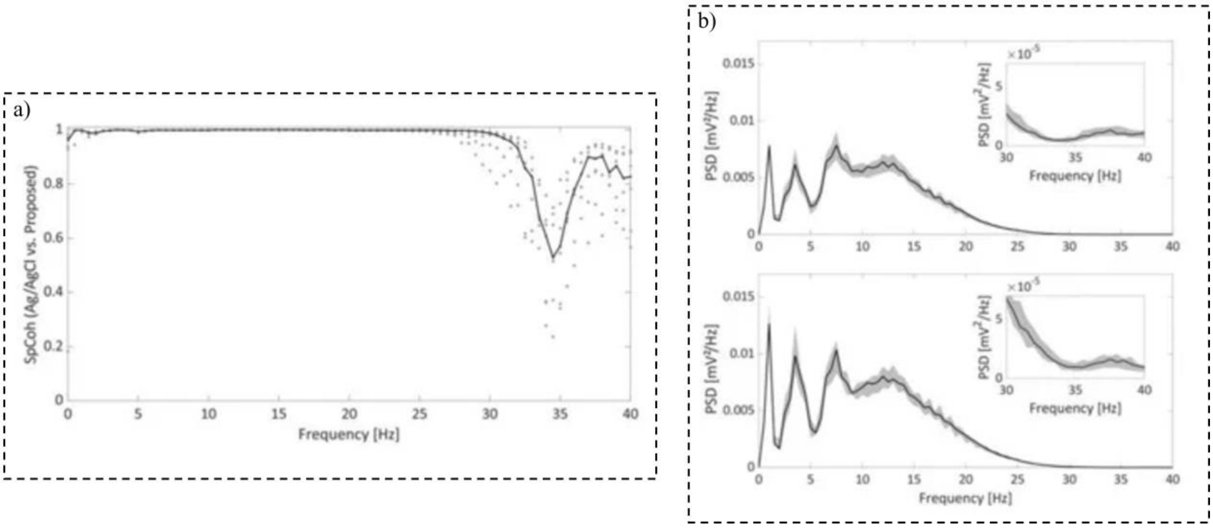

Figure 87frequency-domain analysis. a) SpCoh results obtain from the comparison of the recorded signals acquired by gelled Ag/AgCl and ferrimagnetic-conductive epidermal electrodes. Black line represents the median values of SpCoh across frequencies, whereas grey dots represent the values assumed in the different recording sessions; b) the median PSD trends (in black) with their 5th and 95th percentiles (grey shading) are depicted for the recordings with Ag/AgCl (top) and the ferrimagnetic-conductive epidermal electrodes (bottom), along with an enlarged depiction of the 30–40 Hz range.

6. Chapter VI: High-performing transistors for wearable electronics

Many fields could benefit from flexible and low-cost organic transistors, especially in real application scenarios. In the context of wearable electronics, an all-integrated approach can have different interesting advantages. For example, since the biological signals are usually weak (on the order of microvolts to millivolts), components such as amplifiers or filters are fundamental. In addition, such signals have to be transferred because the front-end processing circuits are located away from the source of the signal and thus, as a consequence, the signals are affected by noise artifacts. In this application, the role of organic transistors can be crucial because they can provide direct signal processing (such as amplification or filtering stages) close to the recording site and suppress the effects of transmission noise.

In addition, the wearable electronics field might exploit the use of cost-effective electronic tags that can enable the link to smart objects. Therefore, highly performing devices are required to intercommunicate and exchange continuous information in real-time at high frequencies (i.e. from MHz to GHz). However, such frequency range is still largely prohibitive for organic OFETs, especially when scalable, large-area processes must be adopted. In fact, up to now, the development of OFETs is mostly limited to those fields where a fast response is not strictly necessary. Reducing the channel length (L) is one of the most commonly employed approaches to enlarge the transistor form factor and thus developed high-performing transistor. Such method have been successfully adopted by standard MOSFET technologies along the years, leading to a continuous miniaturization of the silicon-based transistor area and, as a consequence, to the increase of the density of devices per unit area, as well as the maximum operating frequencies. Nevertheless, scaling the transistor channel length generally requires sophisticated fabrication techniques that can negatively impact on one of the main advantages of organic semiconductors-based technologies, i.e., the possibility of fabricating flexible circuits at low costs and high-throughputs [170]. *This chapter aims to describe the structure and the fabrication process of a new implementation of the organic transistor as a building block for the development of electronic circuits for wearable applications where an all-integrated approach is implemented. Particularly, there will be a description of the fabrication process of the vertical channel transistor, in which the step-edge structure is the core of the* *device* [171], *with a focus on the optimization process of the device architecture. In addition, both static characteristics and frequency response will be reported.*

6.1. Device structure and fabrication process

The proposed device developed during this thesis work is a Bottom-Contact Top-Gate (BCTG) step-edge short-channel OFET based on a Parylene C spacer. Figure 88 shows the schematic cross-section of the transistor architecture. Differently from the coplanar transistor, in which the channel develops along the horizontal plane, vertical transistors present source and drain contact vertically separated and thus the channel is perpendicular with respect the substrate. Specifically, the Parylene C step-edge creates the orthogonal separation between the contacts.

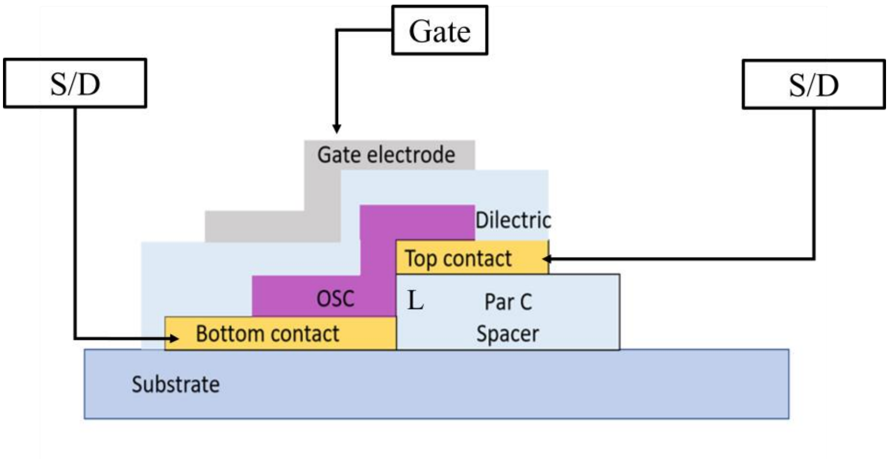

Figure 88 Bottom-Contact Top-Gate (BCTG) step-edge short-channel OFET based on a Parylene C spacer developed during this thesis work. Bottom and Top contact are source and drain electrode, vertically spaced through a Parylene C layer, whose thickness defines the channel length. The organic semiconductor (OSC) is sandwiched between the dielectric and top gate electrode and the step-edge structure

In this work, in order to develop the device structure and optimize the production process, different materials were employed. However, the fabrication process workflow followed the same stages layer by layer.

All devices were fabricated onto a plastic carrier and both polyethylene terephthalate (PET) and polyethylene naphthalate (PEN) substrate were employed. The fabrication process started with a first gold contact (bottom contact from now on) deposition by thermal evaporation directly onto the plastic substrate. Then, the gold film was patterned through a low-resolution photolithographic process. Afterward, a Parylene C spacer was deposited on the whole substrate by chemical vapor deposition (CVD) at room temperature. Such a layer defines the channel length within its thickness. In order to develop a robust transistor with a high yield and performance, such a spacer was between 300-350 nm thick.

On top of the spacer, a second gold contact (top contact from now on) was deposited and then patterned through a low-resolution photolithographic process, in partial overlap (5–20 µm range) with the bottom contact. These two contacts will act as source and drain of the transistors. In order to form the channel, a dry etching technique were exploited. Specifically, the substrate was exposed to oxygen plasma (200 W for 4 minutes) in order to etch the Parylene C from everywhere but under the top contact, thus exposing the bottom contact. The top contact acted here as a mask, making this step self-aligned. It is worth to mention that to prevent the top contact from being exposed too long to high-power oxygen plasma, the photoresist previously deposited and patterned was left in place during the process and removed after the plasma step using acetone.

After the fabrication of the source and drain electrodes, the substrates were cleaned with isopropanol and oxygen plasma (100 w for 60 s). From this stage, the organic semiconductor was deposited onto the vertical channel. In order to optimize the device structure and achieve high-performances, during this thesis, three different materials were employed, namely 6,13-Bis(triisopropylsilylethynyl)pentacene (Tips-pentacene), acting as a p-type semiconductor, and the ActivInk N1400 and the P(NDI2OD-T2 (Polyera ActivInk N2200), acting both as n-type semiconductors.

In particular, the Tips-pentacene (1 % in anisole) was deposited by drop casting directly over the transistor channel and then let dry at 70 °C on a hot plate. The ActivInk N1400 (1 % in dichlorobenzene) was deposited by spin coating (1500 rpm for 45 s) and afterward annealed at 120 °C for 30 min. Differently, the Polyera ActivInk N2200 (7 g L^{-1} in mesitylene) was deposited by off-centered spin-coating, and annealed at 120 °C for 30 min. It is worth to report that the surface of the electrodes was functionalized using a self-assembled monolayer of dimethylamino(benzenethiol) (DABT) right before the deposition of the semiconductor. This functionalization is known to promote an efficient charge injection of electrons into the semiconductor for n-type devices by lowering the work-function of gold [172].

The next step consisted in the deposition of the dielectric layer. Particularly, for the Tips-pentacene- and the ActivInk N1400-based transistors, 200 nm-thick film of Parylene C was deposited through CVD. Differently, for the Polyera ActivInk N2200-based transistor the dielectric film was composed by a thin spin-coated poly(methyl)methacrylate (PMMA) layer (50 nm) and a thicker chemical vapor deposited Parylene C layer (240–260 nm). Finally, the top gate was deposited on top of the device structure. Both Tips-pentacene- and ActivInk N1400-based transistor presented a thermal evaporated top gate, while for the Polyera ActivInk N2200-based transistor the transistor top gate (line width, L_W = 30 µm) was obtained by ink-jet printing of a gold ink (DryCure Au-J 1010B) and annealed at 120 °C for 1 h.

Figure 89 reports the complete fabrication process of the vertical-channel organic transistor.

The use of different materials, here reported, was meant to obtain a high-performance organic transistor within an optimization process of the device developed during this thesis work. However, all the methods employed exploited a low-resolution and low-cost production process, with an up-scalable approach.

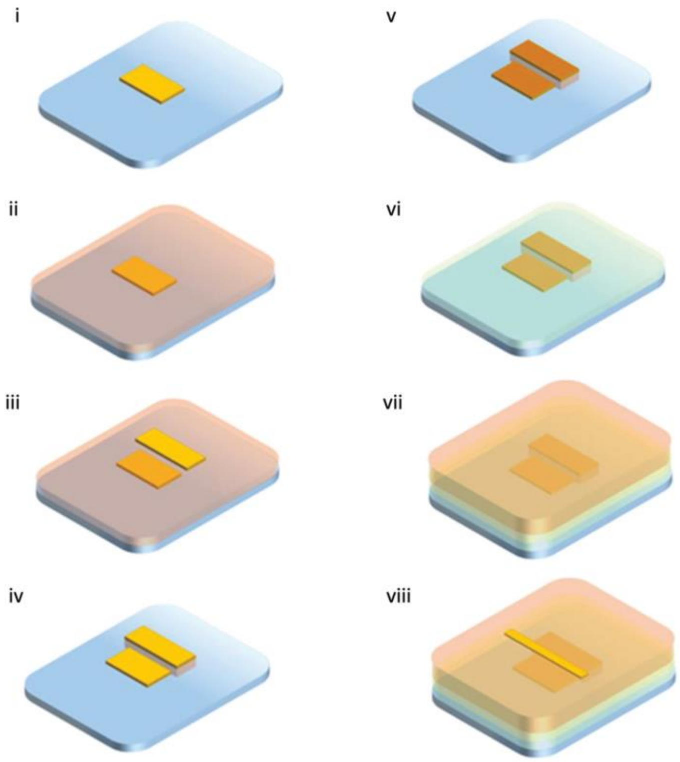

Figure 89 Fabrication process workflow for the vertical channel organic transistor. The first step was the deposition of the (i) bottom gold contact, followed by (ii) the spacer film and the (iii) deposition and patterning of the top gold contact. This two mentalization will act as source and drain contacts of the transistor. Afterwards, the substrate was exposed to the plasma oxygen (200 W for 4 minutes) thus (iv) creating the channel of the transistor, whose thickness is defined by the spacer thickness. In order to report a complete description of the fabrication process workflow, the electrode functionalization with (DABT) is reported (v). On top of the gold contact, (vi) the semiconductor was deposited, followed by the deposition of the (vii) dielectric layer and the (viii) top gate contact.

6.2.Electrical characterization set-up

Both DC and AC electrical characterizations were performed to acquire the transfer and output characteristic curves of the devices and its frequency behavior. From that, the static electrical parameters were extrapolated, as well as the transition frequency.

6.2.1. *DC electrical characterization*

To perform the static electrical characterization, two different acquisition instrument were employed: the Keithley SourceMeter 2636 A (Figure 90 a)) and the B1500a semiconductor device parameter analyzer from Keysight (Figure 90 b)). The SourceMeter 2636 A was connected through a GPIB bus to an external PC, which allows to control the whole acquisition set-up via software. Particularly, a MATLAB Graphic User Interface (GUI) was employed to set electrical parameters for the correct acquisition of the device output current. On the other side, the B1500a is an all-in-one device characterization, with a modular architecture. The system is controllable through a EasyEXPERT group+ software.

Acquisitions were performed both in the linear region and in the saturation region of the device.

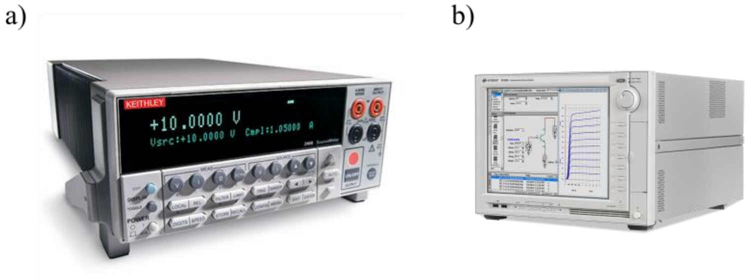

Figure 90 Employed instruments for the static electrical characterization. a) Keithley SourceMeter 2636 A and b) the B1500a from Keysight

From the static characterization curves it is possible to extrapolate both the field effect mobility (μ) and the threshold voltage (V_{th}). Therefore, depending on the region in which the transistor was measured (i.e. linear or saturation region), it is necessary to consider both the equation.

6.2.2. *Linear region*

For the linear region the output current can be described as:

$$I_{DS} = \frac{W}{L} C_i \mu \,(V_{GS} - V_{TH}) V_{DS} \tag{5}$$

considering the simplify version in which V_{DS} is sufficient small.

This equation has a linear behavior with respect to the V_{GS}. A possible method to extrapolate the electrical parameters is the following one:

the intercept (q) and angular coefficient (m) of the measured curve can be easily computed. From these, it is possible to derive the threshold voltage V_{TH} as the opposite of the ratio between the q (intercept) to the m (angular coefficient):

$$V_{TH} = -\frac{q}{m} \tag{6}$$

while the mobility of the device can be calculated as:

$$\mu = \frac{m}{\frac{W}{L}C_i V_{DS}} \tag{7}$$

in which V$_{DS}$ was fixed during the measurement and $\frac{W}{L}$ C_{ins} are the design parameters of the device and the gate capacitance, respectively.

6.2.3. *Saturation region*

The saturation region the output current of a transistor can be described as follow:

$$I_{DS} = \frac{W}{2L}C_i\mu\,(V_{GS} - V_{TH})^2 \tag{8}$$

As the equation is not linear with respect to V_{GS} (i.e. the output current I_{DS} varies in a parabolic way), first of all, the square root of the module of the current ($\sqrt{|I_{DS}|}$) is extrapolated. As for the linear region case, the intercept (q) and the angular coefficient (m) must be computed. In order to perform this extrapolation, from the $\sqrt{|I_{DS}|}$ curve a linear fitting is performed. It has to be noticed that not all the values of the curve $\sqrt{|I_{DS}|}$ are used to compute the linear fitting, but only those points with a linear shape (Pearson correlation coefficient approximately equal to 1).

Therefore, the threshold voltage is computed as reported in (6):

$$V_{TH} = -\frac{q}{m}$$

while the mobility as:

$$\mu = \frac{m^2}{\frac{1}{2}\frac{W}{L}C_{ins}} \tag{9}$$

In addition, from the electrical parameters extrapolated from the static curves, it is possible to obtain the theoretical transition frequency. In fact, the transition frequency (f$_t$) can be described as follow:

$$f_t = \frac{\mu(V_{gs}-V_{th})}{2\pi L(L+2L_{ov})} \tag{10}$$

where μ is the field effect mobility, V_{gs} is the gate-to-source applied voltage, V_{th} described the threshold voltage, L is the channel length and L_{ov} is the overlap between gate and source electrode.

6.3.AC electrical characterization

The AC characterization was performed to experimentally determine the transition frequency (f_T) by separately measuring the channel transconductance (g_m) and the gate-to-source and gate-to-drain capacitances (C_{gs} and C_{gd} respectively), whose sum corresponds to the total gate capacitance C_g. The same electrical setup already introduced in the work of Perinot et al. [173] was employed, as shown in Figure 91.

In fact, differently to what proposed in (9), the transition frequency (f_t) can b also defined as the frequency at which small-signal gate (input) and drain (output) currents become equal. By definition:

$$f_t = \frac{g_m}{2\pi(C_{gs}+C_{gd})} \tag{11}$$

where g_m is the channel transconductance and, C_{gs} and C_{gd} represent the gate-to-source and gate-to-drain capacitances, respectively, whose sum corresponds to the total gate capacitance C_g. Specifically, from the overlap length (L_{ov}), and knowing the channel length (L) and width (W), as well as the dielectric capacitance per unit area (C_{ins}), a theoretical total gate capacitance (C_g) was estimated using a simple parallel plate capacitor model and thus, considering the normalized transconductance g_m, the theoretical transition frequency was then calculated. For the purpose of this work, this model, although an approximation, holds well with the observed electrical characteristics, although further analysis is required to precisely characterize the complex capacitive behavior of this structure.

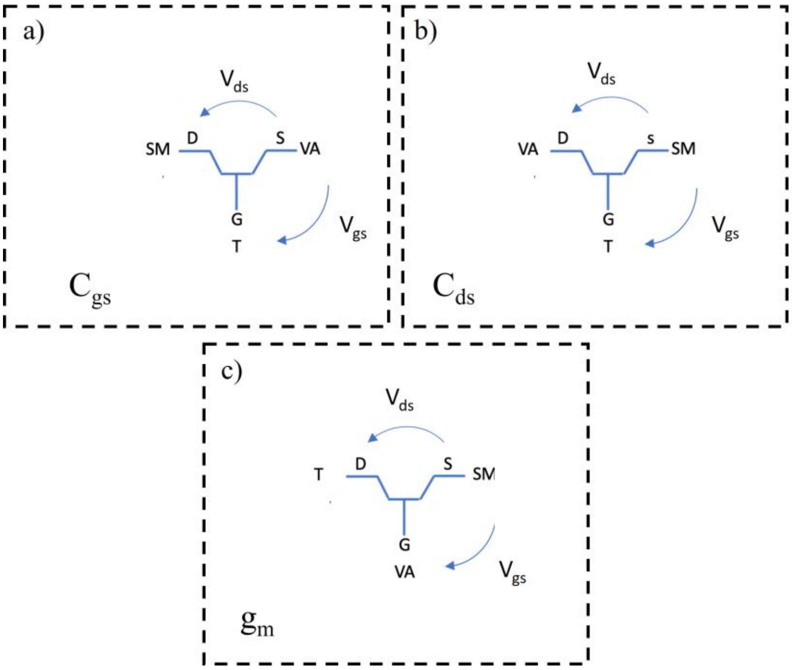

Figure 91 Schematic for separately acquire a) the parasitic capacitance between gate and source contact Cgs, b) gate and drain contact Cgd and c) the transconductance gm [173]

6.4.Device characterization

The optimization process of the short-channel organic transistor passed through the employment of different materials and fabrication methods. This section discusses the results of three different type of vertical channel transistor studied during this work, namely Tips-pentacene, ActivInk N1400, and Polyera ActivInk N2200. It is worth mentioning here that this structure, as well as other step-edge structures, presents for all the three devices category an asymmetry in its electrical characteristics (depending on which contact is set as the source). Therefore, it was decided to focus on the configuration with the best performance in terms of transconductance, in order to optimize the frequency response of the device for all the three types of transistors involved in this study.

6.4.1. *Tips-pentacene-based vertical channel transistor*

The first short-channel organic transistor developed during this thesis work was a Tips-Pentacene-based device, where the organic semiconductor was drop casted directly on the channel region and the top gate contact was an evaporated aluminum film, separated from the semiconductor through a 200 nm thick Parylene C film, employed as dielectric layer.

Figure 92 a) shows an optical polarized image (top view) of the transistor channel region, where the three terminals (gate, drain and source) are highlighted and the inset reports the overlaps between the gate and the source and drain contacts. From the output characteristic and transfer curves, reported in Figure 92 b), it is possible to notice the asymmetrical behavior of the device. Particularly, the bottom source configuration, in which the bottom gold contact was employed as source electrode, while the top gold contacted as drain electrode, shows a typical short-channel transistor behavior, where the current in the saturation region is not completely flat by increasing (in absolute value) the source-drain voltage V_{DS}. Moreover, this effect is much more evident when the source-to-gate voltage V_{GS} was increased. Nevertheless, the transistor showed a relatively good field effect in the output current.

The top source configuration, indeed, showed different characteristics, where linear region and saturation region were not easily distinguishable, as the short-channel effect is predominant. The output current, in fact, increase in a linear way with respect to V_{DS}. In this case, in fact, the electric filed effect was reduced. Nevertheless, the output current was higher in the top source configuration, with the same voltages applied, thus in this configuration showed the best performances in terms of transconductance.

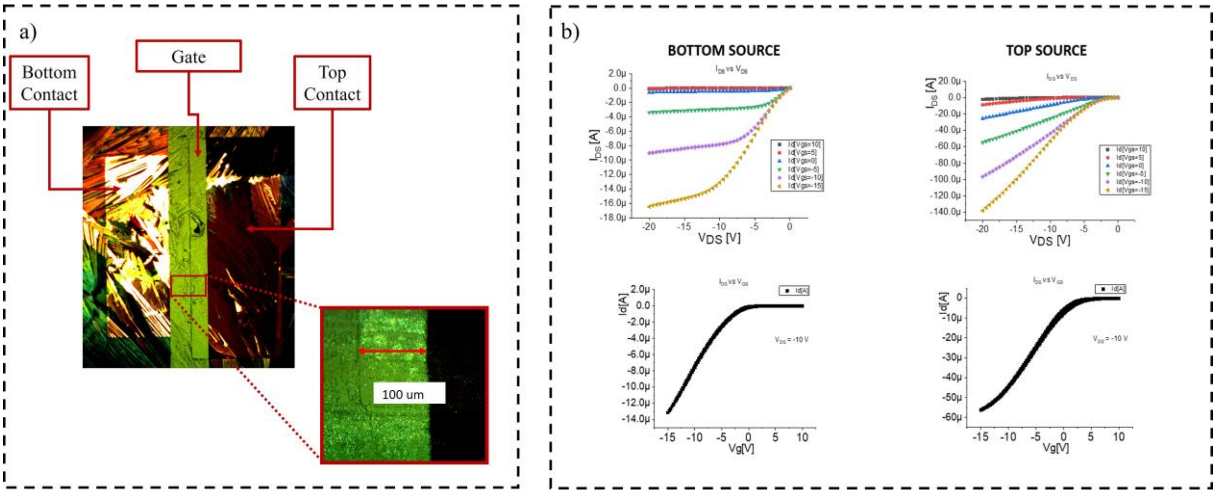

Figure 92 Tips-pentacene-based short vertical channel organic field effect transistor. a) optical polarized image (top view) of the transistor channel region, where gate, drain and source contact are highlighted. The inset shows the overlap between gate and source contact; b) output characteristic and transfer curves for the bottom source (on the right) and top source (on the left) configuration.

From the transfer curves, both the field effect mobility (μ) and the threshold voltage (V_{th}) were extrapolated. In particular, in the saturation regime, an average value of about $9.5 \pm 5\ 10^{-4}$ cm^2/Vs and 4.9 ± 1.7 V for the field effect mobility and the threshold voltage, respectively, were obtained over 10 devices. This values are relatively low with respect to planar organic transistor based on Tips-Pentacene reported at the state-of-the-art [174].

However, two of the best performing devices were characterized in terms of transition frequency and the results are reported in Figure 93.

Concerning the Tips-pentacene vertical transistor (a), the extrapolated field effect mobility was about $\mu_{sat} = 1.8\ 10^{-3}\ cm^2/\ V\ s$, the threshold voltage was $V_{th} = 6.7$ V and the estimated overlap was $L_{ov} = 250$ µm that gave rise to a total parasitic capacitance of $C_{tot} = 0.1$ nF. From such parameters, a theoretical transition frequency of about $f_t = 3.7$ KHz at $V_{gs} = -13$ V was obtained.

Figure 93 a) reports the static curves and the measured transition frequency ($f_t = 2.8$ KHz) for this device. As it possible to notice, f_t was slightly lower than the one obtained from data extracted from DC measurements (probably due to the lower transconductance). In fact, $g_m \sim 1.1$ µA/V was observed, which is slightly lower than the one obtained from the static measurement (1.4 µA/V).

For the second transistor (b), a theoretical value of 7.5 KHz was estimated. Figure 93 b) reports static and dynamic response of the transistor. In this case, a higher transition frequency of 8.5 KHz was obtained due to the transconductance value of $g_m \sim 1.5$ µA/V (slightly higher than the one observed in DC, where $g_m \sim 0.8$ µA/V). In this case, the higher transition frequency with respect to the other Tips-Pentacene-based transistor (a) was due mainly to the lower overlap length ($L_{ov} = 100$ µm) and thus a reduced parasitic capacitance of about $C_{tot} = 0.044$ nF. In fact the field effect mobility was similar to the one of the previous transistor ($\mu_{sat} = 1.7\ 10^{-3}\ cm^2/\ V\ s$).

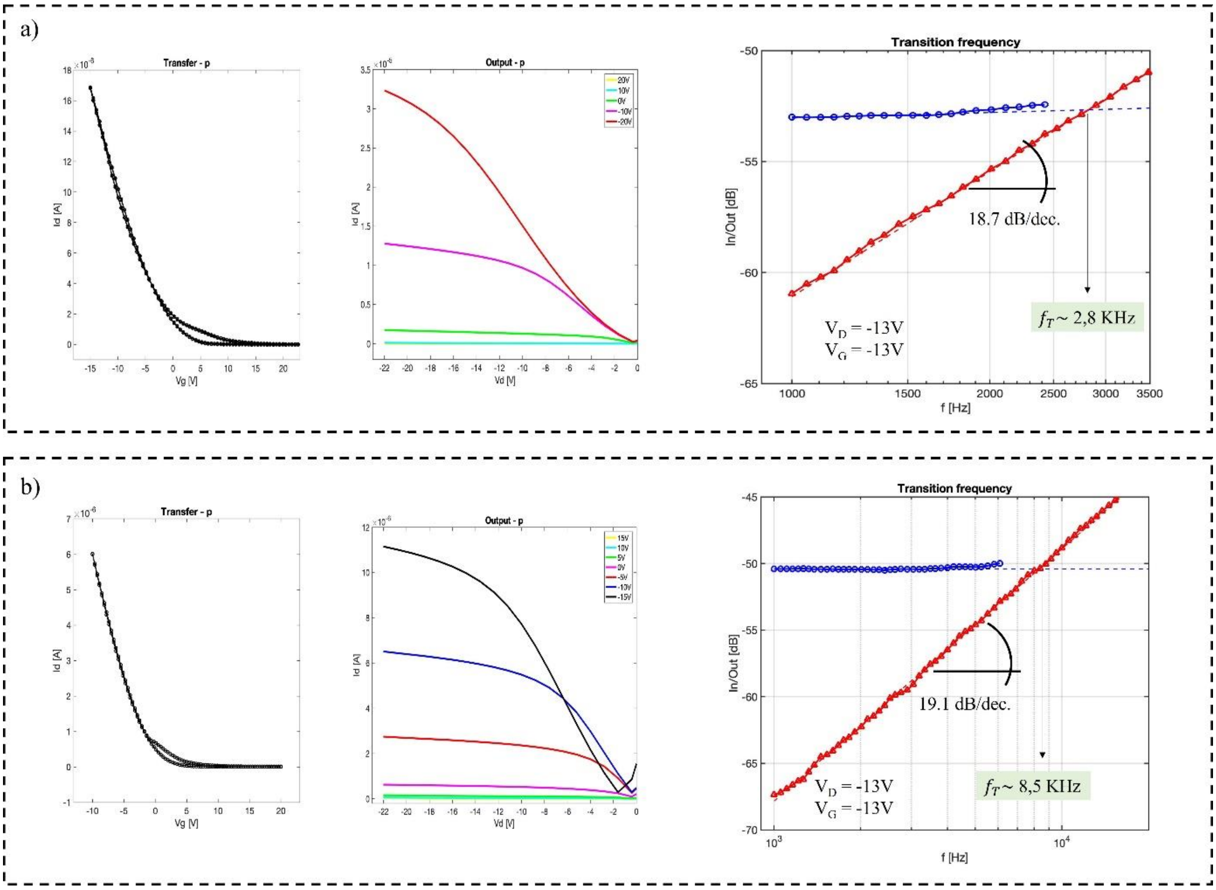

Figure 93 Static and dynamic characterization of the two most performing Tips-Pentacene-based short channel transistors, a) with a transition frequency of about 2.8 KHz and b) with a transition frequency of 8.5 KHz at V_{gs} = -13 V

From the static characterization, it is possible to assert that almost all the devices presented a good static behaviour. However, the performances are low, specifically in terms of field effect mobility and thus transconductance values. In fact, these parameters particularly affect the transition frequency. A possible solution to improve this aspect was found on the employment of a different semiconductor deposited through a different deposition technique.

In addition, the transition frequency was low not only because of the low mobility, but also due to the huge overlap between gate and source/drain electrodes that cause a high total parasitic capacitance C_g. Therefore, to improve the transistor performances, the overlap between gate and source/drain electrodes had to be reduced.

6.4.2. *ActivInk N1400-based vertical channel transistor*

To further improve the device performances, especially in terms of frequency response, a different organic semiconductor was employed. In fact, the ActivInk N1400 spin coated onto the channel region resulted in a thinner n-type semiconductor layer, differently from the Tips-pentacene which formed relatively big crystals. Moreover, a smaller top gate width was employed to developed such n-type transistors, as it is shown in Figure 94 a) where an optical polarized image (top view) of the transistor channel region is shown. In such figure, the inset reports the overlaps between the gate and the source and drain contacts, where it is possible to appreciate the reduced overlap between the top gate and source/drain electrodes. Specifically, in the example reported, the overlap is around 50 µm. Figure 94 b) reports the static curves of the transistors, where a good field effect and behaviour is clearly notable.

From the transfer curves, also in this casa both the field effect mobility (µ) and the threshold voltage (V_{th}) were extrapolated in the saturation regime. Specifically, an average field effect mobility of about $2.14 \pm 1\ 10^{-2}$ cm^2/Vsand an average threshold voltage of 3.4 ± 2.3 V were extracted over 8 devices. Therefore, an improvement of the device electrical characteristic was obtained.

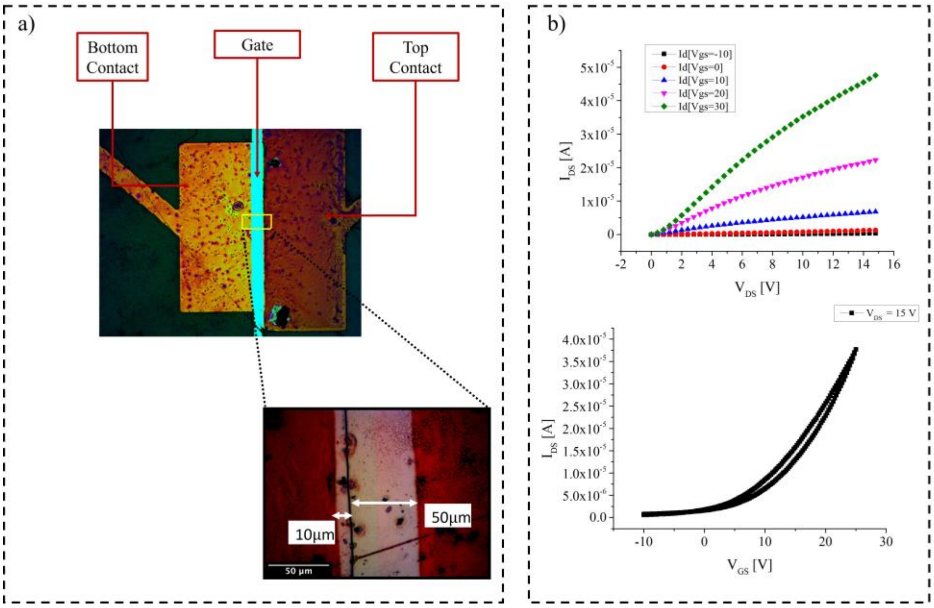

Figure 94 ActivInk N1400-based short vertical channel organic field effect transistor. a) optical polarized image (top view) of the transistor channel region, where gate, drain and source contact are highlighted. The inset shows the overlap between gate and drain/source contacts; b) output characteristic (top) and transfer curve (bottom) of the proposed device, where the n-type behavior is clearly notable.

Specifically, the field effect mobility was increased of one order of magnitude (from $5\ 10^{-4} – 1\ 10^{-3}$ of the Tips-pentacene based transistors, to ~ $2\ 10^{-2}$ for the N1400-based transistors). As a consequence, the transconductance was also increased from 1 to 5 µA/V. In addition, an improvement in the design of the geometrical parameters of the device was also obtained. In fact, the overlap length (L_{ov}) between gate and source/drain electrodes was reduced from 100 – 250 µm to 35 - 50 µm. Consequently, overlap capacitance was also reduced of about one order of magnitude (from 10^{-11} – 10^{-10} F to 10^{-12} F).

Thanks to this improvement, a higher frequency response was obtained. Figure 95 shows the transition frequency of the best N1400 performing device. In particular, a f_t = 200 kHz was obtained for V_{gs} = 30 V and V_{ds} = 15 V, while a transition frequency f_t = 1.2 MHz was obtained for V_{gs} = 30 V and V_{ds} = 30 V.

Therefore, by slightly changing the design of the short-channel step-edge transistor an improvement of order of magnitudes (from a few kHz up to 1 MHz) was achieved in the transition frequency. This result was related both to the different employed organic transistor, since the ActivInk N1400 performs better in top gate architectures, and the smaller overlap length (L_{ov}) between gate and source/drain contacts.

However, to improve the device performances and to reach a transition frequency in the order of the MHz or even tens of MHz with a high yield and throughput, it was necessary to still reduce the overlap length and to employ an organic semiconductor with higher mobility (with values around 0.1 – 0.08 Cm^2/Vs), still maintaining a low-cost and up-scalable production process.

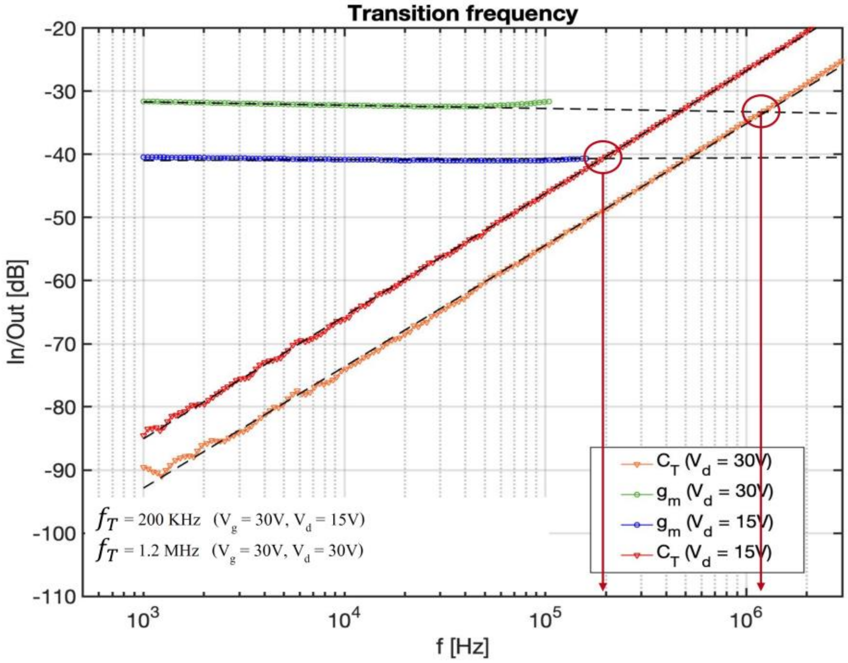

Figure 95 Transition frequency of the ActivInk N1400-based short channel transistor. The best performing device achieved a ft = 200 kHz for Vgs = 30 V and Vds = 15 V, while a transition frequency ft = 1.2 MHz was obtained for Vgs = 30 V and Vds = 30 V.

6.4.3. *ActivInk N2200-based vertical channel transistor*

During this thesis work, the last optimization step of the vertical-channel transistor was obtained by employing the ActivInk N2200 as n-type semiconductor and by depositing the top gate by ink-jet printing. Specifically, the N2200 was deposited by off-centered spin-coating, and annealed at 120 °C for 30 min to improve the semiconductor performances. Moreover, a double film of dielectric was employed, composed by a thin spin-coated poly(methyl)methacrylate (PMMA) layer (50 nm) and a thicker chemical vapor deposited Parylene C layer (240–260 nm). In fact, Parylene-C, owing to the presence of chlorides, is known to degrade the transistor performance when directly in contact with the chosen semiconductor [175]. Therefore, the thin PMMA layer was selected as optimum interlayer to separate the semiconductor from Parylene C. In addition, in order to reduce the overlap between the gate and source/drain contacts and simultaneously maintaining a low-cost and sufficiently easy fabrication process, the top gate was obtained by ink-jet printing of a gold ink (DryCure Au-J 1010B) with line width of 30 µm. Figure 96 shows the optimized short-channel step-edge structure with the employed materials and an optical polarized image of the proposed device. The inset reports the transistor channel region, with the overlaps between the gate and the source and drain contacts.

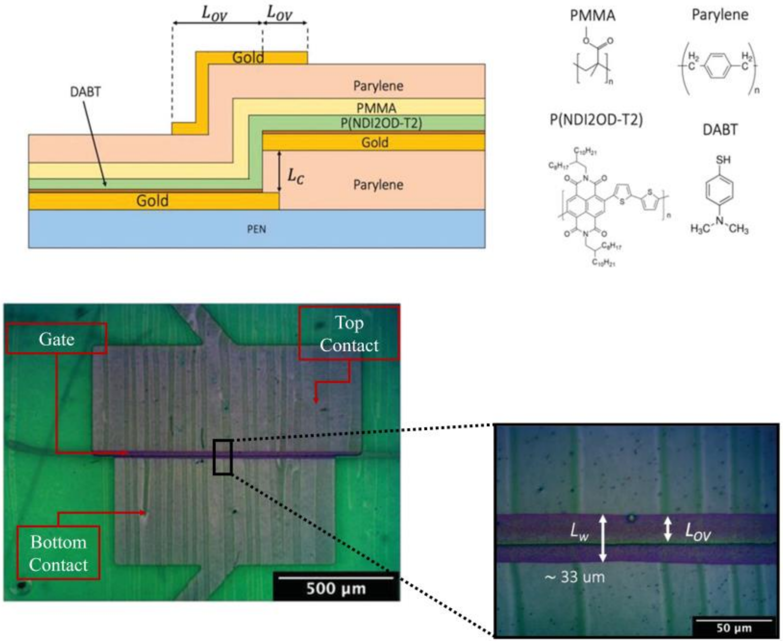

Figure 96 Structure of the vertical channel ActivInk N2200-based organic transistor and employed materials, with an optical polarized image of the proposed device. The inset highlights the transistor channel region, with the overlaps between the gate and the source and drain contacts.

The N2200-based vOFETs were measured inside a glovebox under nitrogen atmosphere, after an overnight annealing at 120 °C. Output characteristics and transfer curves are shown in Figure 97 for the a) top source-bottom drain (TSBD) configuration and b) bottom source-top drain (BSTD) configuration. Figure 97 c) reports the transfer curves for both the two configurations. Also in this case, the structure presents an asymmetry in its electrical characteristics, depending on which contact is set as the source, demonstrating that this behavior depends on the step-edge structure itself and not on the employed materials. In fact, as it was for both the Tips-pentacene-based and N1400-based vOFETs, the top source-bottom drain configuration showed higher output current and a predominant short channel effect.

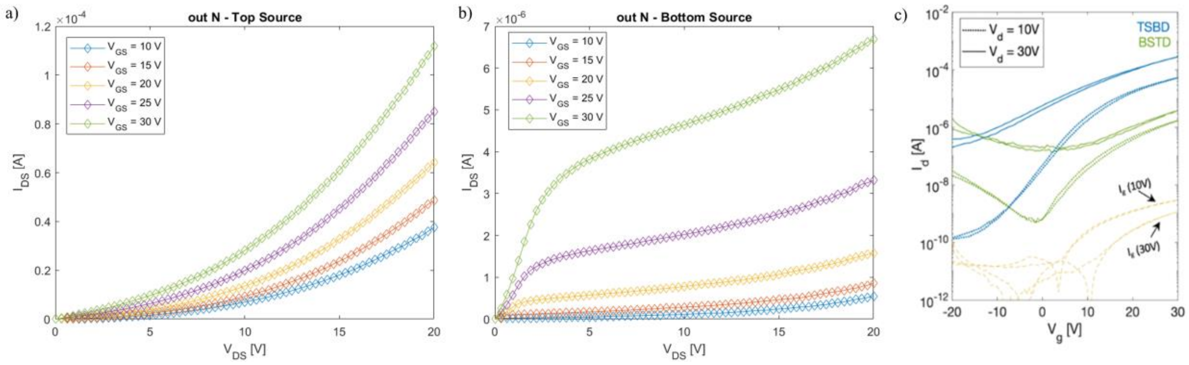

Figure 97 Electrical characterization of a ActivInk N2200-based vOFET. The output characteristic curves for the a) Top source-Bottom drain (TSBD) configuration and b) Bottom Source-Top drain (BSTD) configuration shows an asymmetrical behavior depending on the which contact is set as source electrode; c) shows the transfer curves for both configurations and specifically, an higher output current is clearly notable for the TSBD configuration for both linear and saturation regimes.

Figure 98 a) reports the characteristic transfer curves of the best device, while Figure 98 b) shows an average over ten identical devices at V_{ds} of 10 V (black curve) and 30 V (blue curve) which indicates an overall good reproducibility of the process. In fact, the transistors were characterized by a good linear and quadratic relationship of the output current (I_{DS}) in linear and saturation regime, respectively, with respect to V_{gs}. Moreover, good ON/OFF ratios, in the order of 10^6 (V_{DS} = 10 V) and 10^3 (V_{DS} = 30 V) were obtained, despite of the short channel.

From the transfer curves, as a further analysis, the electrical parameters were extracted. Specifically, the threshold voltage (V_{TH}) weas equal to 15 V in the linear regime and 13 V in the saturation regime. Moreover, the quasistatic average (over ten samples) normalized transconductance ($g_m/W = [\partial I_{ds}/\partial V_{gs}]/W$) was also derived, obtaining a value of 0.5 mS cm^{-1} in saturation (at V_{DS} and V_{GS} of 30 V), with a maximum value of 0.8 mS cm^{-1}, for the best performing device. Therefore, such organic semiconductor allowed to obtain higher transconductance values and, thus, a higher transition frequency was expected.

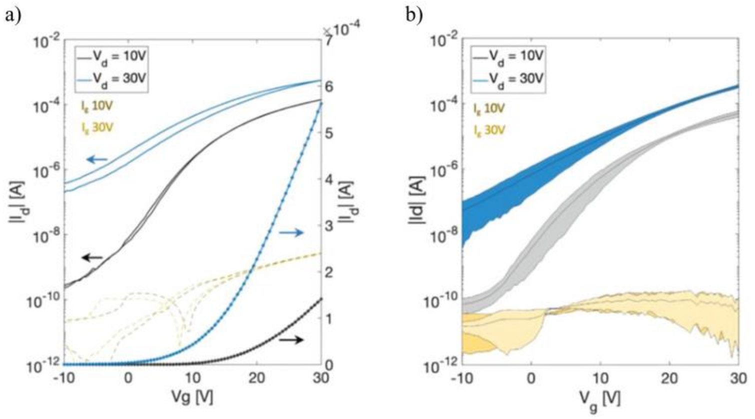

Figure 98 Transfer curves of the N2200-based vOFET. a) best device and b) average transfer over 10 identical samples. The devices showed a good linear and quadratic relationship of the output current (I_{DS}) in linear and saturation regime. In addition, a good ON/OFF ratios, in the order of 10^6 (V_{DS} = 10 V) and 10^3 (V_{DS} = 30 V) were obtained.

Also in this case, in order to assess the frequency performances of the N2200-based vOFETs, the transition frequency f_T was measured. The optimization process and particularly, the ink-jet printed gate, gave rise to an overlap length (L_{ov}) around 15–20 µm. In addition, knowing the channel length (350 nm) and width (1 mm), as well as the dielectric capacitance per unit area (∼14 nF/cm^2), a theoretical total gate capacitance between 2.7 and 3.7 pF was estimated using a simple parallel plate capacitor model. Therefore, considering the normalized transconductance of 0.5 mS cm^{-1} extracted from the DC analysis, a transition frequency f_T of about 2–3 MHz can be estimated.

As for the other two type of vOFET, to experimentally determine f_T, g_m, C_{gd}, and C_{gs} were separately measured. Specifically, an average value of 1.8, 1.6, and 3.5 pF for C_{gd}, C_{gs}, and C_g were, respectively, extracted over ten devices, according to the parallel plates model. Moreover, for the normalized transconductance (g_m/W), an average value of 0.47 mS cm^{-1} was obtained over ten samples, with a maximum of 0.8 mS cm^{-1}. As it is possible to notice, these values are in very good agreement with the quasistatic ones extracted from the transfer curves in the DC analysis. Finally, as shown in Figure 99 a) an average value for the f_T of 2.5 MHz was obtained over 10 devices, while a maximum value of 5.5 MHz (Figure 99 b)) was obtained for the best performing device. Again, a good agreement with the previous estimations was obtained.

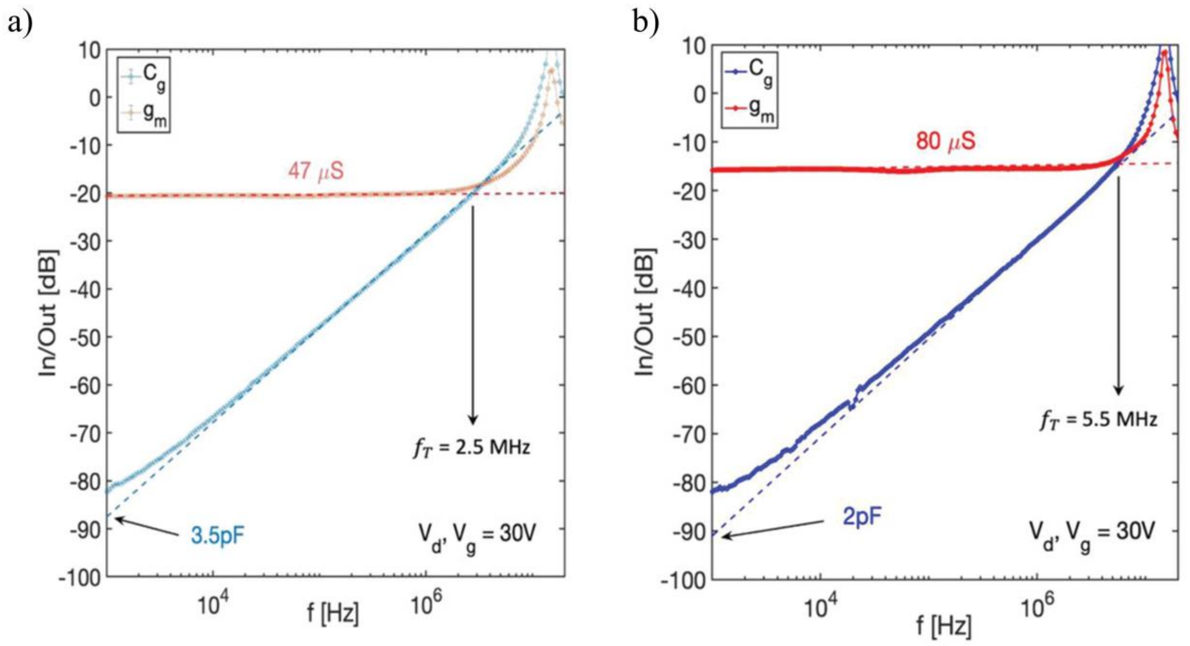

Figure 99 Experimental transition frequency f_T extraction. a) average over ten samples and b) best device.

The transition frequency obtained by the device developed during this thesis work is higher than those obtained by other step-edge vOFETs. In fact, for example, Uno et al. [106] reported a transition frequency of about 4 MHz in a transistor with channel length 1 µm. Kudo et al. [176] developed a step-edge structure with a channel length of 250 nm and a transition frequency of 1.5 MHz. Takano et al. [103] reports a f_T of 900 kHz (channel length 1 µm). Moreover, the obtained results highlight a good reproducibility of the process and a good electrical stability of the devices, which can be operated in continuous mode and repeatedly characterized for extensive periods of time. In fact, another important aspect of this short-channel step-edge transistor is the possibility to operate it both in DC and AC modes without the need of a complicated bias setup [98] and without any specific heat dissipation layer [76]. This aspect, although yet to be specifically characterized, represents an important feature of this structure, since to fully exploit the possibilities offered by high-frequency organic transistors, a continuous-mode operation is highly desirable. Therefore, these features, together with the simple, low-resolution and a large-area approach for the fabrication of submicrometer channel flexible OFETs, can open up interesting new scenarios in the field of organic electronics for sensing and flexible circuits in the wearable electronics and IoT context. Despite the nonidealities of the current version of the device, limitations that can be removed in future iterations by optimizing the semiconductor deposition and the gate/source–drain overlap, the present structure has promising potential applications for the development of high-speed organic logic circuits for flexible RFID tags and displays, flexible communication circuits for IoT applications, and high-density sensor arrays with integrated preamplification circuits for robotic skin.

7. Chapter VII: highly sensitive tactile sensors for artificial skin applications

Artificial electronic skin is a widespread wearable electronic application, where the focus is on the development of devices able to mimic human skin functionalities. Thanks to the development of novel flexible and soft materials, this research topic has found different applications in soft-robotics, healthcare, prosthetics, and rehabilitation fields. Several approaches have been proposed and with the outburst of the organic electronics, different devices and systems able to mimic both sensory and mechanical human skin functionalities have been developed.

The final chapter examines this context since it will report on the development and optimization process of a multimodal tactile sensor able to detect simultaneously temperature and force stimuli. The proposed device is based on a flexible Organic Charge Modulated Field Effect Transistor (OCMFET) coupled with a pyro/piezoelectric element, namely a commercial film of poly-vinylene difluoride (PVDF) Therefore, the first part of this chapter will be devoted on a description of the OCMFET working principles.

Afterward, the key point of this work will be presented. The reduction of the channel length, obtained by employing a low-resolution vertical channel architecture, allowed to maximize the ratio between the sensing area and the transistor's channel area, a technological approach that allows to considerably enhance both temperature and force sensitivity, while at the same time minimize the sensor's dimensions. Therefore, the chapter will reports the short-channel OCMFET fabrication process and the device structure. After a brief description of the electrical characteristic, a complete characterization of the temperature, force and multimodal sensor's response will be report [177].

7.1. OCMFET: working principle

In 2006, Barbaro et al. [178], from the microelectronic group of the University of Cagliari leaded by Raffo and Bonfiglio, proposed an original solid state sensor for charge detection in the range of a few electrons per nanometer. Basically, the device was an evolution of the floating gate MOS and, as it possible to notice from the device's schematic reported in Figure 100, it is composed of a floating-gate transistor (M_0), a control-gate with the role of reference electrode to set the transistor bias (V_{CG}) and an active area (or sensing area) activated by charge induction (A_S).

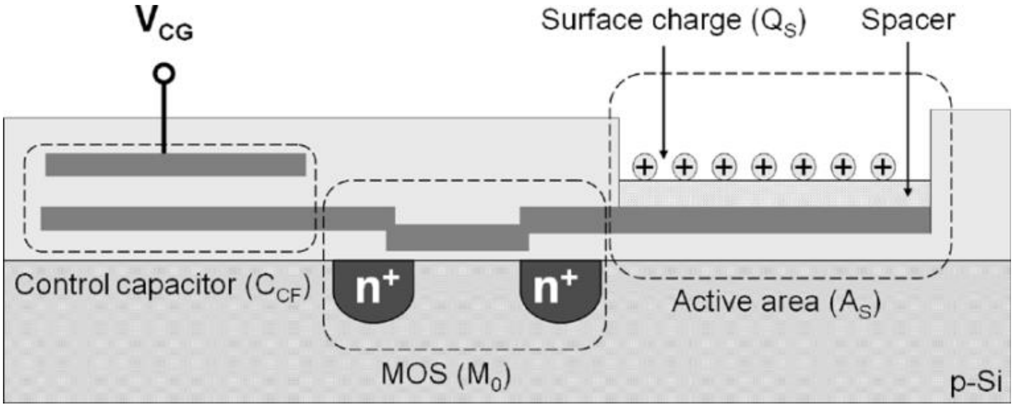

Figure 100 Charge Modulated Field Effect Transistor (CMFET) composed by a floating-gate transistor with a control-gate and an active area [178].

The transduction mechanism of such a sensor is based on the charge variations in the proximity of the active area. In fact, the active area is exposed to the environment, thus making the device a charge sensor. It is easily to notice that, one of the main advantages of the CMFET working principle is that it can be implemented using different technological approaches as, for example, using organic electronics. The Organic-CMFET (OCMFET), in fact, exploits the innovative working principle of the inorganic version, together with the well-known advantages of the organic electronics, such as the possibility to fabricate sensors onto flexible and ultra-flexible substrates using low-cost and large-area fabrication processes, thus making such device suitable for wearable electronic applications.

Therefore, as already mentioned, CMFETs and OCMFETs are floating gate transistors that can be used as charge sensors. Any charge or charge distribution variation that occurs in the near proximity of the sensing area can modulate the charge distribution inside the floating gate, thus affecting the charge carrier density inside the channel of the transistor. As a consequence, the threshold voltage of the transistor is modulated, finally determining a variation in the output current. The control gate-voltage (V_{CG}) and the electric charge, together, play a fundamental role in determining the voltage difference between the floating-gate and the source electrode (V_{FG}), which is usually grounded. Figure 101 reports the schematic of the OCMFET, with the transistor area, control capacitor and sensing area highlighted, and the transfer curve with no induced charges on the sensing area.

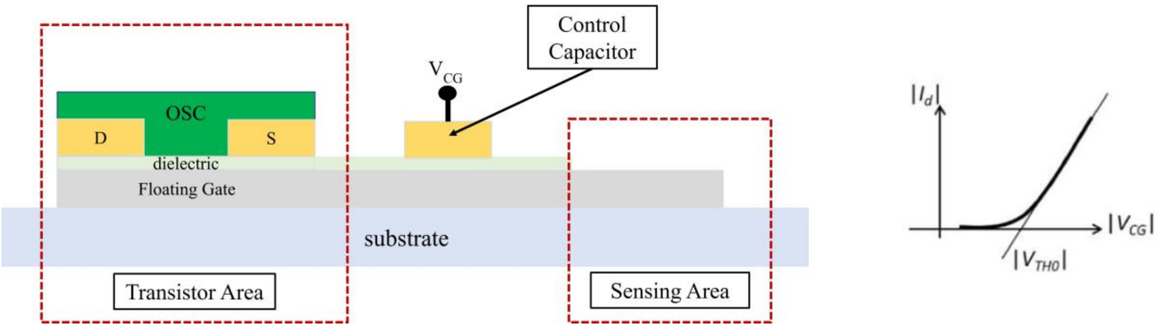

Figure 101 OCMFET structure and transfer characteristic with no induced charges on the sensing area.

It is possible to derive the relationship between the control gate voltage, the induced charge and the transistor's effective threshold starting from Gauss' equation to the common node of the capacitors.

The total charge Q_f in the floating gate can be written as:

$$Q_F = C_{CG}(V_{FG} - V_{CG}) + C_{SF}V_{FG} + C_{DF}(V_{FG} - V_D) + Q_i \tag{12}$$

where V_D is the drain voltage, C_{CG} is the capacitance of the control capacitor, C_{SF} and C_{DF} are the parasitic capacitances between the floating gate and the source and the drain electrodes. The V_{FG} can be obtained as follow:

$$V_{FG}(C_{GD} + C_{SF} + C_{DF}) = (Q_F - Q_i) + C_{CG}V_{CG} + C_{DF}V_D \tag{13}$$

$$V_{FG} = \frac{(Q_F - Q_i)}{C_{TOT}} + \frac{C_{CG}}{C_{TOT}}V_{CG} + \frac{C_{DF}}{C_{TOT}}V_D \tag{14}$$

where C_{TOT} is the sum of the control gate capacitance (C_{CG}) and the parasitic capacitances between the floating gate and the source and the drain electrodes (C_{SF} and C_{DF}).

Moreover, in a floating gate FET structure, it is possible to define the effective threshold voltage (V_{TFH}) as the value of the threshold voltage when the transistor is biased from the control gate, which is different from the value of the threshold voltage V_{TH} of the same transistor biased through the floating gate. In this kind of structure, we can consider the following relation:

$$V_{CG} - V_{THF} = V_{FG} - V_{TH} \tag{15}$$

Consequently:

$$V_{CG} - V_{THF} = V_{FG} - V_{TH} = \frac{(Q_F - Q_i)}{C_{TOT}} + \frac{C_{CG}}{C_{TOT}}V_{CG} + \frac{C_{DF}}{C_{TOT}}V_D - V_{TH} \tag{16}$$

The parasitic capacitances C_{SF} and C_{DF} depend on the overlap between the source/drain electrode and the floating gate. However, this contribution can be considered negligible or it can be minimize with a particular fabrication technique called *self-alignment*. As a consequence, the value C_{CG}/C_{TOT} could be considered equal to 1.

$$V_{CG} - V_{THF} \simeq \frac{(Q_F - Q_i)}{C_{TOT}} + V_{CG} + \frac{C_{DF}}{C_{TOT}} V_D - V_{TH} \tag{17}$$

By solving the equation for V_{THF}:

$$V_{THF} \simeq V_{TH} - \frac{C_{DF}}{C_{TOT}} V_D - \frac{(Q_F - Q_i)}{C_{TOT}} \tag{18}$$

Therefore, considering a change in the charges on the sensing area, assuming that the capacitances and Q. do not vary and assuming that the transistor's biasing has not been changed, it is possible to define the effective threshold voltage shift as:

$$\Delta V_{THF} = \frac{\Delta Q_i}{C_{TOT}} \tag{19}$$

Figure 102 shows the device structure and the effect of the induced charges on the sensing area and consequence shift of the threshold voltage in a OCMFET.

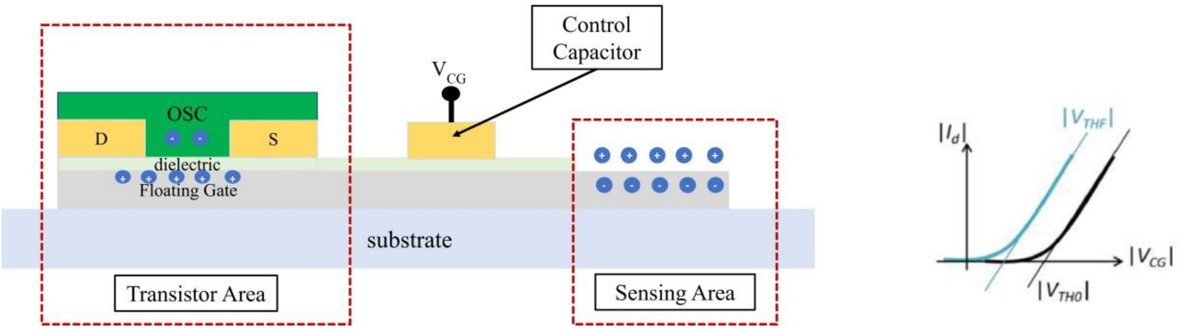

Figure 102 shows the device structure and the effect of the induced charges on the sensing area and consequence shift of the threshold voltage in a OCMFET.

Therefore, the application of such structure are different, in fact it can be employed for the detection of any physical or biological process that can change the total charge accumulated on the sensing area.

Moreover, the most important advantages of this approach are related to the fact that sensing element and the amplification element (the transistor) are here physically separated, thus preventing the external stimulus to damage the intrinsic characteristics of the semiconductor. In addition, the transduction mechanism is completely independent of the specific technological process, the employed materials for the dielectric layer ad semiconductor, thus enabling the possibility to develop the same device concept with different fabrication technologies.

7.2. Vertical channel OCMFET

Interestingly, the OCMFET offers the possibility of modulating its response by acting on geometrical factors such as the ratio between the sensing area and the transistor area, thanks to the fact that the sensing function is not performed by the organic semiconductor itself (as in electrolyte gated field effect transistors [179], [180]) nor by the gate dielectric (as in ion sensitive organic field effect transistors [181], [182]), but is rather due to the capacitive coupling between the physically separated sensing area and the transistor channel. With this structure is thus possible to increase the sensitivity by either increasing the sensing area or by reducing the channel area, a strategy that usually requires high-resolution fabrication techniques.

During this thesis work, a novel architecture for the fabrication of highly sensitive multimodal tactile transducers, for the simultaneous detection of temperature and force was developed. Specifically, a simple large area approach for the fabrication of submicrometer-channel Organic Charge Modulated Field Effect Transistor (OCMFET) was developed based on the vertical channel organic transistor presented in the previous chapter. Such devices were coupled with a pyro/piezoelectric element, namely a commercial film of poly-vinylene difluoride (PVDF) to obtain a multimodal tactile sensor. The reduction of the channel length, obtained by employing a low-resolution vertical channel architecture, allowed to maximize the ratio between the sensing area and the transistor's channel area, a technological approach that allows to considerably enhance both temperature and force sensitivity, while at the same time minimize the sensor's dimensions. Thanks to the employment of a straightforward, up-scalable, and highly reproducible fabrication process, this solution represents an interesting alternative for all those applications requiring high-density, high-sensitivity sensors such as robotics and biomedical applications.

7.3. Fabrication process

The short-channel OCMFET was obtaining by slightly modifying the vertical step-edge organic transistor structure described in the previous chapter.

All the devices developed in this thesis work were fabricated on a 175µm-thick poly(ethylene terephthalate) (PET) substrate. The first step consisted in the deposition and patterning, by means of a standard photolithographic process of two gold contacts, i.e. the bottom contact that will act as source of the transistors and the bottom plate of the control capacitor. Afterwards, a Parylene C spacer was deposited on the whole substrate by chemical vapor deposition (CVD) at room temperature: its thickness defines the channel length of the transistor (500 nm for all the devices). On top of the spacer, a second gold contact (top contact) was deposited and then patterned by a standard photolithography process, thus defining a channel width of 1 mm. Bottom and top contacts will act as source and drain electrodes of the transistor. In order to create the vertical channel, the substrate was exposed to oxygen plasma, which removes the Parylene C from everywhere but under the top contact, which acts here as a mask, thus creating a sub-micrometric step-edge structure that defines the channel of the final organic transistor. Subsequently, a droplet of a TIPS-pentacene solution in anisole (1 wt%) is deposited directly over the transistor channel and let dry at 70 °C on a hot plate. Afterwards, a 200 nm-thick film of Parylene C, acting as gate dielectric, is deposited through CVD, followed by the deposition of the aluminum top floating gate, which has been thermal evaporated and then patterned through a standard photolithographic process. The floating gate presents an elongated design aimed to overlap the bottom plate of the control capacitor (which act as gate terminal in the structure) and it ends with the so-called sensing area. Figure 103 a), b) shows the device fabrication process and the device cross-section, respectively.

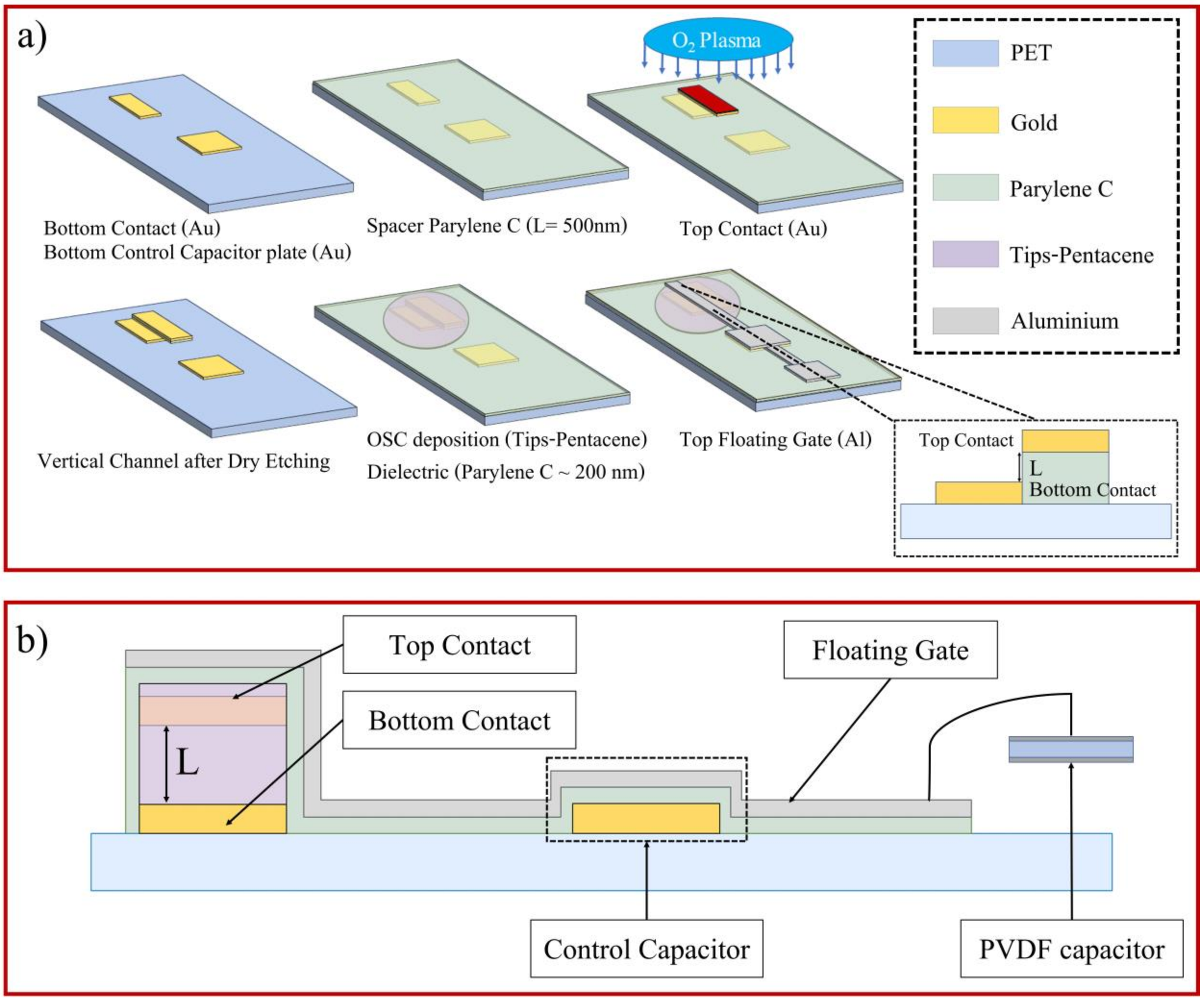

*Figure 103 Fabrication process workflow and employed material for the sub-micrometer vertical channel OCMFET. In the inset, the transferal cross-section through the vertical channel is reported; (**b**) longitudinal cross-section of the proposed device, where the vertical channel is highlighted. The control capacitor is obtained by overlapping the top floating gate and a gold bottom plate. The sensing area of the sensor is connected to the PVDF capacitor for the temperature and mechanical characterization;*

Poly(vinylidene fluoride) (PVDF) capacitors were fabricated using already stretched and poled 28 μm-thick PVDF films from Measurement Specialties Inc.-MEAS. Two thermal evaporated aluminum electrodes were realized on both sides of the film through a shadow mask and cut in different dimensions (1, 0.5 and 0.25 cm^2). In the integrated device, the capacitor was attached on the sensing area of the sub-micrometer vertical channel OCMFET using a couple of droplets of silver ink. After that, the capacitor was pressed and let dry into an oven at 30 °C for one hour.

7.4. Electrical characterization

To perform the electrical characterization a Keithley SourceMeter 2636 A (Figure 104) was employed.

Figure 104 Keithley SourceMeter 2636 A employed for the electrical characterization

The acquisition instrument was connected through a GPIB bus to an external PC, which allowed to control the whole acquisition set-up via software. From the MATLAB Graphic User Interface (GUI), in fact, it is possible to set the electrical parameters for the correct acquisition of the device output current. In particular, it allows setting both the range and the resolution for the voltages applied to the device (V_{GS} and V_{DS}) and the acquisition parameters such as the integration time of the measurement. Therefore, to perform the characterization, the source electrode was connected to the ground of the acquisition system, and a voltage drop between the drain electrode and the source (V_{DS}) was applied. The gate voltage (V_{GS}), indeed, was applied between the control capacitor and the source.

An example of the typical output and transfer curve are reported in Figure 105 a), b), respectively, where it is possible to notice no hysteresis and a low leakage current. It is worth mentioning that, due to the self-encapsulating architecture, the device showed very good electrical behavior even after several months, as reported in Figure 105 c). This aspect of the sensor makes it very suitable specifically for wearable electronics applications, where the stability of the device over time is an important feature not always respected by organic electronic technology-based devices

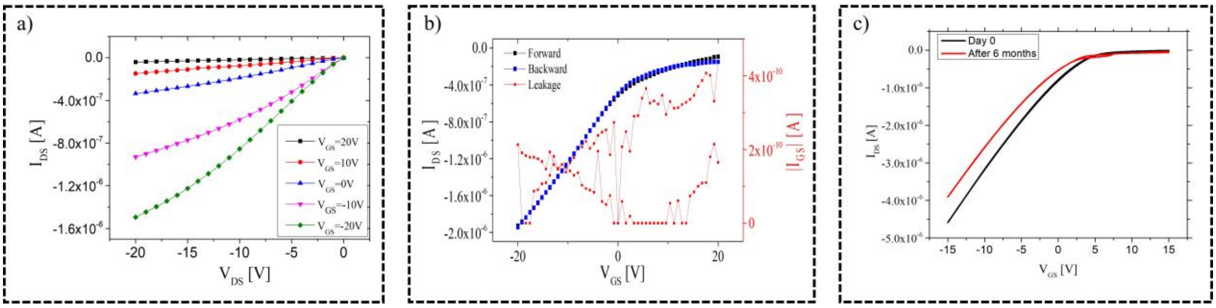

Figure 105 Electrical characterization with (a) output and (b) transfer characteristics of the sub-micrometer vertical channel OCMFET for tactile sensing. The device shows no hysteresis and low leakage current; (c) transfer curves of the submicrometer vertical channel OCMFET. The black curve refers to the measurement performed on day 0, while the red curve to the measurement after 6 months from the fabrication.

7.5. Temperature characterization

The devices were firstly characterized as temperature sensor. The top electrode of the PVDF capacitor was connected through a wire on the sensing area of the OCMFET, while the PVDF capacitor bottom plate was connected to the transistor source electrode. The employment of this solution allowed to mechanically decouple the sensing area of the OCMFET to the device channel, thus making more efficient the characterization of the sensor’s response. Particularly, this approach allowed to apply the temperature stimulation only on the PVDF capacitor, without affecting the transistor active area, whose characteristics are temperature-dependent. Therefore, in order to exercise the temperature stimuli only on the PVDF capacitor, thus exploiting the pyroelectric response, the bottom plate of the capacitor was placed on the top of a Peltier cell, which was powered by a benchtop voltage power supplies, and the overall temperature was controlled by means of an infrared Temperature Sensor (PyroCouple Calex PC21MT-1, Calex electronics limited). Figure 106 reports a schematic of the temperature characterization set-up.

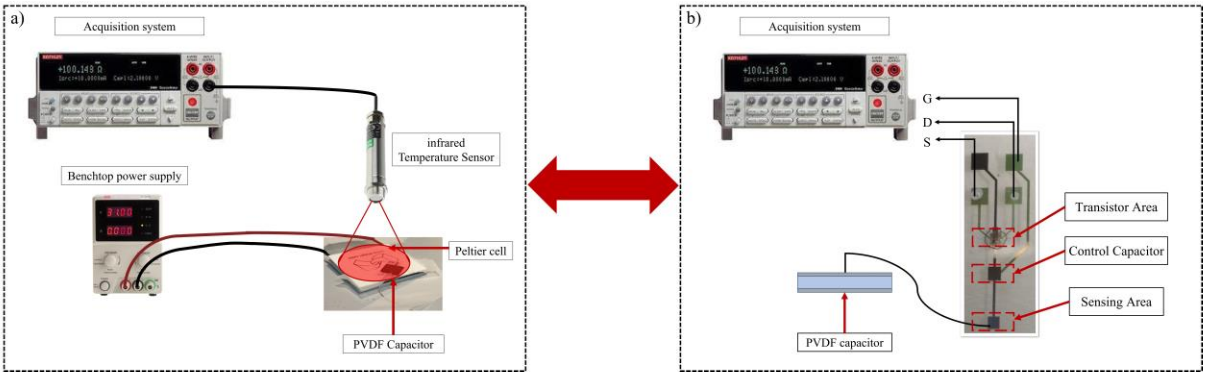

Figure 106 Temperature characterization set-up. (a) PVDF capacitor on top of the Peltier cell (connected to a benchtop power supply) and infrared temperature sensor aimed to control the temperature stimuli; (b) short-channel OCMFET with the sensing area connected through a wire to the PVDF capacitor and connected to the Keithley SourceMeter 2636 A for simultaneously acquire the output current. This acquisition set-up allowed to mechanically decouple the organic transistor and the PVDF capacitor, thus making more efficient the characterization of the sensor's response.

As reported in Figure 107 a), an increase of the temperature created a charge separation, due to its pyroelectricity, into the PVDF film, that perturbated the floating gate charge, thus giving rise to an increase of the output current. Interestingly enough, when the top plate was connected to the floating gate, see Figure 107 b), an increase of the temperature determined a decrease of the output current. This phenomenon is consistent with the fact that in such case opposite charges are induced into the floating gate, thus shifting the device threshold voltage towards more negative values, according to the following equation:

$$\Delta V_{TH} \propto -\frac{\Delta Q_{PVDF}}{C_{TOT}} \tag{20}$$

where ΔQ_{PVDF} is the time varying charge induced by the PVDF during temperature stimulation and C_{TOT} is the total capacitance given by the sum of the control gate capacitance, and the parasitic capacitances due to the superposition between the vertically stacked electrodes and the top gate electrode.

These flipping tests are necessary to demonstrate that the current variations are actually induced by the pyroelectric effect of the PVDF capacitor and not by some random undesired effect.

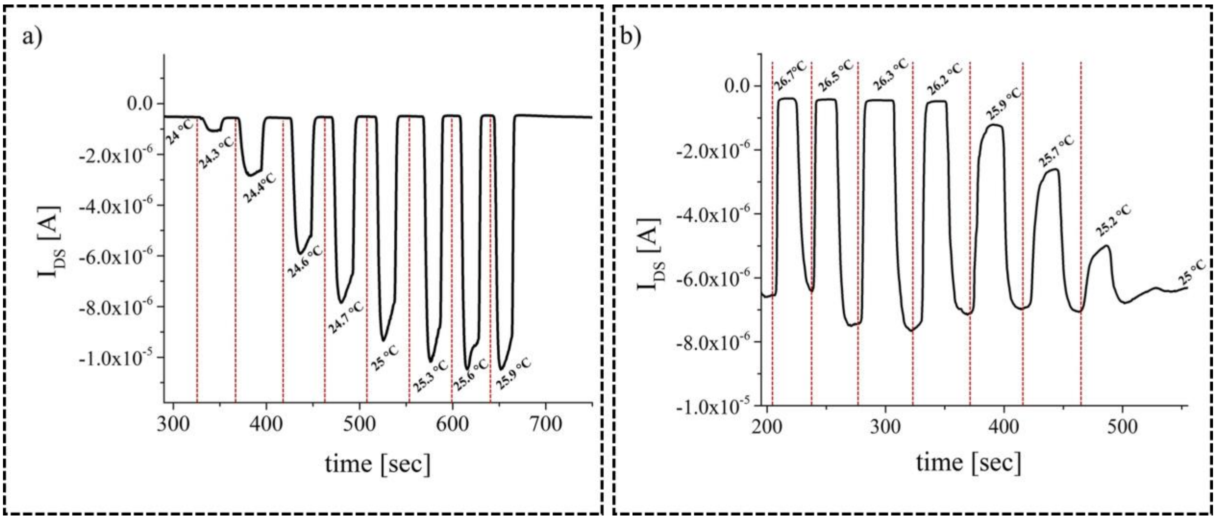

Figure 107 Flipping test of the Vertical-channel OCMFET. (a) The sensor output current increases as the temperature increases; (b) Opposite sensor response, i.e. a decrease of the output current, while the temperature is increased, due to the flipped connection of the PVDF capacitor onto the floating gate

Afterward, a more precise characterization of the temperature sensor was performed. Specifically, the measurement protocol included 5 repetitions for each temperature value. Moreover, different PVDF capacitor areas were employed in this analysis, since the sensitivity depends on the ration between the sensing area ($A_{sensing}$) and the transistor area ($A_{transistor}$), according to:

$$S = \frac{A_{sensing}}{A_{transistor}} \tag{21}$$

In the first case, a 1 cm2 PVDF capacitor was connected by a wire onto the floating gate. As clearly noticeable from Figure 108, the device is capable to quickly respond to temperature variations. Moreover, as the sensitivity of the device depends on the ration between sensing (i.e. the PVDF capacitor area in this case) and transistor area, as described in (21) , the employment of a short channel transistor, allowed to reduce the latter thus achieving a remarkably high sensitivity of 1 µA/°C, with an average sensitivity, measured on a set of 5 different devices, of 900 ± 36 nA/°C.

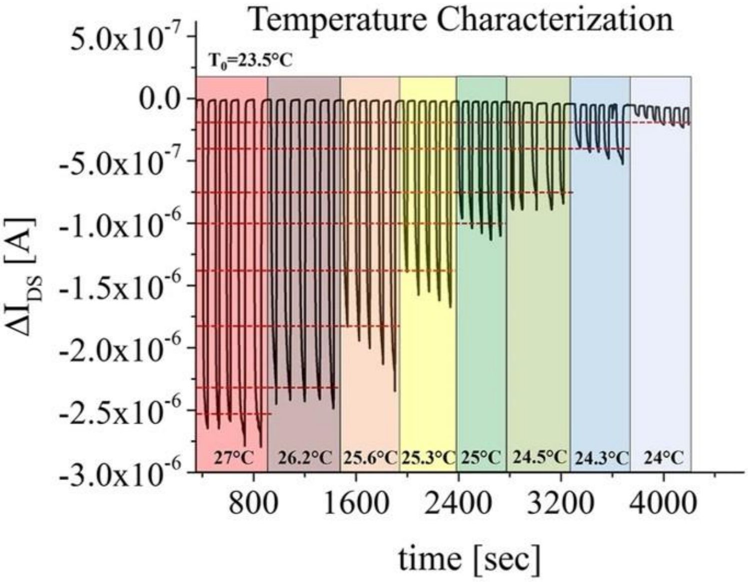

Figure 108 Example of dynamic response for the temperature characterization of the sub-micrometer vertical channel OCMFET.

It is worth noting that all the devices were fabricated in the same day, and were characterized, intentionally, in a period of time of one month. Nevertheless, the average sensitivity did not significantly change during this period of time, as can be observed by the limited error bars reported in the plot (Figure 109).

Interestingly enough, a large increase in the overall sensitivity was achieved, specifically if such results are compared with what previously reported using planar OCMFETs (70 nA/°C)[139], [183], which is also several orders of magnitude higher than what reported by Shin et al. (0.27 nA·°C^{-1})[129].

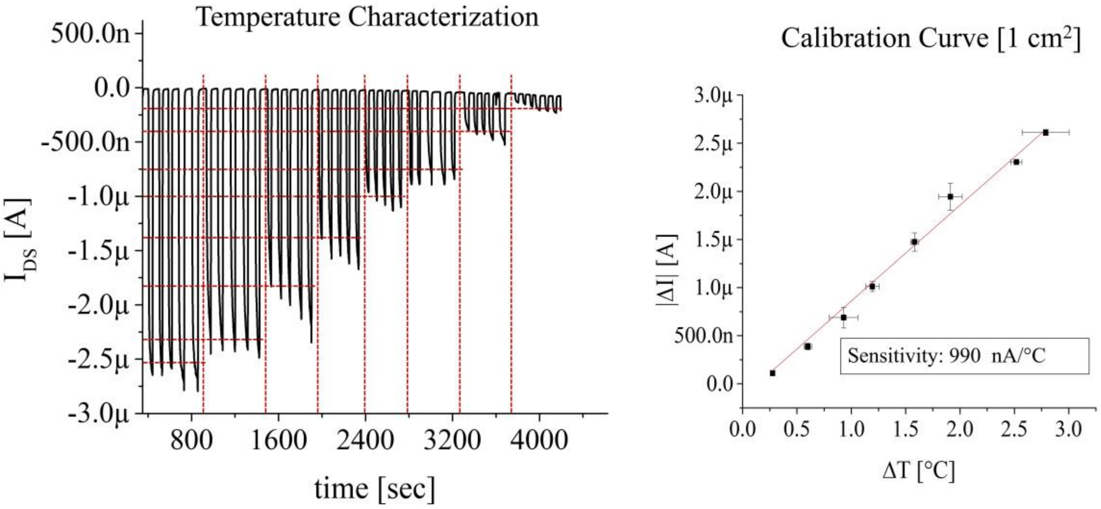

Figure 109 Dynamic response and calibration curve of the vertical-channel OCMFET coupled with a 1 cm^2 PVDF capacitor. The sensitivity was about 1 µA/°C within 2.5 °C.

The same analyses was performed, following the measurement protocol, by connecting the same devices to different PVDF capacitors with different areas namely 0.5 cm^2 and 0.25 cm^2. As can be clearly observed from the plots reported in Figure 110 a), b) a reduction of the area led to an increase of the detection range eventually allowing, when using the smallest sensing area, to fit the human temperature detection range, making such devices suitable for artificial skin applications.

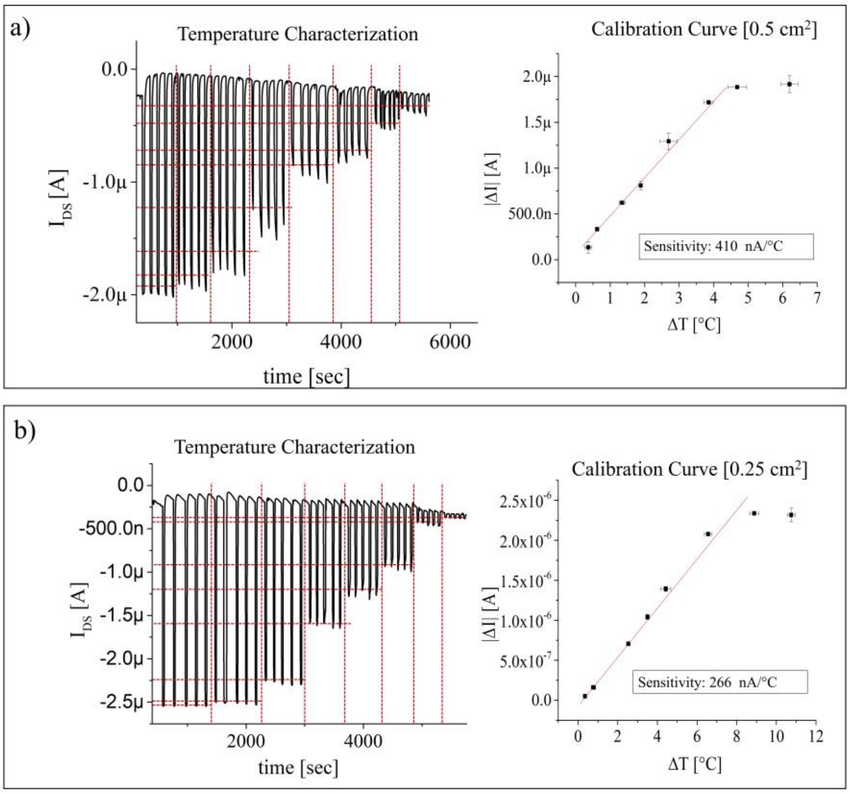

Figure 110 dynamic response and calibration curves for the v-OCMFET coupled with the (a) 0.5 cm^2 and (b) 0.25 cm^2 PVDF capacitor.

Figure 111 summarized the response of the device for the three different PVDF capacitors employed. The v-OCMFET coupled with a capacitor of 1 cm^2 reports a sensitivity of almost 1 μA/°C, while for the capacitor with area equal to 0.5 cm^2 and area of 0.25 cm^2, the reported sensitivity is 410 nA/°C and 266 nA/°C respectively.

In addition., as it possible to notice from the plots, reducing the PVDF capacitor area leaded to an increasing of the detection range and simultaneously reduced the sensitivity. In fact, a reduction of the sensing area by a factor 2 or 4, leads also to a reduction of the sensitivity by the same factor.

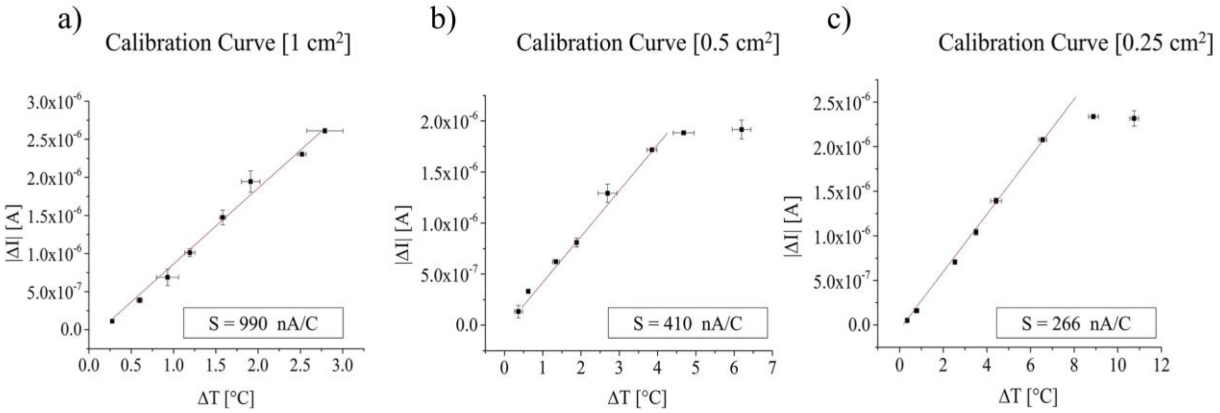

Figure 111 Calibration curve for the temperature analysis. a) PVDF capacitor with an area equal to 1 cm^2. The device shows a linear response within a 2.5 °C range and a high sensitivity about 990 nA/°C; (b) calibration curve for 0.5 cm^2 and (c) for 0.25 cm^2 PVDF capacitor. As the sensing area decreases, the range of response is increased to 4–5 and 8–9 °C respectively for the curve (b) and (c). In addition, a reduction of the sensing area by a factor 2 or 4, leads also to a reduction of the sensitivity by the same factor.

7.6. Force characterization

Similarly, the same approach was employed for the characterization of the device as force sensor. In fact, in order to exploit only the piezoelectric effect of the PVDF, the v-OCMFET and the PVDF capacitors were mechanically decupled. Specifically, the PVDF capacitor was placed onto a load cell (MX2 by IMADA, Northbrook, IL, USA) and a controlled force was exerted onto its area by means of a mechanical indenter (FCA-DS2-50N by IMADA, Northbrook, IL, USA). Simultaneously, the Keithley SourceMeter 2636 A was employed to set and acquire the transistor biasing and output current, respectively. Figure 112 reports a schematic of the force characterization set up.

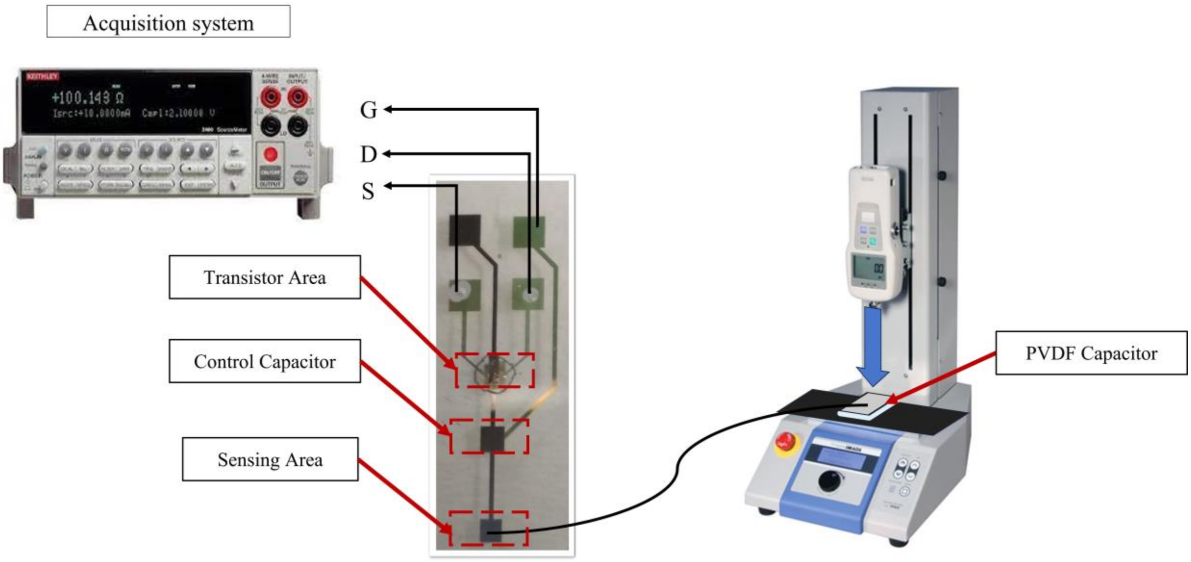

Figure 112 Force characterization set up employed for the analysis of the v-OCMFET as force sensor. The PVDF capacitor was placed onto a load cell (MX2 by IMADA, Northbrook, IL, USA) and a controlled force was exerted onto its area by means of a mechanical indenter (FCA-DS2-50N by IMADA, Northbrook, IL, USA). Simultaneously, the transistor biasing was set (S, D, and G are Source, Drain, and Gate electrode connections respectively) and the output current was acquired by the Keithley SourceMeter 2636 A.

Also in this case, changing the connected plate of the PVDF capacitor to the floating gate, gave rise to a flipping of the sensor response, which, again, is a clear indication that the observed response is due to the piezoelectric behavior of the PVDF capacitor, as shown in Figure 113 a).

In order to study the reproducibility of the fabrication process, the PVDF capacitor area (1 cm^2 for the electromechanical characterization) was fixed for all the devices measured. Specifically, a batch of 8 sensors with the same geometrical parameters, i.e. the transistor channel length, was tested. Different forces, from 0.07 up to 5 N five times for each value, were applied onto the PVDF capacitor. Figure 113 b), shows the force dependent current variations. Interestingly, the sensor's response is highly reproducible, while at the same time being fully recoverable, as can be observed from the stable baseline current.

Figure 113 c) shows the calibration curve for one of the best performing device, where the achieved sensitivity is equal to 194 nA/N, while in Figure 113 d) the average calibration curve over 8 devices is plotted. The average sensitivity is 156 ± 4 nA/N, with a linear response in the range 0.07–5 N, a typical range for artificial skin applications.

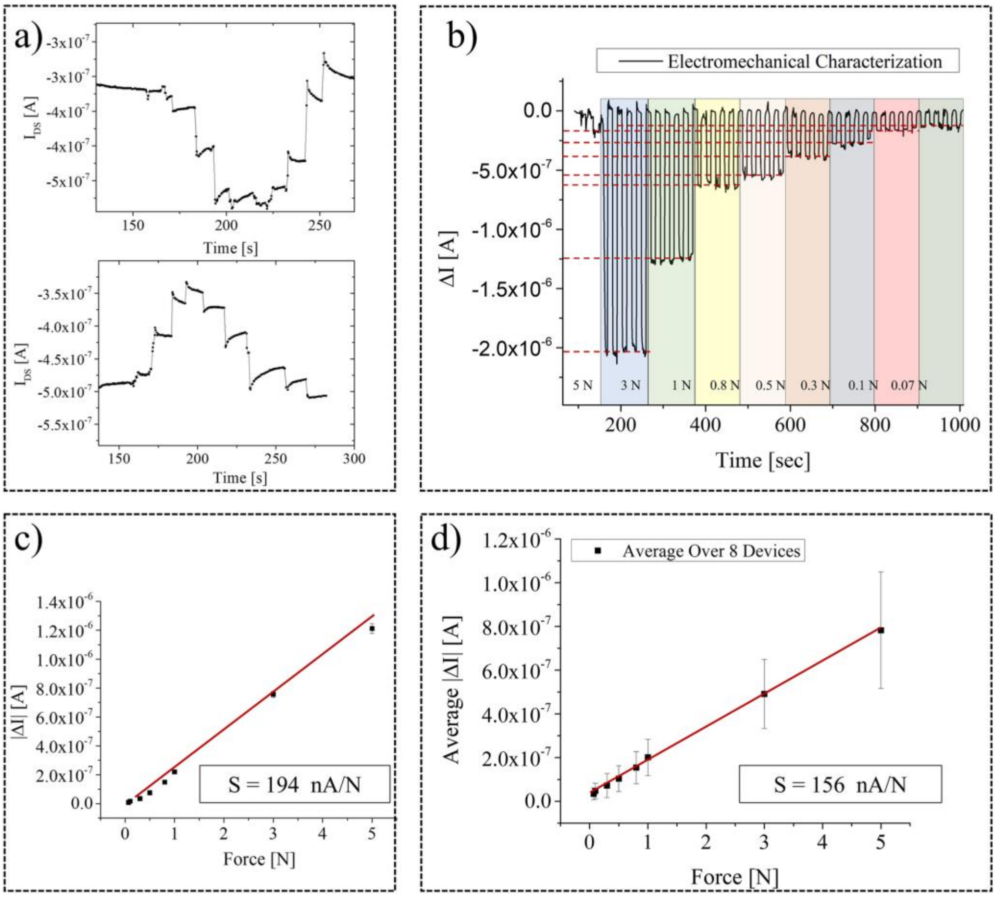

Figure 113 Force characterization for the proposed device. (a) Flipping test: connecting the top or the bottom PVDF capacitor gives rise to an opposite response. (b) Sensor response to different force ranges, from 5 N to 0.07 N. Each force was applied 5 times and reproducibility in sensor response is remarkable; (c) calibration curve of the one of the most performing devices, where the achieved sensitivity is equal to 194 nA/N; (d) average calibration curve, computed as the mean of the variation of the output current (mean[ΔI]), for a batch of 8 devices. The response has a linear shape in the regime 0.07–5 N and the sensitivity, i.e., the slope of the curve, is 156 nA/N.

Also in this case, the fabricated sensors are characterized by a sensitivity which is significantly higher than what previously reported in the literature. Fastier-Wooller et al. [131], for instance, have reported a sensitivity around 2.55% N^{-1}, whereas the highest sensitivity reported in planar OCMFET employed as tactile sensors was around 35 nA/N [138]. Therefore, this approach allowed to obtained higher sensitivity also in the force characterization.

7.7. Multimodal characterization

Once the devices was independently characterized as temperature and force sensor, a prototype of an integrated version of the sensor was fabricated. Specifically, a PVDF capacitor, in this case with 0.25 cm^2 area, was glued directly on the floating gate of the transistor by using a thin conductive glue layer. Figure 114 reports the schematic and an optical image of the integrated prototype of the v-OCMFET.

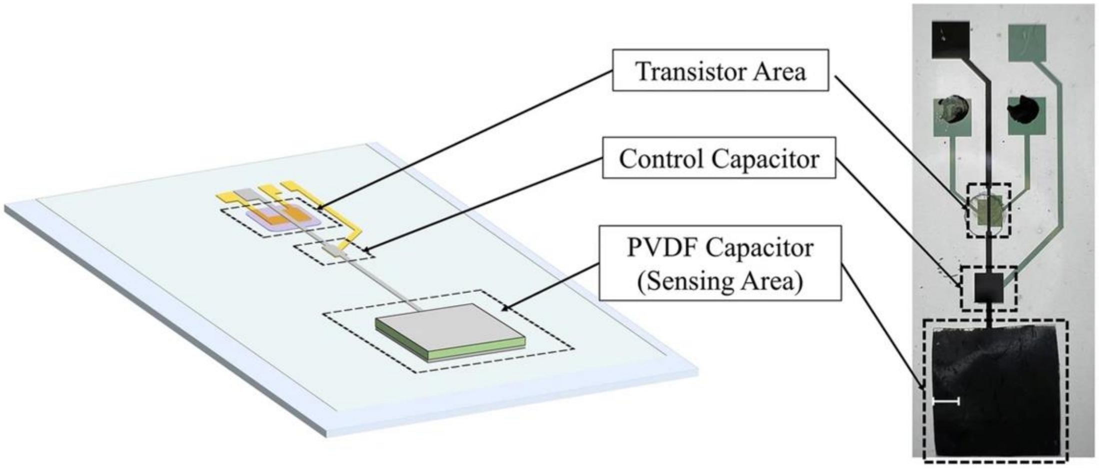

Figure 114 Optical photo and sketch of the integrated vertical channel OCMFET for multimodal tactile sensing. The transistor area, the control capacitor and the PVDF capacitor glued on the floating gate are highlighted. Scale bar 1 mm.

At first, the device was characterized as temperature sensor, using the same approach reported before, obtaining consistent results in terms of detection range and sensitivity. In fact, the device was able to distinguish between different temperature stimuli, as it is possible to clearly observe in Figure 115 a), where the sensor’s dynamic response in the time domain is reported. Moreover, the integrated version of the device exhibited a detection range and sensitivity similar to what reported above. Specifically, the previously presented v-OCMFET with the mechanically decoupled PVDF capacitor with an area of 0.25 cm^2 reported a detection range of 8–9 °C and an average sensitivity of 266 nA/°C (over 8 devices). Similarly, the integrated version of the tactile sensor reported a temperature detection range of 5-6 °C and a sensitivity of 250 nA/°C.

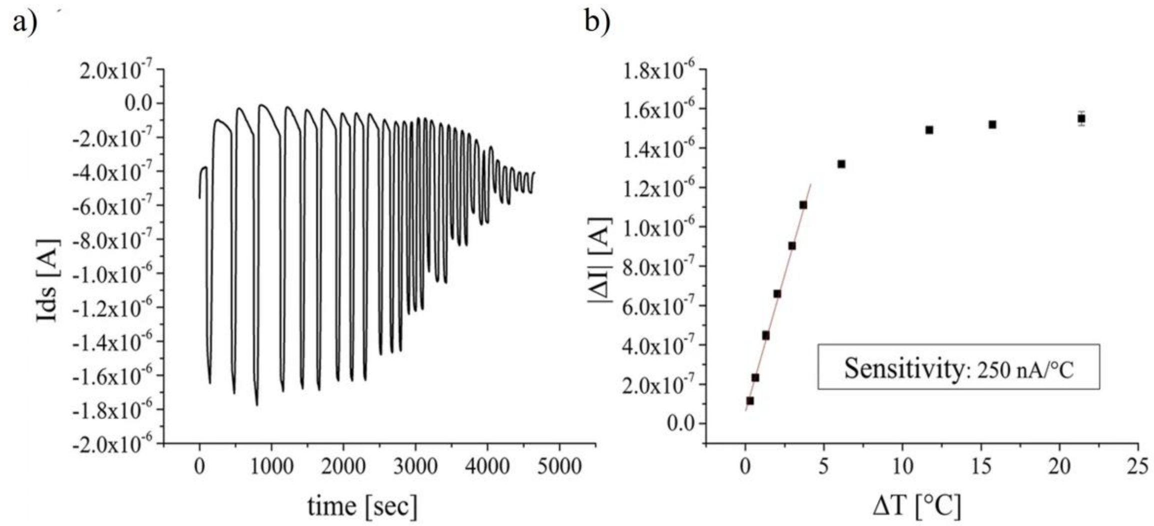

Figure 115 Thermal characterization of the integrated device. (a) Dynamic response of the integrated version of the v-OCMFET for tactile sensing applications;(b) the calibration curve shows a very similar results in terms of detection range and sensitivity with respect the thermal characterization reported above for the v-OCMFET with the PVDF capacitor mechanically decoupled.

Subsequently, the same device was characterized as multimodal tactile sensor by inducing the simultaneous variation of temperature and force. As shown in Figure 116 a), the sensor was capable to clearly detect different applied forces (0.5, 1,3, and 5 N) for all the different temperatures excited. For all the temperature steps, a calibration curve was obtained as shown in Figure 116 b). Moreover, the opposite variation of the current induced by the two stimuli allows a straightforward discrimination of the two, for example using a simple data processing algorithm.

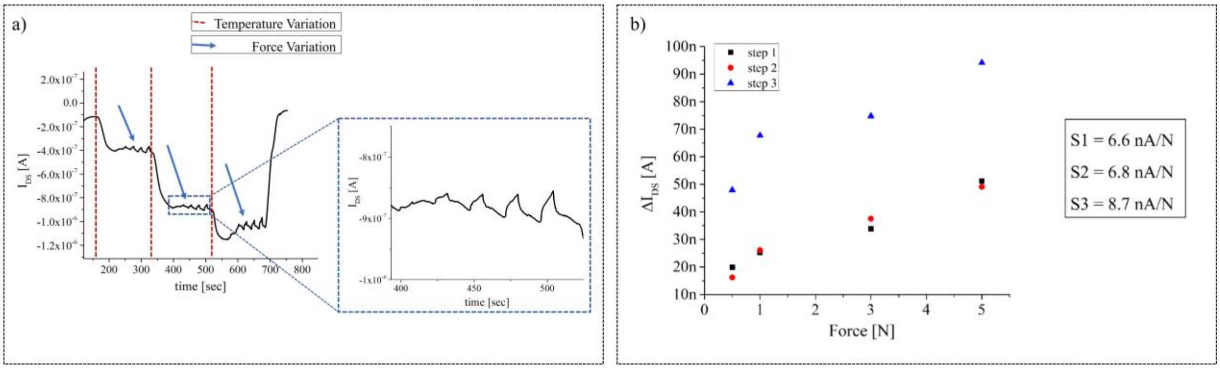

Figure 116 Multimodal characterization. a) Multimodal characterization for the integrated device, where simultaneously temperature and force stimuli are exercised; b) calibration curve and sensitivity of the force response from the multimodal characterization.

Therefore, this approach enabled the possibility to developed a highly reproducible, simple and effective strategy for the fabrication of a flexible multimodal temperature and force sensor based on an organic transistor coupled with the pyro/piezoelectric polymer poly-vinylene difluoride (PVDF). In particular, thanks to a low-resolution, and up-scalable method it was possible to obtain a sub-micrometer vertical channel OCMFET with high sensitivity and a linear response in a wide range of temperature and force variations, while reducing at the same time its overall dimensions. Moreover, the integrated version of the device, characterized as a multimodal sensor, demonstrated the possibility to simultaneously transduce temperature and force stimuli. Ultimately, this innovative approach provides an interesting solution to the problem of device integration and at the same time offers a simple way to increase the sensitivity, thus opening up new possibilities for the fabrication of high spatial resolution arrays of highly sensitive organic transducers. Table 6 reports a comparison between several tactile transducers reported at the state-of-the-art and the proposed device

Table 6 Comparison between the proposed device and different tactile sensors for wearable applications reported at the state-of-the-art .

Reference	**Device configuration**	**Sensitivity (Temperature)**	**Sensitivity (Force/Pressure)**	**Multimodal**
Park et al. [184]	Capacitance variation	//	1.12 MPa^{-1}	no
Ren et al. [127]	Thermistor	20.4 ($\Delta R/R$)	//	no
Liu et al. [120]	OTFT; dielectric capacitance variation	//	452.7 kPa^{-1}	no
Jiang et al. [185]	OTFT; dielectric capacitance variation	//	691.9 kPa^{-1}	no
Zhang et al. [128]	MFSOTE	35.5 μV/K	28.9 kPa^{-1}	yes
Shin et al. [129]	triboelectric and pyroelectric	0.27 nA °C^{-1}	2.2 V kPa^{-1}	yes
Fastier-Wooller et al. [130]	piezoelectric (CNT-PAN based sensor)	–800 ppm K^{-1} (TCR)	0.63% kPa^{-1}	yes
Fastier-Wooller et al. [131]	[P(VDF-TrFE)] micro-nanofiber	//	0.50% kPa^{-1} (2.55% N^{-1})	no
Park et al. [132]	microstructured ferroelectric	2.93%/°C (TCR)	35 μA/Pa (< 2.45 kPa); 5 μA/Pa (2.45-17.15 kPa)	yes
You et al. [133]	ionic-based receptor	10.4%/°C	Not reported	yes
Wang et al. [134]	thermoelectric film and porous microconed elastomer	3.77 mV K^{-1}	37 kPa^{-1}	yes

Trung et al. [137]	Stretchable OTFT	1.34%/°C	Not reported	yes
Meng et al. [138]	OTFT coupled with a piezoelectric ceramic	Not reported	Not reported	yes
Spanu et al. [183]	Planar OCMFET	//	9.78 nA/N (@500 Hz)	no
Viola et al. [139]	Planar OCMFET	70 nA/°C	35 nA/N	yes
This work	Vertical OCMFET	1 µA/°C	194 nA/N	yes

Conclusion

The work presented in this thesis is the result of three years of research in the field of flexible electronics, during which several advancements in realizing wearable and *more-than-wearable* devices based on organic electronics were achieved. The contest of wearable electronics is a continuously growing field, where different devices for various applications are developed, such as sensors for healthcare and continuous monitoring of vital parameters, devices for personal assistance and communication and notifications, or devices for haptic feedback and artificial electronic skin, but also all the required building blocks for the fabrication of the electronic systems necessary for the local processing and conditioning of such signals. In this context, there are a plethora of sensors and devices that could be embedded into objects that come in contact with people and that could be directly attached to the human skin. In addition to the different possible applications developed in this contest, the monetary perspective shows how fast this electronic technology field is growing, leading to a more and more personalized and interconnected world for the final user.

In this large and various field of research, this thesis focused on three main topics.

1. The first part of this work focused on the epidermal electrodes field. Among the different methods to produce dry electrodes for the detection of biopotentials from the surface of the skin, there is still a lack of a definitive solution to provide at the same time a low-cost and easy fabrication process over large areas and ultra-conformable substrates and at the same time capable of reducing skin irritations and issues. In this context, a novel approach to identify a possible solution for these several issues was proposed. Specifically, a simple and up scalable fabrication technique for the fabrication of breathable and ultra-conformable dry tattoo electrodes based on perforated Parylene C nanofilms were presented. Such electrodes present very good breathability, even overcoming that of common textiles and other materials used for realizing wearable sensors in contact with the skin, as well as excellent performances in terms of electrical characteristics and signal recording. In particular, the analysis performed on both breathable and non-breathable tattoo electrodes revealed comparable performance in terms of noise and SNR to commercial disposable gelled Ag/AgCl electrodes, as also confirmed by the cardiologist’s analysis, demonstrating the suitability of the Parylene

C based electrodes for ECG detection. Moreover, the negligible impact of the perforation (at least at values of pore density and dimensions that ensure their breathability) on the quality of the detected electrical signal was demonstrated. Moreover, a further analysis with the aim to demonstrate the suitability of such breathable Parylene C-based electrodes for long term acquisitions was conducted. In fact, even after 9 hours, the quality of the bio-signal detected by the breathable electrode was not significantly worsened. Compared with both non-breathable electrodes made with the same materials and with commercial gelled electrodes, breathable electrodes showed a superior performance in terms of impact on the skin even after several hours. All of these elements corroborate the idea that this technology could represent a valid alternative to commercial electrodes in critical applications, such as bio-monitoring of elderly and new-born patients or intensive care of severely burnt people, where imperceptibility and breathability are of great importance.

Epidermal electrodes are particularly interesting for wearable applications. Therefore, during this thesis work, a new solution for the acquisition of the EEG signal capable of combining the advantages of the wearable approach to those of epidermal imperceptible electrodes was implemented. In particular, the system composed of a custom Printed Circuit Board (PCB) and a modified headband specifically designed to conveniently interface unconventional ultrathin tattoo electrodes, showed the suitability of the Parylene C-based electrodes not only for healthcare and vital parameters monitoring but also for different applications, such as brain-computer interface (BCI). In particular, the idea was to drastically reduce the amount of adhesive required for commercial pre-gelled electrodes, and at the same time develop a new system capable of conveniently and unobtrusively monitoring brain signals. This wearable device, which combined standard off-the-shelf components and a novel epidermal electronic technology, showed the capabilities to detect and distinguish alpha and beta brain waves, which is the starting point for developing BCI applications. However, a critical aspect of this technology is the external connection with the recording devices because of the extremely low thickness of the electrodes. In fact, the interface between ultrathin functional films for epidermal applications and the external recording instruments or readout electronics still represents one of the biggest challenges in the field of tattoo electronics. Therefore, this thesis focused on the production process of a free-standing electrode aimed to overcome these limitations. The proposed novel electrodes, based on ultrathin (3 μm thick in the thinner part) composite films made of a combination of PEDOT:PSS, PVA, and ferrite powder, can be easily connected to a measuring unit using simple magnetic connectors, thus preserving their mechanical stability and without compromising the conformability of the film. Moreover, this approach results in an extremely versatile and scalable fabrication process that allows modulating the intensity of the mechanical connection with the recording system by tuning the amount of ferrimagnetic powder in the blend and simultaneously to adapt the geometrical shape of the electrode according to the needs of the application. The preliminary assessment of the electrodes for ECG signal detection revealed a comparable performance with disposable gelled Ag/AgCl electrodes in terms of SpCoh, SNR, and BW, deserving further investigations with a larger sample size.

2. The second main research activity developed during this thesis work is the realization of high-performing devices as build-block for the next generation of wearable electronics. The core of the electronic circuits is with no doubt the transistor. In a field characterized by soft, flexible materials, the development of high-performing organic transistors is a key solution for several applications, such as all-integrated wearable sensing tattooable patches, vital signal processing and conditioning circuits to limit the noise interference, and devices for intercommunicating and exchanging continuous information in real-time at high frequencies (i.e. from MHz to GHz). However, such performances and frequency range are still largely prohibitive for organic OFETs, especially when scalable, large-area processes must be adopted. In fact, up to now, the development of OFETs is mostly limited to those fields where a fast response is not strictly necessary. However, a common solution to improve the transistor performances is the reduction of the channel length. This strategy can enlarge the transistor form factor and thus lead to a miniaturization of the device and simultaneously improve the transistor performances. Nevertheless, scaling the transistor channel length generally requires sophisticated fabrication techniques that can negatively impact on one of the main advantages of organic semiconductors-based technologies, i.e., the possibility of fabricating flexible circuits at low costs and high-throughputs. Therefore, during this thesis work a simple approach for the fabrication of sub-micrometer channel flexible

OFETs was introduced. The devices have been fabricated using low-resolution photolithography and a large-area, highly reproducible self-aligned technique based on oxygen plasma patterning of Parylene C thin layers. In particular, the core of the short-channel organic transistor is the step-edge architecture, in which the Parylene C layer that forms the step defines the channel length. Therefore, with a easy and controlled technique it was possible to develop sub-micrometer channel length transistors. Interestingly, with the proposed solution, it was possible to obtain transistors with an operation frequency in the MHz range (up to 5.5 MHz) that can be characterized in continuous mode without any heat dissipation layer, thus representing a convenient approach for the development of compact, low-cost and high-performing OFET-based circuits onto flexible plastic substrates. Despite the nonidealities of the current version of the device, limitations that can be removed in future iterations by optimizing the semiconductor deposition and the gate/source–drain overlap, the present structure has promising potential applications for the development of high-speed organic circuits for flexible tags, wearable devices, and also high-density sensor arrays with integrated preamplification circuits for robotic skin.

3. The third and last topic developed during these three years of research is the fabrication and optimization process of tactile sensors for artificial electronic skin applications. Electronic skin is a widespread application in the wearable electronic field, where the focus is on the development of devices able to mimic human skin functionalities. The development of novel flexible and soft materials based on organic compound have led this research topic to rapid growth in the last decades. Several approaches have been proposed and with the outburst of the organic electronics, different devices, and systems able to mimic both sensory and mechanical human skin functionalities have been developed. With the intent to provide an advancement in this field, a highly reproducible, simple and effective strategy for the fabrication of a flexible multimodal temperature and force sensor was developed. Specifically, the proposed tactile sensor is based on an organic transistor coupled with the pyro/piezoelectric polymer poly-vinylene difluoride (PVDF). In particular, thanks to a low-resolution, and up-scalable method it was possible to obtain a sub-micrometer vertical channel Organic Charge Modulated Field Effect Transistor (OCMFET) with high sensitivity and a linear

response in a wide range of temperature and force variations, while reducing at the same time its overall dimensions. It is worth to consider that human skin has various receptor (mainly depending on the specific body region) and thus the possibility to develop high-density sensor array with multimodal tactile capabilities pave the way for a novel wearable patches for artificial skin applications The device was fully characterized in terms temperature and force response, showing a maximum sensitivity of 1 µA/°C and 194 nA/N. respectively. Moreover, in this thesis work, an integrated version of the device was fabricated. Such sensor was characterized as a multimodal sensor, showing the possibility to simultaneously transduce temperature and force stimuli. Ultimately, this innovative approach provides an interesting solution to the problem of device integration and at the same time offers a simple way to increase the sensitivity, thus opening up new possibilities for the fabrication of high spatial resolution arrays of highly sensitive organic transducers.

Bibliography

[1] M. Billinghurst and T. Starner, “Wearable devices: new ways to manage information,” *Computer*, vol. 32, no. 1, pp. 57–64, Jan. 1999, doi: 10.1109/2.738305.

[2] X. Tao and Textile Institute, Eds., *Wearable electronics and photonics*. Cambridge : Boca Raton FL: Woodhead ; CRC Press, 2005.

[3] K. Guk *et al.*, “Evolution of Wearable Devices with Real-Time Disease Monitoring for Personalized Healthcare,” *Nanomaterials*, vol. 9, no. 6, p. 813, May 2019, doi: 10.3390/nano9060813.

[4] G. Aroganam, N. Manivannan, and D. Harrison, “Review on Wearable Technology Sensors Used in Consumer Sport Applications,” *Sensors*, vol. 19, no. 9, p. 1983, Apr. 2019, doi: 10.3390/s19091983.

[5] J. Dunn, R. Runge, and M. Snyder, “Wearables and the medical revolution,” *Pers. Med.*, vol. 15, no. 5, pp. 429–448, Sep. 2018, doi: 10.2217/pme-2018-0044.

[6] W. Heng, S. Solomon, and W. Gao, “Flexible Electronics and Devices as Human–Machine Interfaces for Medical Robotics,” *Adv. Mater.*, vol. 34, no. 16, p. 2107902, Apr. 2022, doi: 10.1002/adma.202107902.

[7] K. Oberhofer, R. Erni, M. Sayers, D. Huber, F. Lüthy, and S. Lorenzetti, “Validation of a Smartwatch-Based Workout Analysis Application in Exercise Recognition, Repetition Count and Prediction of 1RM in the Strength Training-Specific Setting,” *Sports*, vol. 9, no. 9, p. 118, Aug. 2021, doi: 10.3390/sports9090118.

[8] S.-S. Lee, I.-H. Son, J.-G. Choi, D.-H. Nam, Y.-S. Hong, and W.-B. Lee, “Estimated Blood Pressure Algorithm for a Wrist-wearable Pulsimeter Using Hall Device,” *J. Korean Phys. Soc.*, vol. 58, no. 2, pp. 349–352, Feb. 2011, doi: 10.3938/jkps.58.349.

[9] S. Hwang and S. Lee, “Wristband-type wearable health devices to measure construction workers’ physical demands,” *Autom. Constr.*, vol. 83, pp. 330–340, Nov. 2017, doi: 10.1016/j.autcon.2017.06.003.

[10] S. K. Vashist, “Non-invasive glucose monitoring technology in diabetes management: A review,” *Anal. Chim. Acta*, vol. 750, pp. 16–27, Oct. 2012, doi: 10.1016/j.aca.2012.03.043.

[11] R. López-Blanco *et al.*, “Smartwatch for the analysis of rest tremor in patients with Parkinson’s disease,” *J. Neurol. Sci.*, vol. 401, pp. 37–42, Jun. 2019, doi: 10.1016/j.jns.2019.04.011.

[12] Y. K. Ro, A. Brem, and P. A. Rauschnabel, “Augmented Reality Smart Glasses: Definition, Concepts and Impact on Firm Value Creation,” in *Augmented Reality and Virtual Reality*, T. Jung and M. C. Tom Dieck, Eds., in Progress in IS. , Cham: Springer International Publishing, 2018, pp. 169–181. doi: 10.1007/978-3-319-64027-3_12.

[13] S. Mitrasinovic *et al.*, “Clinical and surgical applications of smart glasses,” *Technol. Health Care*, vol. 23, no. 4, pp. 381–401, Jul. 2015, doi: 10.3233/THC-150910.

[14] J. R. Sempionatto *et al.*, “Eyeglasses based wireless electrolyte and metabolite sensor platform,” *Lab. Chip*, vol. 17, no. 10, pp. 1834–1842, 2017, doi: 10.1039/C7LC00192D.

[15] A. Ometov *et al.*, “A Survey on Wearable Technology: History, State-of-the-Art and Current Challenges,” *Comput. Netw.*, vol. 193, p. 108074, Jul. 2021, doi: 10.1016/j.comnet.2021.108074.

[16] T. Skyrme and S. Dale, “Wearable Technology Forecasts 2023-2033.” [Online]. Available: https://www.idtechex.com/en/research-report/wearable-technology-forecasts-2023-2033/928

[17] T. Sekitani, M. Kaltenbrunner, T. Yokota, and T. Someya, “Imperceptible Electronic Skin,” *Inf. Disp.*, vol. 30, no. 1, pp. 20–25, Jan. 2014, doi: 10.1002/j.2637-496X.2014.tb00680.x.

[18] M. Kaltenbrunner *et al.*, “An ultra-lightweight design for imperceptible plastic electronics,” *Nature*, vol. 499, no. 7459, pp. 458–463, Jul. 2013, doi: 10.1038/nature12314.

[19] A. Chortos and Z. Bao, “Skin-inspired electronic devices,” *Mater. Today*, vol. 17, no. 7, pp. 321–331, Sep. 2014, doi: 10.1016/j.mattod.2014.05.006.

[20] J. Y. Oh and Z. Bao, “Second Skin Enabled by Advanced Electronics,” *Adv. Sci.*, vol. 6, no. 11, p. 1900186, Jun. 2019, doi: 10.1002/advs.201900186.

[21] T. Someya and M. Amagai, “Toward a new generation of smart skins,” *Nat. Biotechnol.*, vol. 37, no. 4, pp. 382–388, Apr. 2019, doi: 10.1038/s41587-019-0079-1.

[22] D.-H. Kim *et al.*, “Epidermal Electronics,” *Science*, vol. 333, no. 6044, pp. 838–843, Aug. 2011, doi: 10.1126/science.1206157.

[23] S. Wang *et al.*, “Mechanics of Epidermal Electronics,” *J. Appl. Mech.*, vol. 79, no. 3, p. 031022, May 2012, doi: 10.1115/1.4005963.

[24] S. Park, M. Takakuwa, K. Fukuda, S. Lee, T. Yokota, and T. Someya, “Toward ultraflexible organic electronic devices,” *MRS Bull.*, Sep. 2023, doi: 10.1557/s43577-023-00593-6.

[25] J.-W. Jeong *et al.*, “Materials and Optimized Designs for Human-Machine Interfaces Via Epidermal Electronics,” *Adv. Mater.*, vol. 25, no. 47, pp. 6839–6846, Dec. 2013, doi: 10.1002/adma.201301921.

[26] R. A. Nawrocki, N. Matsuhisa, T. Yokota, and T. Someya, “300-nm Imperceptible, Ultraflexible, and Biocompatible e-Skin Fit with Tactile Sensors and Organic Transistors,” *Adv. Electron. Mater.*, vol. 2, no. 4, p. 1500452, Apr. 2016, doi: 10.1002/aelm.201500452.

[27] R. A. Nawrocki, H. Jin, S. Lee, T. Yokota, M. Sekino, and T. Someya, “Self-Adhesive and Ultra-Conformable, Sub-300 nm Dry Thin-Film Electrodes for Surface Monitoring of Biopotentials,” *Adv. Funct. Mater.*, vol. 28, no. 36, p. 1803279, Sep. 2018, doi: 10.1002/adfm.201803279.

[28] M. J. Mirshojaeian Hosseini *et al.*, “270 nm ultra-thin self-adhesive conformable and long-term air-stable complimentary organic transistors and amplifiers,” *Npj Flex. Electron.*, vol. 7, no. 1, p. 38, Aug. 2023, doi: 10.1038/s41528-023-00267-y.

[29] S. Kabiri Ameri *et al.*, “Graphene Electronic Tattoo Sensors,” *ACS Nano*, vol. 11, no. 8, pp. 7634–7641, Aug. 2017, doi: 10.1021/acsnano.7b02182.

[30] T. An *et al.*, “Self-powered gold nanowire tattoo triboelectric sensors for soft wearable human-machine interface,” *Nano Energy,* vol. 77, p. 105295, Nov. 2020, doi: 10.1016/j.nanoen.2020.105295.

[31] L. M. Ferrari, K. Keller, B. Burtscher, and F. Greco, “Temporary tattoo as unconventional substrate for conformable and transferable electronics on skin and beyond,” *Multifunct. Mater.*, vol. 3, no. 3, p. 032003, Aug. 2020, doi: 10.1088/2399-7532/aba6e3.

[32] L. Bareket *et al.*, “Temporary-tattoo for long-term high fidelity biopotential recordings,” *Sci. Rep.*, vol. 6, no. 1, p. 25727, May 2016, doi: 10.1038/srep25727.

[33] L. Inzelberg, D. Rand, S. Steinberg, M. David-Pur, and Y. Hanein, “A Wearable High-Resolution Facial Electromyography for Long Term Recordings in Freely Behaving Humans,” *Sci. Rep.*, vol. 8, no. 1, p. 2058, Feb. 2018, doi: 10.1038/s41598-018-20567-y.

[34] A. J. Casson, R. Saunders, and J. C. Batchelor, “Five Day Attachment ECG Electrodes for Longitudinal Bio-Sensing Using Conformal Tattoo Substrates,” *IEEE Sens. J.*, vol. 17, no. 7, pp. 2205–2214, Apr. 2017, doi: 10.1109/JSEN.2017.2650564.

[35] X. Guo *et al.*, “A Self-Wetting Paper Electrode for Ubiquitous Bio-Potential Monitoring,” *IEEE Sens. J.*, vol. 17, no. 9, pp. 2654–2661, May 2017, doi: 10.1109/JSEN.2017.2684825.

[36] S. Shustak *et al.*, “Home monitoring of sleep with a temporary-tattoo EEG, EOG and EMG electrode array: a feasibility study,” *J. Neural Eng.*, vol. 16, no. 2, p. 026024, Apr. 2019, doi: 10.1088/1741-2552/aafa05.

[37] Y. Wang *et al.*, “Low-cost, μm-thick, tape-free electronic tattoo sensors with minimized motion and sweat artifacts,” *Npj Flex. Electron.*, vol. 2, no. 1, p. 6, Feb. 2018, doi: 10.1038/s41528-017-0019-4.

[38] Y. Wang *et al.*, “Electrically compensated, tattoo-like electrodes for epidermal electrophysiology at scale,” *Sci. Adv.*, vol. 6, no. 43, p. eabd0996, Oct. 2020, doi: 10.1126/sciadv.abd0996.

[39] L. Zhang *et al.*, “Fully organic compliant dry electrodes self-adhesive to skin for long-term motion-robust epidermal biopotential monitoring,” *Nat. Commun.*, vol. 11, no. 1, p. 4683, Sep. 2020, doi: 10.1038/s41467-020-18503-8.

[40] A. Aguzin *et al.*, “Direct ink writing of PEDOT eutectogels as substrate-free dry electrodes for electromyography,” *Mater. Horiz.*, vol. 10, no. 7, pp. 2516–2524, 2023, doi: 10.1039/D3MH00310H.

[41] A. Zucca *et al.*, “Tattoo Conductive Polymer Nanosheets for Skin-Contact Applications,” *Adv. Healthc. Mater.*, vol. 4, no. 7, pp. 983–990, May 2015, doi: 10.1002/adhm.201400761.

[42] L. M. Ferrari *et al.*, “Ultraconformable Temporary Tattoo Electrodes for Electrophysiology,” *Adv. Sci.*, vol. 5, no. 3, p. 1700771, Mar. 2018, doi: 10.1002/advs.201700771.

[43] L. M. Ferrari, U. Ismailov, J.-M. Badier, F. Greco, and E. Ismailova, “Conducting polymer tattoo electrodes in clinical electro- and magneto-encephalography,” *Npj Flex. Electron.*, vol. 4, no. 1, p. 4, Mar. 2020, doi: 10.1038/s41528-020-0067-z.

[44] S. K. Ameri *et al.*, “Imperceptible electrooculography graphene sensor system for human–robot interface,” *Npj 2D Mater. Appl.*, vol. 2, no. 1, p. 19, Jul. 2018, doi: 10.1038/s41699-018-0064-4.

[45] T. Ha *et al.*, “A Chest-Laminated Ultrathin and Stretchable E-Tattoo for the Measurement of Electrocardiogram, Seismocardiogram, and Cardiac Time Intervals,” *Adv. Sci.*, vol. 6, no. 14, p. 1900290, Jul. 2019, doi: 10.1002/advs.201900290.

[46] L. Liu *et al.*, “Nanofiber-Reinforced Silver Nanowires Network as a Robust, Ultrathin, and Conformable Epidermal Electrode for Ambulatory Monitoring of Physiological Signals,” *Small*, vol. 15, no. 22, p. 1900755, May 2019, doi: 10.1002/smll.201900755.

[47] Z. Jiang *et al.*, “Highly Stretchable Metallic Nanowire Networks Reinforced by the Underlying Randomly Distributed Elastic Polymer Nanofibers via Interfacial Adhesion Improvement,” *Adv. Mater.*, vol. 31, no. 37, p. 1903446, Sep. 2019, doi: 10.1002/adma.201903446.

[48] P. Fayyaz Shahandashti, H. Pourkheyrollah, A. Jahanshahi, and H. Ghafoorifard, “Highly conformable stretchable dry electrodes based on inexpensive flex substrate for long-term biopotential (EMG/ECG) monitoring,” *Sens. Actuators Phys.*, vol. 295, pp. 678–686, Aug. 2019, doi: 10.1016/j.sna.2019.06.041.

[49] J. Cao *et al.*, “Stretchable and Self-Adhesive PEDOT:PSS Blend with High Sweat Tolerance as Conformal Biopotential Dry Electrodes,” *ACS Appl. Mater. Interfaces*, vol. 14, no. 34, pp. 39159–39171, Aug. 2022, doi: 10.1021/acsami.2c11921.

[50] V. Baltatzis, K.-M. Bintsi, G. K. Apostolidis, and L. J. Hadjileontiadis, “Bullying incidences identification within an immersive environment using HD EEG-based analysis: A Swarm Decomposition and Deep Learning approach,” *Sci. Rep.*, vol. 7, no. 1, p. 17292, Dec. 2017, doi: 10.1038/s41598-017-17562-0.

[51] L. Hehenberger *et al.*, “Long-Term Mutual Training for the CYBATHLON BCI Race With a Tetraplegic Pilot: A Case Study on Inter-Session Transfer and Intra-Session Adaptation,” *Front. Hum. Neurosci.*, vol. 15, p. 635777, Feb. 2021, doi: 10.3389/fnhum.2021.635777.

[52] C. Qing, R. Qiao, X. Xu, and Y. Cheng, “Interpretable Emotion Recognition Using EEG Signals,” *IEEE Access*, vol. 7, pp. 94160–94170, 2019, doi: 10.1109/ACCESS.2019.2928691.

[53] S. Katsigiannis and N. Ramzan, “DREAMER: A Database for Emotion Recognition Through EEG and ECG Signals From Wireless Low-cost Off-the-Shelf Devices,” *IEEE J. Biomed. Health Inform.*, vol. 22, no. 1, pp. 98–107, Jan. 2018, doi: 10.1109/JBHI.2017.2688239.

[54] T. Song, W. Zheng, P. Song, and Z. Cui, “EEG Emotion Recognition Using Dynamical Graph Convolutional Neural Networks,” *IEEE Trans. Affect. Comput.*, vol. 11, no. 3, pp. 532–541, Jul. 2020, doi: 10.1109/TAFFC.2018.2817622.

[55] J. Zhang, Z. Yin, P. Chen, and S. Nichele, “Emotion recognition using multi-modal data and machine learning techniques: A tutorial and review,” *Inf. Fusion*, vol. 59, pp. 103–126, Jul. 2020, doi: 10.1016/j.inffus.2020.01.011.

[56] M. Seeck *et al.*, “The standardized EEG electrode array of the IFCN,” *Clin. Neurophysiol.*, vol. 128, no. 10, pp. 2070–2077, Oct. 2017, doi: 10.1016/j.clinph.2017.06.254.

[57] V. Goverdovsky, D. Looney, P. Kidmose, and D. P. Mandic, “In-Ear EEG From Viscoelastic Generic Earpieces: Robust and Unobtrusive 24/7 Monitoring,” *IEEE Sens. J.*, vol. 16, no. 1, pp. 271–277, Jan. 2016, doi: 10.1109/JSEN.2015.2471183.

[58] S. Debener, R. Emkes, M. De Vos, and M. Bleichner, “Unobtrusive ambulatory EEG using a smartphone and flexible printed electrodes around the ear,” *Sci. Rep.*, vol. 5, no. 1, p. 16743, Nov. 2015, doi: 10.1038/srep16743.

[59] K. B. Mikkelsen, S. L. Kappel, D. P. Mandic, and P. Kidmose, “EEG Recorded from the Ear: Characterizing the Ear-EEG Method,” *Front. Neurosci.*, vol. 9, Nov. 2015, doi: 10.3389/fnins.2015.00438.

[60] M. G. Bleichner and S. Debener, “Concealed, Unobtrusive Ear-Centered EEG Acquisition: cEEGrids for Transparent EEG,” *Front. Hum. Neurosci.*, vol. 11, Apr. 2017, doi: 10.3389/fnhum.2017.00163.

[61] A. J. Casson, “Wearable EEG and beyond,” *Biomed. Eng. Lett.*, vol. 9, no. 1, pp. 53–71, Feb. 2019, doi: 10.1007/s13534-018-00093-6.

[62] G. Acar, O. Ozturk, A. J. Golparvar, T. A. Elboshra, K. Böhringer, and M. K. Yapici, “Wearable and Flexible Textile Electrodes for Biopotential Signal Monitoring: A review,” *Electronics*, vol. 8, no. 5, p. 479, Apr. 2019, doi: 10.3390/electronics8050479.

[63] J. J. S. Norton *et al.*, “Soft, curved electrode systems capable of integration on the auricle as a persistent brain–computer interface,” *Proc. Natl. Acad. Sci.*, vol. 112, no. 13, pp. 3920–3925, Mar. 2015, doi: 10.1073/pnas.1424875112.

[64] H.-L. Peng *et al.*, “A novel passive electrode based on porous Ti for EEG recording,” *Sens. Actuators B Chem.*, vol. 226, pp. 349–356, Apr. 2016, doi: 10.1016/j.snb.2015.11.141.

[65] H. Klauk, “Organic thin-film transistors,” *Chem. Soc. Rev.*, vol. 39, no. 7, p. 2643, 2010, doi: 10.1039/b909902f.

[66] W. Shi, Y. Guo, and Y. Liu, “When Flexible Organic Field-Effect Transistors Meet Biomimetics: A Prospective View of the Internet of Things,” *Adv. Mater.*, vol. 32, no. 15, p. 1901493, Apr. 2020, doi: 10.1002/adma.201901493.

[67] M. D. Austin and S. Y. Chou, “Fabrication of 70 nm channel length polymer organic thin-film transistors using nanoimprint lithography,” *Appl. Phys. Lett.*, vol. 81, no. 23, pp. 4431–4433, Dec. 2002, doi: 10.1063/1.1526457.

[68] N. Li, W. Wu, and S. Y. Chou, “Sub-20-nm Alignment in Nanoimprint Lithography Using Moiré Fringe,” *Nano Lett.*, vol. 6, no. 11, pp. 2626–2629, Nov. 2006, doi: 10.1021/nl0603395.

[69] U. Haas, H. Gold, A. Haase, G. Jakopic, and B. Stadlober, “Submicron pentacene-based organic thin film transistors on flexible substrates,” *Appl. Phys. Lett.*, vol. 91, no. 4, p. 043511, Jul. 2007, doi: 10.1063/1.2763973.

[70] M. Leitgeb *et al.*, “Multilength Scale Patterning of Functional Layers by Roll-to-Roll Ultraviolet-Light-Assisted Nanoimprint Lithography,” *ACS Nano*, vol. 10, no. 5, pp. 4926–4941, May 2016, doi: 10.1021/acsnano.5b07411.

[71] U. Zschieschang, F. Letzkus, J. N. Burghartz, and H. Klauk, “Parameter Uniformity of Submicron-Channel-Length Organic Thin-Film Transistors Fabricated by Stencil Lithography,” *IEEE Trans. Nanotechnol.*, vol. 16, no. 5, pp. 837–841, Sep. 2017, doi: 10.1109/TNANO.2017.2655882.

[72] U. Zschieschang, J. W. Borchert, M. Geiger, F. Letzkus, J. N. Burghartz, and H. Klauk, “Stencil lithography for organic thin-film transistors with a channel length of 300 nm,” *Org. Electron.*, vol. 61, pp. 65–69, Oct. 2018, doi: 10.1016/j.orgel.2018.06.053.

[73] K. Tsukagoshi, K. Shigeto, I. Yagi, and Y. Aoyagi, “Interface modification of a pentacene field-effect transistor with a submicron channel,” *Appl. Phys. Lett.*, vol. 89, no. 11, p. 113507, Sep. 2006, doi: 10.1063/1.2348736.

[74] F. Ante *et al.*, “Contact Doping and Ultrathin Gate Dielectrics for Nanoscale Organic Thin-Film Transistors,” *Small*, vol. 7, no. 9, pp. 1186–1191, May 2011, doi: 10.1002/smll.201002254.

[75] B. Passarella *et al.*, “Direct-writing of organic field-effect transistors on plastic achieving 22 MHz transition frequency,” *Flex. Print. Electron.*, vol. 5, no. 3, p. 034001, Aug. 2020, doi: 10.1088/2058-8585/aba3af.

[76] A. Perinot, M. Giorgio, V. Mattoli, D. Natali, and M. Caironi, “Organic Electronics Picks Up the Pace: Mask-Less, Solution Processed Organic Transistors Operating at 160 MHz,” *Adv. Sci.*, vol. 8, no. 4, p. 2001098, Feb. 2021, doi: 10.1002/advs.202001098.

[77] K. Fukuda *et al.*, “Reverse-Offset Printing Optimized for Scalable Organic Thin-Film Transistors with Submicrometer Channel Lengths,” *Adv. Electron. Mater.*, vol. 1, no. 8, p. 1500145, Aug. 2015, doi: 10.1002/aelm.201500145.

[78] Y. Takeda *et al.*, “High-Speed Complementary Integrated Circuit with a Stacked Structure Using Fine Electrodes Formed by Reverse Offset Printing,” *ACS Appl. Electron. Mater.*, vol. 2, no. 3, pp. 763–768, Mar. 2020, doi: 10.1021/acsaelm.9b00829.

[79] T. Sekitani, Y. Noguchi, U. Zschieschang, H. Klauk, and T. Someya, “Organic transistors manufactured using inkjet technology with subfemtoliter accuracy,” *Proc. Natl. Acad. Sci.*, vol. 105, no. 13, pp. 4976–4980, Apr. 2008, doi: 10.1073/pnas.0708340105.

[80] H. Kleemann, K. Krechan, A. Fischer, and K. Leo, “A Review of Vertical Organic Transistors,” *Adv. Funct. Mater.*, vol. 30, no. 20, p. 1907113, May 2020, doi: 10.1002/adfm.201907113.

[81] Z. Xu, S.-H. Li, L. Ma, G. Li, and Y. Yang, “Vertical organic light emitting transistor,” *Appl. Phys. Lett.*, vol. 91, no. 9, p. 092911, Aug. 2007, doi: 10.1063/1.2778751.

[82] M. Greenman, G. Sheleg, C. Keum, J. Zucker, B. Lussem, and N. Tessler, “Reaching saturation in patterned source vertical organic field effect transistors,” *J. Appl. Phys.*, vol. 121, no. 20, p. 204503, May 2017, doi: 10.1063/1.4984053.

[83] G. Lee *et al.*, “Vertical organic light-emitting transistor showing a high current on/off ratio through dielectric encapsulation for the effective charge pathway,” *J. Appl. Phys.*, vol. 121, no. 2, p. 024502, Jan. 2017, doi: 10.1063/1.4974008.

[84] C.-M. Keum, I.-H. Lee, S.-H. Lee, G. J. Lee, M.-H. Kim, and S.-D. Lee, “Quasi-surface emission in vertical organic light-emitting transistors with network electrode,” *Opt. Express*, vol. 22, no. 12, p. 14750, Jun. 2014, doi: 10.1364/OE.22.014750.

[85] M. A. McCarthy *et al.*, “Low-Voltage, Low-Power, Organic Light-Emitting Transistors for Active Matrix Displays,” *Science*, vol. 332, no. 6029, pp. 570–573, Apr. 2011, doi: 10.1126/science.1203052.

[86] L. Ma and Y. Yang, “Unique architecture and concept for high-performance organic transistors,” *Appl. Phys. Lett.*, vol. 85, no. 21, pp. 5084–5086, Nov. 2004, doi: 10.1063/1.1821629.

[87] A. J. Ben-Sasson *et al.*, “Patterned electrode vertical field effect transistor fabricated using block copolymer nanotemplates,” *Appl. Phys. Lett.*, vol. 95, no. 21, p. 213301, Nov. 2009, doi: 10.1063/1.3266855.

[88] G. Sheleg, M. Greenman, B. Lussem, and N. Tessler, “Removing the current-limit of vertical organic field effect transistors,” *J. Appl. Phys.*, vol. 122, no. 19, p. 195502, Nov. 2017, doi: 10.1063/1.5005800.

[89] Y. Liu, H. Zhou, N. O. Weiss, Y. Huang, and X. Duan, “High-Performance Organic Vertical Thin Film Transistor Using Graphene as a Tunable Contact,” *ACS Nano*, vol. 9, no. 11, pp. 11102–11108, Nov. 2015, doi: 10.1021/acsnano.5b04612.

[90] J. S. Kim, B. J. Kim, Y. J. Choi, M. H. Lee, M. S. Kang, and J. H. Cho, “An Organic Vertical Field-Effect Transistor with Underside-Doped Graphene Electrodes,” *Adv. Mater.*, vol. 28, no. 24, pp. 4803–4810, Jun. 2016, doi: 10.1002/adma.201505378.

[91] T. Dogan, R. Verbeek, A. J. Kronemeijer, P. A. Bobbert, G. H. Gelinck, and W. G. Der Wiel, “Short-Channel Vertical Organic Field-Effect Transistors with High On/Off Ratios,” *Adv. Electron. Mater.*, vol. 5, no. 5, p. 1900041, May 2019, doi: 10.1002/aelm.201900041.

[92] K. Kudo, D. Xing Wang, M. Iizuka, S. Kuniyoshi, and K. Tanaka, “Schottky gate static induction transistor using copper phthalocyanine films,” *Thin Solid Films*, vol. 331, no. 1–2, pp. 51–54, Oct. 1998, doi: 10.1016/S0040-6090(98)00945-6.

[93] Y.-C. Chao *et al.*, “Polymer space-charge-limited transistor as a solid-state vacuum tube triode,” *Appl. Phys. Lett.*, vol. 97, no. 22, p. 223307, Nov. 2010, doi: 10.1063/1.3513334.

[94] Y. Yang and A. J. Heeger, “A new architecture for polymer transistors,” *Nature*, vol. 372, no. 6504, pp. 344–346, Nov. 1994, doi: 10.1038/372344a0.

[95] S. Fujimoto, K. Nakayama, and M. Yokoyama, “Fabrication of a vertical-type organic transistor with a planar metal base,” *Appl. Phys. Lett.*, vol. 87, no. 13, p. 133503, Sep. 2005, doi: 10.1063/1.2061866.

[96] A. Fischer, R. Scholz, K. Leo, and B. Lüssem, “An all C60 vertical transistor for high frequency and high current density applications,” *Appl. Phys. Lett.*, vol. 101, no. 21, p. 213303, Nov. 2012, doi: 10.1063/1.4767391.

[97] M. P. Klinger *et al.*, “Organic Power Electronics: Transistor Operation in the kA/cm2 Regime,” *Sci. Rep.*, vol. 7, no. 1, p. 44713, Mar. 2017, doi: 10.1038/srep44713.

[98] B. Kheradmand-Boroujeni, M. P. Klinger, A. Fischer, H. Kleemann, K. Leo, and F. Ellinger, “A Pulse-Biasing Small-Signal Measurement Technique Enabling 40 MHz Operation of Vertical Organic Transistors,” *Sci. Rep.*, vol. 8, no. 1, p. 7643, May 2018, doi: 10.1038/s41598-018-26008-0.

[99] E. Guo *et al.*, “Integrated complementary inverters and ring oscillators based on vertical-channel dual-base organic thin-film transistors,” *Nat. Electron.*, vol. 4, no. 8, pp. 588–594, Jul. 2021, doi: 10.1038/s41928-021-00613-w.

[100] E. Guo, F. Dollinger, B. Amaya, A. Fischer, and H. Kleemann, “Organic Permeable Base Transistors – Insights and Perspectives,” *Adv. Opt. Mater.*, vol. 9, no. 14, p. 2002058, Jul. 2021, doi: 10.1002/adom.202002058.

[101] R. Parashkov *et al.*, “Vertical channel all-organic thin-film transistors,” *Appl. Phys. Lett.*, vol. 82, no. 25, pp. 4579–4580, Jun. 2003, doi: 10.1063/1.1584786.

[102] R. Parashkov *et al.*, “Organic vertical-channel transistors structured using excimer laser,” *Appl. Phys. Lett.*, vol. 85, no. 23, pp. 5751–5753, Dec. 2004, doi: 10.1063/1.1833551.

[103] T. Takano, H. Yamauchi, M. Iizuka, M. Nakamura, and K. Kudo, “High-Speed Operation of Vertical Type Organic Transistors Utilizing Step-Edge Structures,” *Appl. Phys. Express*, vol. 2, p. 071501, Jul. 2009, doi: 10.1143/APEX.2.071501.

[104] Y. Chen and I. Shih, “Fabrication of vertical channel top contact organic thin film transistors,” *Org. Electron.*, vol. 8, no. 6, pp. 655–661, Dec. 2007, doi: 10.1016/j.orgel.2007.05.004.

[105] N. Stutzmann, R. H. Friend, and H. Sirringhaus, “Self-Aligned, Vertical-Channel, Polymer Field-Effect Transistors,” *Science*, vol. 299, no. 5614, pp. 1881–1884, Mar. 2003, doi: 10.1126/science.1081279.

[106] M. Uno *et al.*, “High-Speed Flexible Organic Field-Effect Transistors with a 3D Structure,” *Adv. Mater.*, vol. 23, no. 27, pp. 3047–3051, Jul. 2011, doi: 10.1002/adma.201101179.

[107] H. Kleemann, A. A. Günther, K. Leo, and B. Lüssem, “High-Performance Vertical Organic Transistors,” *Small*, vol. 9, no. 21, pp. 3670–3677, Nov. 2013, doi: 10.1002/smll.201202321.

[108] J. Lenz, F. Del Giudice, F. R. Geisenhof, F. Winterer, and R. T. Weitz, “Vertical, electrolyte-gated organic transistors show continuous operation in the MA cm−2 regime and artificial synaptic behaviour,” *Nat. Nanotechnol.*, vol. 14, no. 6, pp. 579–585, Jun. 2019, doi: 10.1038/s41565-019-0407-0.

[109] J. Lenz *et al.*, “High-Performance Vertical Organic Transistors of Sub-5 nm Channel Length,” *Nano Lett.*, vol. 21, no. 10, pp. 4430–4436, May 2021, doi: 10.1021/acs.nanolett.1c01144.

[110] M. J. Donahue *et al.*, “High-Performance Vertical Organic Electrochemical Transistors,” *Adv. Mater.*, vol. 30, no. 5, p. 1705031, Feb. 2018, doi: 10.1002/adma.201705031.

[111] Y. Cotur, M. Kasimatis, M. Kaisti, S. Olenik, C. Georgiou, and F. Güder, “Stretchable Composite Acoustic Transducer for Wearable Monitoring of Vital Signs,” *Adv. Funct. Mater.*, vol. 30, no. 16, p. 1910288, Apr. 2020, doi: 10.1002/adfm.201910288.

[112] S. Lai, A. Garufi, F. Madeddu, G. Angius, A. Bonfiglio, and P. Cosseddu, “A Wearable Platform for Monitoring Wrist Flexion and Extension in Biomedical Applications Using Organic Transistor-Based Strain Sensors,” *IEEE Sens. J.*, vol. 19, no. 15, pp. 6020–6028, Aug. 2019, doi: 10.1109/JSEN.2019.2909174.

[113] T. Someya, T. Sekitani, S. Iba, Y. Kato, H. Kawaguchi, and T. Sakurai, “A large-area, flexible pressure sensor matrix with organic field-effect transistors for artificial skin applications,” *Proc. Natl. Acad. Sci.*, vol. 101, no. 27, pp. 9966–9970, Jul. 2004, doi: 10.1073/pnas.0401918101.

[114] S. C. B. Mannsfeld *et al.*, “Highly sensitive flexible pressure sensors with microstructured rubber dielectric layers,” *Nat. Mater.*, vol. 9, no. 10, pp. 859–864, Oct. 2010, doi: 10.1038/nmat2834.

[115] G. Schwartz *et al.*, “Flexible polymer transistors with high pressure sensitivity for application in electronic skin and health monitoring,” *Nat. Commun.*, vol. 4, no. 1, p. 1859, May 2013, doi: 10.1038/ncomms2832.

[116] S. Baek, G. Y. Bae, J. Kwon, K. Cho, and S. Jung, “Flexible Pressure-Sensitive Contact Transistors Operating in the Subthreshold Regime,” *ACS Appl. Mater. Interfaces*, vol. 11, no. 34, pp. 31111–31118, Aug. 2019, doi: 10.1021/acsami.9b09636.

[117] D.-I. Kim *et al.*, “A Sensor Array Using Multi-functional Field-effect Transistors with Ultrahigh Sensitivity and Precision for Bio-monitoring,” *Sci. Rep.*, vol. 5, no. 1, p. 12705, Jul. 2015, doi: 10.1038/srep12705.

[118] Y. Zang, F. Zhang, D. Huang, X. Gao, C. Di, and D. Zhu, “Flexible suspended gate organic thin-film transistors for ultra-sensitive pressure detection,” *Nat. Commun.*, vol. 6, no. 1, p. 6269, Mar. 2015, doi: 10.1038/ncomms7269.

[119] S.-H. Shin *et al.*, “Integrated arrays of air-dielectric graphene transistors as transparent active-matrix pressure sensors for wide pressure ranges,” *Nat. Commun.*, vol. 8, no. 1, p. 14950, Mar. 2017, doi: 10.1038/ncomms14950.

[120] Z. Liu, Z. Yin, J. Wang, and Q. Zheng, “Polyelectrolyte Dielectrics for Flexible Low-Voltage Organic Thin-Film Transistors in Highly Sensitive Pressure Sensing,” *Adv. Funct. Mater.*, vol. 29, no. 1, p. 1806092, Jan. 2019, doi: 10.1002/adfm.201806092.

[121] Y. Jiang, Z. Liu, Z. Yin, and Q. Zheng, “Sandwich structured dielectrics for air-stable and flexible low-voltage organic transistors in ultrasensitive pressure sensing,” *Mater. Chem. Front.*, vol. 4, no. 5, pp. 1459–1470, 2020, doi: 10.1039/D0QM00062K.

[122] B. Arman Kuzubasoglu and S. Kursun Bahadir, “Flexible temperature sensors: A review,” *Sens. Actuators Phys.*, vol. 315, p. 112282, Nov. 2020, doi: 10.1016/j.sna.2020.112282.

[123] M. D. Dankoco, G. Y. Tesfay, E. Benevent, and M. Bendahan, “Temperature sensor realized by inkjet printing process on flexible substrate,” *Mater. Sci. Eng. B*, vol. 205, pp. 1–5, Mar. 2016, doi: 10.1016/j.mseb.2015.11.003.

[124] T. Vuorinen, J. Niittynen, T. Kankkunen, T. M. Kraft, and M. Mäntysalo, “Inkjet-Printed Graphene/PEDOT:PSS Temperature Sensors on a Skin-Conformable Polyurethane Substrate,” *Sci. Rep.*, vol. 6, no. 1, p. 35289, Oct. 2016, doi: 10.1038/srep35289.

[125] C. Zhu, H.-C. Wu, G. Nyikayaramba, Z. Bao, and B. Murmann, “Intrinsically Stretchable Temperature Sensor Based on Organic Thin-Film Transistors,” *IEEE Electron Device Lett.*, vol. 40, no. 10, pp. 1630–1633, Oct. 2019, doi: 10.1109/LED.2019.2933838.

[126] X. Wu *et al.*, “Thermally Stable, Biocompatible, and Flexible Organic Field-Effect Transistors and Their Application in Temperature Sensing Arrays for Artificial Skin,” *Adv. Funct. Mater.*, vol. 25, no. 14, pp. 2138–2146, Apr. 2015, doi: 10.1002/adfm.201404535.

[127] X. Ren *et al.*, “A Low-Operating-Power and Flexible Active-Matrix Organic-Transistor Temperature-Sensor Array,” *Adv. Mater.*, vol. 28, no. 24, pp. 4832–4838, Jun. 2016, doi: 10.1002/adma.201600040.

[128] F. Zhang, Y. Zang, D. Huang, C. Di, and D. Zhu, “Flexible and self-powered temperature–pressure dual-parameter sensors using microstructure-frame-supported

organic thermoelectric materials," *Nat. Commun.*, vol. 6, no. 1, p. 8356, Sep. 2015, doi: 10.1038/ncomms9356.

[129] Y. Shin, Y. Park, S. K. Ghosh, Y. Lee, J. Park, and H. Ko, "Ultrasensitive Multimodal Tactile Sensors with Skin-Inspired Microstructures through Localized Ferroelectric Polarization," *Adv. Sci.*, vol. 9, no. 9, p. 2105423, Mar. 2022, doi: 10.1002/advs.202105423.

[130] J. W. Fastier-Wooller, V. T. Dau, T. Dinh, C.-D. Tran, and D. V. Dao, "Pressure and temperature sensitive e-skin for in situ robotic applications," *Mater. Des.*, vol. 208, p. 109886, Oct. 2021, doi: 10.1016/j.matdes.2021.109886.

[131] J. W. Fastier-Wooller *et al.*, "Multimodal Fibrous Static and Dynamic Tactile Sensor," *ACS Appl. Mater. Interfaces*, vol. 14, no. 23, pp. 27317–27327, Jun. 2022, doi: 10.1021/acsami.2c08195.

[132] J. Park, M. Kim, Y. Lee, H. S. Lee, and H. Ko, "Fingertip skin–inspired microstructured ferroelectric skins discriminate static/dynamic pressure and temperature stimuli," *Sci. Adv.*, vol. 1, no. 9, p. e1500661, Oct. 2015, doi: 10.1126/sciadv.1500661.

[133] I. You *et al.*, "Artificial multimodal receptors based on ion relaxation dynamics," *Science*, vol. 370, no. 6519, pp. 961–965, Nov. 2020, doi: 10.1126/science.aba5132.

[134] Y. Wang *et al.*, "High-sensitivity self-powered temperature/pressure sensor based on flexible Bi-Te thermoelectric film and porous microconed elastomer," *J. Mater. Sci. Technol.*, vol. 103, pp. 1–7, Mar. 2022, doi: 10.1016/j.jmst.2021.07.008.

[135] T. Someya *et al.*, "Conformable, flexible, large-area networks of pressure and thermal sensors with organic transistor active matrixes," *Proc. Natl. Acad. Sci.*, vol. 102, no. 35, pp. 12321–12325, Aug. 2005, doi: 10.1073/pnas.0502392102.

[136] T. Q. Trung, N. T. Tien, Y. G. Seol, and N.-E. Lee, "Transparent and flexible organic field-effect transistor for multi-modal sensing," *Org. Electron.*, vol. 13, no. 4, pp. 533–540, Apr. 2012, doi: 10.1016/j.orgel.2011.12.015.

[137] T. Q. Trung, S. Ramasundaram, B.-U. Hwang, and N.-E. Lee, "An All-Elastomeric Transparent and Stretchable Temperature Sensor for Body-Attachable Wearable

Electronics,” *Adv. Mater.*, vol. 28, no. 3, pp. 502–509, Jan. 2016, doi: 10.1002/adma.201504441.

[138] Z. Meng *et al.*, “Lead Zirconate Titanate (a piezoelectric ceramic)-Based thermal and tactile bimodal organic transistor sensors,” *Org. Electron.*, vol. 80, p. 105673, May 2020, doi: 10.1016/j.orgel.2020.105673.

[139] F. A. Viola, A. Spanu, P. C. Ricci, A. Bonfiglio, and P. Cosseddu, “Ultrathin, flexible and multimodal tactile sensors based on organic field-effect transistors,” *Sci. Rep.*, vol. 8, no. 1, p. 8073, May 2018, doi: 10.1038/s41598-018-26263-1.

[140] A. Spanu *et al.*, “Parylene C-Based, Breathable Tattoo Electrodes for High-Quality Bio-Potential Measurements,” *Front. Bioeng. Biotechnol.*, vol. 10, p. 820217, Mar. 2022, doi: 10.3389/fbioe.2022.820217.

[141] H.-L. Peng, J.-Q. Liu, Y.-Z. Dong, B. Yang, X. Chen, and C.-S. Yang, “Parylene-based flexible dry electrode for bioptential recording,” *Sens. Actuators B Chem.*, vol. 231, pp. 1–11, Aug. 2016, doi: 10.1016/j.snb.2016.02.061.

[142] P. Gibson, D. Rivin, C. Kendrick, and H. Schreuder-Gibson, “Humidity-Dependent Air Permeability of Textile Materials1,” *Text. Res. J.*, vol. 69, no. 5, pp. 311–317, May 1999, doi: 10.1177/004051759906900501.

[143] X. Peng *et al.*, “A breathable, biodegradable, antibacterial, and self-powered electronic skin based on all-nanofiber triboelectric nanogenerators,” *Sci. Adv.*, vol. 6, no. 26, p. eaba9624, Jun. 2020, doi: 10.1126/sciadv.aba9624.

[144] W. Yang and X. Lu, “Triboelectric Power Generation from Heterostructured Air-Laid Paper for Breathable and Wearable Self-Charging Power System,” *Adv. Mater. Technol.*, vol. 4, no. 12, p. 1900745, Dec. 2019, doi: 10.1002/admt.201900745.

[145] G.-S. Liu *et al.*, “In Situ Electrospinning Iodine-Based Fibrous Meshes for Antibacterial Wound Dressing,” *Nanoscale Res. Lett.*, vol. 13, no. 1, p. 309, Dec. 2018, doi: 10.1186/s11671-018-2733-9.

[146] R. Cao *et al.*, “Screen-Printed Washable Electronic Textiles as Self-Powered Touch/Gesture Tribo-Sensors for Intelligent Human–Machine Interaction,” *ACS Nano*, vol. 12, no. 6, pp. 5190–5196, Jun. 2018, doi: 10.1021/acsnano.8b02477.

[147] S. Qiang, T. Carey, A. Arbab, W. Song, C. Wang, and F. Torrisi, “Wearable solid-state capacitors based on two-dimensional material all-textile heterostructures,” *Nanoscale*, vol. 11, no. 20, pp. 9912–9919, 2019, doi: 10.1039/C9NR00463G.

[148] Q. Wang *et al.*, “Multifunctional and Water-Resistant MXene-Decorated Polyester Textiles with Outstanding Electromagnetic Interference Shielding and Joule Heating Performances,” *Adv. Funct. Mater.*, vol. 29, no. 7, p. 1806819, Feb. 2019, doi: 10.1002/adfm.201806819.

[149] Figen SELLİ and Yıldıray TURHAN, “INVESTIGATION OF AIR PERMEABILITY AND MOISTURE MANAGEMENT PROPERTIES OF THE COMMERCIAL SINGLE JERSEY AND RIB KNITTED FABRICS,” *Investig. AIR PERMEABILITY MOISTURE Manag. Prop. Commer. SINGLE JERSEY RIB Knitt. Fabr.*, [Online]. Available: https://dergipark.org.tr/en/pub/tekstilvekonfeksiyon/issue/28634/306053#article_cite

[150] A. Mascia, R. Collu, A. Spanu, M. Fraschini, M. Barbaro, and P. Cosseddu, “Wearable System Based on Ultra-Thin Parylene C Tattoo Electrodes for EEG Recording,” *Sensors*, vol. 23, no. 2, p. 766, Jan. 2023, doi: 10.3390/s23020766.

[151] S. Meek, “ABC of clinical electrocardiography: Introduction. I---Leads, rate, rhythm, and cardiac axis,” *BMJ*, vol. 324, no. 7334, pp. 415–418, Feb. 2002, doi: 10.1136/bmj.324.7334.415.

[152] F. A. Castaño, A. M. Hernández, and G. Soto-Romero, “Assessment of artifacts reduction and denoising techniques in Electrocardiographic signals using Ensemble Average-based method,” *Comput. Methods Programs Biomed.*, vol. 182, p. 105034, Dec. 2019, doi: 10.1016/j.cmpb.2019.105034.

[153] R. Collu, A. Mascia, A. Spanu, M. Fraschini, P. Cosseddu, and M. Barbaro, “A wearable electronic system for EEG recording,” in *2022 17th Conference on Ph.D Research in Microelectronics and Electronics (PRIME)*, Villasimius, SU, Italy: IEEE, Jun. 2022, pp. 345–348. doi: 10.1109/PRIME55000.2022.9816817.

[154] T. C. Ferree, P. Luu, G. S. Russell, and D. M. Tucker, “Scalp electrode impedance, infection risk, and EEG data quality,” *Clin. Neurophysiol.*, vol. 112, no. 3, pp. 536–544, Mar. 2001, doi: 10.1016/S1388-2457(00)00533-2.

[155] G. Li, S. Wang, M. Li, and Y. Y. Duan, “Towards real-life EEG applications: novel superporous hydrogel-based semi-dry EEG electrodes enabling automatically ‘charge–discharge’ electrolyte,” *J. Neural Eng.*, vol. 18, no. 4, p. 046016, Aug. 2021, doi: 10.1088/1741-2552/abeeab.

[156] C. Cannard, H. Wahbeh, and A. Delorme, “Validating the wearable MUSE headset for EEG spectral analysis and Frontal Alpha Asymmetry,” in *2021 IEEE International Conference on Bioinformatics and Biomedicine (BIBM)*, Houston, TX, USA: IEEE, Dec. 2021, pp. 3603–3610. doi: 10.1109/BIBM52615.2021.9669778.

[157] C. M. Wilkinson, J. I. Burrell, J. W. P. Kuziek, S. Thirunavukkarasu, B. H. Buck, and K. E. Mathewson, “Predicting stroke severity with a 3-min recording from the Muse portable EEG system for rapid diagnosis of stroke,” *Sci. Rep.*, vol. 10, no. 1, p. 18465, Oct. 2020, doi: 10.1038/s41598-020-75379-w.

[158] C. Simar, M. Petieau, A. Cebolla, A. Leroy, G. Bontempi, and G. Cheron, “EEG-based brain-computer interface for alpha speed control of a small robot using the MUSE headband,” in *2020 International Joint Conference on Neural Networks (IJCNN)*, Glasgow, United Kingdom: IEEE, Jul. 2020, pp. 1–4. doi: 10.1109/IJCNN48605.2020.9207486.

[159] J. Malmivuo, *Bioelectromagnetism—Principles and Applications of Bioelectric and Biomagnetic Fields—The Internet Version*. Oxford University Press. UK, 1995.

[160] A. Delorme and S. Makeig, “EEGLAB: an open source toolbox for analysis of single-trial EEG dynamics including independent component analysis,” *J. Neurosci. Methods*, vol. 134, no. 1, pp. 9–21, Mar. 2004, doi: 10.1016/j.jneumeth.2003.10.009.

[161] S. D. Muthukumaraswamy, “High-frequency brain activity and muscle artifacts in MEG/EEG: a review and recommendations,” *Front. Hum. Neurosci.*, vol. 7, 2013, doi: 10.3389/fnhum.2013.00138.

[162] M. Fraschini, M. Demuru, A. Crobe, F. Marrosu, C. J. Stam, and A. Hillebrand, “The effect of epoch length on estimated EEG functional connectivity and brain network organisation,” *J. Neural Eng.*, vol. 13, no. 3, p. 036015, Jun. 2016, doi: 10.1088/1741-2560/13/3/036015.

[163] A. Spanu *et al.*, “Epidermal Electrodes with Ferrimagnetic/Conductive Properties for Biopotential Recordings,” *Bioengineering*, vol. 9, no. 5, p. 205, May 2022, doi: 10.3390/bioengineering9050205.

[164] S. Choi, H. Lee, R. Ghaffari, T. Hyeon, and D.-H. Kim, “Recent Advances in Flexible and Stretchable Bio-Electronic Devices Integrated with Nanomaterials,” *Adv. Mater.*, vol. 28, no. 22, pp. 4203–4218, Jun. 2016, doi: 10.1002/adma.201504150.

[165] M. Drack, I. Graz, T. Sekitani, T. Someya, M. Kaltenbrunner, and S. Bauer, “An Imperceptible Plastic Electronic Wrap,” *Adv. Mater.*, vol. 27, no. 1, pp. 34–40, Jan. 2015, doi: 10.1002/adma.201403093.

[166] K. Jang *et al.*, “Ferromagnetic, Folded Electrode Composite as a Soft Interface to the Skin for Long-Term Electrophysiological Recording,” *Adv. Funct. Mater.*, vol. 26, no. 40, pp. 7281–7290, Oct. 2016, doi: 10.1002/adfm.201603146.

[167] S. Taccola *et al.*, “Toward the Use of Temporary Tattoo Electrodes for Impedancemetric Respiration Monitoring and Other Electrophysiological Recordings on Skin,” *Sensors*, vol. 21, no. 4, p. 1197, Feb. 2021, doi: 10.3390/s21041197.

[168] W. Dai *et al.*, “Flexible Magnetoelectrical Devices with Intrinsic Magnetism and Electrical Conductivity,” *Adv. Electron. Mater.*, vol. 5, no. 6, p. 1900111, Jun. 2019, doi: 10.1002/aelm.201900111.

[169] F. Greco *et al.*, “Ultra-thin conductive free-standing PEDOT/PSS nanofilms,” *Soft Matter*, vol. 7, no. 22, p. 10642, 2011, doi: 10.1039/c1sm06174g.

[170] T. Park, M. Kim, E. K. Lee, J. Hur, and H. Yoo, “Overcoming Downscaling Limitations in Organic Semiconductors: Strategies and Progress,” *Small*, p. 2306468, Oct. 2023, doi: 10.1002/smll.202306468.

[171] A. Spanu, T. Losi, A. Mascia, A. Bonfiglio, M. Caironi, and P. Cosseddu, “Submicrometer-Channel Organic Transistors with MHz Operation Range on Flexible Substrates by a Low-Resolution Fabrication Technique,” *Adv. Mater. Technol.*, vol. 8, no. 1, p. 2200891, Jan. 2023, doi: 10.1002/admt.202200891.

[172] M. Kitamura, Y. Kuzumoto, S. Aomori, M. Kamura, J. H. Na, and Y. Arakawa, “Threshold voltage control of bottom-contact n-channel organic thin-film transistors using modified drain/source electrodes,” *Appl. Phys. Lett.*, vol. 94, no. 8, p. 083310, Feb. 2009, doi: 10.1063/1.3090489.

[173] A. Perinot, P. Kshirsagar, M. A. Malvindi, P. P. Pompa, R. Fiammengo, and M. Caironi, “Direct-written polymer field-effect transistors operating at 20 MHz,” *Sci. Rep.*, vol. 6, no. 1, p. 38941, Dec. 2016, doi: 10.1038/srep38941.

[174] S. Wang *et al.*, “Dielectric Selection for Solution-Processed High-Mobility TIPS-Pentacene Microwire Field-Effect Transistors,” *Adv. Mater. Interfaces*, vol. 6, no. 13, p. 1801984, Jul. 2019, doi: 10.1002/admi.201801984.

[175] E.-Y. Shin, E.-Y. Choi, and Y.-Y. Noh, “Parylene based bilayer flexible gate dielectric layer for top-gated organic field-effect transistors,” *Org. Electron.*, vol. 46, pp. 14–21, Jul. 2017, doi: 10.1016/j.orgel.2017.04.005.

[176] K. Kudo, T. Takano, H. Yamauchi, M. Iizuka, and M. Nakamura, “High-Speed Operation of Step-Edge Vertical-Channel Organic Transistors with Pentacene and 6,13-Bis(triisopropyl-silylethynyl) Pentacene,” *Jpn. J. Appl. Phys.*, vol. 49, no. 4S, p. 04DK03, Apr. 2010, doi: 10.1143/JJAP.49.04DK03.

[177] A. Mascia, A. Spanu, A. Bonfiglio, and P. Cosseddu, “Multimodal force and temperature tactile sensor based on a short-channel organic transistor with high sensitivity,” *Sci. Rep.*, vol. 13, no. 1, p. 16232, Sep. 2023, doi: 10.1038/s41598-023-43360-y.

[178] M. Barbaro, A. Bonfiglio, and L. Raffo, “A charge-modulated FET for detection of biomolecular processes: conception, modeling, and simulation,” *IEEE Trans. Electron Devices*, vol. 53, no. 1, pp. 158–166, Jan. 2006, doi: 10.1109/TED.2005.860659.

[179] M. Berto *et al.*, “EGOFET Peptide Aptasensor for Label-Free Detection of Inflammatory Cytokines in Complex Fluids,” *Adv. Biosyst.*, vol. 2, no. 2, p. 1700072, Feb. 2018, doi: 10.1002/adbi.201700072.

[180] M. Berto *et al.*, “Label free detection of plant viruses with organic transistor biosensors,” *Sens. Actuators B Chem.*, vol. 281, pp. 150–156, Feb. 2019, doi: 10.1016/j.snb.2018.10.080.

[181] Q. Li *et al.*, “Integrated Low Voltage Ion Sensing Organic Field Effect Transistor System on Plastic,” *IEEE Electron Device Lett.*, vol. 39, no. 4, pp. 591–594, Apr. 2018, doi: 10.1109/LED.2018.2808192.

[182] A. Loi, I. Manunza, and A. Bonfiglio, “Flexible, organic, ion-sensitive field-effect transistor,” *Appl. Phys. Lett.*, vol. 86, no. 10, p. 103512, Mar. 2005, doi: 10.1063/1.1873051.

[183] A. Spanu *et al.*, “A high-sensitivity tactile sensor based on piezoelectric polymer PVDF coupled to an ultra-low voltage organic transistor,” *Org. Electron.*, vol. 36, pp. 57–60, Sep. 2016, doi: 10.1016/j.orgel.2016.05.034.

[184] S. W. Park, P. S. Das, and J. Y. Park, “Development of wearable and flexible insole type capacitive pressure sensor for continuous gait signal analysis,” *Org. Electron.*, vol. 53, pp. 213–220, Feb. 2018, doi: 10.1016/j.orgel.2017.11.033.

[185] Y. Jiang, Z. Liu, Z. Yin, and Q. Zheng, “Sandwich structured dielectrics for air-stable and flexible low-voltage organic transistors in ultrasensitive pressure sensing,” *Mater. Chem. Front.*, vol. 4, no. 5, pp. 1459–1470, 2020, doi: 10.1039/D0QM00062K.